UNIVERSIDADE FEREDAL DE SÃO CARLOS
CENTRO DE CIÊNCIAS EXATAS E DE TECNOLOGIA
PROGRAMA DE PÓS-GRADUAÇÃO EM CIÊNCIA E ENGENHARIA DE MATERIAIS

SPRAY FORMING OF WEAR AND CORROSION RESISTANT BIMETALLIC PIPES: FROM THE ALLOY DESIGN TO THE SEMI-INDUSTRIAL PROCESS

Guilherme Zepon

São Carlos
2016

UNIVERSIDADE FEREDAL DE SÃO CARLOS
CENTRO DE CIÊNCIAS EXATAS E DE TECNOLOGIA
PROGRAMA DE PÓS-GRADUAÇÃO EM CIÊNCIA E ENGENHARIA DE MATERIAIS

SPRAY FORMING OF WEAR AND CORROSION RESISTANT BIMETALLIC PIPES: FROM THE ALLOY DESIGN TO THE SEMI-INDUSTRIAL PROCESS

Guilherme Zepon

Tese apresentada ao Programa de Pós-Graduação em Ciência e Engenharia de Materiais como requisito parcial à obtenção do título de DOUTOR EM CIÊNCIA E ENGENHARIA DE MATERIAIS

Orientador: Dr. Claudemiro Bolfarini
Agência Financiadora: FAPESP

São Carlos
2016

Ficha catalográfica elaborada pelo DePT da Biblioteca Comunitária UFSCar
Processamento Técnico
com os dados fornecidos pelo(a) autor(a)

Z57s

Zepon, Guilherme
Spray forming of wear and corrosion resistant bimetallic pipes : from the alloy design to the semi-industrial process / Guilherme Zepon. -- São Carlos : UFSCar, 2016.
169 p.

Tese (Doutorado) -- Universidade Federal de São Carlos, 2016.

1. Ligas. 2. Conformação por spray. 3. Desgaste. 4. Corrosão. I. Título.

DEDICATION

This doctoral thesis is dedicated to my family, Eleodora, Antonio Carlos, Muriel Tamires and Cibele.

VITAE DO CANDIDATO

Mestre em Ciência em Engenharia de Materiais pela UFSCar (2013), Engenheiro de Materiais pela UFSCar (2011).

UNIVERSIDADE FEDERAL DE SÃO CARLOS

Centro de Ciências Exatas e de Tecnologia
Programa de Pós-Graduação em Ciência e Engenharia de Materiais

Folha de Aprovação

Assinaturas dos membros da comissão examinadora que avaliou e aprovou a Defesa de Tese de Doutorado do candidato Guilherme Zepon, realizada em 29/02/2016:

Prof. Dr. Claudemiro Bolfarini
UFSCar

Prof. Dr. Claudio Shyinti Kiminami
UFSCar

Prof. Dr. Walter José Botta Filho
UFSCar

Prof. Dr. Ricardo Pereira Nogueira
PI

Dr. Volker Uhlenwinkel
UNI-BREMEN

Certifico que a sessão de Defesa realizou-se com a participação à distância dos membros Ricardo Pereira Nogueira e Volker Uhlenwinkel e, depois das arguições e deliberações realizadas, os participantes à distância estão de acordo com o conteúdo do Parecer da Comissão Julgadora redigido neste Relatório de Defesa.

Prof. Dr. Claudemiro Bolfarini – Presidente de Comissão Julgadora

AKNOWLEDGEMENT

I would like to thank FAPESP for its financial support. Doctorate scholarship (Grant number: 12/25352-4) and the scholarship abroad (Grant number: 14/07384-1).

I am very grateful to my supervisor Professor Claudemiro Bolfarini for his advice, support and encouragement.

I would like to thank Dr. Volker Uhlenwinkel and Prof. Ricardo Nogueira for welcoming me in their laboratories and for all attention they have given me during my period abroad.

I also would like to thank the laboratory technicians Beto and Lemão for all support in the practical work.

Special thanks to my friends of our research group Eric, Banzo, Brunão, Braulio, Otani, Pama, Ferrugem, Witor, Negão and the LCE staff.

I am also deeply grateful to my dear friends Mono, Bia, Zigoto, Fer, Jeremias, Márcio, Tuco and Jana for sharing with me special moments.

Finally, I would like to thank my parents Eleodora and Antonio Carlos, my sisters Muriel and Tamires, and my girlfriend Cibele for their constant love and support throughout all these years.

ABSTRACT

The oil exploitation and production at the pre-salt fields in a safety and efficient way depends on the development of materials that withstand the severe work conditions found in these fields. For instance, pipes, such as drilling risers and casings, are often subjected to severe wear and corrosion conditions. This thesis is dedicated to evaluate the technical feasibility to produce wear and corrosion resistant bimetallic pipes by spray forming. The processing-microstructure-properties relationship of the spray-formed boron-modified supermartensitic stainless steel (SMSS) grades was comprehensively studied. Deposits of SMSS with boron contents ranging from 0.3 %wt. to 1.0 %wt. were processed by spray forming. The spray-formed boron-modified SMSS deposits had the wear resistance evaluated through different wear tests and their corrosion resistances by means of electrochemical techniques. It was demonstrated that the wear resistance of the spray-formed boron-modified SMSS is determined by the presence of the eutectic network of M_2B-type borides resulted from the spray forming process. On the other hand, the corrosion resistance of the spray-formed boron-modified SMSS is controlled by the chemical composition of the martensitic matrix. Furthermore, spray-formed bimetallic pipes composed of boron-modified SMSS and conventional SMSS were produced in the unique semi-industrial scale spray-forming plant of the Foundation Institute of Materials Science (IWT-University of Bremen, Germany). The relationship between the process parameters and the metallurgical quality of the pipes was addressed. It was shown that the key to produce a spray-formed bimetallic pipe with good metallurgical quality is adjusting the process parameters in such a way that the deposition zone's temperature is kept within the alloy's solidification temperature range during the whole deposition process. Moreover, solidification and grain size evolution models in spray forming were proposed. Finally, the mechanical properties of one of the spray-formed bimetallic pipes in the as-spray formed condition and after heat treatments were evaluated.

CONFORMAÇÃO POR SPRAY DE TUBOS BIMETÁLICOS RESISTENTES AO DESGASTE E À CORROSÃO: DA CONCEPÇÃO DAS LIGAS AO PROCESSAMENTO SEMI-INDUSTRIAL

RESUMO

A exploração e produção de petróleo nos poços do pré-sal de modo seguro e eficiente dependem do desenvolvimento de ligas que suportem severas condições de trabalho. Por exemplo, tubos como *risers* de perfuração e *casings* são frequentemente submetidos à severas condições de desgaste e corrosão. Esta tese se dedica a avaliar a viabilidade técnica de produzir tubos bimetálicos resistentes à corrosão e ao desgaste conformados por spray. A relação processamento-microestrutura-propriedade do aço inoxidável supermartensítico (AISM) modificado com boro e conformado por spray foi estudada de forma abrangente. Depósitos de AISM com teores de boro variando de 0,3%p. a 1,0%p. foram processados por conformação por spray. Os depósitos tiveram a resistência ao desgaste avaliada através de diferentes ensaios e a resistência à corrosão por meio de técnicas eletroquímicas. Demonstrou-se que a resistência ao desgaste das ligas modificadas com boro é determinada pela presença de boretos eutéticos, do tipo M_2B, oriunda do processo de conformação por spray. Por outro lado, a resistência à corrosão das ligas modificadas com boro é controlada pela composição química da matriz. Além disso, tubos bimetálicos compostos de AISM modificado com boro e AISM convencional foram produzidos em escala semi-industrial na planta de conformação por spray do Instituto de Ciência dos Materiais (IWT-Universidade de Bremen). A relação entre os parâmetros de processo e a qualidade metalúrgica dos tubos foi tratada. Mostrou-se que a chave para produzir tubos bimetálicos conformados por spray com boa qualidade metalúrgica é o ajustar os parâmetros do processo de tal modo que a temperatura da zona de deposição permaneça dentro do intervalo de solidificação da liga durante todo processo. Além disso, modelos de solidificação e evolução de tamanho de grão em conformação por spray foram propostos. Finalmente, avaliou-se as propriedades mecânicas de um dos tubos bimetálicos conformado por spray, com e sem tratamentos térmicos.

PUBLICATIONS

- ZEPON, G.; NASCIMENTO, A.R.C.; KASAMA, A.H.; NOGUEIRA, R.P.; KIMINAMI, C.S.; BOTTA, W.J.; BOLFARINI, C. Design of wear resistant boron-modified supermartensitic stainless steel by spray forming process. **Materials & Design** 83 (2015) 214-223.

- ZEPON, G.; ELLENDT, N.; UHLENWINKEL, V.; BOLFARINI, C. Solidification sequence of spray-formed steels. **Metallurgical and Materials Transactions A** 47 (2016) 842-851.

- ZEPON, G.; NOGUEIRA, R.P.; KIMINAMI, C.S.; BOTTA, W.J.; BOLFARINI, C. Electrochemical Corrosion Behavior of Spray-formed Boron-modified Supermartensitic Stainless Steel. Submitted to **Journal of Alloys and Compounds** (January 2016).

x

INDEX

TABLE INDEX

FIGURE INDEX

1 INTRODUCTION

The extraction of oil in the pre-salt layers in the coast of Brazil brought new challenges concerning the development of materials that can withstand the severe work conditions (mainly wear and corrosion issues) found during drilling and exploitation operations. Drilling risers (steel pipes that links the well head on the sea floor to the platform) and casings (steel pipes used to protect the wall of wells during the drilling operations), for example, are frequently subjected to severe wear conditions due to the contact with rotating tool joints of the drill pipes, as represented in Figure 1.1. Moreover, these pipes work in contact with rock debris conduct by the drilling fluids (water or oil based fluids containing mainly bentonite), which increases the wear damage. Such drilling fluids are usually rich in chlorides, increasing the susceptibility of failure caused by wear and corrosion. Figure 1.2 shows examples of failed drilling risers and casings subjected to severe wear and corrosion conditions.

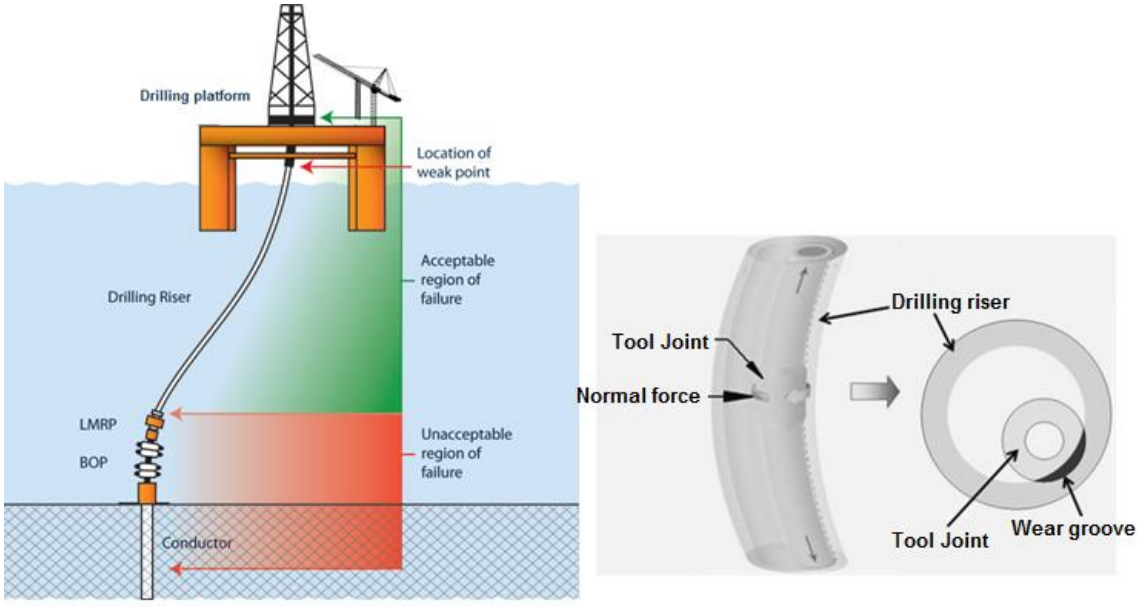

Figure 1.1 - **(a)** Bending of the drilling riser due to the movement of the drilling platform. **(b)** Wear of the drilling riser wall caused by the contact with the rotating tool joint (connectors of the drill pipe).

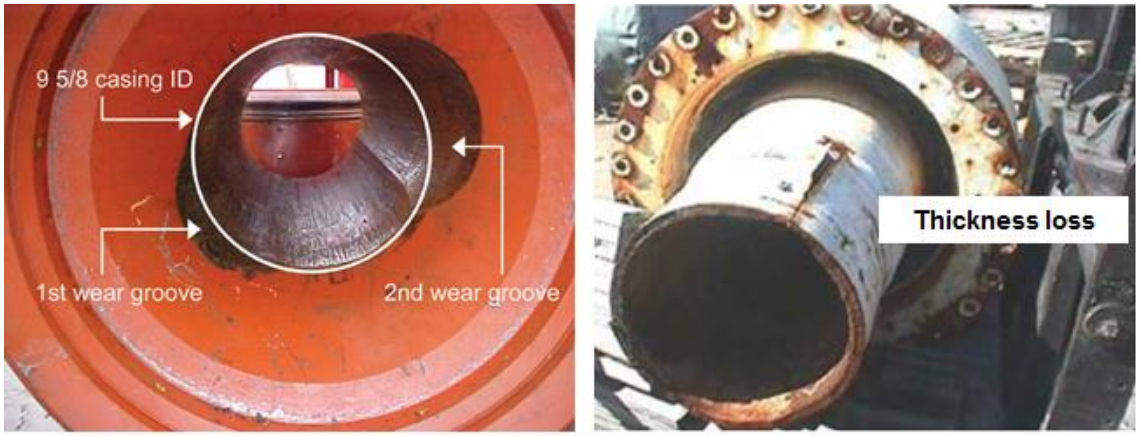

Figure 1.2 - **(a)** Wear grooves caused by the contact of rotating tool joints in the inner wall of a casing. **(b)** Drilling riser failed by thickness loss caused by wear and corrosion.

Over the past few years, encouraged by this challenge, the research group coordinate by Prof. Dr. Claudemiro Bolfarini of the Materials Engineering Department at the Federal University of São Carlos has been studying and developing alloys, which have at same time high wear and corrosion resistance. Several classes of metallic materials such as iron-based amorphous alloys, high intermetallic content alloys and boron-modified stainless steels have been studied aiming at producing coatings for the oil industry equipment [1–7]. Spray forming process was the main process used to develop the wear resistant alloys due to the possibility to produce deposits with high microstructural homogeneity, presenting refined and uniform distribution of second phases and free of macro segregation, even for alloy compositions that are problematical in conventional casting process. Among the developed materials, the spray formed boron-modified stainless steels stood out [1,4,5,7]. Boron contents ranging from 0.3 %wt. up to 3.5 %wt. were added to the chemical composition of different stainless steel grades, such as superduplex, ferritic and supermartensitic. Boron addition combined to spray forming process led to microstructures with different fractions of hard borides uniformly distributed in the steel matrixes, which resulted in considerable increase of the steel's wear resistance. However, two issues were raised from these previous works. Firstly, the formation of borides such as M_2B

and M_3B_2 (where M = Fe, Cr, Ni, Mo) alters significantly the chemical composition of the steel's matrixes, resulting in changes of the stables phases of the systems. For instance, the boron-modified superduplex stainless steel presented a matrix preferentially austenitic and, high boron contents in the ferritic stainless steel resulted in a final martensitic microstructure. Secondly, the question of how the spray-formed alloys could be applied as pipe coatings was brought to light.

Based on these issues, this thesis will present a comprehensive study of the spray-formed boron-modified supermartensitic stainless steel (SMSS) grades, aiming at (i) addressing the composition-processing-microstructure relationship, and (ii) addressing the microstructure-properties relationship regarding the wear and corrosion resistances. Furthermore, this thesis is dedicated to study the processing of spray-formed bimetallic pipes composed of boron-modified SMSS (inner layer or wear resistant coating) and conventional SMSS (outer layer). The main objective of the thesis is to address the challenges to produce such spray-formed bimetallic pipes.

2 LITERATURE

2.1 Spray Forming and Co-Spray Forming Fundamentals

Spray forming is an advanced casting process in which the molten metal is directly converted to an homogeneous solid with refined structure. As shown schematically in Figure 2.1, spray forming comprises two steps: (i) atomization: the melt stream is gas atomized to produce a spray of 10 to 500 μm-diameter alloy droplets. Under action of the atomizing gas the droplets are accelerate up to 100 $m.s^{-1}$ and cooled during the flight at typically 10^2 to 10^4 $K.s^{-1}$; and (ii) deposition: fully liquid, partially solid and complete solid droplets are deposited onto a substrate generating a growing spray-formed deposit. During the deposition the cooling rate of the spray-formed deposit is relatively lower, typically from 0.1 to 10 $K.s^{-1}$, depending on the alloy properties and the process conditions applied [8,9]. Billets, sheets, rings and tubes can be successfully spray formed by using appropriate substrate geometry and relative movements, see Figure 2.1 [10–21].

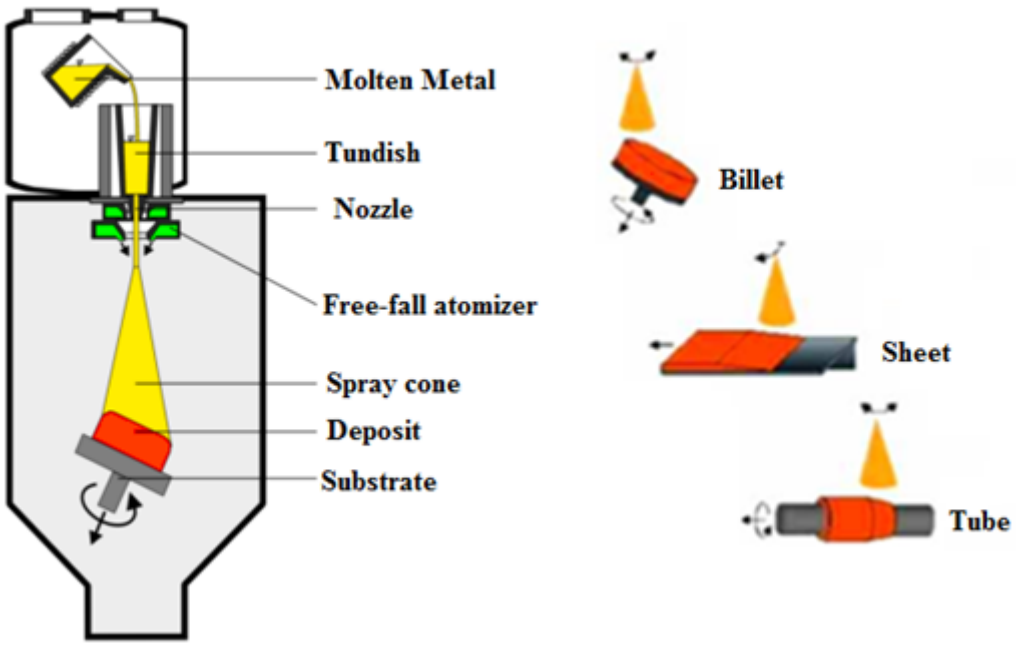

Figure 2.1 - Schematic representation of spray forming process.

Spray-formed microstructures are typically composed of equiaxed grains with diameter ranging from 10 to 100 μm, complete absence of columnar/dendritic morphologies, high levels of microstructural homogeneity and low levels of macrosegregation. The main advantage of the spray forming process arises from the ability to produce this characteristic spray-formed microstructure regardless the engineering alloy system, allowing the manufacture of alloy compositions that are problematical in conventional casting processes. Al-based alloys [22–30], high alloy tool steels [13,14,31–35], Ni superalloys [17,36,37] and high-chromium cast irons [38–41] are examples of alloys successfully produced by spray forming.

The advantageous microstructure produced by the spray-forming process is well-known from research; however, solidification mechanism at the deposition zone and the creation of such a characteristic microstructure are still an open discussion in literature. How the microstructure of the droplets (usually columnar/dendritic) that impact the deposition zone completely solidified turns into the equiaxed microstructure of spray-formed deposits, is neither well explained nor understood yet. Different solidification models to explain the generation of the equiaxed grains in spray deposited alloys have been reported in the literature [9,42–44]. The first one, called dendrite arm fragmentation model, argues that dendritic arms present in the partially solidified droplets are extensively fragmented because of: (i) the mechanical forces produced by the impact of the droplets on the deposition zone; and (ii) the shear stresses induced by the turbulent fluid convection in the deposition zone. Such dendrite fragments become potent nuclei for solidification, which grow and generate the equiaxed grains microstructure [42,44]. Subsequently, P. Grant [9] proposed that the deposition zone must have an equilibrium temperature above the *solidus* temperature, which is constant during the deposition process. Consequently, part of the solid fraction of the droplets is remelted in the deposition zone in order to reach the equilibrium liquid fraction. According to the author, the significant liquid fraction and the temperature gradient present in the deposition zone facilitate the spheroidization of the remaining solid fragments in an attempt to minimize the solid/liquid interfacial area. Although this model is well supported by theoretical aspects, experimental validation was missing. For instance, no measurements of

the equilibrium temperature were presented and only microstructures with considerable grain coarsening after solidification were shown. Recently, H. Henein [43] argued that solidification must occur in discrete regions and that there cannot be any liquid merging between adjacent droplets at the deposition zone. The argument is because the same eutectic fraction (lower than the equilibrium fraction) was observed in both the impulse atomized droplets and in the deposit formed by impulse spray of the Al-0.61%wt.Fe alloy. The lower eutectic fraction suggests that eutectic undercooling is taking place. The author suggests that when the droplets are atomized, they are covered by a nano-thick oxide coating which is not broken when the droplets impact the deposition zone, preserving what the author calls the “droplet region”. According to the author, solidification at the deposition zone of the “droplet regions” continues independently of the solute in adjacent “droplet regions”. When the deposit cools further, each “droplet region” must nucleate its own second phase, achieving the same fraction of eutectic as the atomized droplets. Nevertheless, the formation of the nano-thick oxide layer was not validated. Moreover, this model does not explain the formation of the equiaxed grains characteristic of spray-formed alloys.

In contrast to the remarkable as-spray formed microstructure, the main disadvantages of the spray forming process includes (i) the presence of some level of porosity which, depending on the application, requires closing by further processing steps; and (ii) process yield, i.e. the ratio of feedstock and final deposit mass, usually in the range of 60 to 90% [45]. This yield range arises from the fact that not all droplets created by atomization end up in the spray-formed deposit [46–48]. The metallurgical quality of spray-formed deposits, e.g., microstructure, porosity, segregation, residual stresses, and presence or absence of cracks, is determined by the thermal history of the deposit during the deposition process. The thermal history of the deposit is strongly influenced by: (i) alloy’s physical properties such as thermal conductivity, thermal emissivity, latent heat of solidification; (ii) process parameters such as melt superheat (over temperature above the alloy's *liquidus* temperature), melt flow rate, gas to metal ratio (GMR), spray distance, substrate temperature and geometry of the preform; and (iii) physical properties of the substrate material [10,20,36,49,50]. Figure 2.2 shows

a comparison between the thermal gradient of spray-formed billets in different stages of the deposition process for two different alloys: CuSn6 and 100Cr6 tool steel (AISI 52100). The numerical simulations were performed using approximately the same process conditions (see Table 2.1) and the differences in the thermal history arises mainly from the different materials properties [10,50].

Table 2.1 - Materials properties and standard boundary conditions used for the numerical simulation of spray forming of CuSn6 and 100Cr6 steel billets [10,50].

	CuSn6	**100Cr6 (AISI 52100)**
Liquidus temperature [K]	1325	1724
Solidus temperature [K]	1189	1570
Latent heat of solidification [kJ.kg^{-1}]	200	287
Average thermal conductivity [W.m^{-1}.K^{-1}]	153	30
Density [kg.m^{-3}]	8484	7810
Average specific heat [J.kg^{-1}.K^{-1}]	478 (Cu, 1023 K-1301 K)	640 (1570 K-1800 K) 724 (1570 K-1400 K)
Average liquid fraction of the spray	**0.5**	**0.5**
Average temperature of the impinging spray [K]	1295	1648
Convective heat transfer coefficient (billet surface) during spray [W.m^{-2}.K^{-1}]	280	$hg = h_{max}\exp\left[-1.65\left(\frac{\mathrm{D}}{\mathrm{D_{max}}}\right) + 0.85\left(\frac{\mathrm{D}}{\mathrm{D_{max}}}\right)^2\right]$ where D= distance to the top surface of the billet and D_{max}= reference distance = 400mm
Convective heat transfer coefficient (billet surface) after spray [W.m^{-2}.K^{-1}]	10	10
Temperature of ambient air and spray chamber [K]	523	523
Emissivity of the billet surface	0.18	0.5
Coefficient heat transfer between billet and substrate [W.m^{-2}.K^{-1}]	1000	1000
Initial temperature of the substrate [K]	303	303

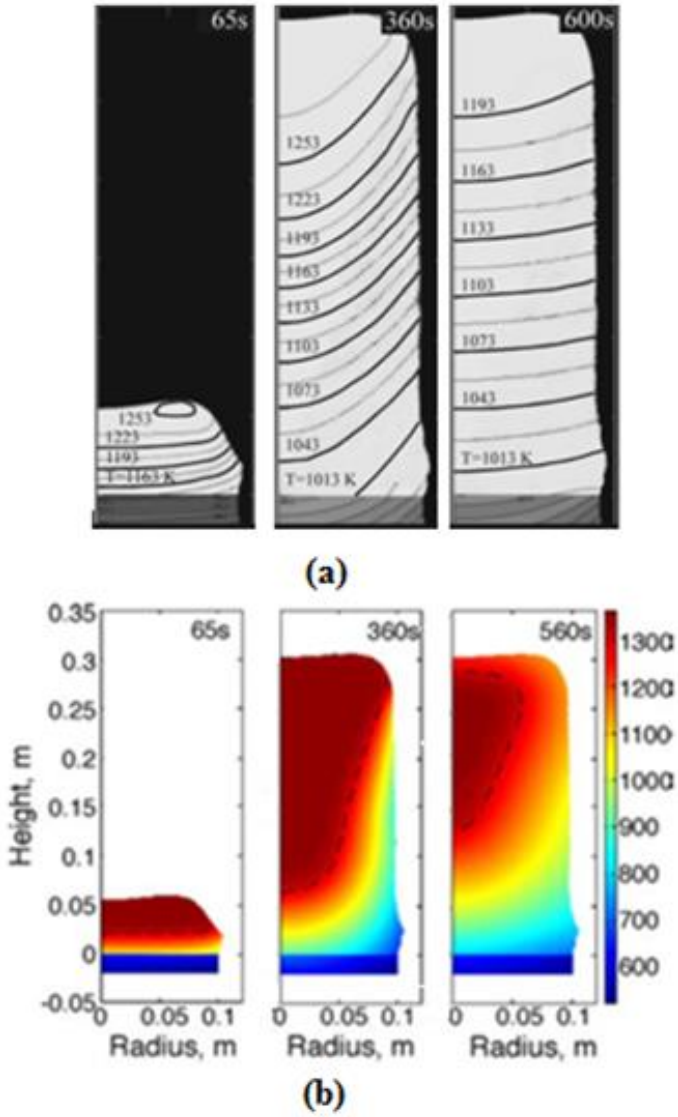

Figure 2.2 - Numerical simulation results showing the overall temperature at different times of **(a)** CuSn6 and **(b)** 100Cr6 steel (AISI 52100) billets spray-formed using similar process conditions. Total time of the spraying process: 360 s [10,50].

One can see that in both cases with increasing of time and growing of the billet, a heat flux from the top surface toward the substrate is observed and an axial temperature gradient is created. However, it can be seen that after the spraying period (t > 360 s) the CuSn6 billet presents a relative low radial gradient whereas the 100Cr6 steel billet shows a high temperature gradient in both axial and radial directions. Such different temperature gradients arise mainly from the different thermal conductivity of both materials: 153 $W.m^{-1}.K^{-1}$ and 30 $W.m^{-1}.K^{-1}$

for CuSn6 and 100Cr6 steel, respectively. The high thermal conductivity of the cooper alloy allows easy homogenization of the billet temperature leading to uniform solidification, that is essential for obtaining an uniform microstructure. On the other hand, after the spraying period (>360 s) the billet cools down slowly due to the high temperature gradient caused by the low thermal conductivity of 100Cr6 steel. In this case, the residual liquid is enclosed by the completely solidified material and, if shrinkage is suppressed, residual stress may rise and initiate hot cracks.

Whereas the materials properties are fixed, the process parameters can be varied in order to optimize the thermal history of the spray-formed deposits and, consequently, their final metallurgical quality. Three major parameters can be changed: (i) the specific enthalpy of the impacting spray; (ii) the heating loss during the spray process; and (iii) the heating loss after the spraying period. The specific enthalpy of the spray can be easily changed by varying the melt superheat and/or the gas to metal ratio (GMR), which results in change of the average liquid fraction of the impacting spray. Heat loss during the spray process is influenced by the temperature of the ambient gas and the initial substrate temperature. Preheating systems are often used to control the substrate temperature and influences the heat flux at the bottom of the deposit in the initial stages of the deposition process. Preheating systems are mainly important for production of spray-formed plates, strips and tubes, which are relatively thin and the region near the substrate cannot be neglected. During the cooling after the spraying period the convective heat transfer and the environment temperature can be easily controlled. For instance, by maintaining the gas flux on the deposit surface after the end of the melt flux, the convective heat transfer at the surface of the deposit can be considerably increased, and the thermal gradient and cooling rate of the deposit considered altered.

The substrate geometry also has a great influence in the thermal history of the spray-formed deposits. Figures 2.3 (a)-(c) show the surface distribution of a 100Cr6 steel tubular preform at different spray times calculated using the same standard conditions showed in Table 2.1 (initial temperature of the substrate of 1373 K) [20]. In this case, the mandrel substrate rotates anti-clockwise at a speed

of 2.5 Hz and translates to the left at a speed of 2 mm.s^{-1}, collecting the impinging droplets on its surface and forming a tubular deposit [20]. The highest temperature is positioned below the spray cone and moves to the right as the deposit grows. Once the atomizing gas is spraying toward the preform during the whole deposition period, the mandrel cools fast and the temperature of the early depositing material decreases. The temperature variation along the circumference of the deposit and the mandrel is considerably small due to the fast mandrel rotation. Figures 2.3 (d)-(f) show the temperature distributions across the deposit and the mandrel at different times. During processing the residual liquid region within the deposit (indicate by the isothermal curve of 1570K) is considerably smaller when compared to the 100Cr6 steel billet illustrated in Figure 2.2 (a). In the case of the billet, the enthalpy of the impacting spray is uniformly distributed on the surface of the deposit during the whole deposition, generating a temperature gradient from the top to the bottom of the billet. On the other hand, in the case of the tubular preform, the input enthalpy of the impacting spray acts only in the region under the deposition zone. Moreover, the previously deposited layer will cool down by heat transfer to the gas environment and the substrate, generating a temperature gradient from the centerline of the spray cone towards the left side of the deposit (translation direction). The depositing material has a strong influence on the substrate, but limited in the area below the deposit. The regions of the mandrel, which are not covered by the deposit, are more influenced by the environment gas cooling. As can be seen in Figures 2.4 (a) and (b) the amount of residual liquid within the tubular deposit can also be controlled by changing the input enthalpy from the impinging spray in the same way shown for the billet.

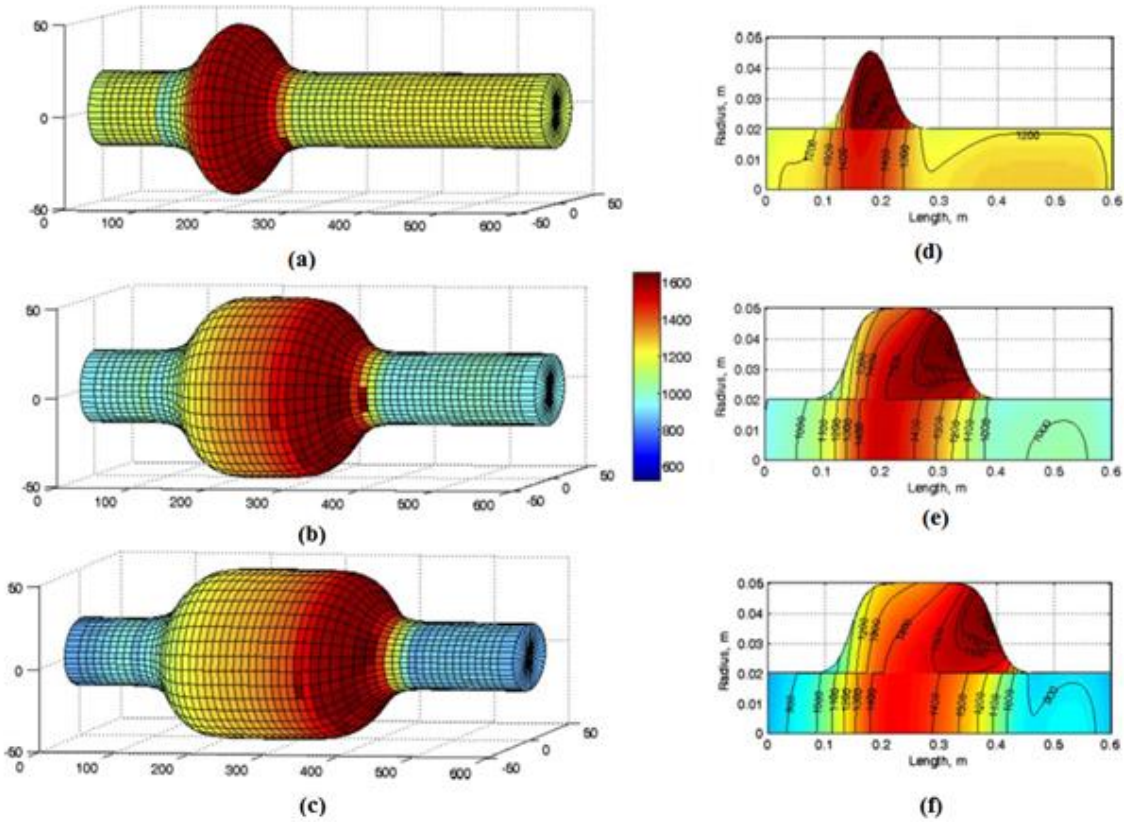

Figure 2.3 - Surface temperature distribution and temperature distribution through the longitudinal section of tubular preform of 100Cr6 steel (AISI 52100) under standard spray condition at spraying time of: **(a)** and **(d)** 30 s; **(b)** and **(e)** 90 s; **(c)** and **(f)** 120 s [20].

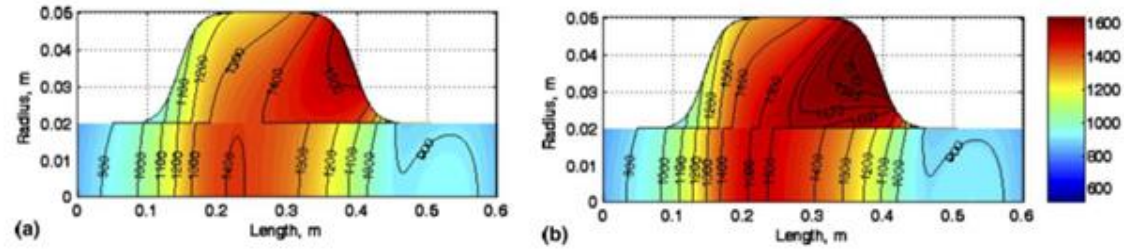

Figure 2.4 - Effect of the enthalpy input from the spray on the thermal profiles of a 100Cr6 steel (AISI 52100) tubular preform at the deposition time of 120 s with average liquid fraction in the spray of **(a)** 0.3 and **(b)** 0.7 [20].

Finding the process parameters that result in the best spray-formed product quality can be challenging. Hardly the set of parameters such as, atomization pressure, GMR, atomization distance, etc. can be extrapolated from one equipment to another. This because different spray-forming equipment, with different atomizer and chamber designs, will produce different mass flux and heat flux distribution for the same set of process parameters. However, V. Uhlenwinkel and N. Ellendt [45] have shown that the surface temperature of the deposit during the deposition process is an important value to predict the porosity level of the spray-formed product. Regardless the processing parameters, the authors proposed that for a specific material, the same porosity level is achieved if the deposit surface temperature is kept constant. Figure 2.5 presents an example of porosity level as function of deposition surface temperature from collected data of several spray forming runs of Ni superalloy rings. The porosity values vary with the deposit surface temperature by a V-shaped behavior, with higher porosity values found when low deposit surface temperatures are measured. Meyer et al. [16] have shown that the same relationship between the porosity level and the deposit surface temperature can be observed in spray-formed sheets and different materials such as Cu alloys (Al-bronze and Sn-bronze) and nitriding steel. Moreover, by using the concept of dimensionless enthalpy of deposit surface (h^*_{surf}), the authors have shown that the lower porosity levels are always obtained when the deposit surface temperature is above the alloy's *solidus* temperature – Figure 2.6. The authors also showed that cold porosity in the vicinity of the substrate can be considerably reduced by preheating the substrate at temperatures close to the alloy's *solidus* temperature. However, the magnitude of the minimum porosity level is strongly dependent on the material.

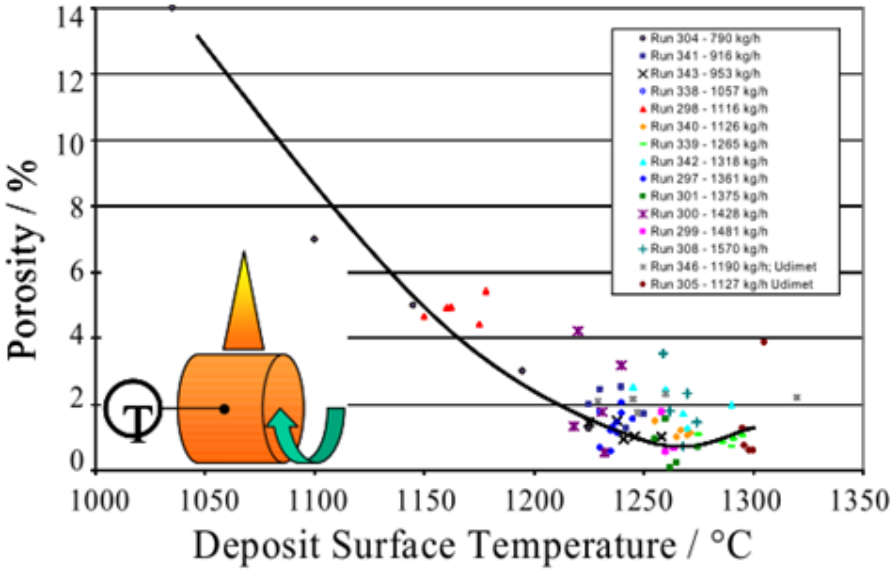

Figure 2.5 - Porosity versus deposit surface temperature of spray-formed Ni superalloy rings [45].

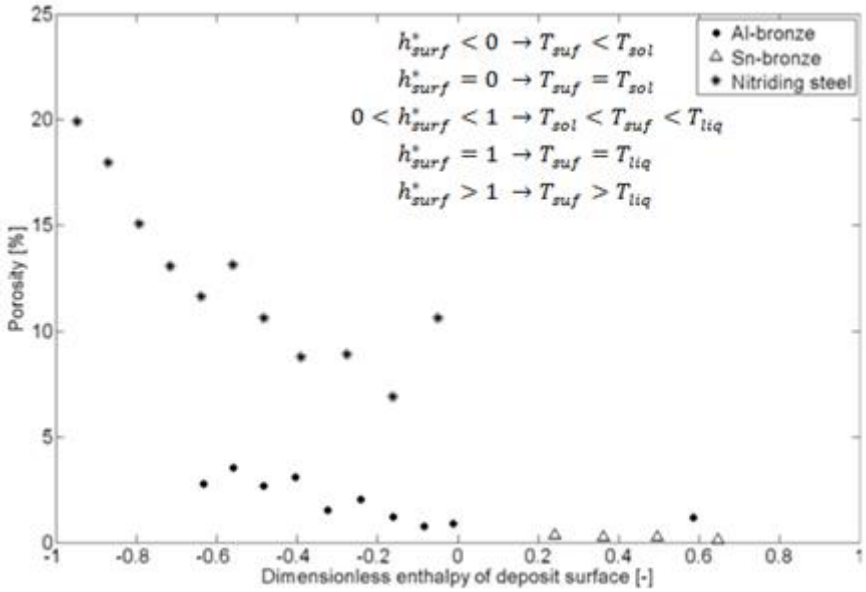

Figure 2.6 - Effect of the dimensionless enthalpy of deposit surface on porosity of Al-bronze, Sn-bronze and nitriding steel [16].

Recently, spray forming of multi-layer deposits with two sprays of different alloys has been developed [51–53]. Figure 2.7 shows schematic representation of the so-called co-spray forming process. Two sets of induction heating furnaces and pouring systems are used to delivery and atomize simultaneously different

alloys by free fall atomizer. When the substrate, tube or plate-shaped, moves through the two sprays successively, a two-layer deposit in the corresponding shape is obtained. Such multi-layer deposits are of great interest in applications where different set of properties is necessary in a single product [51]. When the two sprays are separated and parallel to each other, as represented in Figure 2.5, both spray cones do not interact to each other before they reach the substrate. In this case, the interface between the two deposited layers is relatively flat with an abrupt transition from one layer to another. Figure 2.8 presents a co-spray formed tube, which combines a Co-based alloy (Stellite 21) and a hot working steel (AISI H13) to be used in a blade for the hot forming industry. The abrupt transition between both layers can be clearly seen and a porous interface is observed by liquid penetrant inspection [53]. The major challenge in the co-spray forming process is to create an interface between the two different alloys without a porous zone.

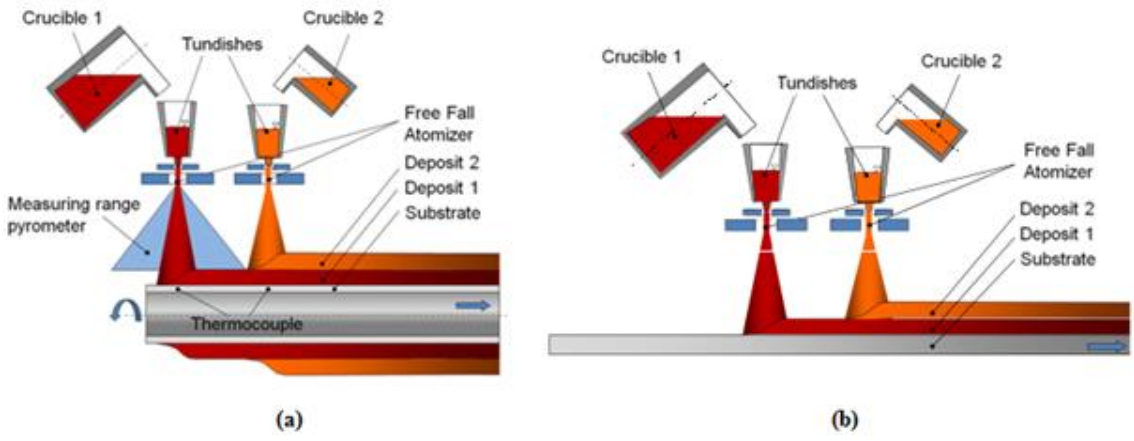

Figure 2.7 - Schematic representation of co-spray forming process by-layer **(a)** tubes and **(b)** plates.

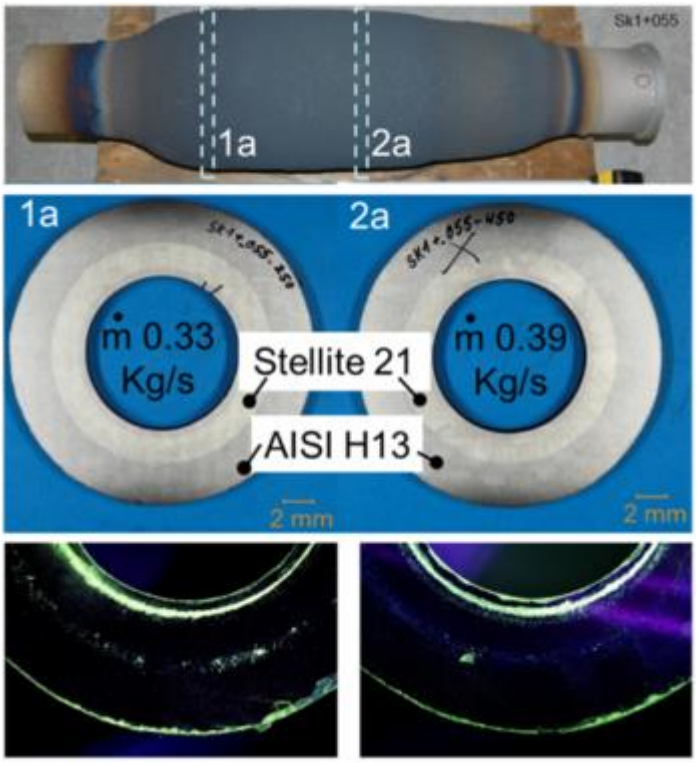

Figure 2.8 - Cross sections of a Stellite21/AISI H13 steel co-spray formed tube processed with different parameters and the results of their liquid penetrant inspection [53].

It is possible to vary the distance between both spray cones by tilting the atomizers as shown in Figure 2.9. In this case, an overlapping of both spray cones can be achieved, which leads to a gradual transition zone between the deposited layers. Accordingly, a gradual transition of chemical composition, microstructure and properties within the spray-formed product is possible to be achieved. The thickness of the gradient zone can be adjusted by changing the distances and the amount of overlapping between the two spray cones [51,52]. The characteristic of the gradient zone will strongly depend on the chemical interaction between the two different alloys.

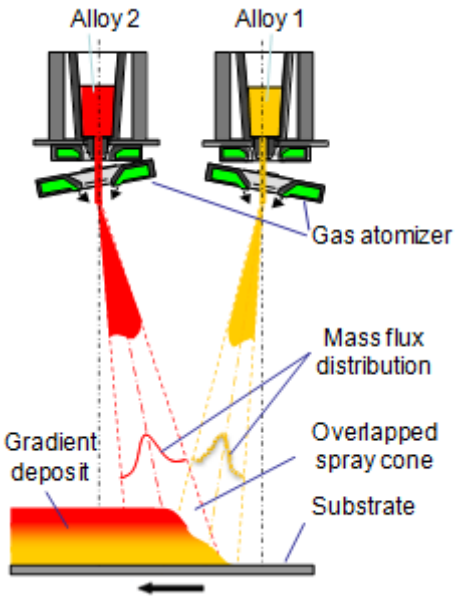

Figure 2.9 - Schematic of co-spray forming of a gradient deposit from two different alloys using scanning gas atomizers [51].

2.2 Supermartensitic Stainless Steel

Since the early 1980s, the use of 13%Cr martensitic stainless steel grades was widely accepted in OCTG (Oil Country Tubular Goods) segment, such as pipelines, casings and risers, because of their excellent corrosion resistance, mainly in oil and gas wells containing some level of carbon dioxide [54]. However, the use of conventional type of 12-13% Cr steels, such as AISI 410 and AISI 420, has the inconvenience of their limited weldability, which requires preheating prior to welding and post weld heat treatment (PWHT) [55]. In 1990s, the duplex and superduplex stainless steel grades were extensively applied in pipelines replacing the conventional martensitic steel grades [54]. In the same period the weldable 13%Cr martensitic stainless steel grades, also called “Super 13Cr” or supermartensitic stainless steel (SMSS), were developed with improved resistance to general and localized corrosion and to sulfide stress cracking (SSC) [55,56]. Because of its enhanced properties and price, considerably cheaper than the duplex and superduplex grades, the SMSSs became an economical choice for combating CO_2 corrosion and mildly sour conditions [54,57]. Between 1996 and 2002, approximately 650 km of SMSS pipelines were installed, being 91.3%

seamless pipes, 4.4% centrifugally-cast pipes and 4.3% produced by laser or other welding process [54,57].

The SMSS grades are based on the Fe-Cr-Ni-Mo system with up to 13 %wt. of Cr, 2-7 %wt. of Ni, 0.1-2.5 %wt. of Mo, low amounts of carbon, nitrogen, phosphorus and sulfur (C ≤ 0.03 %wt., N, P, S ≤ 0.03 wt.%) [55,56]. The main metallurgical concept of this steel is to increase the effective Cr content by reducing carbon to ultra-low contents (<0.03%wt.), which diminishes considerably the precipitation of $M_{23}C_6$ type carbides (where the main constituent of M has been reported to be Cr). Since the low carbon content reduces considerably the hardenability of the steels, the possibility to improve the weldability by restraining the hardness of the heat-affected zone (HAZ) is also expected. However, the reduction of carbon content should be accompanied to the addition of Ni, a strong austenite-stabilizing element, in order to maintain the martensitic phase without δ-ferrite [55]. Moreover, molybdenum content up to 2.5%wt. is added aiming to improve the general, localized and sulfide stress cracking corrosion resistance.

SMSSs are normally divided into three types: (i) Lean-alloyed grade (11Cr2Ni); (ii) Medium-alloyed grade (12Cr4.5Ni1.5Mo); and (iii) High-alloyed grade (12Cr6Ni2.5Mo) [56]. Table 2.2 outlines the typical chemical composition for the three grades. Beyond the good weldability using industrial welding techniques, such steel grades have been designed to meet requirements in respect of: (i) stress corrosion cracking resistance in the presence of H_2S; (ii) toughness at usual onshore and offshore temperatures; and (iii) high strength.

Table 2.3 shows the relationship between the designed chemical composition and the aimed corrosion resistance. In order to meet higher corrosion requirements higher addition of Ni and Mo are necessary. Figure 2.10 shows that Mo has a strong effect on the general corrosion rate at elevated temperatures – Figure 2.10 (a) – and reduces sulfide stress cracking susceptibility – Figure 2.10 (b) [58]. Kondo et. al [55] show that Mo also improves the resistance of SMSS grades to localized corrosion at elevated temperatures. However, as Mo is a strong ferrite-stabilizing element, its addition must be balanced by a reduction of Cr content (also ferrite-stabilizing element) and by increasing Ni content. The

diagram presented in Figure 2.11 shows that the presence of Mo narrows remarkably the region of martensitic single phase.

Table 2.2 - Typical chemical composition of SMSS grades [56].

	11Cr2Ni (lean)	**12Cr4.5Ni1.5Mo (medium)**	**12Cr6.5Ni2.5Mo (high)**
C (max %wt.)	0.015	0.015	0.015
Mn (max %wt.)	2.0	2.0	2.0
P (max %wt.)	0.030	0.030	0.030
S (max %wt.)	0.002	0.002	0.002
Si (max %wt.)	0.4	0.4	0.4
Cu (max %wt.)	0.2-0.6	0.2-0.6	0.2-0.6
Ni (%wt.)	1.5-2.5	4.0-5.0	6.0-7.0
Cr (%wt.)	10.5-11.5	11.0-13.0	11.0-13.0
Mo (%wt.)	0.1	1.0-2.0	2.0-3.0
N (max %wt.)	0.012	0.012	0.012

Table 2.3 - Alloy design of the SMSS grades to meet target corrosion resistance [57].

Environmental parameter	**11Cr2Ni (lean)**	**12Cr4.5Ni1.5Mo (medium)**	**12Cr6.5Ni2.5Mo (high)**
Temperature	20-100 ºC	20-100 ºC	20-100 ºC
P (CO_2)	10 bar	20 bar	20 bar
P(H_2S)	-	0.005 bar	0.050 bar
pH	3.5-4.5	3.5-4.5	3.5-4.5
Cl^-	600-100,000ppm	600-100,000ppm	600-100,000ppm

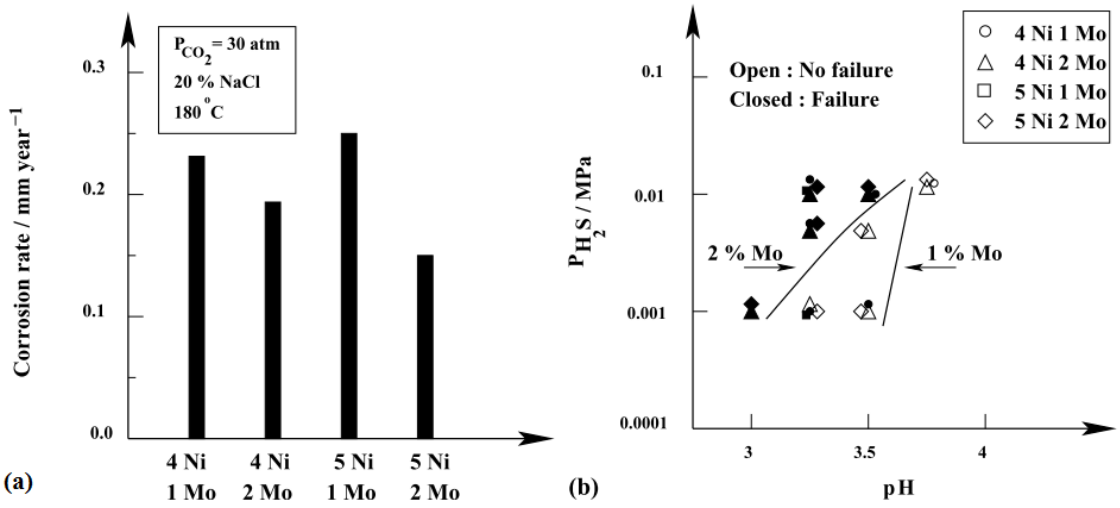

Figure 2.10 - **(a)** Effect of molybdenum on CO_2 corrosion resistance at 180 ºC for two different nickel concentration. **(b)** Effect of molybdenum on the resistance to sulfide stress-corrosion cracking (applied stress: 100% yield strength). Base composition 0.025C-13Cr-0.45Mn (wt%.) [58].

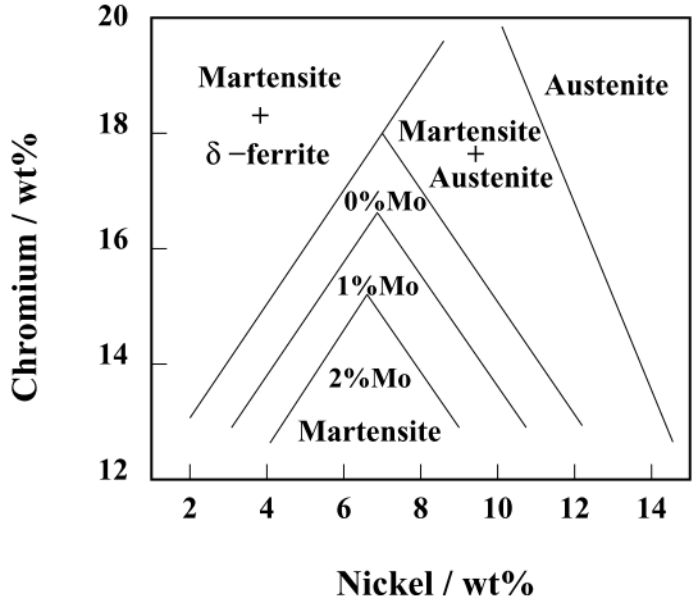

Figure 2.11 - Experimental diagram showing the boundaries of the austenite, ferrite and martensite phases as function of Cr, Ni and Mo concentration for 0.01 wt.% C after austenitization at 1050 ºC and air cooling [55].

Besides the corrosion resistance, controlling the chemical composition and, consequently, the final microstructure is crucial to meet the mechanical properties requirements. For instance, it is well established that coarse δ-ferrite grains strongly reduce the impact resistance of low carbon martensitic steels [59]. On

the other hand, the presence of retained austenite is reported to be beneficial to the impact toughness by means of a localized transformation-induced plasticity (TRIP) effect [60–62]. However, it has been shown that the presence of high fraction of retained austenite increases the hydrogen solubility of the alloy, which increases the susceptibility of hydrogen-induced failure [63,64]. In sub sea oil and gas pipelines, the main hydrogen sources are cathodic protection and hydrogen in weld metal. Figure 2.12 shows the impact resistance at low temperatures (chary-V tests) of rolled plates of the three typical SMSS grades after quenching and tempering heat treatments. One can see that when the microstructure is optimized trough heat treatment and no δ-ferrite is present, the three grades of SMSS present remarkable impact resistances at sub-zero temperatures. Table 2.4 shows the typical tensile properties of the three SMSS grade after such optimized heat treatment [56]. Some authors reported that the mechanical properties of the SMSS grades can be increased by addition of low amounts of Ti and Nb (about 0.1 %wt.) due to the precipitation of fine titanium/niobium carbonitrite particles in the martensitic matrix [65,66]. Moreover, adding Ti/Nb decreases the amount of Cr-rich precipitates, as both combine preferentially with residual nitrogen and carbon to form nano-scale precipitates during tempering, which is also beneficial to the corrosion resistance.

Table 2.4 - Mechanical properties of the three SMSS grades. Hot rolled plates after optimized heat treatments with tempering temperatures close to AC_1 [56].

	11Cr2Ni (lean)	**12Cr4.5Ni1.5Mo (medium)**	**12Cr6.5Ni2.5Mo (high)**
Yield Stress $Rp_{0.2}$ (MPa)	641	738	705
Tensile Stress (MPa)	826	889	878
5d Elongation (%)	18	19	22

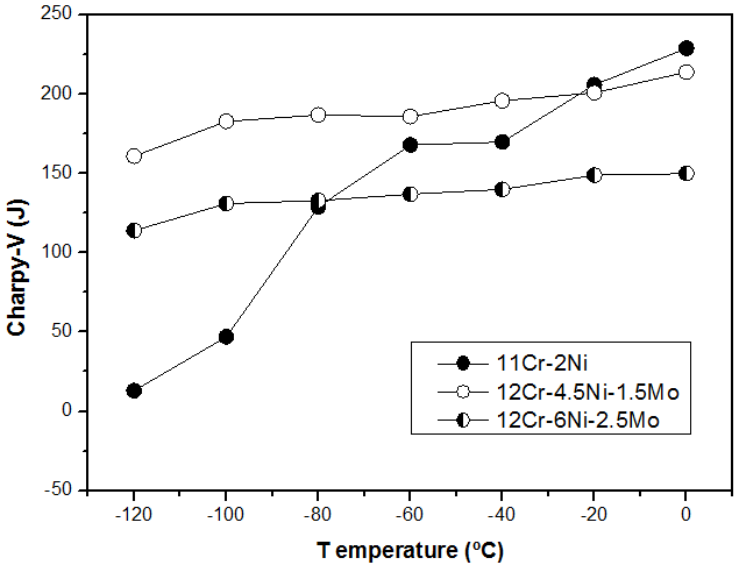

Figure 2.12 - Impact resistance (Charpy-V) at sub-zero temperatures of the three typical SMSS grades. Optimized microstructure free of δ-ferrite. The hot rolled plates were heated over 800 ºC and water quenched. The optimum balance between strength and toughness is achieved after tempering in a narrow range of temperatures close to AC_1. Typical grain size is ASTM: 7-10.

2.3 Boron modified stainless steels

In spite of good mechanical and corrosion properties, stainless steel grades are usually known for presenting low wear resistance. Several applications such as tubing, pumps and valves found in oil exploitation and production require materials that combine high mechanical and corrosion resistance to high wear resistance. Typical examples are the drilling casings and risers which must present: i) high mechanical properties to withstand the high stresses; ii) high corrosion resistance due to the marine environment and the often presence of CO_2 and H_2S contents; and iii) high wear resistance due to the contact of the rotating drilling pipe to its inner wall. However, it is a big challenge to find a material presenting this set of properties. Based on this, many developments of alloys to be applied as wear and corrosion resistant coatings to conventional steels have been performed.

Since 1960's it is well known that boriding is one of the most effective methods for increasing the wear resistance of steel parts due to the formation of hard borides such as Fe_2B (1600 HV) and FeB (1800 HV) [67,68]. In the last few years,

the research group of the Materials Engineering Department at the Federal University of São Carlos has reported several developments of boron modified stainless steels processed by spray forming [1,4,5,7]. The addition of boron to the chemical composition of stainless steel grades leads to formation of hard borides, mainly M_2B-type borides (where M is composed of the transition metal usually present in stainless steels such as Fe, Cr, Ni, Mo), while maintaining the features of the stainless steel matrix. In 2011, Beraldo, L. [1] reported the first developments on boron modified superduplex stainless steel (SDSS). Figure 2.13 shows the microstructure of the SDSS modified with 3.7 %wt. of boron processed by spray forming. The addition of high boron content led to formation of high fraction of primary M_2B-type borides embedded in the duplex ferrite/austenite matrix with some fraction of Mo-rich eutectic borides (M_3B_2-type). However, changing in the chemical composition by boron addition resulted in a much higher volume fraction of austenite in the matrix, as high as 90%, far from the usual 50% of conventional SDSS grades. Although such results have shown that controlling the microstructure of boron-modified SDSS may be difficult, the presence of the hard M_2B-type borides in the stainless steel microstructure yields an abrasion wear resistance, measured by the rubber wheel against dry sand method (ASTM G65), as good as Stellite 1016 coatings (commercial wear resistant Co-based alloy). Such promising result led to a series of further developments on different boron-modified stainless steel grades.

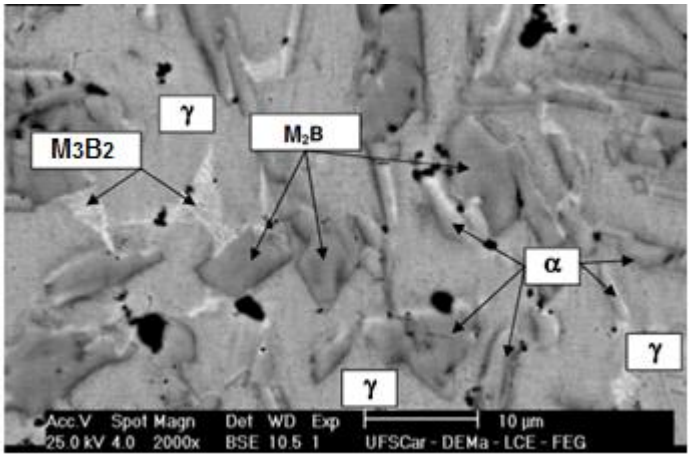

Figure 2.13 - Microstructure of the spray-formed SDSS modified with 3.5%wt. of boron [1].

Nascimento, A.R.C [4] has reported the effect of different boron contents (1.0, 2.0 and 4.0 %wt.) on the microstructure and wear resistance of spray-formed ferritic AISI 430 stainless steel. The author has shown that changing the boron content in the alloy can considerably alter their solidification path resulting in completely different microstructures. When 1.0 and 2.0 %wt. of boron are added, the alloys solidification comprises the formation of primary δ-ferrite, followed by the peritectic reaction $\delta + L \rightarrow M_2B$. During the peritectic reaction, Cr diffuses from the edges of the primary dendrites toward the borides yielding a final microstructure composed of borides embedded in ferritic matrix with a Cr-poor zone around the borides (see Figure 2.14 (a) and (b)). On the other hand, the addition of 4.0 %wt. of boron leads to the formation of primary M_2B borides, which reduces the Cr content of the remaining liquid. When boron is completely consumed by the boride formation, the final remaining liquid has a composition within the γ-austenite field where the solidification is completed. Due to the high levels of alloying elements and the cooling rate of the small spray-formed deposit, the final alloy microstructure comprises large primary borides embedded in a martensitic matrix. The results presented by Nascimento, A.R.C. [4] showed that addition of high boron contents makes more difficult the maintenance of the stainless steel matrix characteristic of the base alloy, which may reduce the corrosion properties as, for instance, in the case of the alloys presenting Cr-poor regions. However, despite the differences between the final microstructures, the wear resistance (evaluated by a plate-on-cylinder wear test) of the boron modified AISI 430 stainless steels are considerably higher than the low alloy high strength steel API X80 (often used in risers and casings manufacture) [4].

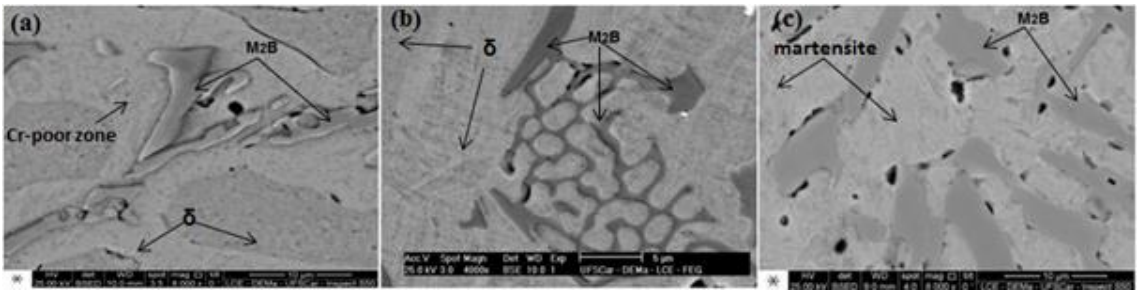

Figure 2.14 - Microstructure of the spray-formed AISI 430 modified with **(a)** 1.0 %wt., **(b)** 2.0 %wt. and **(c)** 4.0 %wt. of boron [4].

Aiming at the achievement of a boron-modified stainless steel grade with high wear resistance and the maintenance of the features and corrosion properties of the base alloy, the development of the boron-modified supermartensitic stainless steel with lower boron contents (up to 1.0 %wt.) was proposed [5]. The first results showed that addition of small boron contents in the SMSS medium alloy grade processed by spray forming results in a microstructure composed of equiaxed martensitic grains with eutectic M_2B-type borides at the grain boundaries (see Figure 2.15). Moreover, when the boron content is increased two effects can be observed: (i) increase in the borides fraction; and (ii) reduction of the equiaxed grain size. Both effects have shown to be beneficial to the alloys' abrasive wear resistance [5,7] . In this doctoral thesis, the complete designing of the spray-formed boron-modified SMSS is present. The microstructural evolution, the relationship between the boride fraction and the wear resistance in different wear mechanisms, and the effect of boron addition on the corrosion properties will be addressed.

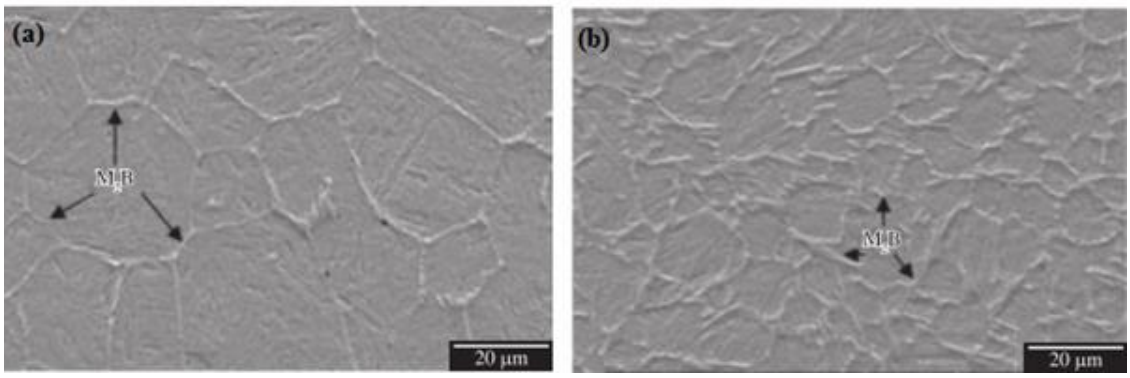

Figure 2.15 - Microstructure of spray-formed SMSS modified with **(a)** 0.3 %wt. and (b) 0.7%wt. of boron [7].

3 OBJECTIVES

The objective of this work is to evaluate the technological feasibility of producing in semi-industrial scale a spray-formed bimetallic pipe, which combines the high wear and good corrosion resistance of a boron-modified SMSS with the high mechanical and corrosion properties of the medium-alloyed SMSS grade.

4 MATERIALS AND METHODS

In order to achieve the stated objective, this work was divided into three parts with well defined goals. Firstly, the comprehensive development of the spray-formed boron-modified SMSS grade will be presented aiming: (i) to understand the relationship between the solidification features of the spray forming process and the final microstructure of the boron-modified SMSS; (ii) to address the relationship between the microstructure of spray-formed boron-modified SMSS grades and their wear resistance; and (iii) to address the effect of the boron addition on the corrosion resistance of the spray-formed boron-modified SMSS with different chemical compositions. Secondly, bimetallic pipes of boron-modified SMSS (inner layer) and conventional medium-alloyed SMSS (outer layer) were produced in a semi-industrial spray-forming plant aiming at: (i) verifying the effects of the larger scale process on the final microstructure of the boron-modified SMSS and the conventional SMSS; and (ii) evaluating the possibility to achieve a high quality product in terms of porosity and microstructural homogeneity. Finally, the mechanical properties of both layers of a bimetallic pipe obtained were evaluated in the as-spray-formed condition, and after heat treatments, aiming to evaluate which level of mechanical properties is possible to be achieved directly from the spray-forming process, which means without further thermomechanical treatments that is beyond the scope of this thesis. The description of the materials and experimental methods applied to each part is described in the next sections.

4.1 Design of Spray-formed boron-modified SMSS

4.1.1 Laboratory Scale Spray Forming

Four different compositions of boron-modified SMSS, hereinafter named SM-0.3B, SM-0.7B, SM-1B and SM-14Cr-1B, were spray formed in the close-coupled spray forming equipment – Figure 4.1 – at the Materials Engineering Department (DEMa) in the Federal University of São Carlos (UFSCar). Commercial medium-alloyed SMSS bar (supplied by Villares Metals S/A.), iron-

boron alloy with 16%wt. of boron, iron-molybdenum alloy with 62 %wt. Mo, commercial pure chromium and nickel were used as raw materials. Table 4.1 shows the aimed chemical composition of the four alloys. In the SM-0.3B, SM-0.7B and SM-1B, the selected composition aimed at adding boron while maintaining the same Cr, Ni and Mo content of the commercial medium-alloyed grade of the SMSS used as base alloy. On the other hand, in the SM-14Cr-1B composition, the addition of 1 %wt. of boron was accompanied by an increase of the Cr content up to 14 %wt. while keeping the same levels of Ni and Mo.

In each spray forming run, approximately 4 kg of raw materials were melted in an induction furnace and spray formed onto a rotating carbon steel disc substrate using N_2 as atomization gas. The pouring temperature of all materials was 1650 ºC, the spray distance 460 mm and the substrate speed 45 rpm. The average melt flow and gas flow of all spray forming runs were approximately 0.133 $kg.s^{-1}$ and 0.170 $kg.s^{-1}$, respectively, resulting in a gas-to-metal ratio (GMR) of approximately 1.2.

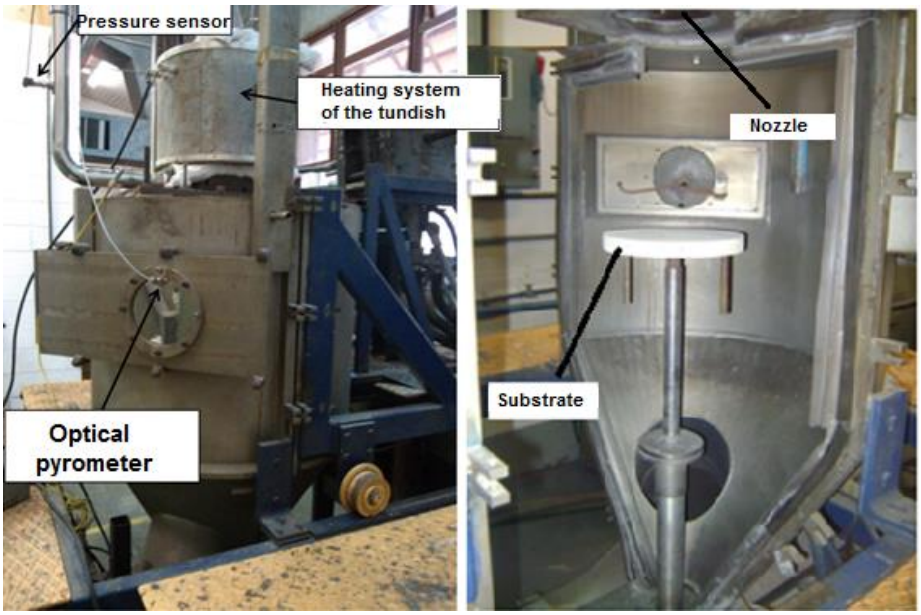

Figure 4.1 - Close-coupled spray forming equipment of the DEMa-UFSCar.

Table 4.1 - Aimed chemical composition of the four spray-formed boron-modified SMSS.

SM-0.3B	**%C**	**%Cr**	**%Ni**	**%Mo**	**%B**	**%Si**	**%Mn**	**%S**
	0.01	11.90	5.80	2.00	0.3	0.25	0.45	<0.01
	%P	**%W**	**%Co**	**%Cu**	**%V**	**%Nb**	**Ti**	**%Fe**
	0.02	0.01	0.03	0.06	0.03	0.01	0.13	Bal.
SM-0.7B	**%C**	**%Cr**	**%Ni**	**%Mo**	**%B**	**%Si**	**%Mn**	**%S**
	0.02	11.90	5.80	2.00	0.7	0.25	0.45	<0.01
	%P	**%W**	**%Co**	**%Cu**	**%V**	**%Nb**	**Ti**	**%Fe**
	0.02	0.01	0.03	0.06	0.03	0.01	0.13	Bal.
SM-1B	**%C**	**%Cr**	**%Ni**	**%Mo**	**%B**	**%Si**	**%Mn**	**%S**
	0.02	11.90	5.80	2.00	1.0	0.25	0.45	<0.01
	%P	**%W**	**%Co**	**%Cu**	**%V**	**%Nb**	**Ti**	**%Fe**
	0.02	0.01	0.03	0.06	0.03	0.01	0.13	Bal.
SM-14Cr-1B	**%C**	**%Cr**	**%Ni**	**%Mo**	**%B**	**%Si**	**%Mn**	**%S**
	0.03	14.00	5.80	2.00	1.00	0.25	0.45	<0.01
	%P	**%W**	**%Co**	**%Cu**	**%V**	**%Nb**	**Ti**	**%Fe**
	0.02	0.01	0.03	0.06	0.03	0.01	0.12	Bal.

4.1.2 Microstructure Characterization

The chemical compositions of the final alloys were determined by inductively coupled plasma atomic emission spectrometry-ICP-AES, excepting C and S that were analyzed by direct combustion. Phase's identification was performed by XRD analysis using a Rigaku Geigerflex ME210GF2 model diffractometer with Cu-Kα radiation. The microstructures were characterized by scanning electron microscopy (SEM) using a FEI Inspect S50 Scanning Electron Microscope. In order to reveal the microstructures the polished samples were etched with a 3HCl:1HNO_3 solution. Deep etching with 10 mL HCl, 3 ml HNO_3, 5 mL $FeCl_3$ and 82 mL ethyl alcohol solution were performed in order to reveal the borides morphologies. Vickers microhardness was measured in accordance with ASTM E384 standards.

4.1.3 Equilibrium Solidification path determination

Thermodynamic simulations by using the Thermo-Calc software were performed to determine the equilibrium solidification path of the boron-modified SMSS grades. The database used was the TCFE7. The pseudo-binary phase diagram of the composition Fe-12%Cr-5%Ni-2%Mo-X%B (%wt.) was calculated using the equilibrium calculator function. The same function was used to calculate the equilibrium phase fractions at different temperatures, ranging from 1000 ºC to 1600 ºC, of the boron-modified SMSSs with the exact chemical composition of the spray-formed deposits produced.

It is worth stressing that recent works of our research group (not published yet) have shown that thermodynamic simulations using Thermo-Calc is an useful tool to determine the equilibrium solidification path of boron-modified stainless steels. However, it is important to point out that such works have shown that since the thermodynamic data available is usually obtained for steels containing low boron contents (< 0.1 %wt. of boron), the *solidus* and *liquidus* temperatures of iron-based alloys with higher boron contents (> 1%wt.) differ considerably from the experimental values.

4.1.4 Wear tests

Wear test specimens were machined from equivalent radial positions of the spray-formed deposits. Two different wear testing were performed in order to evaluate the wear resistance of the spray-formed boron-modified SMSSs. Firstly, the dry sand against rubber wheel abrasive wear test was performed in accordance with the procedure A of ASTM G65-04 standard.

Secondly, a home-made wear testing machine was used to perform a plate-on-cylinder (POC) wear test. Figure 4.2 presents a schematic illustration of the wear test performed. The wear test machine consists of three separate chambers inside each one machined samples with dimensions of 25 x 90 x 10 mm are forced against a rotating quenched and tempered AISI 1040 steel axis with hardness of 55 HRC. Both the samples and axis were surface grinded to average roughness Ra = 1.7 μm. A normal force is applied to the sample by an arm system. In this work an initial normal force of 539.34 N was applied; however,

during the wear tests this initial normal force is slightly increased due to changing in the relative position of the mass center of the arms as consequence of the thickness loss of the sample. This increase of the normal force can be accurately described as a function of the loss thickness (h) by the following polynomial equation: $FN = 539.34 + 7.1267h + 0.0865h^2 + 0.0004h^3$, where the units of FN and h are N and mm, respectively; and these increments were considered to perform the calculus of contact pressure. In all tests, the rotation speed used was 252 rpm. In order to simulate the wear conditions found in risers and casing, the chambers were filled with 6 liters of drilling fluid donated by System Mud ltda. with the composition shown in Table 4.2. Three samples of each material were tested and the values presented here are the mean value and standard deviation of these samples.

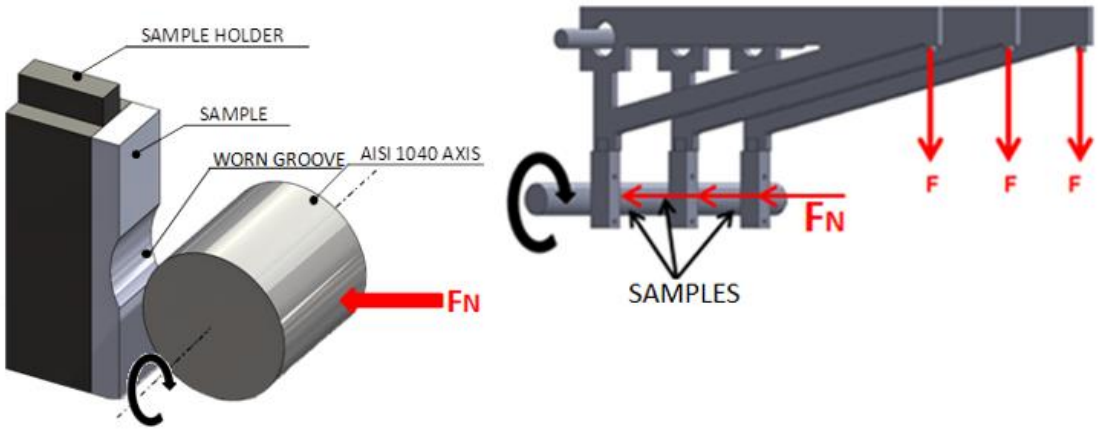

Figure 4.2 - Schematic representation of the plate-on-cylinder wear test.

Table 4.2 - Composition of the drilling MUD used in the plate-on-cylinder wear tests.

	Content
Bentonite	50 g/L
KCl	40 g/L
Viscosifier polymer	3.3 g/L
Sand (AFS 50/70)	85g/L

When the cylinder slides in contact with the sample, a crescent worn groove is formed as shown in Figure 4.2. The groove volume, or the accumulated worn volume, was measured at each 30 min along 10 hours and plotted as function of the sliding distance. The obtained curves were fitted using equation 4.1, which is similar to the empirical model presented by Hall and Malloy [69] to describe the wear behavior of casings and risers in real scale wear tests.

$$V = A\{1 - exp[-B(s^c)]\} \qquad (4.1)$$

Where V is accumulated worn volume in m^3, s is the sliding distance in m and A, B and C are constants parameters that describe the evolution of wear with the sliding distance. As reported in [69], this function in equation 4.1 can represent a remarkable variety of shapes, all of which have one characteristic in common: As the sliding distance increases, the accumulated worn volume approaches to the limiting value A. In other words, this function shows that the wear rate decreases with the increasing of the sliding distance. Physically, reaching the limit A value does not mean that the wear completely stops, but that the wear rate reached very low values, which can be neglected. After fitting the experimental data with equation 4.1, the wear rate (dV/ds) can be calculated by using the equation 4.2.

$$\frac{dV}{ds} = A.B.C.\exp[-B(s^c)].s^{(c-1)} \qquad (4.2)$$

According to the authors [69], the decrease of the wear rate is associated with the reduction of the contact pressure caused by the increase of the contact area when the groove grows. When the limiting A value is reached the contact pressure also reach a constant value, so called threshold contact pressure (TCP). The TCP is now an important wear property, and the lower the TCP values obtained and the faster they are reached in a system, the better is the materials wear resistance.

The commercial medium-alloyed SMSS, whose the microstructure is shown in Figure 4.3, was used as reference alloy in both wear tests, and the results were compared with the spray-formed boron-modified SMSSs.

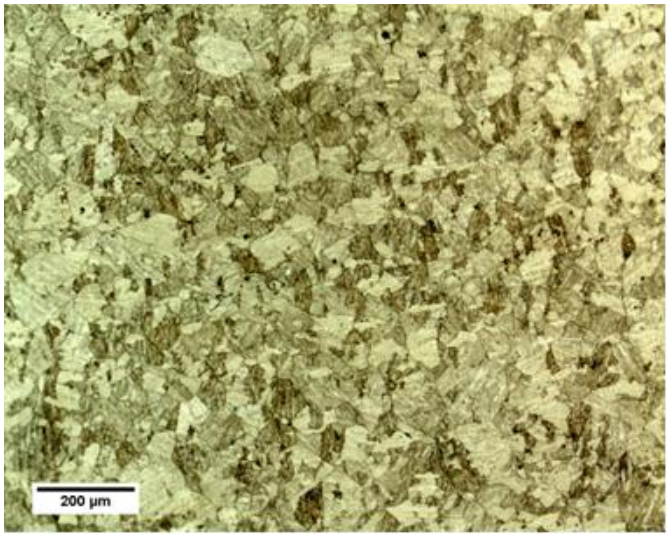

Figure 4.3 - Microstructure of the commercial SMSS bar used as reference alloy for the wear tests. Etching: Vilela.

4.1.5 Electrochemical corrosion tests

Electrochemical corrosion tests were performed in order to evaluate the corrosion resistance of the spray-formed boron-modified SMSSs. The electrochemical tests were carried out at the Laboratory of electrochemistry and physicochemical of materials and interfaces (LEPMI/Grenoble-INP, France). Theoretical fundamentals of the techniques applied in this work can be found in Appendix A. The working electrodes (WE) were the cross section of cylindrical samples with 13 mm-diameter cut by electrical erosion from the SM-0.3B, SM-0.7B, SM-1B and SM-14Cr-1B deposits. Since the spray forming is prone to yield some level of porosity at the external surface layers, the cross section samples of the cylindrical deposits could thus present a high porosity periphery. To avoid this drawback, the top surface of the cylindrical deposits' samples were previously sandpapered until the high porosity region be completed removed (for all samples, removing 2 mm of material was enough to reach the low porosity region, about 1% measured by area fraction). The analyses were hence performed in the low porosity central regions of the cross section samples which were further sandpapered until #600 grit.

Electrochemical impedance spectroscopy (EIS) and potentiodynamic polarization analyses were performed using a conventional three electrodes set up. As counter-electrode (CE) and reference electrode (RE) a platinum sheet and a saturated calomel electrode (SCE) were used, respectively. A schematic representation and a photography of the electrochemical cell used are presented in Figure 4.4. The analyses were carried out using a Gamry potentiostat. A solution of 35 g/L of NaCl in deionized water and pH = 4.0 (controlled by addition of H_2SO_4) was used as electrolyte. Three test protocols were applied:

(I) The samples were immersed 24 h in deionized water for a pre-passivation treatment. After pre-passivation, it was carried out 1 hour of open circuit potential (OCP) measurements in the electrolyte. Subsequently, EIS analysis, with potential amplitude of 10 mV around the OCP value and frequencies varying from 10^5 Hz to 10^{-2} Hz, was performed. Since EIS is a non-destructive technique, after EIS analysis, the sample was kept 10 minutes longer in OCP, and potentiodynamic polarization was carried out in sequence. The potentiodynamic polarization curves were obtained by sweeping the potential from 50 mV below the corrosion potential to a maximum potential (named critical potential - E_{crit}) corresponding to a current of 0.1 $mA.cm^{-2}$.

(II) The samples were directly subjected to 1 hour of OCP measurements, without pre-passivation treatment. Subsequently, the EIS and polarization tests were carried out following the same protocol described above.

(III) The samples were maintained 12 hours in solution while measuring the open circuit potential (OCP). Subsequently, the EIS and polarization tests were carried out following the same protocol described in protocol (I). In this case, after EIS measurements the samples were left 1 hour in OCP before the polarization test.

To observe the corroded surfaces of the spray-formed boron-modified SMSSs, the samples with polished surfaces (using alumina suspension with particle size up to 1 µm) were polarized anodically until the current density has reached 5 $mA.cm^{-2}$. The corroded surfaces were observed by optical microscopy technique.

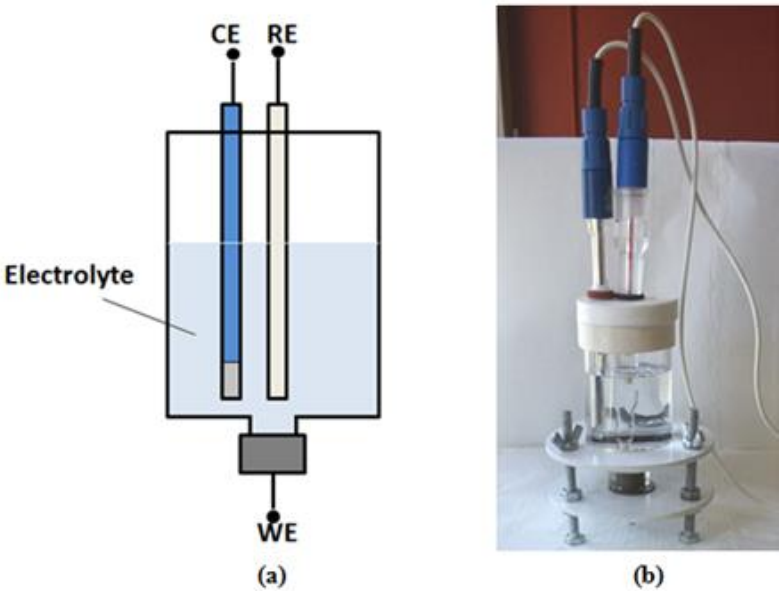

Figure 4.4 - **(a)** Schematic representation and **(b)** photography of the electrochemical cell used for potentiodynamic and EIS analyses.

Electrochemical noise (EN) analyses were carried out in order to evaluate the repassivation kinetics of the spray-formed boron-modified SMSS after a simulated wear event, in the same line of the scratch tests that have been used since several years [70]. Two identical samples of the same alloy were connected as CE and WE at the electrochemical cell in a zero resistance ammeter, ZRA, configuration. After assembling the electrochemical cell, both samples were maintained for 24 hours immersed in the solution. The coupling current between both samples was measured during the last hour of immersion before being interrupted. The surface of the sample acting as CE was then abraded through a #240 grit sandpaper for 10 seconds (using a hand drill with constant rotation), simulating an abrasive or wear event upon the metallic surface. Immediately after finishing the abrasion, the coupling current record was resumed to the survey of the repassivation tendency.

In order to have a comparative basis, the same electrochemical analyses were carried out in a commercial medium-alloyed SMSS (the same one used as reference alloy for the wear tests). Table 4.3 presents the chemical composition of the commercial SMSS used.

Table 4.3 - Chemical composition of the commercial supermartensitic stainless steel (%wt.).

%C	%Cr	%Ni	%Mo	%Si	%S	%P	%Mn
0.007	11.86	5.87	2.00	0.25	0.001	0.016	0.45
%Nb	**%W**	**%Co**	**%N**	**%Cu**	**%V**	**Ti**	**%Fe**
0.01	0.01	0.03	0.0095	0.06	0.03	0.135	Bal.

4.2 Spray forming of semi-industrial scale bimetallic pipes

4.2.1 Spray Forming runs

Three spray forming runs hereinafter named SF1, SF2, and SF3 were carried out at the SK1+ spray forming plant in the IWT-University of Bremen. The Sk1+ spray forming plant has two sets of induction heating furnaces (with capacities of 5 L and 12 L) and pouring systems, which are used to delivery and atomize simultaneously different alloys by free fall atomizer. Figure 4.5 shows the schematic representation of the SK1+ spray forming set up. A rotating cylindrical preform was used as substrate. The boron-modified SMSS and the medium-alloyed SMSS are atomized simultaneously while the substrate translates in such a way that the boron-modified is firstly deposited. The SMSS is then deposited onto the previously deposited boron-modified layer forming the bimetallic pipe.

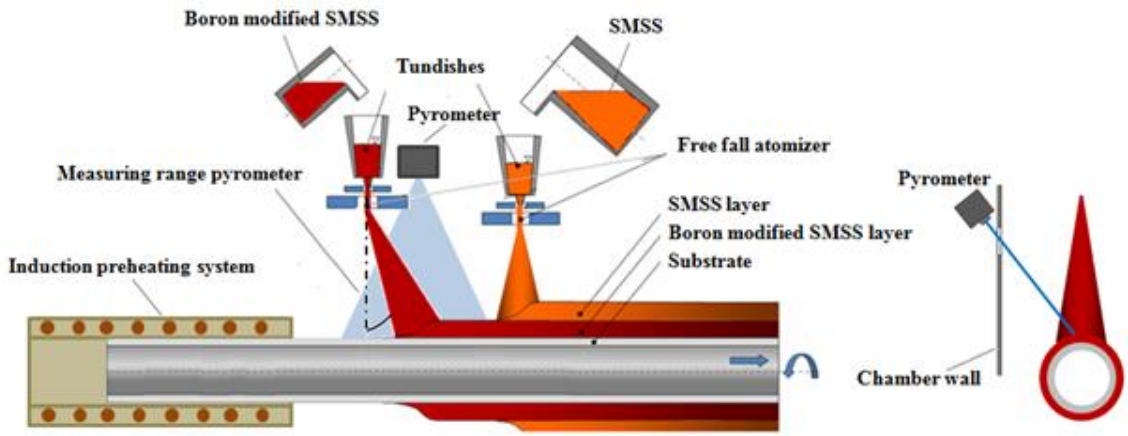

Figure 4.5 - Schematic representation of the co-spray forming process performed at the SK1+ plant in the IWT showing the induction preheating system and optical pyrometer positioning.

In the SF1 run, AISI 316L stainless steel was used as feedstock material. On the other hand, commercial medium-alloyed SMSS was used as base material in the SF2 and SF3 runs. Fe-Mo alloy, Fe-B alloy, Fe, Ni and Cr (commercially pure grades) were added in order to obtain the aimed chemical composition. Table 4.4 shows the chemical composition of the feedstock materials. The amount of material used in each run and the target chemical composition of each spray-formed alloy are shown in Table 4.5 and 4.6, respectively.

Table 4.4 - Chemical composition (%wt.) of the feedstock materials.

AISI 316 L	**%C**	**%Si**	**%Mn**	**%Cr**	**%Ni**	**%S**	**%P**	**%Mo**
	0.03	0.402	1.78	16.00	10.00	0.031	0.039	2.00
	%Nb	**%W**	**%Co**	**%Cu**	**%V**	**%B**	**Ti**	**%Fe**
	0.004	0.048	0.163	0.336	0.056	0	0.011	69.11
SMSS	**%C**	**%Cr**	**%Ni**	**%Mo**	**%Si**	**%S**	**%P**	**%Mn**
	0.007	11.86	5.87	2.00	0.25	0.001	0.016	0.45
	%Nb	**%W**	**%Co**	**%N**	**%Cu**	**%V**	**Ti**	**%Fe**
	0.01	0.01	0.03	0.0095	0.06	0.03	0.135	Bal.
Fe*	**%C**	**%Si**	**%Mn**	**%Cr**	**%Ni**	**%S**	**%P**	**%Mo**
	0.005	0.05	0.2	0.2	0.3	0.025	0.025	-
	%Cu	**%Fe**						
	0.2	98.995						
Fe-Mo	**%C**	**%Si**	**%S**	**%P**	**%Mo**	**%Cu**	**%Fe**	
	0.028	2.23	0.0288	0.1	62.68	0.34	34.59	
Fe-B	**%C**	**%Si**	**%S**	**%P**	**%B**	**%Fe**		
	0.326	0.57	0.002	0.034	16.54	82.528		
Cr**	**%Cr**							
	100							

** Commercially pure iron from Höganäs (Compacted powder)
** Commercially pure chromium (No chemical composition analysis was performed)

Table 4.5 - Amounts of feedstock material used in each spray-forming run.

	SF1		SF2	SF3	
	SM13Cr1B	**SMSS**	**SM14Cr1B**	**SMSS**	**SM14Cr1B**
AISI 316L (kg)	12.945	29.956	-	-	-
SMSS (kg)	-	-	20.414	64.100	20.414
Fe (kg)	10.812	28.671	-	-	-
Cr (kg)	1.4289	3.274	0.930	-	0.930
Ni (kg)	-	-	0.150	-	0.150
Fe-Mo (kg)	0.178	0.389	0.066	-	0.066
Fe-B (kg)	1.634	-	1.439	-	1.439
Total weight (kg)	***27.00***	***62.90***	***23.00***	***64.10***	***23.00***

Table 4.6 - Target chemical composition of the spray-formed alloys.

	SF1		SF2	SF3	
%wt.	**SM13Cr1B**	**SMSS**	**SM14Cr1B**	**SM14Cr1B**	**SMSS**
C	0.034	0.017	0.027	0.027	0.01
Cr	13.00	13.00	14.5	14.5	11.86
Ni	4.90	4.95	5.87	5.87	5.84
Mo	1.37	1.35	19.95	19.95	2.00
B	1.00	-	1.00	1.00	-
Fe/minor elements	Bal.	Bal.	Bal.	Bal.	Bal.

The processing parameters used in each spray-forming run are displayed in Table 4.7. The process parameters of the SF1 run were set up based on previous experience of the IWT research group. In this case, the pouring temperatures were 1564 ºC for the SM-13Cr-1B and 1633 ºC for the SMSS, which resulted in 299 ºC and 150 ºC of overheating, respectively. It is worth to point out that the *liquidus* temperature of the boron-modified SMSSs were determined after the spray forming experiments because of the non-availability of suitable DSC instruments at that time. The resulted GMR of the SM-13Cr-1B and SMSS were 1.47 and 0.58, respectively. The first atomizer of the boron-modified SMSS was

tilted 12º in in order to reduce the distance between both spray cones (as shown in Figure 4.5). In addition, the atomizer of the SMSS was scanned ± 6º relatively to the axial axis of the cone increasing the range of the second spray cone. The substrate was not preheated and its initial temperature was the room temperature. In this run, it was not possible to measure the surface temperature of the deposit during the process.

Based on the results obtained from the SF1, the SF2 run was set up aiming to improve the quality of boron-modified SMSS layer (as it will be discussed further in the results). In the SF2 run, only the first layer of boron-modified SMSS was spray-formed. The main difference from the SF1 to the SF2 run is the utilization of a preheat system as depicted in Figure 4.5. In the SF2 run, the substrate was preheated at 950 ºC before starting the process. In order to counterbalance the hotter process conditions imposed by the substrate preheating, the metl flow rate was decreased by reducing the nozzle diameter from 5.0 mm to 4.0 mm, which resulted in higher GMR (about 3.2).

Finally, in the SF3 run, both layers were spray-formed again. The substrate was preheated at 950 ºC and the process parameters applied to the atomization of the boron-modified SMSS was similar to those applied in SF2. To counterbalance the hotter process conditions imposed by the substrate preheating, the parameters applied to the SMSS layer were also changed. Both the atomizer gas pressure and the nozzle diameter were reduced from 0.6 MPa and 6.5 mm to 0.5 MPa and 6.25 mm, respectively. In addition, in this experiment, the atomizer was not scanned. Such set of parameters resulted in higher GMR (0.79) when compared to the SF1 run (0.58).

In the SF2 and SF3 runs the surface temperature of the deposit was measured during the process by an optical pyrometer positioned in the region of the SM-14Cr-1B cone as shown in Figure 4.6

Table 4.7 - Process parameters of the semi-industrial scale spray-forming runs.

	Run Number		SF-1	SF-2	SF-3
First layer (5 L crucible)	*Material*		***SM-13Cr-1B***	***SM-14Cr-1B***	
	Weight of material	***(kg)***	*27*	*23*	*23*
	T liquidus	***(°C)***	*1265 (DSC measurements)*		
	Overheating	***(°C)***	***299***		
	Pouring temperature	***(°C)***	*1564*		
	Nozzle diameter	***(mm)***	*5.0*	*4.0*	
	Metl flow rate	***(kg/s)***	*0.25*	*0.12*	*0.10*
	Atomizer angle	***(º)***	*12*		
	Scan angle	***(º)***	*0*		
	Atomizer gas pressure	***(MPa)***	*0.6*		
	Gas flow rate	***(kg/s)***	0.386		
	GMR	***(-)***	**1.47**	**3.22**	**3.86**
Second layer (12 L crucible)	*Material*		***SMSS***	***-***	***SMSS***
	Weight of material	***(kg)***	*62.9*	*-*	*64.1*
	T liquidus	***(°C)***	*1483*	*-*	*1483*
	Overheating	***(°C)***	***150***	***-***	***150***
	Pouring temperature	***(°C)***	*1633*	*-*	*1633*
	Nozzle diameter	***(mm)***	*6.5*	*-*	*6.25*
	Metl flow rate	***(kg/s)***	*0.67*	*-*	*0.42*
	Atomizer angle	***(º)***	*0*	*-*	*0*
	Scan angle	***(º)***	*±6*	*-*	*0*
	Atomizer gas pressure	***(MPa)***	*0.6*	*-*	*0.5*
	Gas flow rate	***(kg/s)***	*0.386*	*-*	*0.331*
	GMR	***(-)***	***0.58***		***0.79***
	Protection gas		*Argon*		
	Atomization gas		*Nitrogen*		
	Spray distance	***(mm)***	*390*	*380*	
	Substrate material		*Mild steel*		
	Substrate Temperature	***(ºC)***	***RT***	***950 ºC***	
	Rotation speed (Rotation)	***(Hz)***	*2.48*		
	Withdraw speed	***(mm/s)***	*6.0*	*4.0*	
	Substrate dimensions	***(mm)***	*Outer diameter:114 Thickness: 4.15 Length: 600*	*Outer diameter: 139.7 Thickness: 10 Length: 600*	

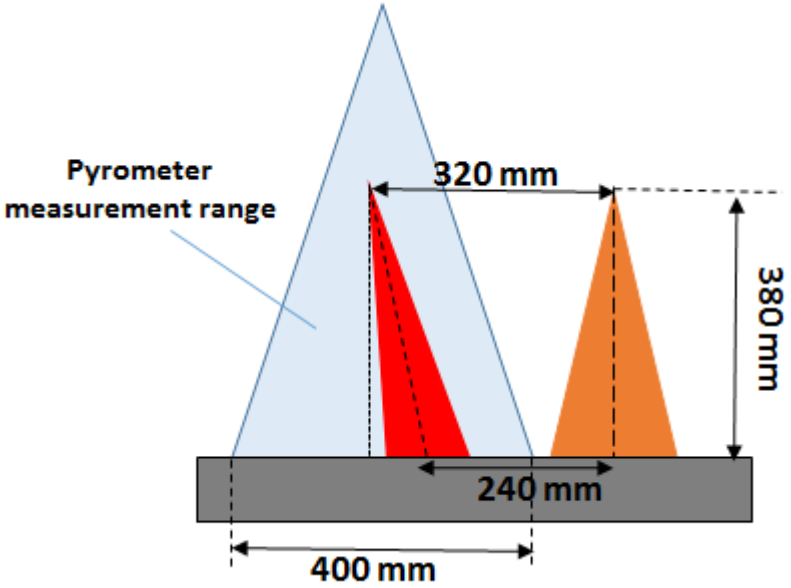

Figure 4.6 - Schematic representation of the pyrometer measurement range around the SM-14Cr-1B spray cone in the SF2 and SF3 runs.

4.2.2 Porosity and microstructure characterization

The porosity of the spray-formed products was analyzed by area fraction measurements. Optical microscopy images of polished samples were captured and the area fraction of pores were determined by using an image analyzer software. The quantitative porosity analyzes were performed in several regions of the spray-formed pipes. At least five images of each region were captured in order to calculate the average porosity and the respective standard deviation.

The microstructure of the spray-formed pipes was characterized by optical microscopy (OM) and scanning electron microscopy (SEM). In order to reveal the microstructure of the pipes Vilella's reagent (2 g of picric acid, 5 ml of HCl and 100 ml of ethanol) was used. Deep etching (10 mL HCl, 3 ml HNO3, 5 mL FeCl3 and 82 mL ethanol) was carried out to reveal the borides morphologies of the boron-modified SMSS layers. To reveal the prior austenite grain size of the SMSS layer, polished samples were left for 15 minutes in a furnace at 235 ºC and thereafter etched using Vilella's reagent (procedure described in ASTM E112-13). The average grain sizes were determined by the line intercept procedure in accordance with ASTM E112-13.

4.3 Mechanical Properties

4.3.1 Hardness and Heat treatments

Samples from the middle ring of the SF3 bimetallic pipe were used to study quenching and tempering heat treatments of both SM-14Cr-1B and SMSS layers. The AC_1 and AC_3 phase transition temperatures were determined by dilatometry using a Netsch DIL 402C model dilatometer. The dilatometry measurement was carried out at 5 ºC/min of heating rate from 20 ºC to 1000 ºC. Thermodynamic simulations (using Thermo-Calc software) calculated the amount of equilibrium phases as function of the temperature in order to determine the temperature range of χ-phase precipitation. The database used was the TCF7. The simulated chemical composition was that of the commercial SMSS presented in Table 4.3. The quenching and tempering heat treatments were carried out in an electric resistance furnace. Rockwell C hardness was measured in accordance with ASTM E18-05.

4.3.2 Sampling and mechanical tests

Mechanical properties, named tensile and impact strength, of the SM-14Cr-1B and SMSS layers of the SF3 bimetallic pipe were measured in accordance with ASTM A370-14. The specimens were machined from longitudinal samples of both layers as shown in Figure 4.7.

The high porosity region of the SMSS layer was removed and only the dense region was considered when machining the specimens. Small-size tension specimens proportional to the standard one (ASTM A 370-14) with dimensions shown in Figure 4.8 were used for both SM-14Cr-1B and SMSS. The tensile tests were carried out in an Instron tester. The speed of testing was 0.4 mm/min in both elastic and plastic region.

Standard Charpy impact test specimens were used to evaluate the impact strength at room temperature of the SMSS layer, also in accordance with A370-14. However, the impact strength of the SM-14Cr-1B layer was evaluated by using a sub-sized specimen (55 mm-long, 10 mm-high and 5 mm-thick) without notch. This specimen was chosen because of the SM-14Cr-1B layer thickness,

which was thinner than 10 mm (dimension of the standard Charpy specimen). Moreover, since the presence of M_2B borides in the microstructure may lead to low impact strength, it was decided to carry out the tests without notch.

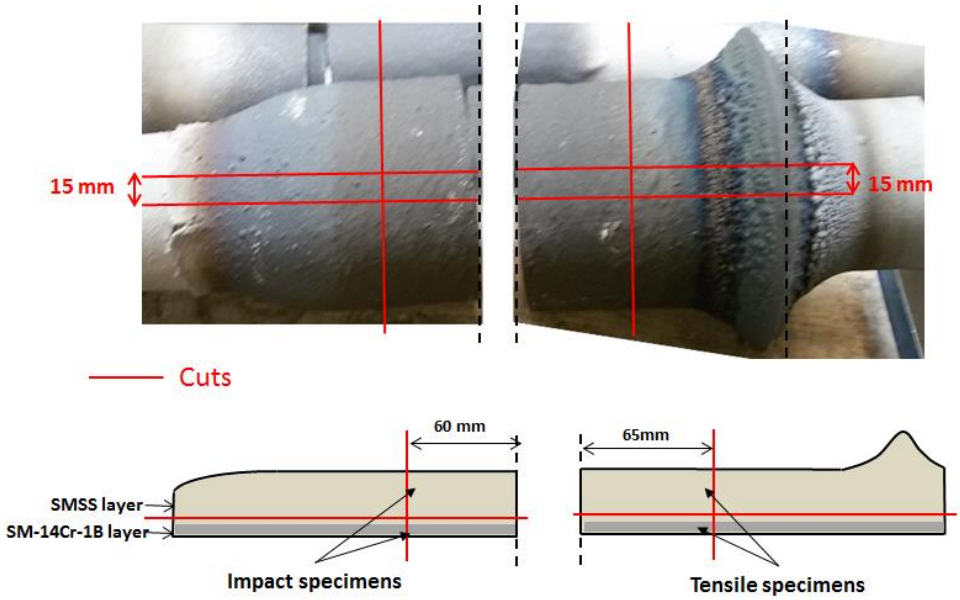

Figure 4.7 - Representation of sampling regions of the SF3 bimetallic pipe for mechanical tests.

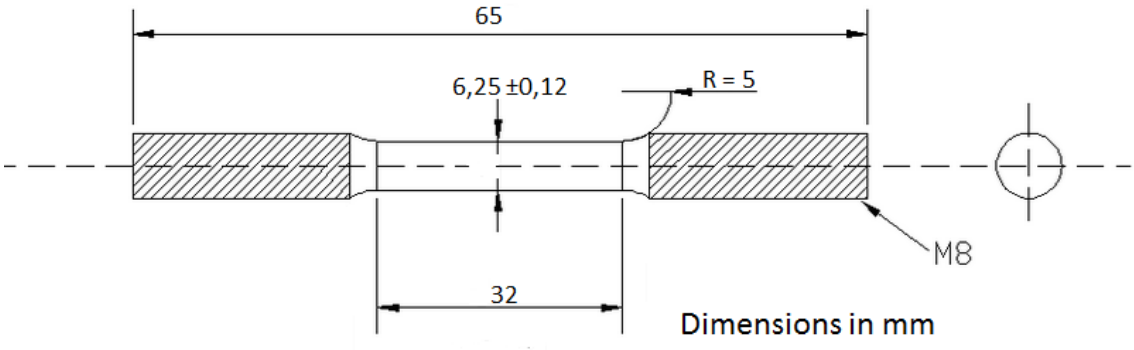

Figure 4.8 - Dimensions of the sub-sized tension test specimen used in this work.

5 RESULTS AND DISCUSSION

5.1 Design of spray-formed boron modified SMSS

5.1.1 Deposits characterization

Figure 5.1 presents the photographs of the SM-0.3B, SM-0.7B, SM-1B and SM-14Cr-1B spray-formed deposits. The deposits presented approximately the same Gaussian shape with 250 mm-diameter and thickness at the center ranging from 12-15 mm. The yield of all deposits was about 60 %, showing that the process parameters applied in all experiments were roughly reproduced. It is worth noting that the spray-formed deposits presented porosity levels lower than 1 % at their central part (measured by area fraction).

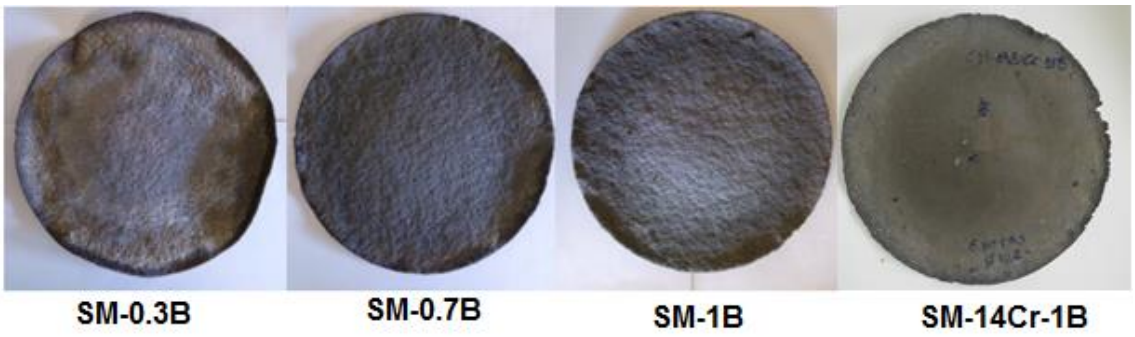

Figure 5.1 - Spray-formed boron-modified SMSS deposits produced at the close-coupled spray forming equipment at DEMa-UFScar.

Table 5.1 shows the chemical compositions of the spray-formed alloys. One can see that the chemical compositions of the deposits were slightly different from the aimed chemical composition shown in Table 4.1. The boron contents achieved for the SM-0.3B, SM-0.7B, SM-1B and SM-14Cr-1B were 0.37 %wt., 0.544 %wt., 0.69 %wt., and 0.71 %wt., respectively. Such reduction of boron content in the final chemical composition of the B-richer alloys is because of its tendency to undergo air oxidation at high temperatures forming B_2O_3, which evaporates from the liquid metal. Although the Cr, Ni and Mo contents of the boron-modified alloys are within the range of the SMSS grades, some variation of Cr content can be noted. Whereas the SM-0.3B and SM-1B achieved the

aimed Cr content, about 12 %wt., the SM-0.7B has presented only 10.85 %wt. of Cr, which can have a detrimental effect on its corrosion resistance. On the other hand, the SM-14Cr-1B presents chromium content of 13.56 %wt., higher than all supermartensitic grades (maximum Cr content of 13 %wt.). As can be seen, the carbon content in all alloys were in the range of 0.06-0.09 %wt., also higher than the conventional SMSS grades (maximum of 0.03 wt%). This increase in the carbon contents came from impurities of the raw materials and as result of contamination during the melt process.

Table 5.1 - Chemical composition of the spray-formed boron-modified SMSSs.

%wt	%C	%Cr	%Ni	%Mo	%B	%Ti	%Mn	%Fe
SM-0.3B	0.066 ±0.005	12.00 ±0.17	5.68 ±0.03	2.09 ±0.01	0.37 ±0.03	0.044 ±0.004	0.40 ±0.06	Bal.
SM-0.7B	0.068 ±0.001	10.85 ±0.52	5.38 ±0.25	1.90 ±0.09	0.54 ±0.04	0.044 ±0.004	0.38 ± 0.05	Bal
SM-1B	0.096 ±0.004	11.88 ±0.13	5.88 ±0.03	2.09 ±0.01	0.69 ± 0.02	0.041 0.006	0.49 ± 0.06	Bal.
SM-14Cr-1B	0.039 ±0.004	13.56 ±0.26	5.42 ±0.03	1.82 ±0.04	0.71 ±0.08	0.040 ±0.006	0.52 ± 0.05	Bal.

The XRD patterns of the spray-formed alloys, Figure 5.2 (a), show that all compositions presented high intensity peaks related to low carbon martensite (α'). By a detailed analysis of the XRD patterns of the SM-1B and SM-14Cr-1B, Figure 5.2 (b), it can be clearly seen low intensity peaks of the orthorhombic M_2B-type boride. Figure 5.3 (a), (c), (e) and (g) show the microstructure of the SM-0.3B, SM-0.7B, SM-1B and SM-14Cr-1B, respectively. In all cases, the microstructure is composed of equiaxed martensitic grains with the hard M_2B, salient phases, at the grain boundaries. As can be seen in Figure 5.2 (b), (d), (f) and (h) these borides present morphologies of an interconnected eutectic network extending along the whole microstructure. The solidification mechanisms

and the microstructure evolution of the spray-formed boron-modified SMSSs will be described in detail in section 5.1.2.

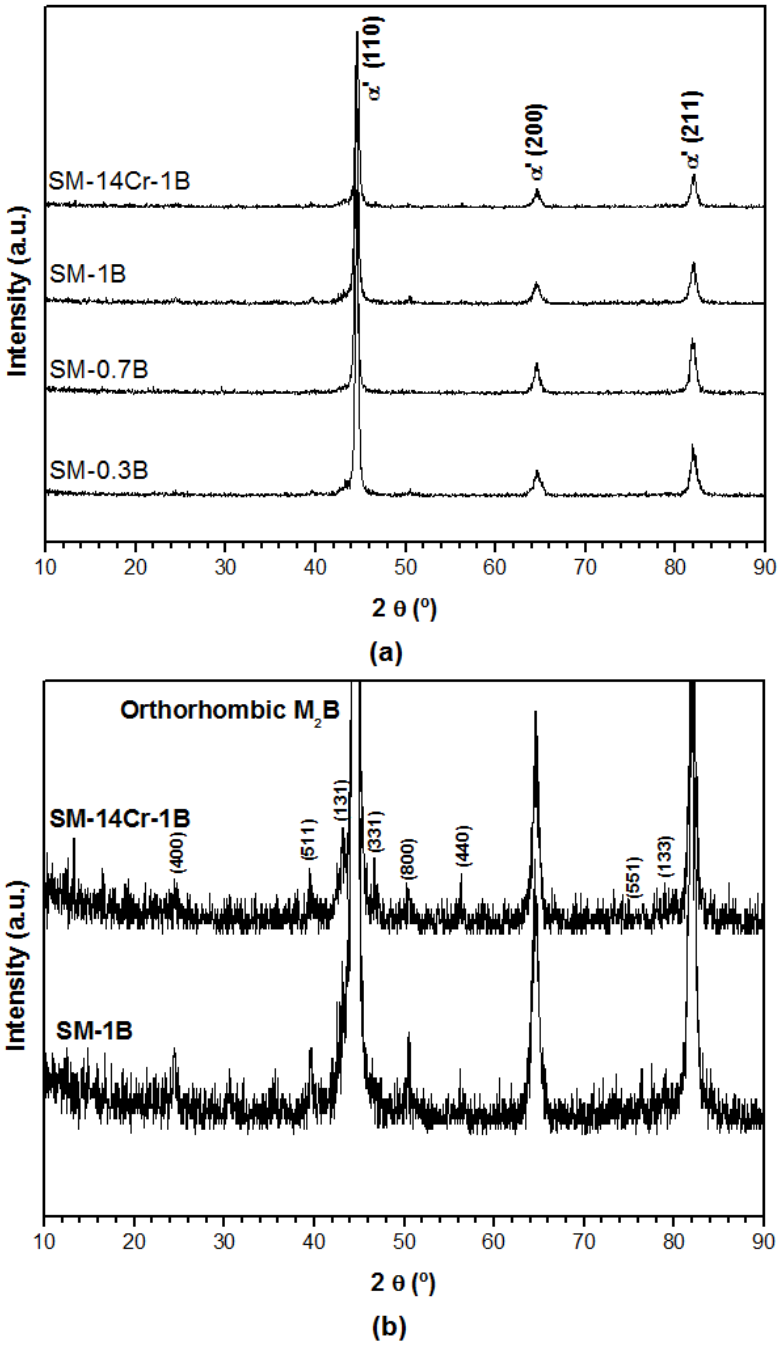

Figure 5.2 - **(a)** XRD patterns of the spray-formed boron-modified SMSSs. **(b)** Zoom of the SM-1B and SM-14Cr-1B XRD patterns.

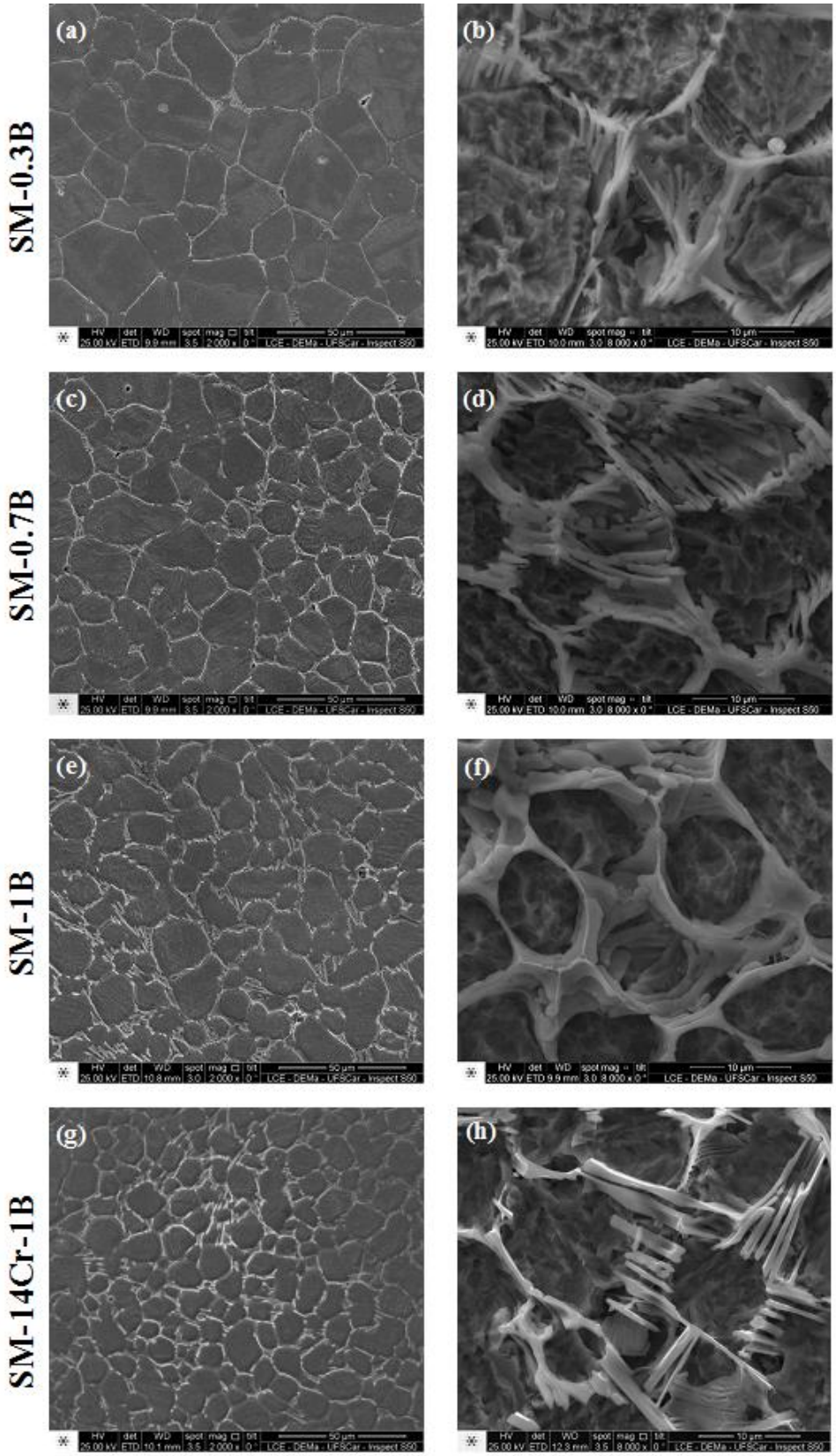

Figure 5.3 - Microstructures and borides morphology of **(a) (b)** SM-0.3B, **(c) (d)** SM-0.7B, **(e) (f)** SM-1B and **(g) (h)** SM-14Cr-1B observed by SEM images (secondary electrons).

Table 5.2 shows the EDS microanalysis results of both the martensitic matrix and the M_2B-type borides of the spray-formed alloys. It can be seen that, in all cases, the M_2B borides are Fe-rich phases containing different contents of Cr, Ni and Mo. Although minor in comparison with Fe, the presence of these last elements in the M_2B borides (mainly Cr) is far from being negligible. This means that we should reasonably expect to find martensitic matrixes with reduced Cr and Mo contents compared to the overall composition depicted in Table 5.1. It must be stressed, however, that a straightforward comparison between the values given in the two tables is not feasible. Indeed, the local chemical compositions presented in Table 5.2 do not consider the presence of boron, whose detection is limited by EDS analysis. In addition, the composition fractions are calculated only considering the detected elements (low fraction elements are not considered), which means that the values given in Table 5.2 are forcibly overestimated. In spite of the drawback in terms of quantitative evaluation, some interesting results can be pointed out. In the case of the SM-0.7B and SM-1B, the remaining (overestimated) Cr contents of the martensitic matrixes were 11.0 and 10.7 %wt., which is reported in literature as the threshold content to allow passivation. On the other hand, the Cr content at the matrix of the SM-0.3B was about 11.6 %wt, which (although also overestimated) remains within the range of conventional medium alloy SMSS grade. In the case of the SM-14Cr-1B, the martensitic matrix presented a remaining Cr content still higher than the conventional high alloy SMSS grade, about 13.4 %wt. In all cases, the remaining Mo and Ni contents of the martensitic matrixes were about 1.0%wt. and 6.0 %wt., respectively.

An important aspect of the microstructure of the spray-formed boron-modified SMSSs is that the increase of boron content has two important effects: (i) increase the borides fraction at the grain boundaries; and (ii) reduce the grain size. Both the increase of boride fraction and the reduction of grain size result in an increasing of the hardness, as can be seen in Figure 5.4, which can be also benefit for the wear properties.

Table 5.2 - EDS microanalyses of the martensitic matrixes and the M_2B-type borides of the spray-formed boron-modified SMSSs.

	Matrix					M_2B			
Wt.%	**%Fe**	**%Cr**	**%Ni**	**%Mo**	**%Si**	**%Fe**	**%Cr**	**%Ni**	**%Mo**
SM-0.3B	80.8	***11.6***	6.0	1.3	0.3	56.2	***30.8***	1.7	11.0
SM-0.7B	82.0	***11.0***	5.7	1.1	0.1	66.0	***14.2***	4.0	15.4
SM-1B	81.7	***10.7***	6.1	1.0	0.4	67.1	***23.8***	3.0	5.8
SM-14Cr-1B	78.3	***13.4***	6.1	0.9	0.5	60.6	***33.5***	2.4	3.0

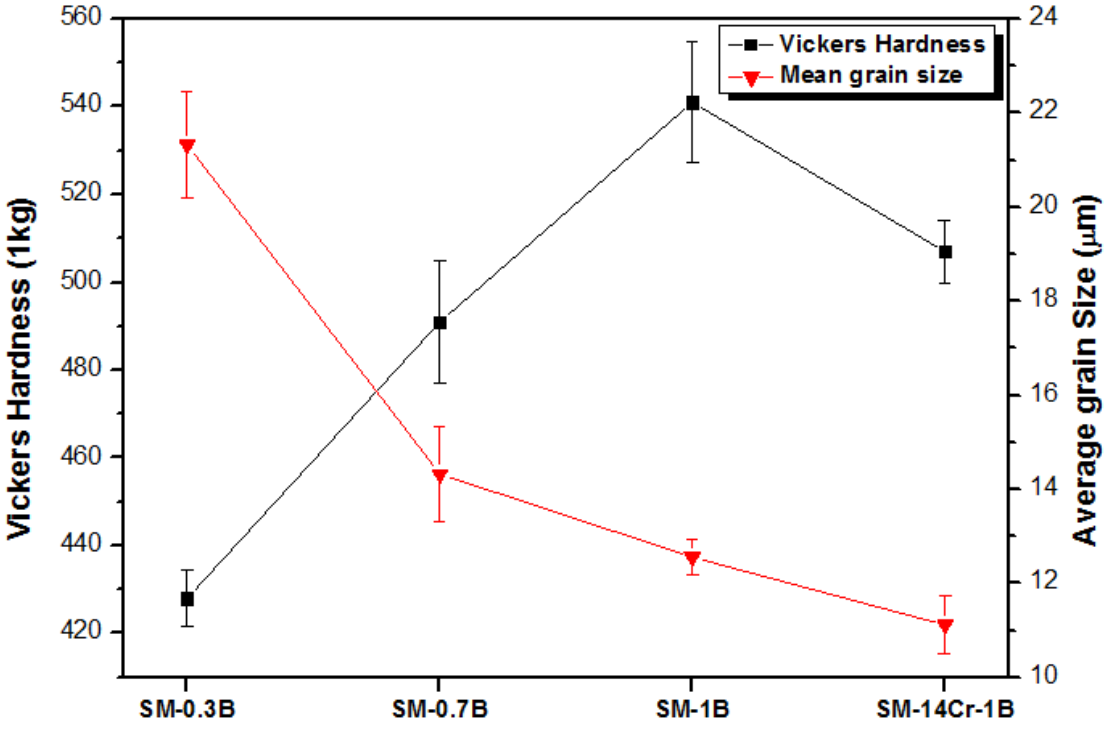

Figure 5.4 - Grain size and hardness of the spray-formed boron-modified SMSS.

5.1.2 Microstructural evolution in spray forming

Understanding how the microstructure of the boron-modified SMSS is created during the spray forming process is an important step to scale-up the production to semi-industrial facilities. Figure 5.5 presents the calculated pseudo-binary phase diagram of a medium-alloyed SMSS grade as function of boron content. This is an eutectic phase diagram with eutectic composition at 1.3 %wt. of B, meaning that all compositions studied in this work are hypoeutectic alloys. Moreover, in this case, it can be seen that three solidification paths are possible for hypoeutectic compositions:

(i) Up to 0.7 %wt. of boron, the liquid initially solidifies as δ-ferrite. At certain point, the ɣ-austenite starts to solidify within a field containing L + δ + ɣ. The solidification is then completed with the last liquid solidifying through the eutectic reaction L → ɣ + M_2B. Therefore, the as-solidified microstructure is composed of δ + ɣ + M_2B. When cooled, the primary δ-ferrite is transformed into ɣ-austenite in a solid-state reaction.

(ii) Between 0.7%wt. and 10.%wt. of boron, the liquid initially solidifies as δ-ferrite. However, still in the liquid-solid field the δ-ferrite is transformed into ɣ-austenite in the peritectic reaction L + δ → ɣ. At the eutectic temperature, the last liquid is solidified trough the eutectic reaction L → ɣ + M_2B. In this case, the as-solidified microstructure is only composed of ɣ + M_2B.

(iii) Above 1.0 %wt. of boron, the liquid solidifies directly as ɣ-austenite, being followed by the eutectic reaction L → ɣ + M_2B. Therefore, the final as-solidified microstructure is also only composed of ɣ + M_2B.

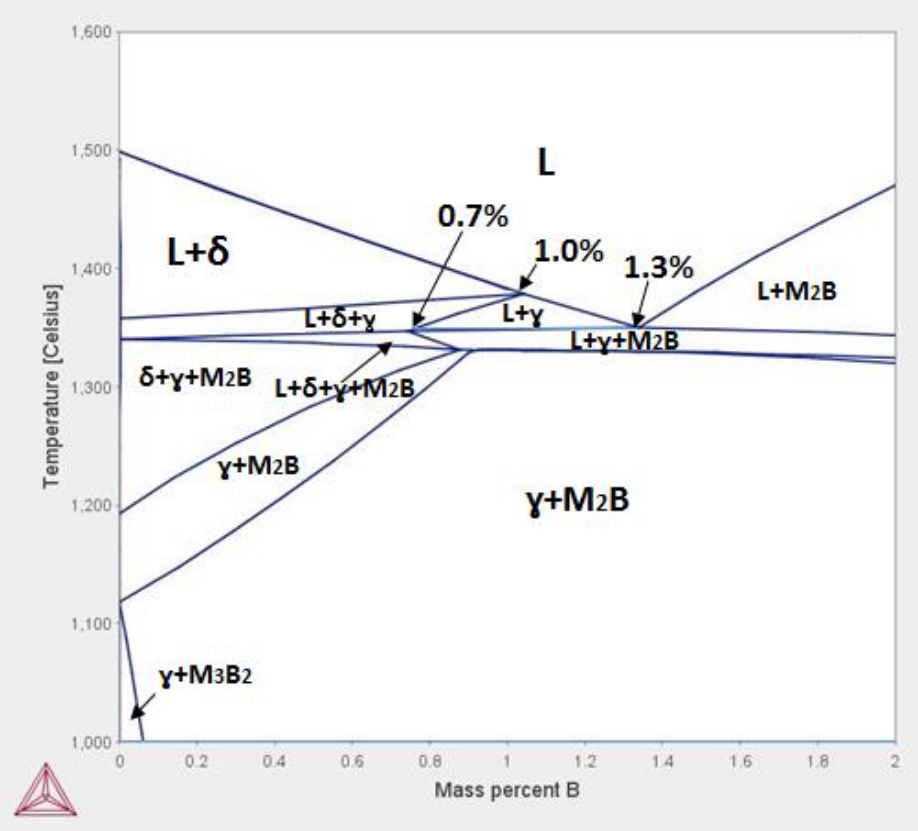

Figure 5.5 - Pseudo-binary phase diagram of the boron-modified SMSS medium-alloyed grade (Fe-12Cr-5Ni-2Mo).

Obviously, changes in the chemical composition, mainly in terms of Cr and Ni contents, which are strong ferrite and austenite stabilizers, respectively, may change the fields where each solidification path takes place. Figure 5.6 shows the calculated solidification sequence of the SM-0.3B, SM-0.7B, SM-1B and SM-14Cr-1B using the chemical compositions presented in Table 5.1. Observing the set of diagrams shown in Figure 5.6, one can see that small changes in the chemical composition of the boron-modified SMSS can change considerably its solidification sequence. The SM-0.3B – Figure 5.6 (a) – solidifies in accordance with the solidification path as described before in (ii). Most probably due to the higher Ni content of this alloy (5.68 %wt.), the δ-ferrite field is considerably reduced and when compared to the diagram shown in Figure 5.5. In this case, when the liquid achieves the eutectic temperature only ɣ-austenite is present, and, the as-solidified microstructure is only composed of ɣ + M_2B. The same is observed for the SM-0.7B – Figure 5.6 (b) – which in addition to the higher Ni

content (5.38 %wt.) also presents lower Cr content (10.85 %wt.). In the last case, the amount of δ-ferrite formed during the solidification is considerably lower than the first case as well. On the other hand, the SM-14Cr-1B, – Figure 5.6 (d) – that presents considerably higher Cr content (13.56 %wt.), solidifies following the sequence described in (i), presenting some fraction of δ-ferrite in the as-solidified microstructure. In this case, the δ-ferrite is transformed into ɣ-austenite in a solid-state reaction. In the case of the SM-1B – Figure 5.6 (c) – the equilibrium solidification sequence follow what is described in (iii). In this case, the ɣ-austenite solidifies directly from the initial liquid, and no δ-ferrite is present.

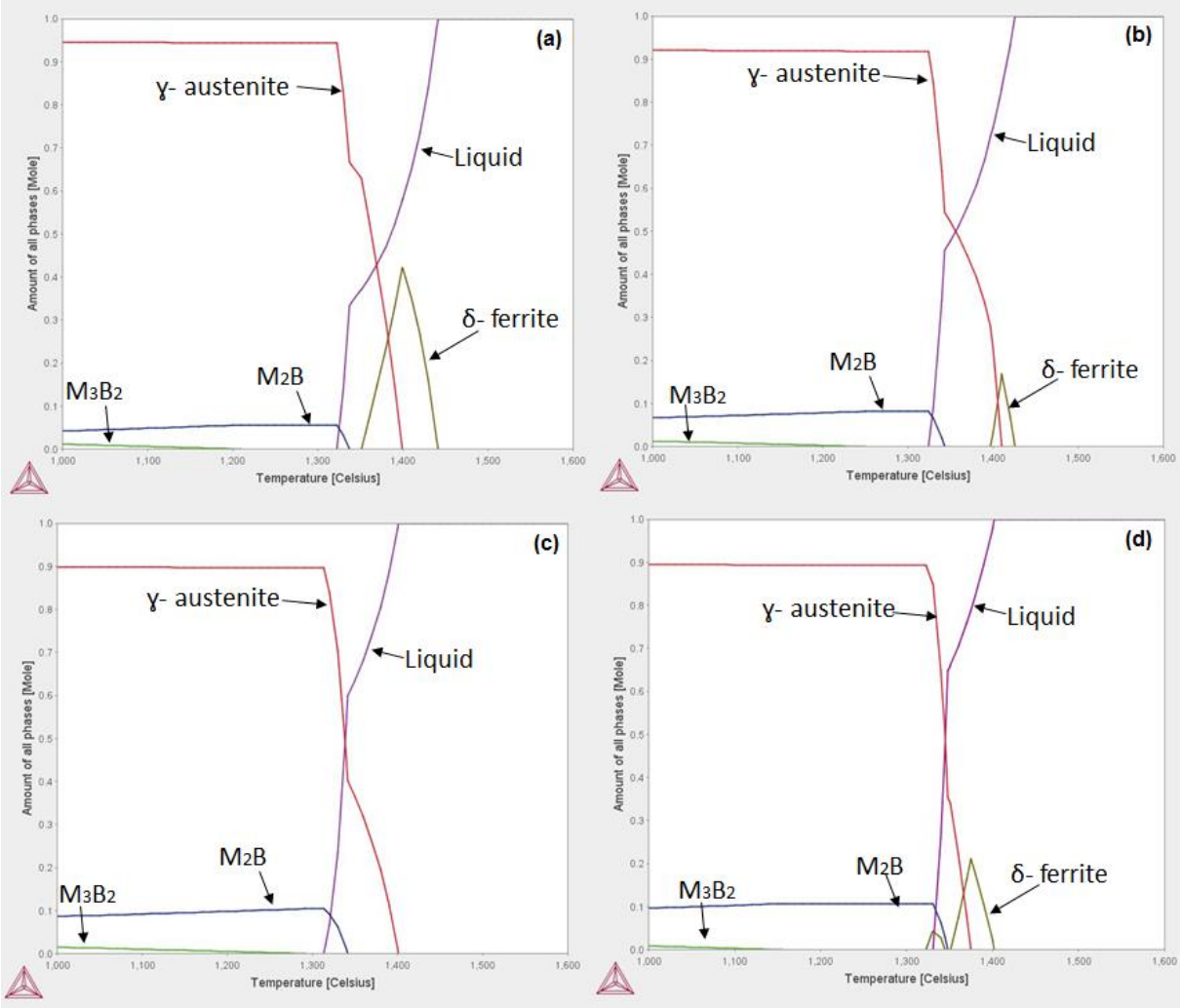

Figure 5.6 - Calculated amount of phases (in mole fraction) showing the equilibrium solidification path of the **(a)** SM-0.3B, **(b)** SM-0.7B, **(c)** SM-1B, and **(d)** SM-14Cr-1B.

The boron-modified SMSS grades, mainly the SM-1B, have some features that may be helpful to understand how the equiaxed microstructure with an eutectic network interconnected containing M_2B (Figure 5.3) is created during the solidification in the spray forming process:

(I) As reported in literature, and shown in the thermodynamic simulations, boron has a very limited solubility in steel (<0.008%wt.), even at the high temperature.

(II) As shown above, the SM-1B have an hypoeutectic composition, whose equilibrium solidification path follows the sequence: solidification of ɣ-austenite as primary phase followed by the eutectic reaction $L \rightarrow M_2B + ɣ$.

(III) The limited solubility of boron in the steel matrix does not allow the M_2B-type borides to be dissolved, which means that the borides are present in the as-solidified form. Moreover, due to the limited solubility of boron in steel, the formation of M_3B_2 is also unlikely to take place in solid-state reaction.

It is also important to point out that after solidification the austenite is transformed into martensite, even at low cooling rates, for instance, when the deposit is air cooled inside the spray chamber. However, such solid-state transition has no effect on the understanding of solidification in the spray-forming process.

Figure 5.7 (a) shows the microstructure of an SM-1B overspray particle with a diameter of about 200 µm. The particle microstructure is composed of a dendritic martensitic matrix with M_2B borides present in the eutectic constituent between the interdendritic arms. The high cooling rates promoted by the gas atomization led to a very refined powder microstructure, in this case with average secondary dendrite arm spacing about 2.5 µm. As demonstrated by P. Grant [9], droplets larger than 200 µm are expected to reach the substrate still fully liquid under conventional spray-forming conditions. Therefore, the droplets that land on the deposition zone completely solidified (usually droplet size < 50 µm) were cooled at higher rates than the 200 µm droplets, resulting in a more refined microstructure. Figure 5.7 (b) shows the microstructure of a 50-µm diameter

droplet. It can be clearly seen that the microstructure is still dendritic, but strongly finer than the one presented in the 200-µm droplet, making it difficult to measure the secondary dendrite arm spacing.

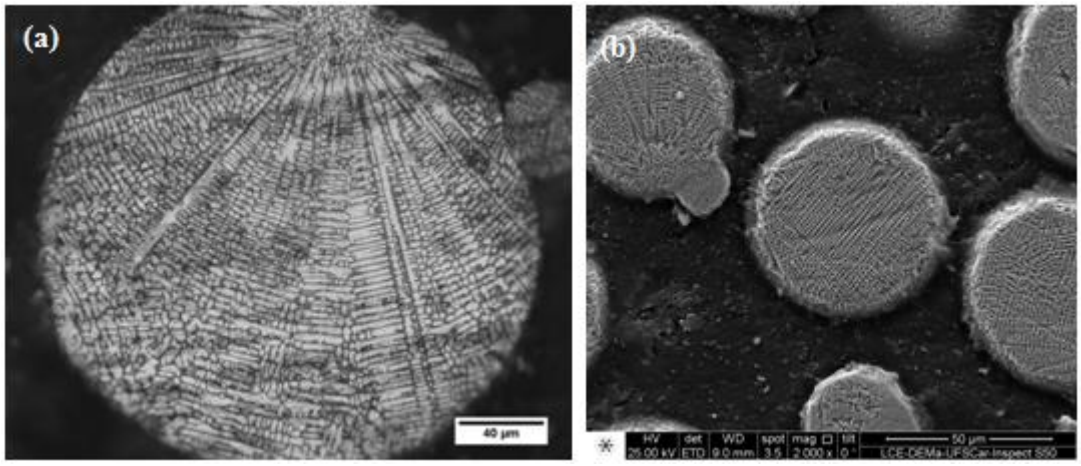

Figure 5.7 - Microstructure of the overspray powder of SM-1B with **(a)** 200 µm (OM) and **(b)** 50 µm (SEM – secondary electrons image).

One can see that the microstructure of the SM-1B deposit – Figure 5.3 (e) – is composed of equiaxed martensitic grains with M_2B borides present around the grain boundaries. The average grain size is around 15 µm, which is much coarser than the powder microstructures, even considering the larger particles. The M_2B borides present in the spray-formed microstructure are also considerably coarser than in the overspray droplets. It is worth noting that no remnants of the dendritic microstructures from the completely solidified droplets are present in the spray-formed microstructure. As pointed out before, the borides after solidification cannot be dissolved in the steel matrix due to the very limited solubility of boron. Based on this, the only possible explanation for the disappearance of the droplet microstructure in the final spray-formed deposit is the remelting and/or redissolution of the borides present in the interdendritic arm spaces at the deposition zone. As shown in Figure 5.3 (d), the M_2B borides appear in the SM-1B spray-formed deposit as a continuous eutectic network interconnected along the microstructure. It is worth stressing that as the borides were solidified at the grain boundaries, no further grain growth was possible after

the solidification. Hence, this microstructure is identical to the as-solidified structure (despite the martensitic transformation).

As introduced in section 2.1, how the completely solidified droplets are mixed with the partially and fully liquid droplets at the deposition zone and create the characteristic spray-formed microstructure is an open discussion in literature. Some authors have reported that spray-formed products with a low porosity level and high yield are achieved only when the deposit surface temperature at the deposition zone is kept above the solidus temperature of alloy [16,46,71]. Based on this, and in the previous observation of the overspray particles and spray-formed deposit microstructures, a solidification model for spray-forming in which the equilibrium solidification path takes place in the deposition zone will be addressed to explain the microstructural evolution of the boron-modified SMSSs.

The solidification model proposed has two main assumptions:

(i) When steady deposition condition is reached, the deposition zone has an equilibrium temperature above the alloy's *solidus* temperature, which is approximately the surface temperature of the deposit during the deposition process. The deposition zone's temperature is strongly dependent on the processing parameters applied.

(ii) The liquid and solid fractions in equilibrium are attained for the equilibrium temperature of the deposition zone.

Let us consider the simplified pseudo-binary phase diagram – Figure 5.8 – showing the solidification path of the SM-1B (red line). When the deposition starts, a distribution of fully liquid, partially solidified and completely solidified droplets impinge onto a substrate. The liquid droplets spread across the substrate, drawing in the partially and totally solidified droplets and the deposit starts to build up. In the first stages of deposition, the spray cone is still being stabilized and most of the heat in the droplets is transferred to the substrate. It was extensively reported that the non-stationary deposition conditions that occur at the initial stages of spray-forming lead to a microstructure with very high cold porosity (porosity caused if the fraction of liquid is too low and insufficient to fill the interstices between the solid particles in the deposition zone) in the vicinity of the substrate [16,71].

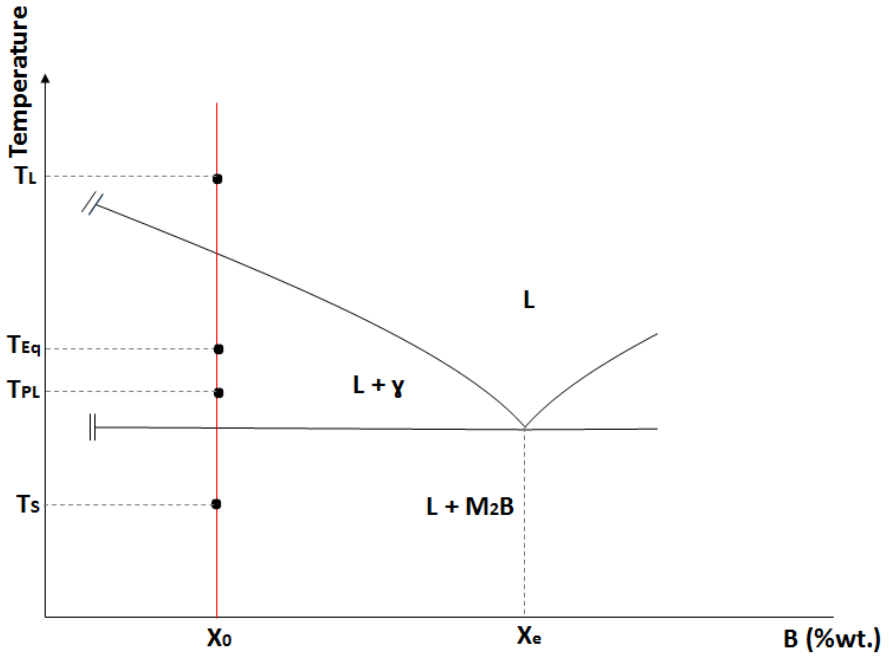

Figure 5.8 - Pseudo-binary phase diagram showing the solidification path of the SM-1B. T_L = temperature of the fully liquid droplets; T_{PL} = temperature of partially solidified droplets; T_S = temperature of completely solidified droplets; and T_{eq} = equilibrium temperature of the deposition zone.

When the deposition process reaches its steady-state condition, the deposit surface temperature remains constant and should be above *solidus* temperature to achieve a dense material. This model does not consider the transient deposition period and the microstructure evolution will be described from the point where the constant surface temperature is attained. At this point, the completely solidified droplets with temperature T_S (see Figure 5.8) reach the deposition zone with chemical composition X_0. Considering that these droplets continued under conditions close to equilibrium during solidification, the droplets microstructure is composed of X_0/X_e fraction of eutectic constituent (ɣ+M_2B) and 1-(X_0/X_e) fraction of primary dendritic ɣ-austenite. The partially liquid droplets with T_{PL} present only ɣ-austenite phase solidified and boron-rich liquid phase. Figure 5.9 shows a schematic representation of the proposed solidification model. When the droplets impact on the deposition zone the following sequence of events takes place:

(I) The fully liquid droplets spread, maintaining a liquid pool in the deposition zone. The completely liquid and partially liquid droplets are cooled to T_{eq} and the ɣ-austenite phase is solidified until the liquid fraction reaches the equilibrium fraction at this temperature. Meanwhile, the completely solidified droplets are heating up to T_{eq} and the eutectic constituent and part of the primary ɣ-austenite is remelted or dissolved in the liquid present, until the equilibrium liquid fraction is attained. It is important to point out that practically all boron is now only present in the liquid, since solubility of boron in ɣ-austenite is extremely limited.

(II) At this point, in the deposition zone only the ɣ-austenite embedded in a boron-rich liquid is present. With the cooling of the deposition zone, the ɣ-austenite originally from the solidification of the liquid and partially liquid droplets and from the remaining solid phase after the partial remelting and/or dissolution of the solidified droplets, starts to grow. However, the continuous impacting of droplets induces a turbulent fluid convection and the liquid present in the deposition zone flows around the ɣ-austenite “nuclei”. The movement of the liquid in the deposition zone plays two very important roles in the evolution of the microstructure: (i) chemical homogenization of the remaining liquid while solidification proceeds and (ii) thermal homogenization of the remaining liquid, resulting in the gradient temperature around the ɣ-austenite “nuclei” being almost the same in all directions. The isotropic thermal gradient makes the “nuclei” grow without any preferential direction, which results in the development of equiaxed grains, following the Scheil-Gulliver model of solidification. As there is practically no solubility of boron in ɣ-austenite, the nuclei are solidified equiaxially, while the remaining liquid is enriched with boron until eutectic composition is attained.

(III) When the remaining liquid reaches the eutectic temperature, all the liquid is solidified through the eutectic reaction. When solidification is finished, the final microstructure is composed of equiaxed grains of ɣ-

austenite with the eutectic constituent (ɣ + M_2B) present at the grain boundaries around the primary ɣ-austenite.

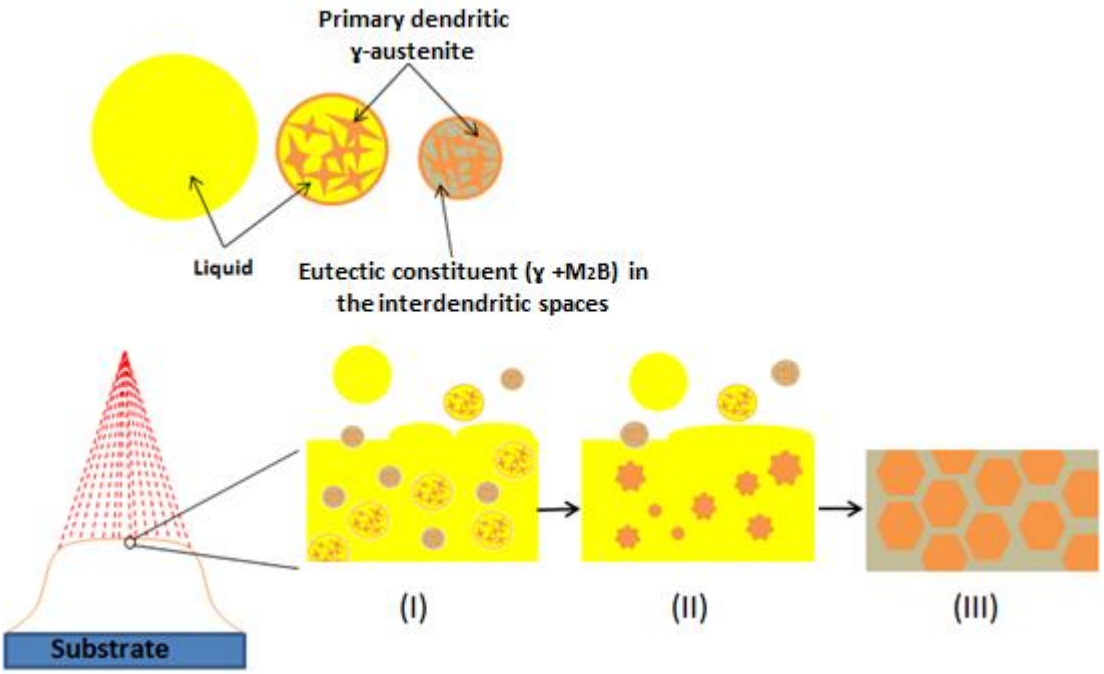

Figure 5.9 - Schematic representation of the solidification model of the SM-1B.

An important aspect of this model is that when the equilibrium liquid fraction is attained, all the liquid present in the deposition zone is continuous. This means that the liquid from different droplets is mixed and that the solidification will be completed around the equiaxed ɣ-austenite with constant conditions for all pre-formed grains. In short, the proposed solidification model states that the solidified droplets, which land on the deposition zone, must be partially remelted and/or redissolved and that the equilibrium phase fractions at the deposition zone temperature must be attained. Such statement is well-supported by the disappearance of the very refined M_2B borides present in the completely solidified droplets, as observed in the overspray droplet microstructures, in the final spray-formed microstructure. Boron has very limited solubility in steel, which means that borides cannot be dissolved in the steel matrix. Thus, the only possible explanation for the disappearance of the borides present between the interdendritic arms of the droplets, which are supposed to land completely

solidified at the deposition zone, is by remelting and/or redissolving of this phase. This leads to an increase in the liquid fraction in the deposition zone. Observing the microstructure of all spray-formed boron-modified SMSSs – Figure 5.3 – it is clear that all the borides were formed from the eutectic reaction when the liquid in the deposition zone reached the eutectic composition. Furthermore, the M_2B boride morphologies of the continuous eutectic network along the microstructures support the idea that the liquid in the deposition zone indeed must be continuous, and no “droplet regions” are preserved.

In the solidification model with simplified pseudo-binary phase diagram of the SM-1B composition – Figure 5.8 – if a composition $X_1<X_0$ (lower boron content) is chosen, the equilibrium liquid fraction at the same T_{eq} must be lower than in the case of the composition X_0. This means that for composition X_1 the primary ɣ-austenite nuclei must grow more during the cooling of the deposition zone, and a lower amount of liquid will reach the eutectic composition. Thus, the final microstructure expected for the composition, X_1, would be larger equiaxed grains and a lower fraction of eutectic constituent at the grain boundaries when compared to the X_0 composition. This situation is well-represented by the different equiaxed grain sizes between the SM-0.3B and SM-0.1B. Although it has been shown that the equilibrium solidification path of the SM-0.3B differs from the SM-1B by formation the δ-ferrite as primary phase, the different average grain sizes provides strong evidence that the “nuclei” grow freely in the deposition zone until the remaining boron-rich liquid reaches the eutectic composition. This results in a much coarser grain size in the SM-0.3B than in the SM-1B as shown in Figures 5.3 and 5.4. The equiaxed growth of the “nuclei” (considering here “nuclei” as being the remaining solid fraction of the particles that partially remelted) is attributed to the homogeneous gradient temperature in the deposition zone.

Based on such results, it is stated that the solidification of steel in spray-forming occurs in conditions near equilibrium and, therefore, cannot be considered a rapid solidification process. Moreover, the high cooling rates prevailing during the atomization step do not contribute to the evolution of the spray-formed microstructure, since the rapidly solidified droplets are remelted and/or redissolved after being deposited. It has been reported that high cooling

rates promoted by the atomization can lead to the formation of a primary phase with extended solubility [72]. In the case of boron-modified SMSSs, if the high cooling rates of the atomization step had led to formation of ɣ-austenite or δ-ferrite supersaturated in boron, it would be expected that borides would precipitate within the grains, since the cooling rate after the deposition process is quite slow. As no precipitates can be seen, there are two possible explanations: either (i) even with high cooling rates, the droplet solidification occurs in almost equilibrium conditions, and no extended solubility of boron in the austenite occurs; or (ii) the high cooling rates lead to the formation of austenite with extended solubility of boron. However, when the droplets are partially remelted, the boron in the "nuclei" diffuses back to the remaining liquid in a phenomenon called "back diffusion". This should be possible since the "nuclei" are considerably small (smaller than 10 μm) and the temperature in the deposition zone is sufficiently high to allow the diffusion of boron. The second explanation seems to be most likely to occur. In any event, it is clear that the effects on the microstructure promoted by the rapid solidification of the droplets, in these cases, are not present in the final spray-formed microstructure. Thus, if the completely solidified droplets reach the deposition zone with phase fractions out of equilibrium, when remelted, the equilibrium phase fractions and compositions are restored, and the solidification sequence continues in near equilibrium conditions. However, the atomization step plays two very important roles in the evolution of the spray-formed microstructure: (i) the atomization supplies liquid droplets with very high chemical homogeneity to the deposition zone, which solidify in very small regions (hundreds or few micrometers) avoiding macrosegregation; (ii) the impacting of the droplets is essential to create the liquid convection in the deposition zone, allowing the primary nuclei to grow equiaxed.

The proposed solidification model was also validated for a D2 tool steel billet spray-formed in semi-industrial scale. In this case, the surface temperature were measured during the whole process and the assumption that the equilibrium temperature of the deposition zone is practically constant and above the *solidus* temperature was proved. The complete description of the experiments and the results of the spray-formed D2 tool steel can be found elsewhere [73].

5.1.3 Effect of boron content on the wear resistance

5.1.3.1 Dry sand against rubber wheel abrasive wear test

In order to evaluate the effect of boron content in the wear resistance of the alloys, samples of SM-0.3B, SM-0.7B, SM-1B deposits, and commercial SMSS were tested. The results of volume loss in the dry sand against rubber wheel abrasive wear test are presented in Figure 5.10.

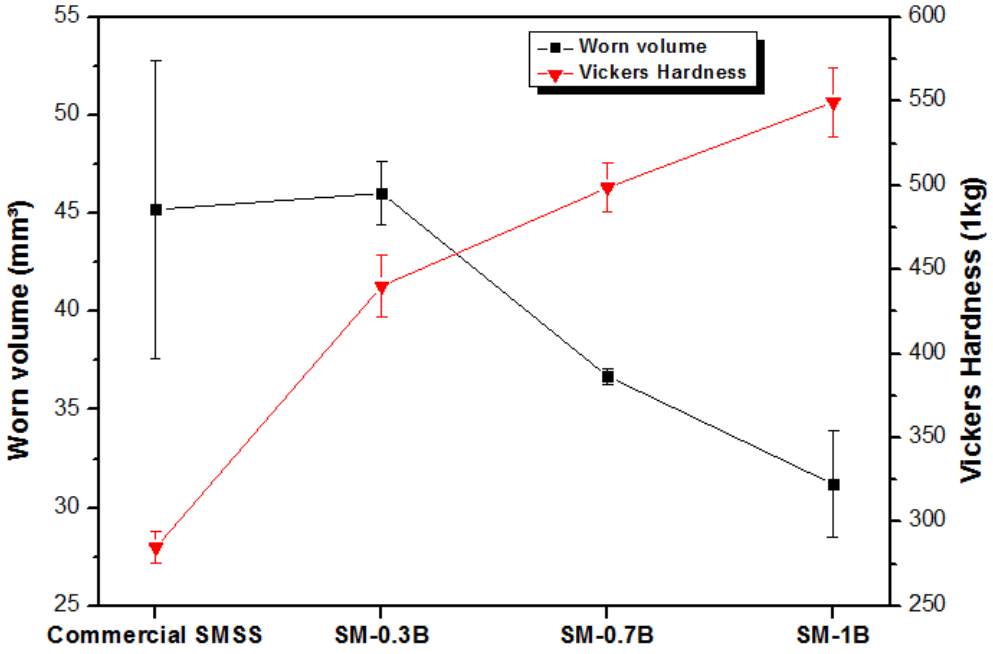

Figure 5.10 - Hardness and volume loss of the commercial SMSS, SM-0.3B, SM-0.7B and SM-1B in the dry sand against rubber wheel abrasive wear test (ASTM G65-04 procedure A).

It can be seen that hardness of the commercial SMSS (284 HV) is considerably lower than the boron-modified SMSSs. Even with higher hardness, the SM-0.3B (440 HV) showed a similar volume loss value than the commercial SMSS, 45.2 mm³ and 44.9 mm³, respectively. However, with the increase of the boron content in the SM-0.7B (498 HV) and the SM-1B (549 HV), the increase of hardness is also accompanied by the reduction of volume loss, 36.9 mm³ and 29.3 mm³, respectively. Figure 5.11 shows the worn surfaces of the tested samples.

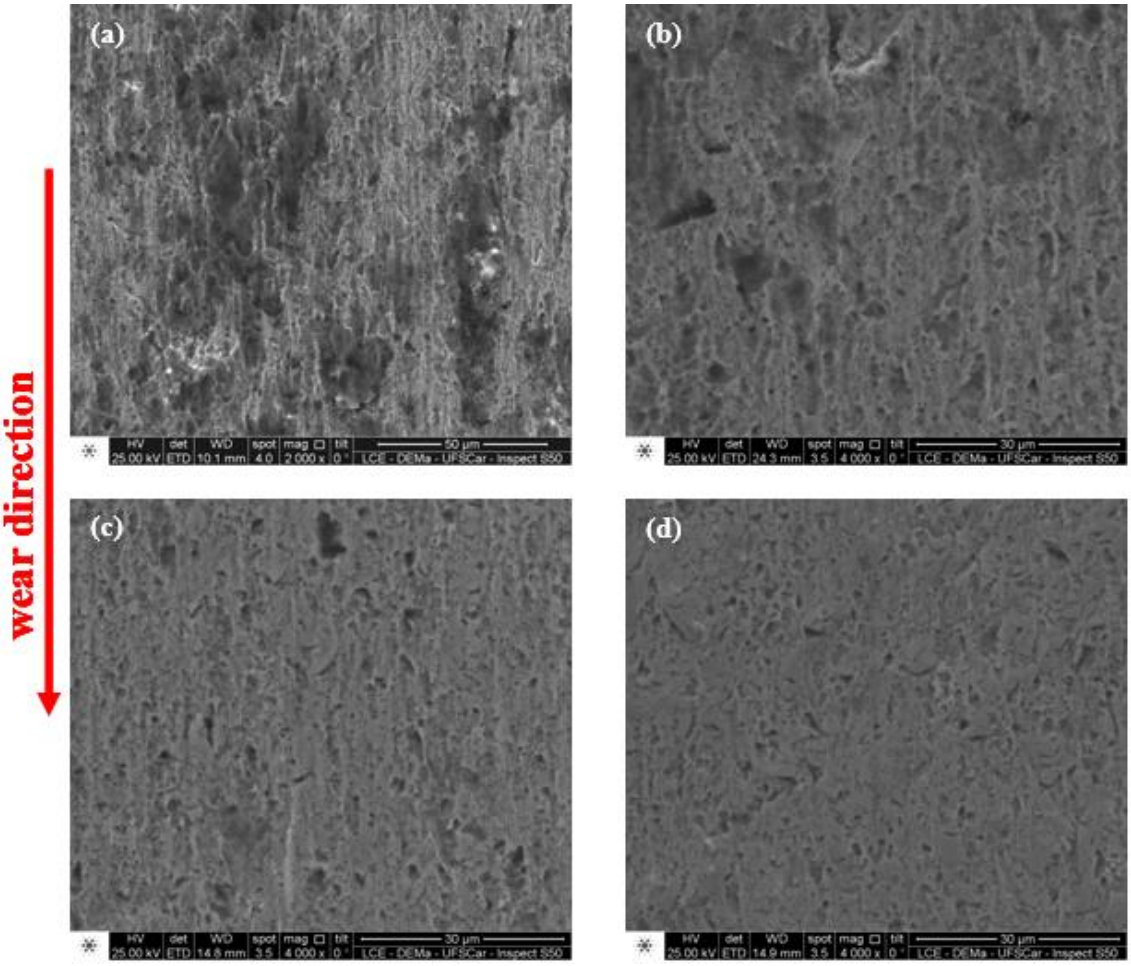

Figure 5.11 - SEM images (secondary electrons) of the worn surfaces of **(a)** commercial SM, **(b)** SM-0.3B, **(c)** SM-0.7B and **(d)** SM-1B after the dry sand against rubber wheel abrasive wear test.

One can see the presence of several holes in the worn surfaces of all materials, which suggest that a three-body wear mechanism has taken place. In this sort of wear mechanism the abrasive sand particles can roll between the rubber and sample surfaces and the surface material is removed as debris by subsequent indentations of the sharp corners of the rolling abrasive particles. Figure 5.12 illustrates schematically the effect of the hard M_2B borides network on such three-body wear mechanism. As illustrated, the larger grain size, and consequently the greater distance between the hard borides, in the SM-0.3B is not effective to prevent indentation of the soft matrix – see Figure 5.12 (b) – and in this case the debris is easily removed. This is a reasonable explanation for the similar results of loss volume of the SM-0.3B and the commercial SMSS – Figure

5.12 (a). On the other hand, when the boron content is increased, the volume fraction the hard M_2B borides increases and the grain size decreases so that mean free path between borides is reduced, resulting in an effective protection of the martensitic matrix against the indentations of the rolling abrasive particles. Consequently, less debris is generated and the wear rate is reduced, – Figure 5.12 (c) – resulting in lower values of volume loss of the SM-0.7B and SM-1B.

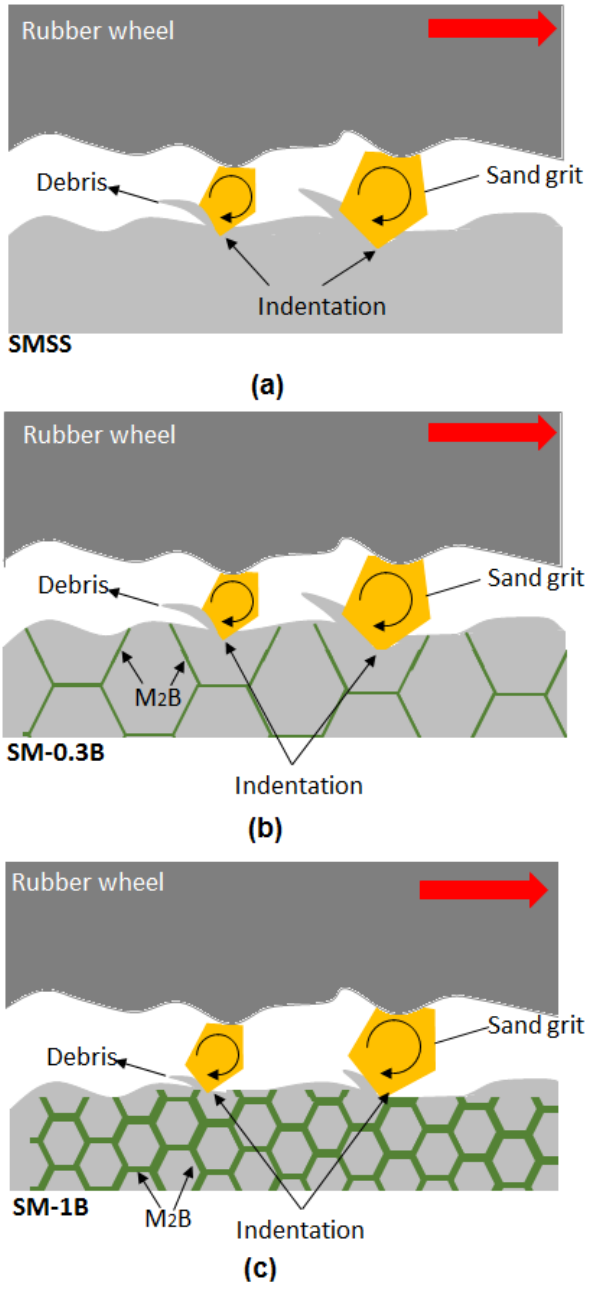

Figure 5.12 - Schematic illustration of the three-body wear mechanism in the dry sand against rubber wheel wear test of **(a)** SMSS, **(b)** SM-0.3B, and **(c)** SM-1B.

5.1.3.2 Plate-on-cylinder wear test

Figure 5.13 (a) and (b) show the experimental results of the POC wear tests for the SM-0.3B, SM-0.7B, SM-1B and commercial SMSS. It can be seen that the accumulated worn volume after 25000 m of sliding distance reduces from $5.2x10^{-7}$ m³ for the SM-0.3B to $4.4x10^{-7}$ m³ for the SM-0.7 and to $4.0x10^{-7}$ m³ for the SM-1B, showing that the increase of boron content also presented positive effects in the POC wear test – Figure 5.13 (a). However, it can be seen that at the same sliding distance the accumulated worn volume of the commercial SMSS is $3.9x10^{-6}$ m³, i.e., one order of magnitude higher than the spray-formed boron-modified SMSSs – Figure 5.13 (b). This means that even small additions as 0.3 %wt. of boron are effective to improve the wear resistance of the supermartensitic stainless steel in this tribosystem. Figure 5.14 shows the samples of the four alloys after the POC wear test. One can see that the damage caused on the commercial SMSS sample and the amount of material removed from its surface is quite higher than in the spray-formed boron-modified SMSSs.

It is worth noting that, even with the small increase of the normal force caused by the sample thickness loss, all materials presented the tendency of reducing the wear rate with increased sliding distance, as reported by Hall and Malloy [69]. In Figure 5.13 and Table 5.3 can be seen the fitted curves and the fitted parameters of the experimental data with the equation 4.1. The experimental data of all materials were well fitted by the empirical equation purposed as can be seen by the R-squared values. The most important value of this equation is the limiting value A, which indicates the maximum accumulated worn volume until the wear rate becomes negligible. The maximum accumulated worn volumes were calculated by fitting the experimental data, being $8.3x10^{-7}$ m³ for the SM-0.3B, $6.0x10^{-7}$ m³ for the SM-0.7B, $4.7x10^{-7}$ m³ for the SM-1B and $5.9x10^{-6}$ m³ for the commercial SMSS.

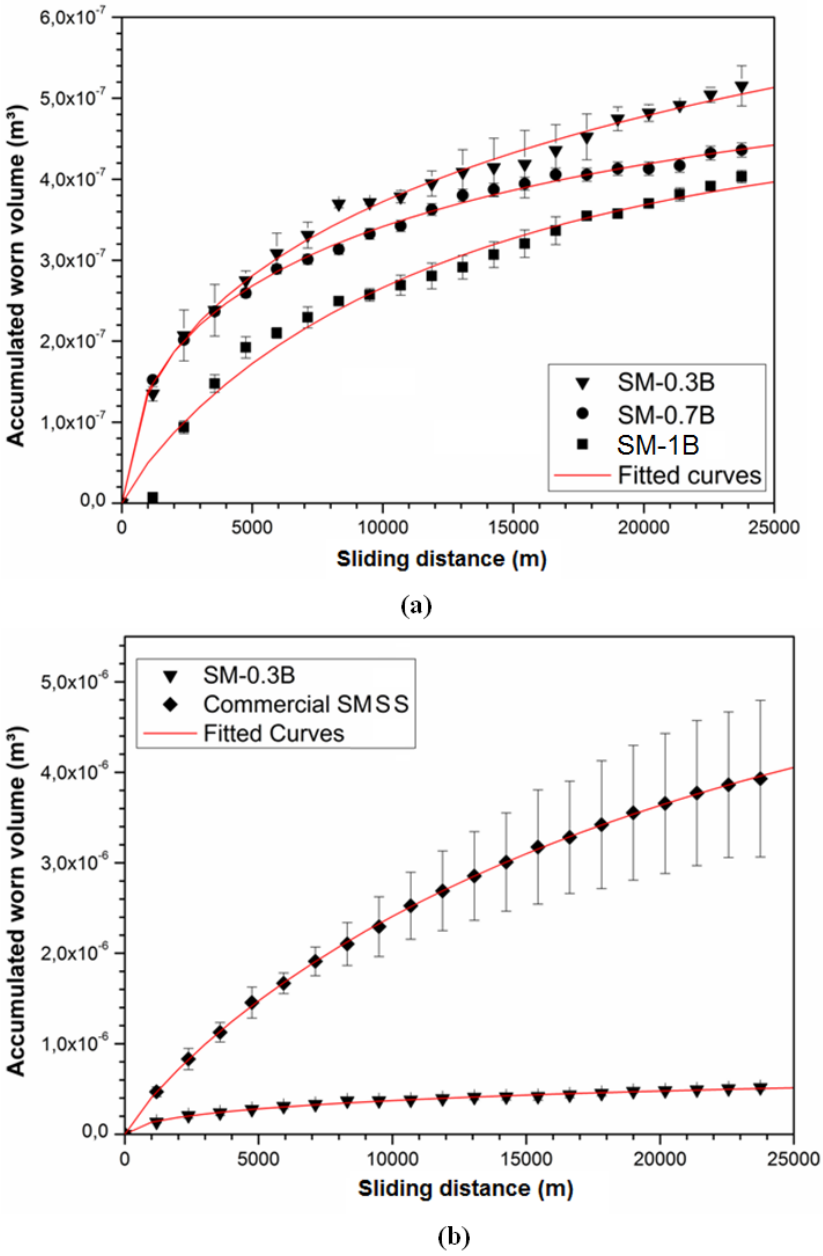

Figure 5.13 - Experimental data and fitted curves of accumulated worn volume versus sliding distance in the POC wear test.

Table 5.3 - Fitted parameters from experimental POC wear test data.

$V = A \times \{(1-\exp[-B \times (s^C)]\}$				
	A	**B**	**C**	**R^2**
SM-0.3B	8.276×10^{-7}	4.67×10^{-3}	0.527	0.99447
SM-0.7B	5.972×10^{-7}	7.99×10^{-3}	0.506	0.99772
SM-1B	4.701×10^{-7}	2.71×10^{-3}	0.872	0.98043
Commercial SMSS	5.908×10^{-6}	1.78×10^{-4}	0.867	0.9998

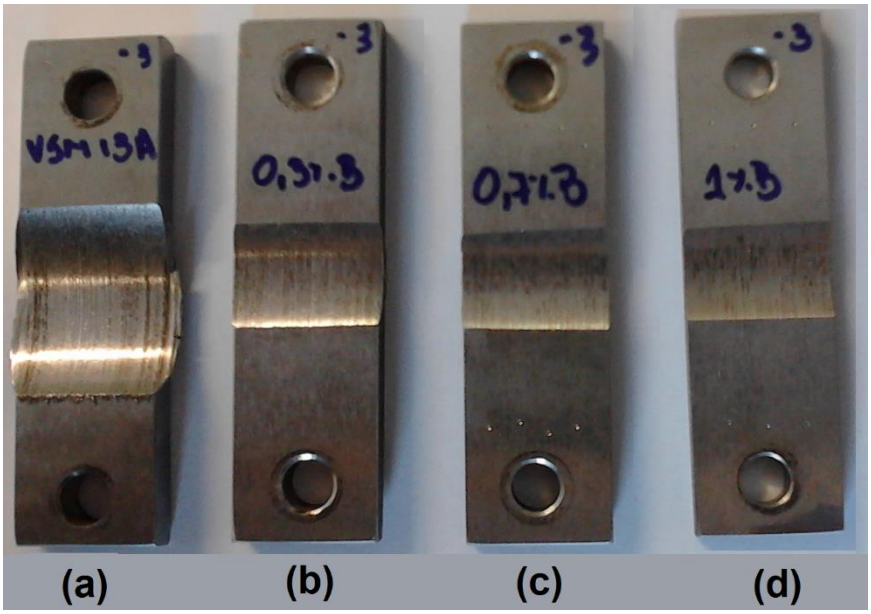

Figure 5.14 - Samples of the **(a)** commercial SMSS, **(b)** SM-0.3B, **(c)** SM-0.7B, and **(d)** SM-1B after the POC wear test.

By using this model to evaluate the alloys' wear resistance in the POC wear test, the better is the alloy's wear resistance, the lower is its maximum accumulated wear volume and the faster it reaches this value. Figure 5.15 (a) shows the wear rate versus sliding distance, calculated by equation 4.2, of all alloys. As it can be seen, in all cases by increasing the sliding distance the wear rate approaches to zero, but very high sliding distances are necessary in fact to reach the null value. However, the wear rates of the spray-formed boron-modified SMSSs decay faster as higher is the boron content of the sample. As expected, for shorter sliding distances the wear rate of the commercial SMSS is much higher than the boron-modified alloys, but for very high sliding distances it also decays approaching the null value. One can see that for 150 km of sliding distance the wear rate of the commercial SMSS is almost the same of the SM-0.3B, approximately $1.0x10^{-12}$ m^3/m (or 1 mm^3/km), which is a very low wear rate. At the same distance the wear rate of the SM-0.7B is $2.5x10^{-13}m^3/m$ (or 0.25 mm^3/km) and of the SM-1B practically reached zero. Figure 15.5 (b) shows the evolution of the contact pressure versus the sliding distance. The contact pressure of the alloys decays with the increasing of the sliding distance approaching to the value of the TCP. As the wear rate, the alloys' TCP would be

reached only for very high sliding distances. The TCP values found for the SM-0.3B, SM-0.7B, SM-1B and commercial SMSS are 1.02 MPa, 1.13 MPa, 1.23 MPa and 0.56 MPa, respectively. Based on this, one can see that adding small amounts of boron in the spray-formed SMSS clearly improved the wear resistance in the POC wear test by reducing the wear rates as well as the maximum accumulated worn volumes and, consequently, increasing the TCPs.

It is interesting to observe that in the case of the dry sand against rubber wheel abrasive wear test almost no difference between the wear resistance of the commercial SMSS and the SM-0.3B could be seen. On the other hand, in the POC wear test the behavior of the SM-0.3B was very similar to the SM-1B and much superior to the commercial SMSS. Such different results can be explained by looking to the worn surfaces and the collected debris of the plate-on-cylinder wear test samples in Figure 5.16. It can be seen that when the hard cylinder slides against the commercial SMSS, its asperities and the abrasive particles present in the fluid push the surface material forward in a process that involves considerable plastic deformation. During the sliding the material is detached from the surface in form of debris with plate morphology, as can be clearly seen in Figure 5.16 (a) and (b). Once the presence of the hard M_2B-type borides in the microstructure restrain the plastic deformation of the alloy, the wear mechanism observed in the commercial SM is less effective in the boron-modified alloys. Through the analysis of Figures 5.16 (c) - (h), it can be noted that the same wear mechanism of pushing and removing plate-like debris occurs in the SM-0.3B, SM-0.7B and SM-1B, but in reduced scale. When the boron content and the borides fraction are increased, the restriction to plastic deformations also increases resulting in higher wear resistances.

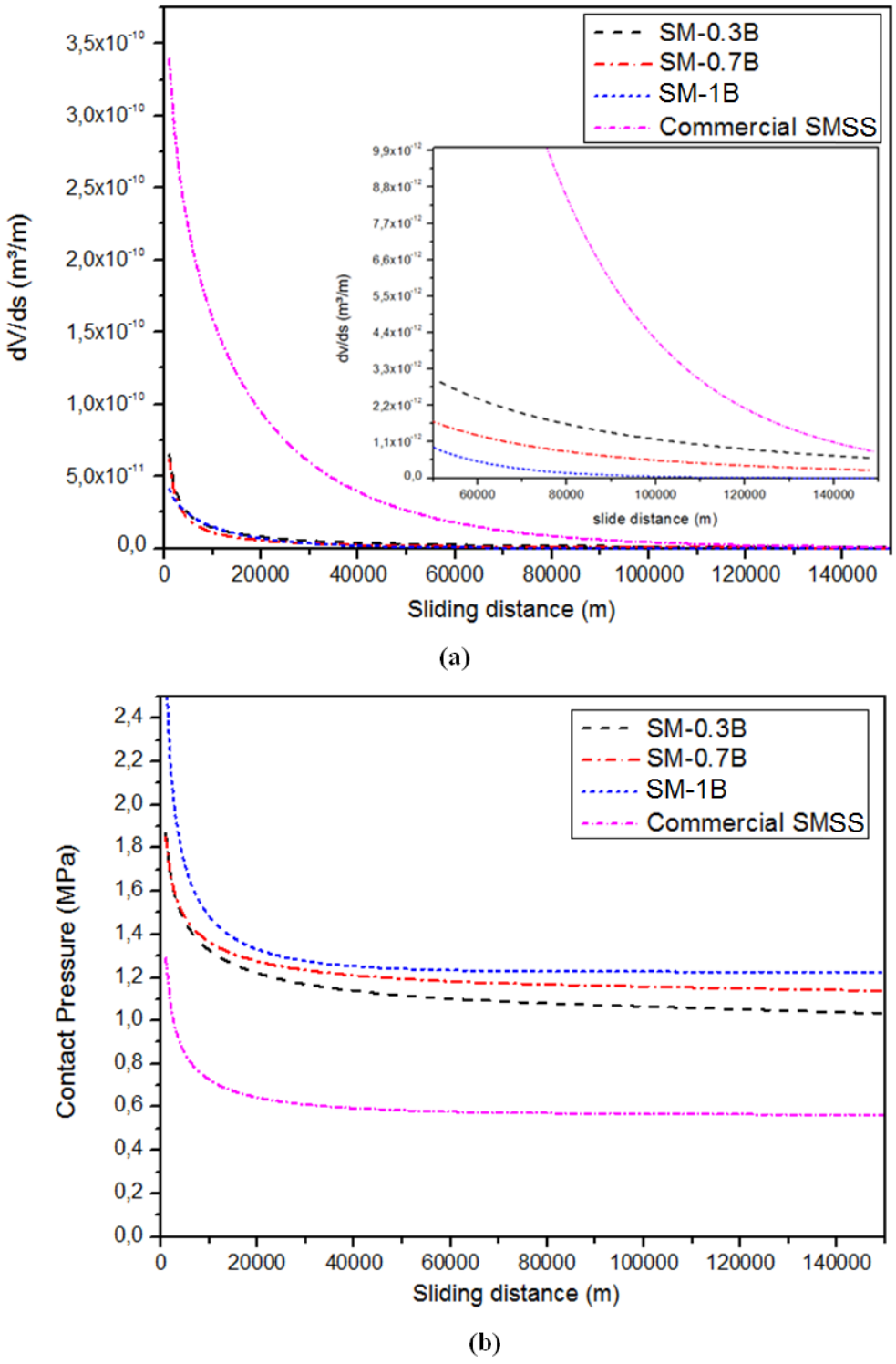

Figure 5.15 - **(a)** Wear rate and **(b)** contact pressure versus sliding distance in the plate-on-cylinder wear test.

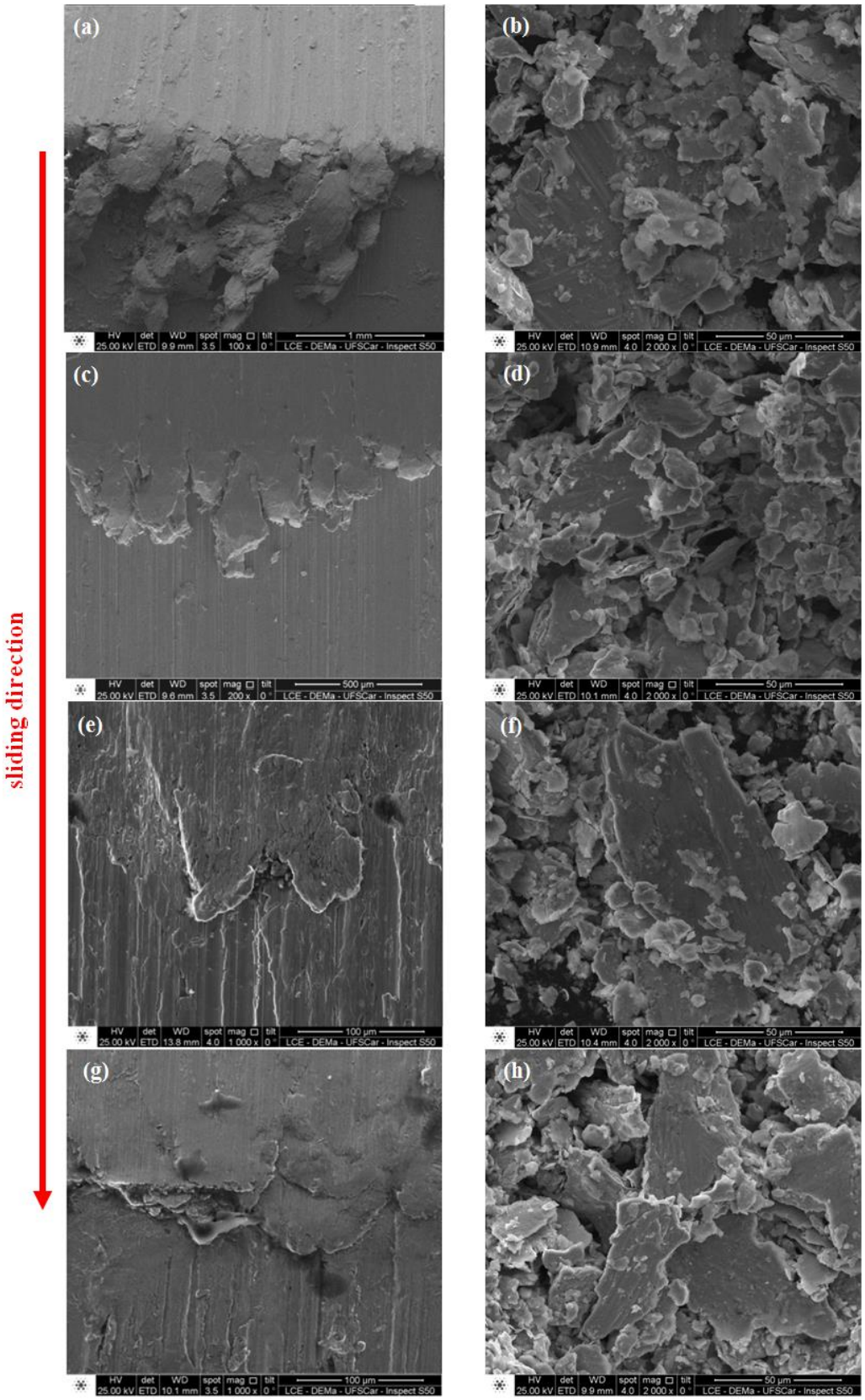

Figure 5.16 - SEM images (secondary electrons) of the worn surfaces and plate-like debris of **(a)** and **(b)** commercial SMSS, **(c)** and **(d)** SM-0.3B, **(e)** and **(f)** SM-0.7B and **(g)** and **(h)** SM-1B after the POC wear test.

5.1.4 Effect of boron content on the corrosion Resistance

The electrochemical corrosion behaviors in an acid chloride media of the SM-0.3B, SM-0.7B, SM-1B, and SM-14Cr-1B by EIS and potentiodynamic polarization tests using three different protocols were carried out as described in section 4.1.4. In order to have a comparative basis, the same electrochemical analyses were carried out in the commercial SMSS. Figure 5.17 (a) presents the EIS results of the commercial SMSS tested using the protocols I, II and III. It can be seen that the EIS results when the commercial SMSS is subjected to pre-passivation treatment (protocol I), and when it is maintained only 1 h in solution (protocol II) were quite similar. These results show that the pre-passivation treatment in water has practically no effect to improve the quality of the passive film of the commercial SMSS. On the other hand, when the commercial SMSS is maintained for 12 h in the test solution (protocol III), the impedance values are considerably higher than in the two previous cases. Such results show that a long immersion time in the test solution, which is considerably more oxidizing than deionized water, favors the formation of the passive film. Thus, a more protective passive film is probably formed in protocol III, which results in higher impedance values. Figure 5.17 (b) shows the polarization curves of the commercial SMSS after the three test protocols. One can see that all curves presented similar behavior with passive plateaus and no activation peak, meaning that the passive films are present throughout the polarization tests. For the commercial SMSS, similar values of E_{corr} (around -200 mV/SCE) and E_{pit} (about 140 mV/SCE) were found regardless the test protocol. However, the corrosion current density (j_{corr}) and the current density throughout the passive plateau of the commercial SMSS subjected to protocol III were slightly lower than those observed when protocols I and II are applied (see Table 5.4, which summarizes the results obtained from the ensemble of polarization curves). Such reduction of the anodic current when the samples stay longer in the test solution before the polarization tests corroborates the assumption that a more protective passive film is formed in protocol III. Nevertheless, it must be stressed that this apparent improvement of the film for samples treated according to protocol III did not correspond to an increase in the pitting potential. Indeed, as seen in this figure and in the E_{pit} values

complied in Table 5.4, this better behavior is limited to the region close to the corrosion potential, the pitting potential being roughly the same regardless the measurement protocol.

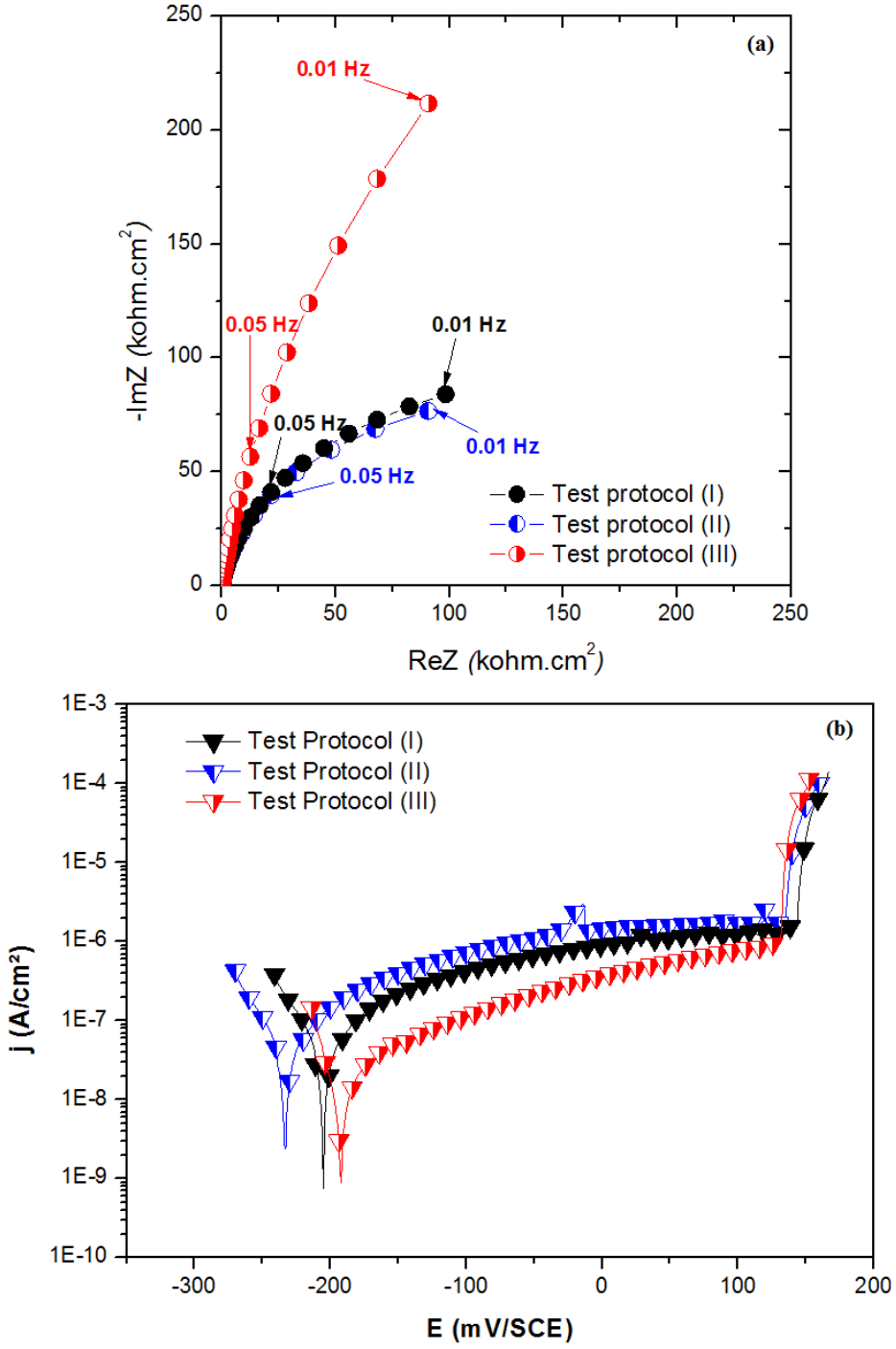

Figure 5.17 - **(a)** EIS and **(b)** polarization results of the commercial SMSS. Electrolyte: 35 g/L NaCl, pH = 4.0.

Table 5.4 - Mean values of the corrosion properties obtained from the polarization curves for the three test protocols applied. Solution: 35 g/L NaCl and pH=4.0.

		Commercial SMSS	SM-0.3B	SM-0.7B	SM-1B	SM-14Cr-1B
Protocol I	**j_{corr} (A/cm^2)**	$4x10^{-8}$	$4x10^{-8}$	$4x10^{-8}$	$5x10^{-8}$	$4x10^{-8}$
	E_{corr} (mV)	-205	-220	-220	-232	-229
	$E_{pit\ or}\ E_{crit}$ (mV)	146	70	13	-19	88
	$\Delta E = E_{pit} - E_{corr}$ (mV)	351	290	233	212	317
Protocol II	**j_{corr} (A/cm^2)**	$5x10^{-8}$	$9x10^{-8}$	$4x10^{-7}$	$4x10^{-7}$	$5x10^{-8}$
	E_{corr} (mV)	-240	-257	-347	-268	-165
	$E_{pit\ or}\ E_{crit}$ (mV))	146	0	-244	-102	59
	$\Delta E = E_{pit} - E_{corr}$ (mV)	386	257	103	166	225
Protocol III	**j_{corr} (A/cm^2)**	$1x10^{-8}$	$2x10^{-8}$	$3x10^{-7}$	$3x10^{-7}$	$1x10^{-8}$
	E_{corr} (mV)	-182	-178	-375	-429	-189
	$E_{pit\ or}\ E_{crit}$ (mV)	136	137	-249	-297	129
	$\Delta E = E_{pit} - E_{corr}$ (mV)	318	315	125	132	318

Figure 5.18 shows the EIS and the potentiodynamic polarization results of the four spray-formed boron-modified SMSSs after being pre-passivated for 24 h in deionized water (protocol I). The EIS results – Figure 5.18 (a) – shows that the

impedance values are similar to the commercial SMSS regardless the alloys' chemical composition. This is a quite interesting result, which shows that in less oxidizing environments or, in other words, as far as the service conditions remain close to corrosion potential conditions, all the boron-modified SMSSs show roughly the same behavior as the commercial alloys. This is confirmed by the polarization curves depicted in Figure 5.18 (b) where it can be seen that the different curves almost merge in the corrosion potential region with a less than 30 mV difference in E_{corr} and almost identical j_{corr} values, as seen in Table 5.4. Nevertheless, E_{pit} values for the different boron-modified samples appeared to be lower than the commercial one. This was mainly the case of SM-0.7B and SM-1B, which presented considerably lower values (13 and -19 mV/SCE, respectively) when compared to the commercial SMSS (146 mV/SCE), whilst samples SM-0.3B and SM-14Cr-1B presented a better behavior (70 and 88 mV/SCE, respectively) although still below the commercial reference.

Figure 5.19 presents the EIS and polarization results of the spray-formed boron-modified SMSSs carried out using protocol II. In this case, the behavior of the boron-modified alloys showed to be different of the commercial one yet at corrosion potential conditions. The impedance values of the SM-0.3B and SM-14Cr-1B – Figure 5.19 (a) – were lower than the commercial SMSS. By observing their respective polarization curves – Figure 5.18 (b) – it can be seen that the behavior presented by the SM-0.3B and SM-14Cr-1B has tended to the one shown by the commercial SMSS. Both alloys showed low j_{corr} ($9x10^{-8}$ A/cm^2 and $5x10^{-8}$ A/cm^2, respectively) and formation of passive plateaus. However, the length of the passive plateau, which can be estimated as $\Delta E = E_{pit} - E_{corr,}$ was considerably shorter when compared to the commercial SMSS (see Table 5.4). This set of results shows that the passive films formed on the SM-0.3B and SM-14Cr-1B surfaces during 1 h of OCP are less protective, probably thinner and/or less uniform than the one formed in the commercial SMSS in the same conditions. On the other hand, the SM-0.7B and SM-1B showed considerably higher j_{corr} than the other alloys, about $4x10^{-7}$ Acm^{-2}, followed by an increase in the anodic current up to 10^{-4} A cm^{-2} without presenting passive plateaus. Accordingly, the EIS results showed smaller loops, tending to accentuated lower

polarization values, which is consistent with the absence of passivating plateau and an activation-like kinetic evolution of the metal-electrolyte interface as the overpotential increases.

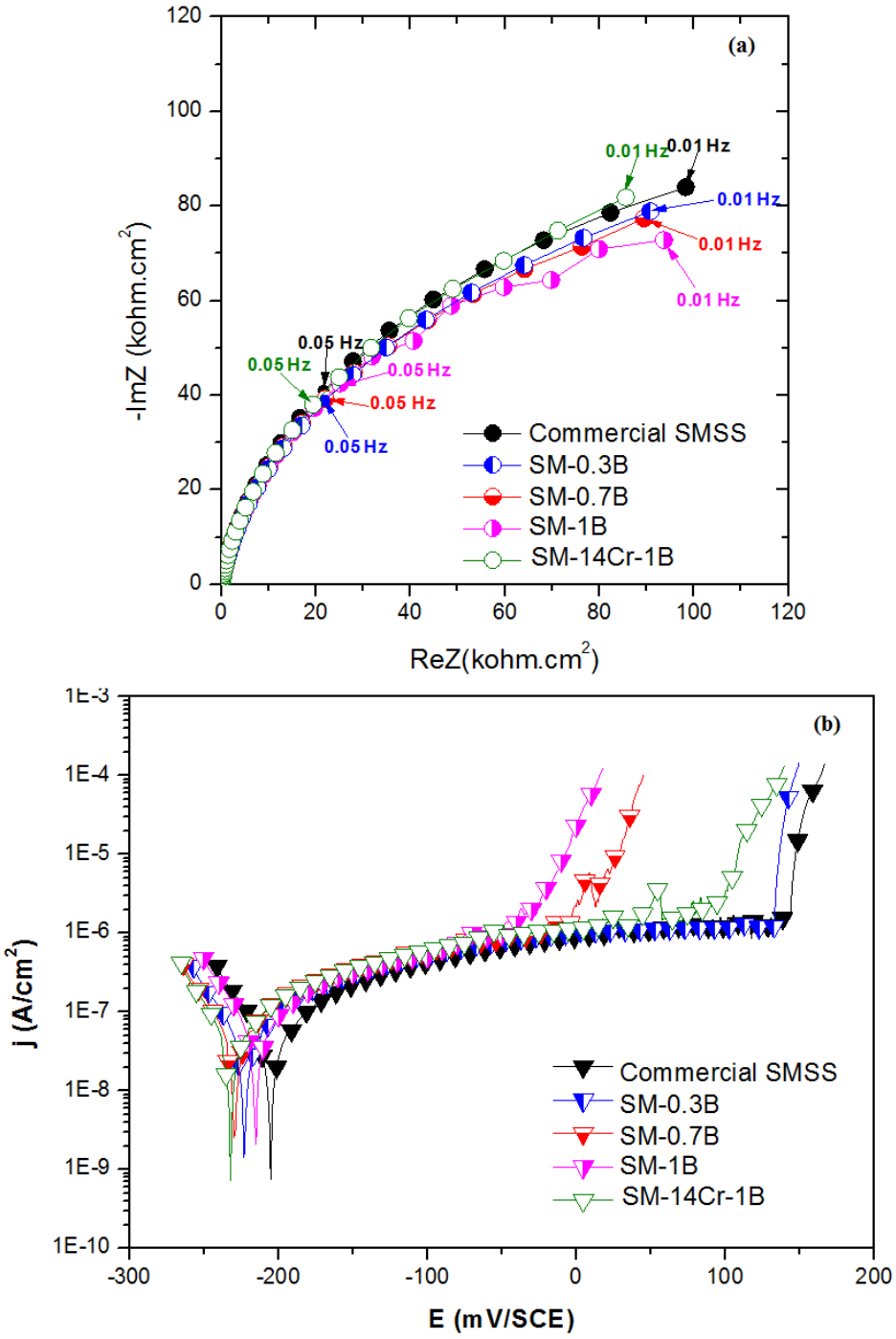

Figure 5.18 - **(a)** EIS and **(b)** polarization results of the spray-formed boron-modified SMSSs in protocol I.

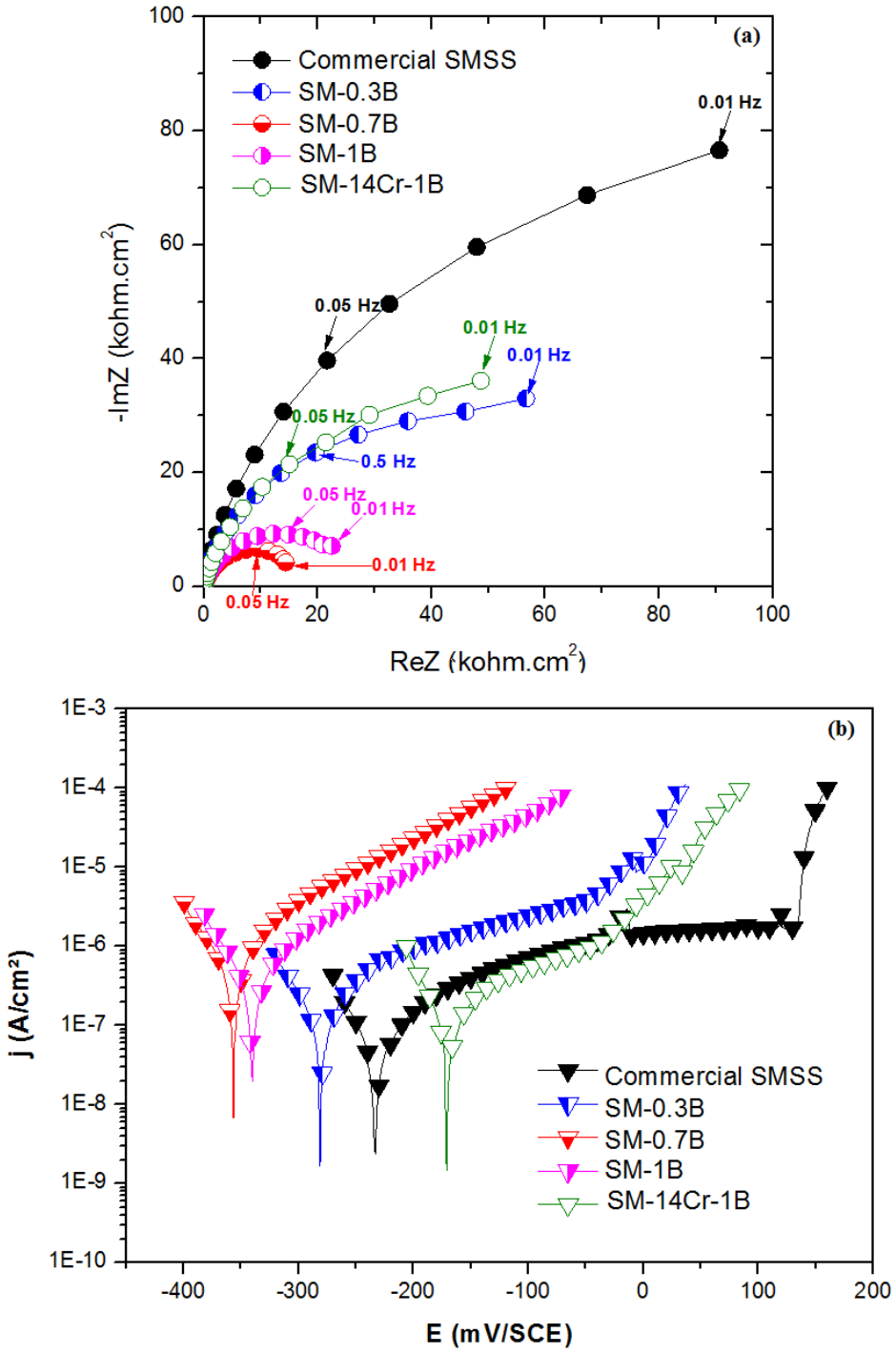

Figure 5.19 - **(a)** EIS and **(b)** polarization results of the spray-formed boron-modified SMSSs in protocol II.

Figure 5.20 presents the results of the analyses carried out using the test protocol III. The EIS results – Figure 5.20 (a) – show that when the SM-0.3B and SM-14Cr-1B stay longer in solution, their impedance values are quite similar to

the commercial SMSS. The same can be seen in the polarization curves – Figure 5.20 (b). When the SM-0.3B and SM-14Cr-1B stay longer in solution, their corrosion behavior are practically the same than the commercial SMSS. The E_{corr}, E_{pit} and j_{corr} are practically the same (see Table 5.4). Such results make clear that the SM-0.3B and SM-14Cr-1B need longer periods in solution, when compared to the commercial SMSS, to form a stable and uniform passive film. However, if sufficient time is given, the corrosion properties of these two spray-formed boron-modified SMSS no longer differ from the commercial SMSS. Meanwhile, the EIS and potentiodynamic polarization results of the SM-0.7B and SM-1B are virtually the same when the protocols II and III are applied. Since both alloys are not able to passivate in such acid chloride media during the open circuit procedure, they can tend to a steady state where the surface is uniformly corroded.

Figure 5.21 shows the corroded surfaces of the spray-formed boron-modified SMSSs after being anodically polarized until the density current reach 5 mA/cm^2. Since the SM-0.3B and SM-14Cr-1B showed that they are able to passivate in the acid chloride media used, the polished samples were left for 12 h in solution before being polarized (as in the test protocol III). As can be seen in Figure 5.21 (a) and (d) the deep polarization induced the nucleation of pits that grew deeply and confined all the anodic current whilst the outer surface around remained clearly passive. Both images clearly show that the pit grew by consuming the martensitic matrix while the M_2B-type borides network remained intact. These results indicate that the borides, in such test condition, have higher corrosion resistance than the steel matrixes and the corrosion process takes place preferentially in the martensitic matrixes. Once it was shown that the SM-0.7B and SM-1B are not able to passivate in the acid chloride media, these samples were left only 1h in OCP before polarization. The corroded surfaces of both alloys is presented in Figure (b) and (c). In both cases, unlike to the previous passivated samples, an uniform corrosion is observed yielding the borides distribution to be revealed. Again, the corrosion process occurs preferentially in the martensitic matrixes, the M_2B borides remaining apparently inert at the grain boundaries.

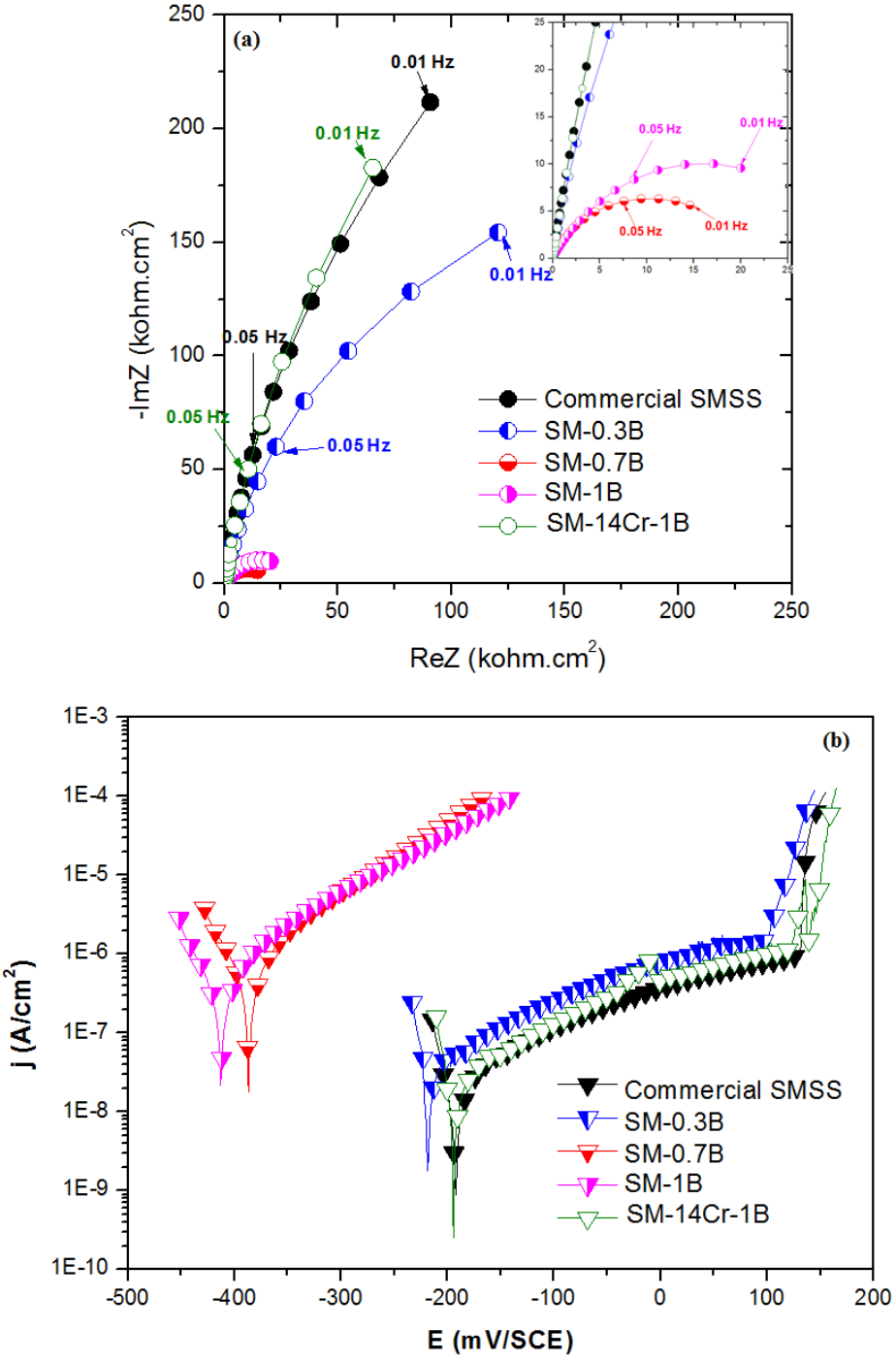

Figure 5.20 - **(a)** EIS and **(b)** polarization results of the spray-formed boron-modified SMSSs in protocol III.

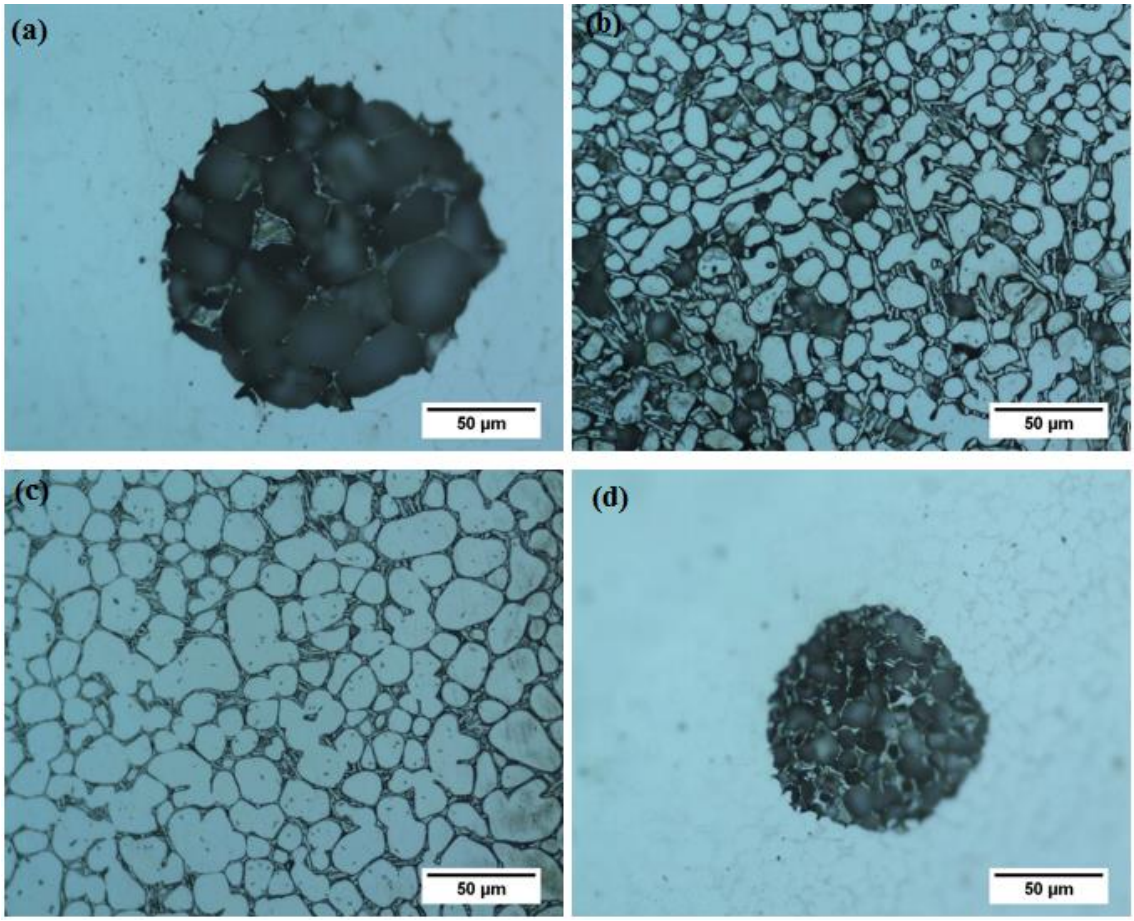

Figure 5.21 - Corroded surfaces of **(a)** SM-0.3B, **(b)** SM-0.7B, **(c)** SM-1B and **(d)** SM-14Cr-1B.

The results so far show that the SM-0.3B and SM-14Cr-1B presents similar corrosion resistance to the commercial SMSS when the samples are subjected to a long resting protocol that allows the passive films to be reinforced increasing their efficiency. This issue brings to the forefront of the problem the question of their capability to repassivate, to keep or recover their corrosion resistance when subjected to mechanical impacts. The spray-formed boron-modified SMSS grades were developed to be used in applications where severe wear and corrosion conditions take place. This means that in service conditions, the passive film will be often locally damaged by abrasion. In these situations, the kinetic of repassivation of the surface is expected to be a crucial issue. Based on this, EN measurements were performed to evaluate the passivation kinetic of the passive film of the SM-0.3B and SM-14Cr-1B compared to the commercial SMSS after a simulated abrasion event imposed to the sample connected to the CE

terminal. Figure 5.22 presents the coupling current between the identical samples recorded before and after abrasion. Before abrasion, the samples were maintained 24 h immersed in the solution aiming to have all surfaces covered by a long-aged passive film, which would result in extremely low coupling currents (near zero) that were effectively obtained as seen in the different curves. After the wear simulation, the abraded CE surface (without passive film) should behave anodically while the intact WE should behave cathodically, delivering a negative sign current flow. One can effectively see that in all cases immediately after abrasion the recorded currents were negative as high as 10^{-6} A in absolute values. Such currents result from the oxidation reactions taking place on the surface of the abraded samples resulting in their repassivation. With the repassivation process, the currents decrease along the time until recovering low current values (near zero), indicating that both surfaces are almost identical again.

To further evaluate comparatively the repassivation kinetics of the alloys two approaches were used. First, the time for the coupling current to reach 10% of the maximum recorded current was determined for each alloy. Figure 5.23 (a) shows the time evolution of the normalized current (regarding the maximum current). It can be seen that the commercial SMSS reach 10% of the maximum current (represented by the dashed red line at (I/I_{max} = 0.1) in only 8.1 s, whereas the SM-0.3B and SM-14Cr-1B took 51.6 s and 184.4 s, respectively. These results show that the current recovery of the commercial SMSS is considerably faster than the SM-0.3B and SM-14Cr-1B. However, in all cases the current decreases to 10% of the maximum value in the first minutes after abrasion. The second approach was to determine the time taken to the current to recover the I_{corr} determined by the polarization curves of the samples obtained when the test protocol III were applied (see Table 5.4). Figure 5.23 (b) presents the graphic of I/I_{corr} versus time for the three alloys. One can see that in about 18 min the I_{corr} of the commercial SMSS was achieved, which means that after this time, the condition before the abrasion was practically restored. For the SM-0.3B this time was around 32 min, whereas for the SM-14Cr-1B, even after two hours the current was still 3 times higher than the previously measured I_{corr}.

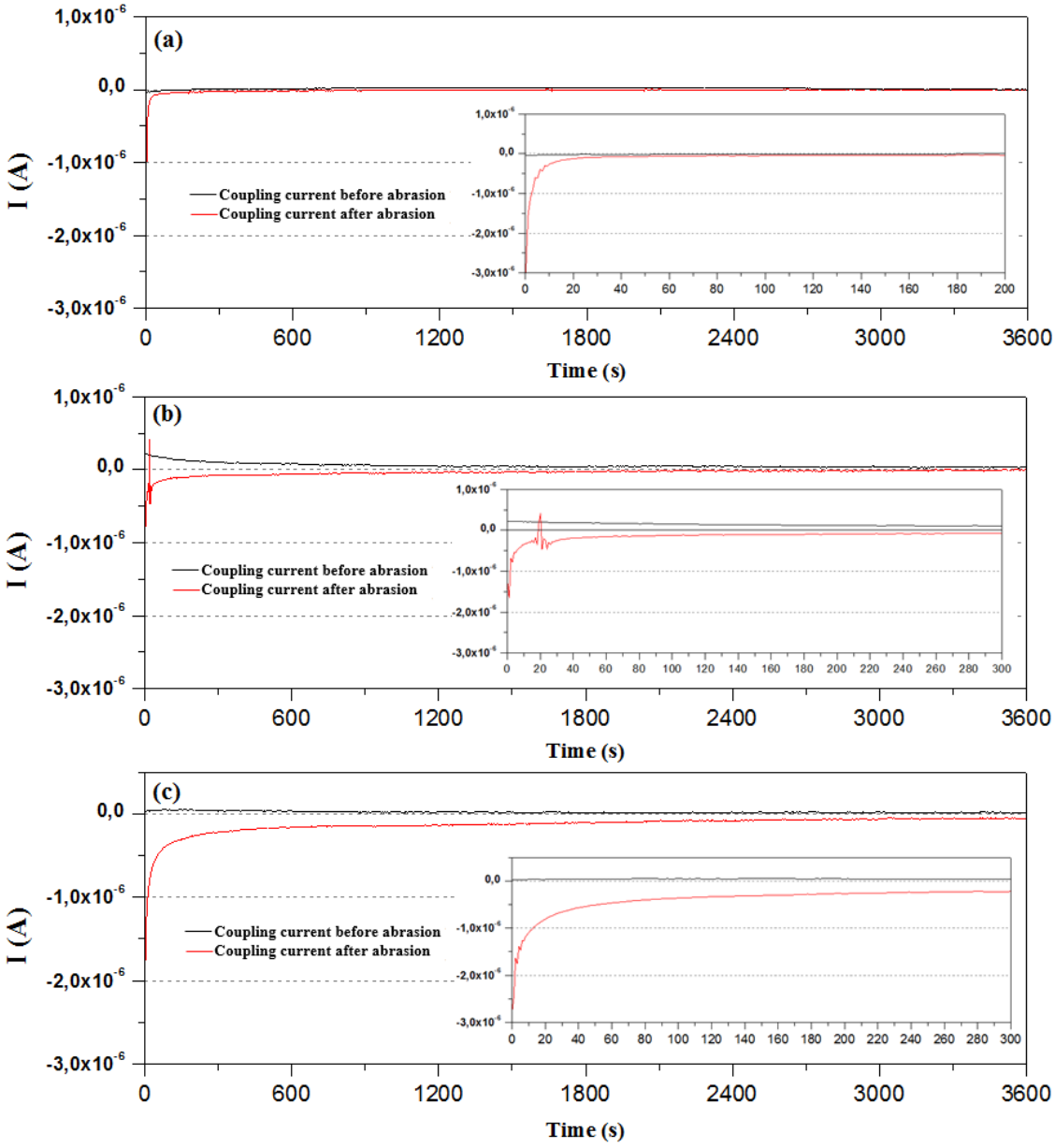

Figure 5.22 - Coupling currents measured by EN before and after abrasion of **(a)** commercial SMSS, **(b)** SM-0.3B, and **(b)** SM-14Cr-1B. Arbitrary zero time origin.

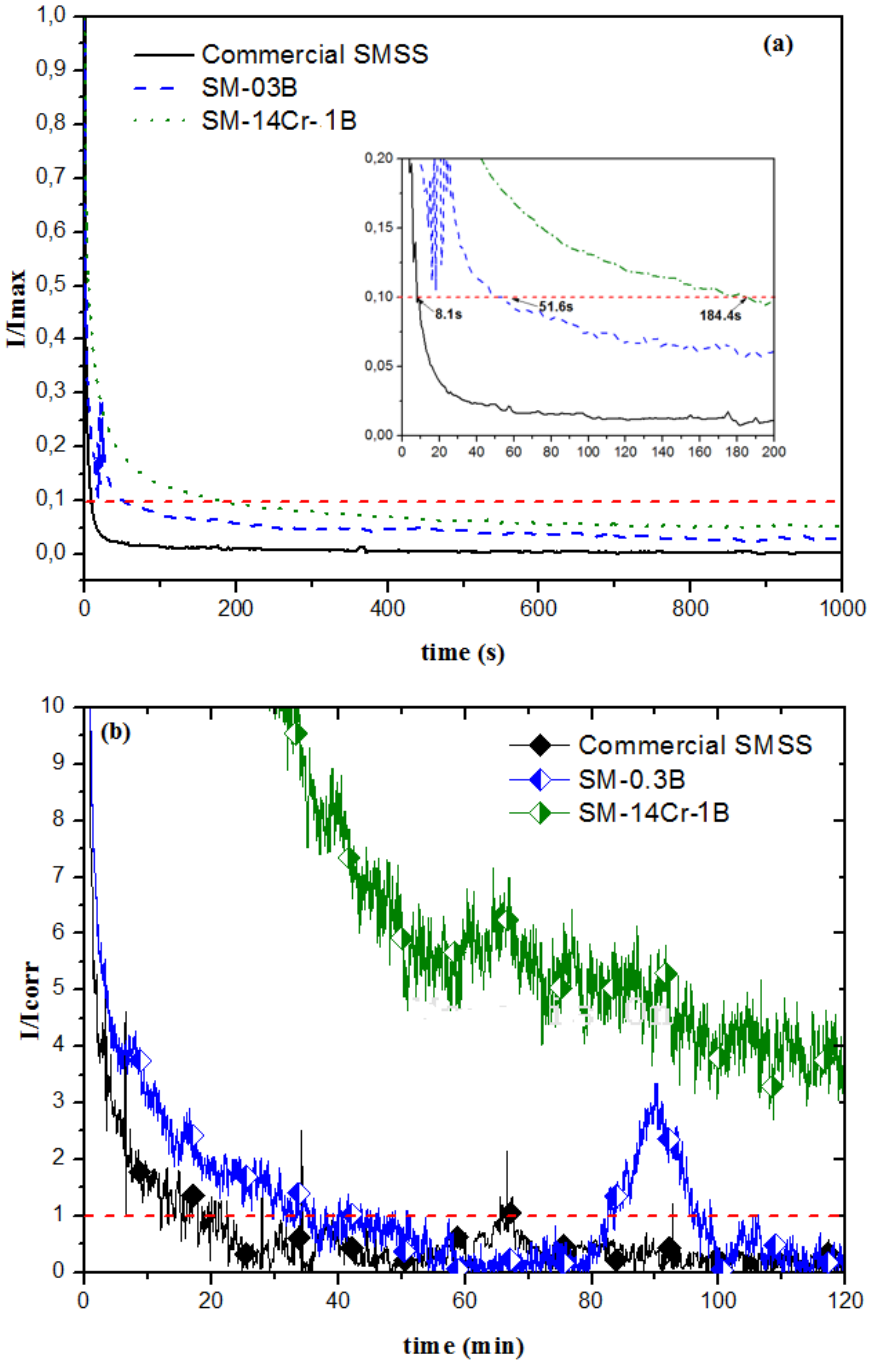

Figure 5.23 - **(a)** I/Imax and **(b)** I/Icorr measured by EN after abrasion of the commercial SMSS, SM-0.3B, and SM-14Cr-1B. Arbitrary zero time origin.

Based on the electrochemical analyses presented above, it can be seen that in the case of the spray-formed boron-modified SMSS grades, the chemical composition of the alloys play the central role on their corrosion behavior. The

results show that the formation of M_2B reduces the overall Cr content in the martensitic matrix. The EIS and polarization results show that the chemical composition of the final martensitic matrixes determines the corrosion resistance of the alloy. When immersed in the acid chloride media, the SM-0.7B and SM-0.1B, which have the remaining Cr content in the matrixes below the threshold value of stainless steels (about 11 %wt.), did not present passivation and behave as an active metal, presenting generalized corrosion during polarization. On the other hand, the SM-0.3B and SM-14Cr-1B, whose matrixes presented Cr contents above the 11 %wt. (11.6 %wt. and 13.4 %wt., respectively), when immersed for long periods in the acid chloride media, behave quite similar to the commercial SMSS. The test protocol III showed that both alloys (SM-0.3B and SM-14Cr-1B) are able to passivate in the more aggressive media presenting practically the same corrosion properties as the commercial SMSS. The corroded surfaces presented in Figure 5.21, indeed, show that the martensitic matrixes are the microstructural features that control the corrosion process, while the borides network seems to be inert. This is clearly seen by the pits of the SM-0.3B and SM-14Cr-1B surfaces – Figures 5.21 (a) and (d) – where martensitic matrixes were corroded and the borides network remained apparently intact.

The results of the test protocol II showed that when the SM-0.3B and SM-14Cr-1B are maintained only one hour in solution, the electrochemical behavior of both alloys are quite different from the commercial SMSS, mainly by presenting lower impedance values and E_{pit} (see Figure 5.19 and Table 5.4). Such results suggest that the passivation kinetics of the spray-formed boron-modified SMSSs might be slower than the commercial SMSS. This was corroborated with the EN measurements, which showed that the coupling current of the commercial SMSS, after the simulated abrasion event, decreased considerably faster than the SM-0.3B and SM-14Cr-1B. However, surprisingly the repassivation kinetics of the SM-0.3B was faster than the SM-14Cr-1B, even the first one having lower remaining Cr content in the martensitic matrix. This result suggests that the boride fraction (when the minimum chromium content to guarantee the passivation of the matrix is present) may have an important influence on the repassivation kinetics of the spray-formed boron-modified stainless steels. However, to

understand how the presence of borides and the boride fraction affect the passivation mechanisms of this sort of alloy, deeper studies must be carried out. In any event, the most important result was to show that the SM-0.3B and SM-14Cr-1B are able to repassivate themselves after a wear event in the acid chloride media.

These results demonstrate that if the Cr content of the spray-formed boron-modified SMSSs, regardless the boron content, is controlled in such a way that the Cr content of the martensitic matrix remains within the range of the conventional commercial SMSS grades, the corrosion behavior of the alloy is not impaired. This is a quite encouraging result, since addition of alloying elements to form second phases or precipitates aiming at increasing the hardness and/or wear resistance is usually expected to be accompanied by a reduction of the corrosion properties.

5.2 Spray Forming of semi-industrial bimetallic pipes

5.2.1 Effect of process parameters on the shape, porosity, and surface temperature

Figure 5.24 shows the spray-formed pipe obtained from the SF1 run. Its irregular shape arose from the constantly fracturing and releasing of the SM-13Cr-1B during the first periods of the deposition. This sequence of events can be observed in Figure 5.25. Such result is attributed to the high cooling rate of the SM-13Cr-1B deposit caused by the presence of a cold substrate. As mentioned before, during the solidification of boron-modified SMSSs, an eutectic network of M_2B-type boride is formed. The presence of such interconnected network along the whole microstructure has an embrittlement effect on the alloy. When the SM-13Cr-1B is deposited onto the substrate at room temperature, the deposit is rapidly cooled. Rapid cooling rates can lead to a rapid contraction of the boron-modified SMSS, which generates high internal stresses. Since the boron-modified SMSS are not able to accommodate the stress through plastic deformation, the deposited layer fails and is expelled from substrate due to its rotation. However, after some period of deposition, the substrate is heated up and, consequently, the cooling rate of the deposited layer decreases. After approximately two thirds of the total deposition period, the release of the first layer from the substrate was interrupted. One can see in Figure 5.24 (b) that the last part of the spray-formed pipe presented bimetallic structure.

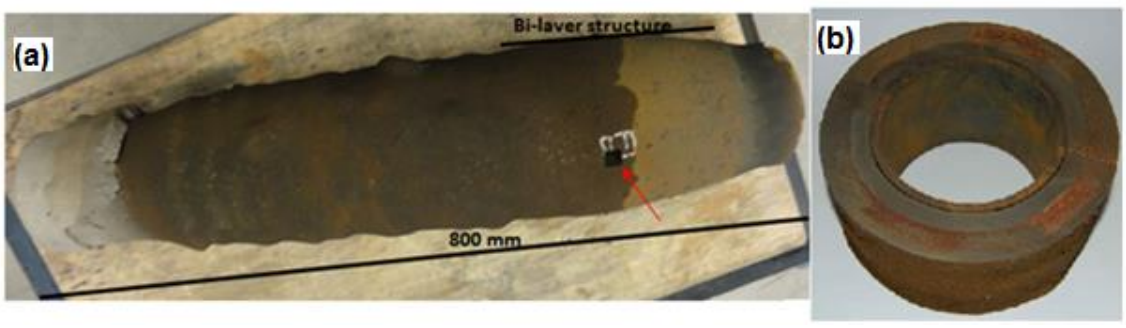

Figure 5.24 - **(a)** Spray-formed SM-13Cr-1B/SMSS bimetallic pipe produced in the SF1 run. **(b)** Transversal section of the bimetallic section.

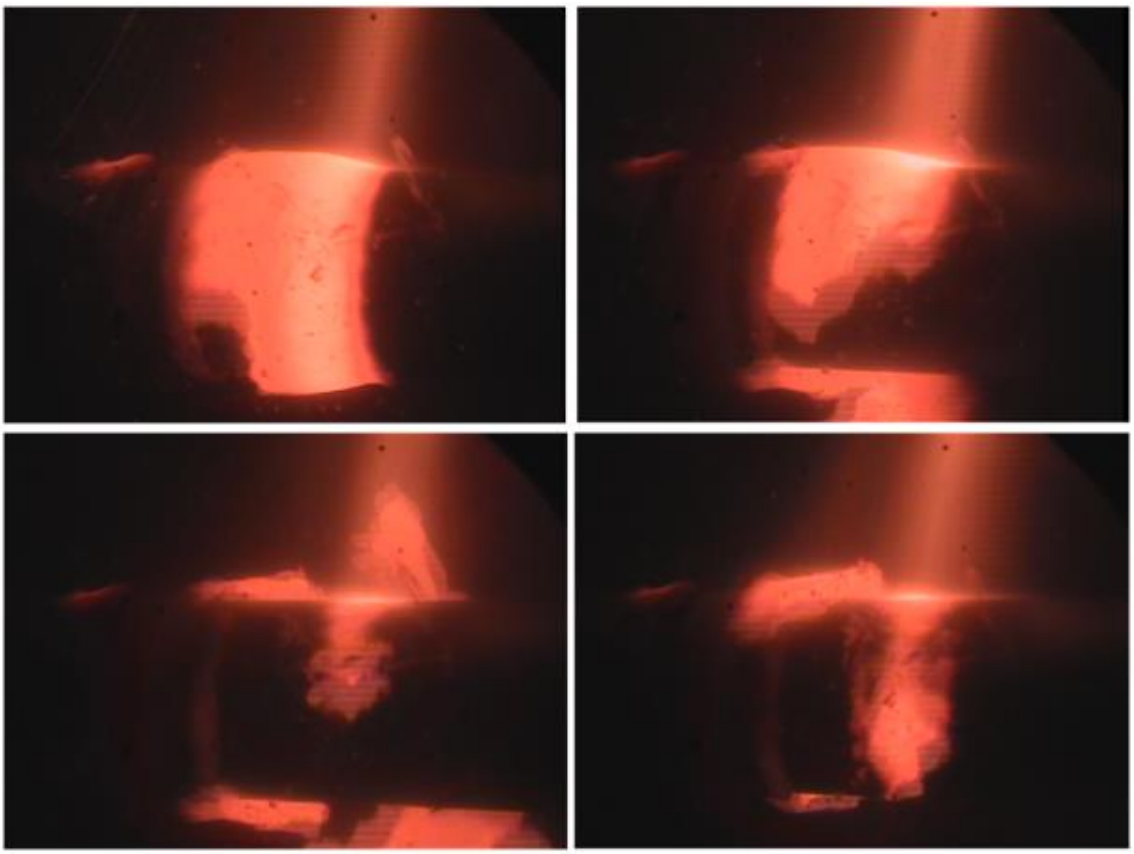

Figure 5.25 - Sequence showing the fracturing and expelling of the SM-13Cr-1B layer during deposition in SF1.

A sample from the bimetallic section was cut by electric wire erosion (red arrow in Figure 5.24 (a)). The thickness of the bimetallic region, measured from this sample, is 29 mm, being the SM-13Cr-1B layer 11 mm-thick and the SMSS layer 18 mm-thick. The porosity profile of this sample is shown in Figure 5.26. It can be seen that the porosity level of the SM-13Cr-1B vary from 0.2 % to 2.2 %, being the higher porosity values found close to the bottom of the sample (near the substrate). The SMSS layer presented very high porosity level, ranging from 5 % to 25 %. In this case, the higher porosity values are observed at the region near the interface between both layers. Figure 5.27 presents optical microscopy images showing the porosity profile of the bimetallic section. It can be seen that there is an abrupt transition between the SM-13Cr-1B layer and the SMSS layer (Figure 5.27 (b). It can be seen that the porosity present in the SM-13Cr-1B are relatively round and isolated, which suggests that the porosity is formed by gas

entrapment or by solidification shrinkage. On the other hand, the porosity observed in the SMSS is completely interconnected and non-uniform (see Figure 5.27 (a)) and (b). This sort of porosity is typical of cold processing conditions, which results in insufficient liquid fraction in the deposition zone. In this case, the equilibrium temperature of the deposition zone is likely to be lower than the alloy's *solidus* temperature and the liquid present in the deposition zone is rapidly solidified. In Figure 5.27 (e), it can be clearly seen the boundaries of the droplets that reached the substrate completely solidified.

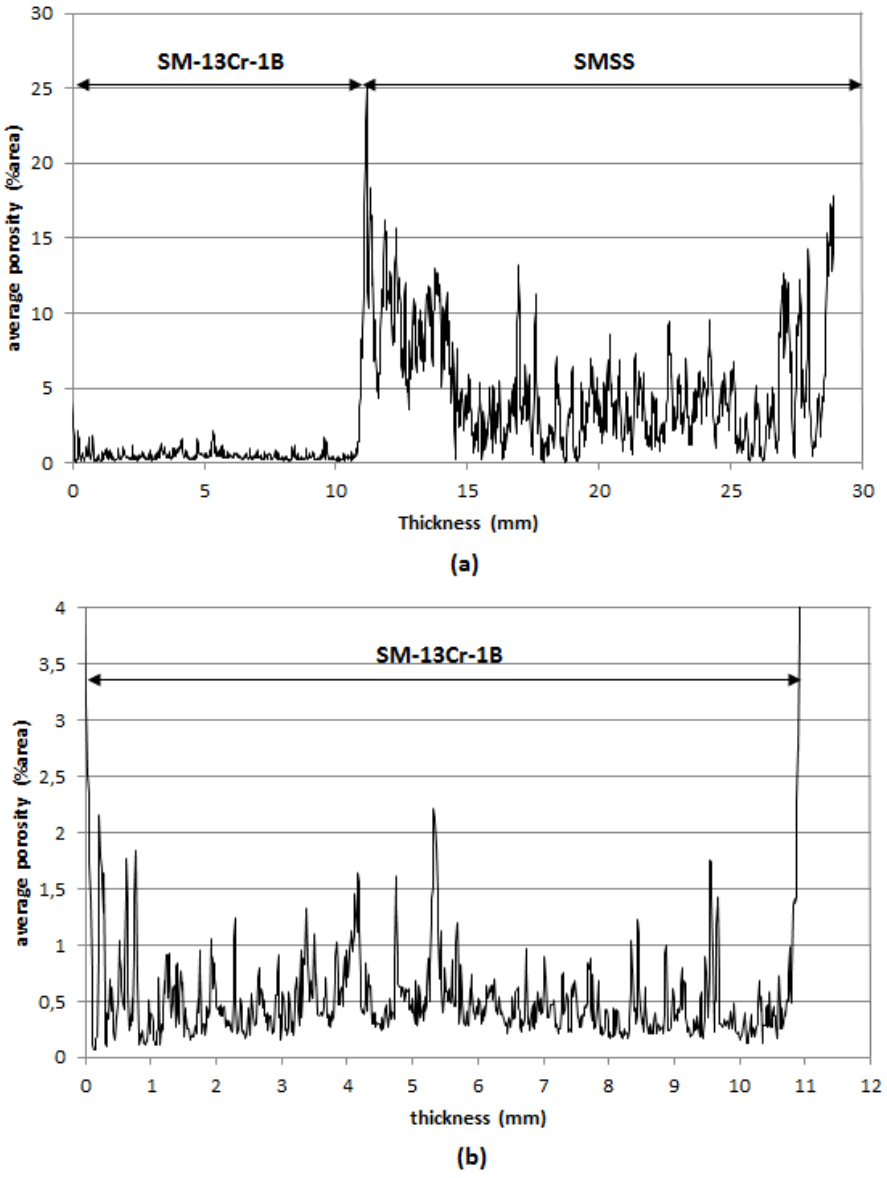

Figure 5.26 - **(a)** Porosity profile of the bimetallic pipe spray formed in SF1 run. **(b)** Zoom of the porosity profile of the SM-13Cr-1B layer.

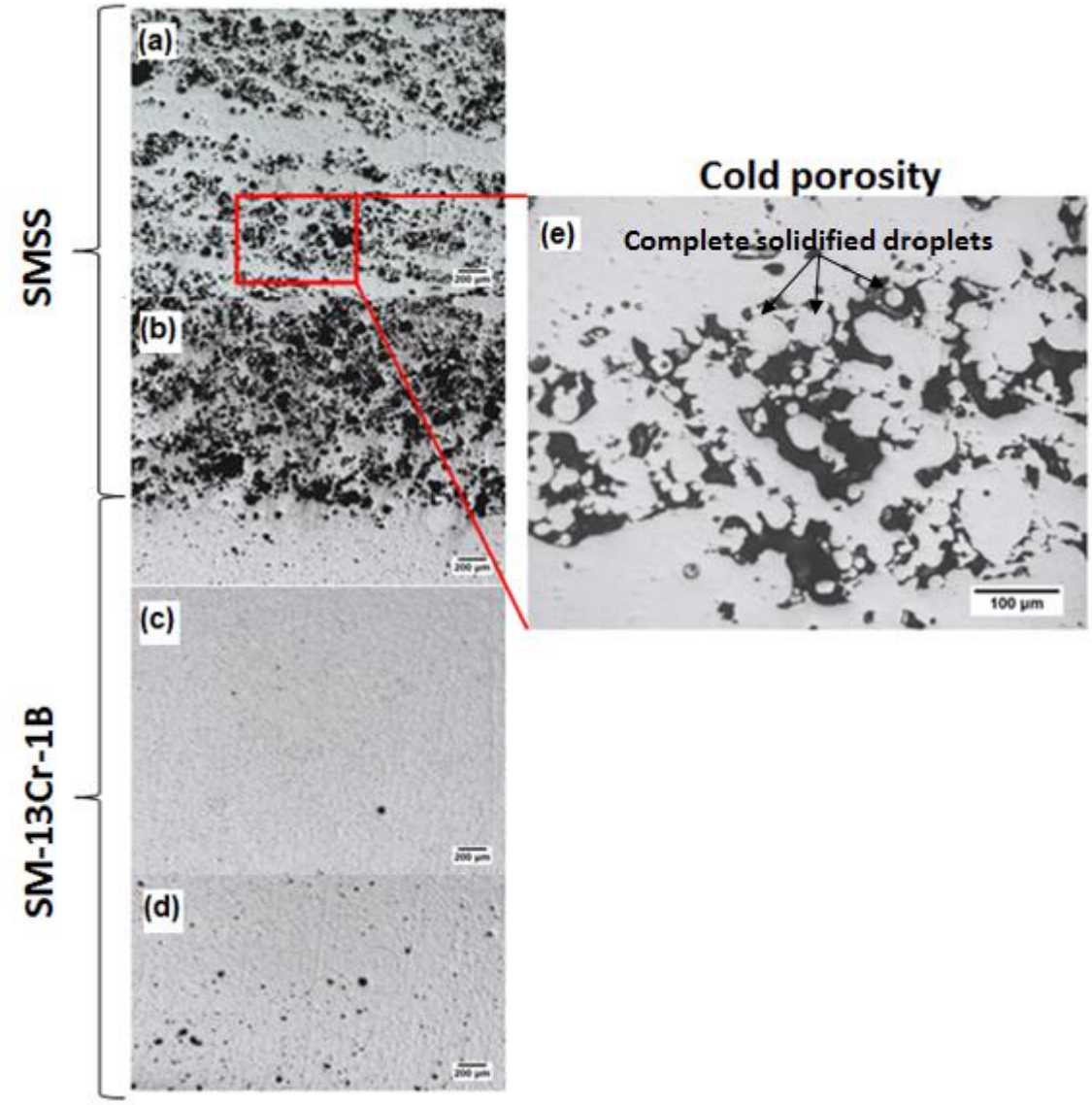

Figure 5.27 - OM images showing the porosity profile of the SF1 spray-formed pipe. **(a)** Middle of the SMSS layer, **(b)** interface region, **(c)** middle of the SM-13Cr-1B layer, **(d)** bottom of the SM-13Cr-1B layer. **(e)** Zoom of the porosity in the SMSS layer.

From these results, it can be concluded that the process parameters applied to both layers led to cold processing conditions that caused two different problems: (i) fracturing of the SM-13Cr-1B layer during the first deposition stages; and (ii) high cold porosity level of the SMSS layer.

Aiming to investigate if the fracture of the boron-modified layer was indeed caused by the high cooling rate promoted by the cold substrate, only the boron-modified SMSS was spray-formed in the SF2 run. In this run, the substrate was preheated at 950 ºC by using a preheating system installed inside the atomization chamber. However, such increase of the initial substrate temperature could lead to extremely hot process condition, which can also be non-ideal. For instance, hot deposition conditions can considerably increase the liquid fraction in the deposition zone, which may cause high levels of hot porosity by gas entrapment or even ejection of liquid from the deposition zone due to the substrate rotation. Based on this, the melt flow rate was also reduced from 0.25 kg/s to 0.12 kg/s (by reducing the nozzle diameter) to balance the process condition. In order to attain approximately the same layer thickness, the substrate withdraw speed was also changed, from 6 mm/s to 4 mm/s for the SF1 and SF2 run, respectively. Figure 5.28 (a) shows the picture of the SM-14Cr-1B pipe resulted from the SF2 run. One can see that changing the process parameters was effective to avoid the fracture and releasing of the boron-modified SMSS. The spray formed pipe presented a smooth surface with regular thickness along the length. The higher thickness region at the last part of the pipe is because of the interruption of the substrate translation before that the spraying period was completed. Another surprising result is the high yield (ratio of feedstock and final deposit mass) of the SF2 run, about 85.3 %, which is considerably high for spray-formed pipes. Observing the transversal section of the pipe – Figure 5.28 (b) – it can be seen that the thickness of the pipe was quite uniform (11.05 mm ±0.11 mm) and with low visual porosity.

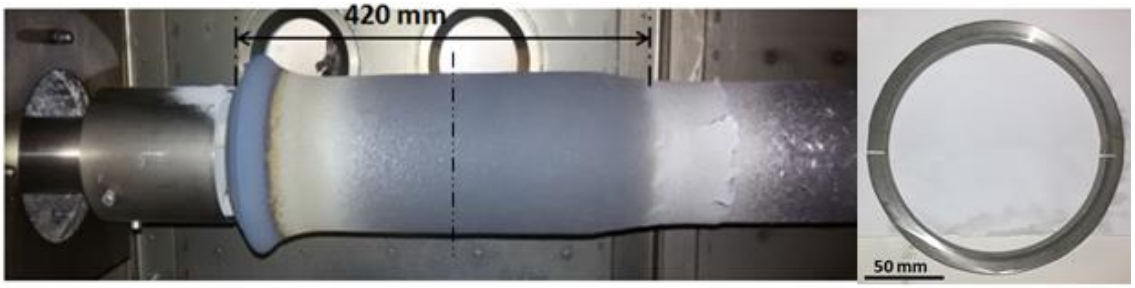

Figure 5.28 - **(a)** Spray-formed SM-14Cr-1B pipe produced in the SF2 run. **(b)** Transversal section at the middle of pipe (dashed lined in (a)).

Figure 5.29 shows the porosity profile of a sample from the middle ring shown in Figure 5.28 (b). It can be seen that the porosity at the bottom part (near the substrate) is around 5.0 %, however, the porosity reduces sharply and is maintained lower than 1.0% throughout the thickness of the pipe. The porosity level is slightly increased up to 1.5% just next to the top surface.

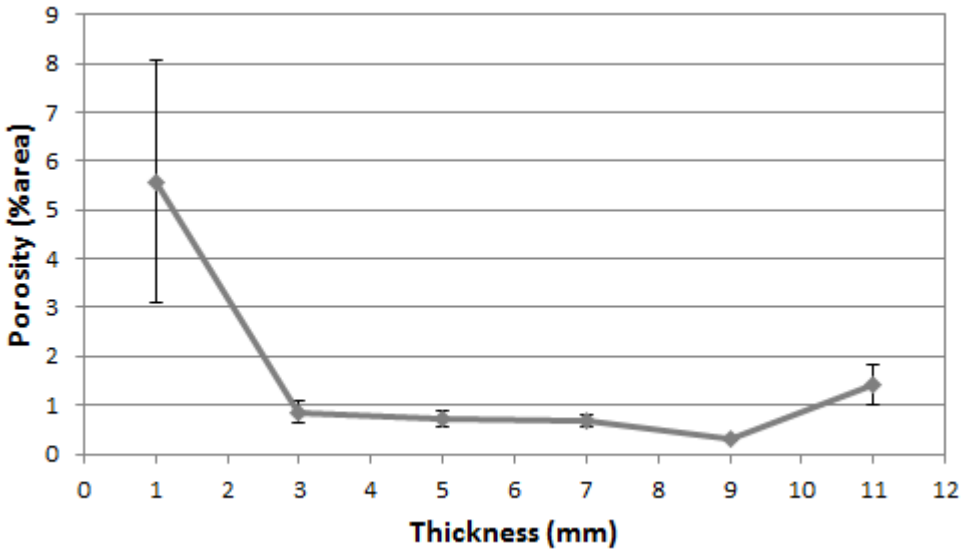

Figure 5.29 - Porosity profile of the SM-14Cr-1B pipe spray-formed in the SF2 run.

Since at first glance the results of the SF2 run were satisfactory, the same process parameters were applied to the first spray of the SF3 run. In the second spray, the process parameters were changed in order to reduce the porosity level observed in the SMSS layer. To avoid cold porosity, hotter spray condition was applied in SF3 by: (i) Reducing the atomizer gas pressure from 0.6 MPa to 0.5

MPa; (ii) reducing the scanning angle of the atomizer from 6º to 0º (no scanning); and (iii) preheating the substrate to 950 ºC. Again, to avoid extremely hot deposition conditions and to maintain approximately the same layer thickness than the SF1 bimetallic pipe, the melt flow was reduce from 0.67 kg/s to 0.42 kg/s and the substrate withdraw speed reduced from 6.0 mm/s to 4.0 mm/s. Figure 5.30 (a) presents the picture of the bimetallic pipe produced in the SF3 run. The SF3 bimetallic pipe also presented uniform thickness throughout the length, with a higher thickness region in its last part (same reason than the SF2 pipe). The surface of the SMSS layer was rougher than the SM-14Cr-1B in the SF2 run. The yield was 79.3 %, still considerably high. However, as the overspray powders of each alloy cannot be separated, the individual yield of each layer cannot be directly measured.

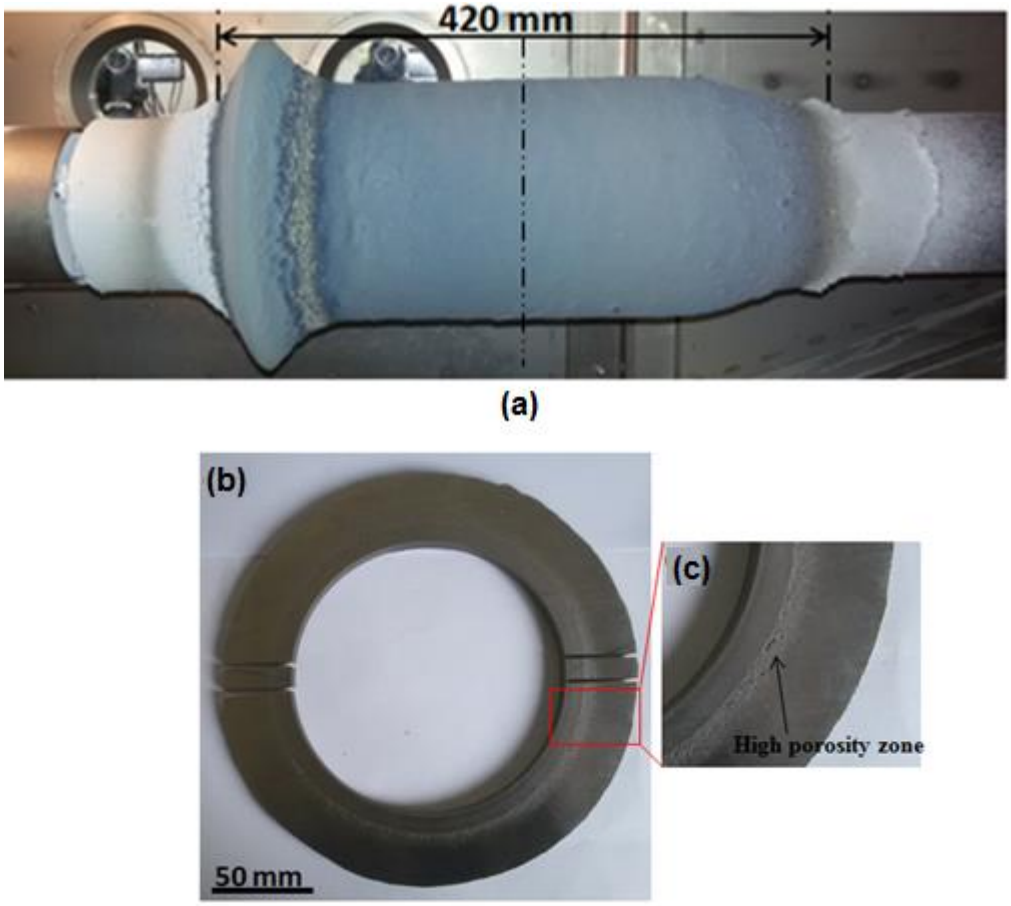

Figure 5.30 - **(a)** Spray-formed SM-14Cr-1B/SMSS bimetallic pipe produced in the SF3 run. **(b)** Transversal section at the middle of pipe (dashed lined in (a)). **(c)** Zoom detailing the porous zone at the bi-layer tube.

Figure 5.30 (b) shows the transversal section of the spray-formed pipe. The thickness of the pipe (measured in the central ring) was also quite uniform (35.61 mm ± 0.49 mm). However, the thickness of the SM-14Cr-1B layer (8.93 mm ± 0.15 mm) was thinner than the thickness of the SF2 pipe. Such difference was caused by the slightly smaller melt flow rate observed in the SF3 run (0.10 kg/s) than in the SF2 run (0.12 kg/s), which may be caused by small variations of the nozzle dimension. The SM-14Cr-1B layer did not present visual porosity and seems to be quite dense. The SMSS layer presented a region with high porosity near to the interface (see Figure 5.30 (c)). However, the regions far from the interface, the major part of the SMSS layer, also did not present high visual porosity levels. Figure 5.31 presents the porosity profile along the thickness of the middle ring. One can see that the SM-14Cr-1B layer presented the same

porosity profile than the SF2 pipe, with a higher value of porosity at the bottom part, which decreases sharply to porosity levels around 1.0%. On the other hand, just above the interface between both layers the SMSS layer present a high porosity region of about 10 mm with porosity levels as high as 50.0 %. However, above this region the porosity level is practically constant and lower than 1.0%. The porosity increases again only near the top surface of the pipe. The OM images showing the porosity profile of the SF3 pipe are displayed in Figure 5.32. One can see that the high porosity level region next to the interface – Figure 5.32 (c) – presents irregular shape characteristic of cold processing condition. Such porosity profiles in the SF2 and SF3 pipes must be related to the surface temperature of the deposit during the deposition.

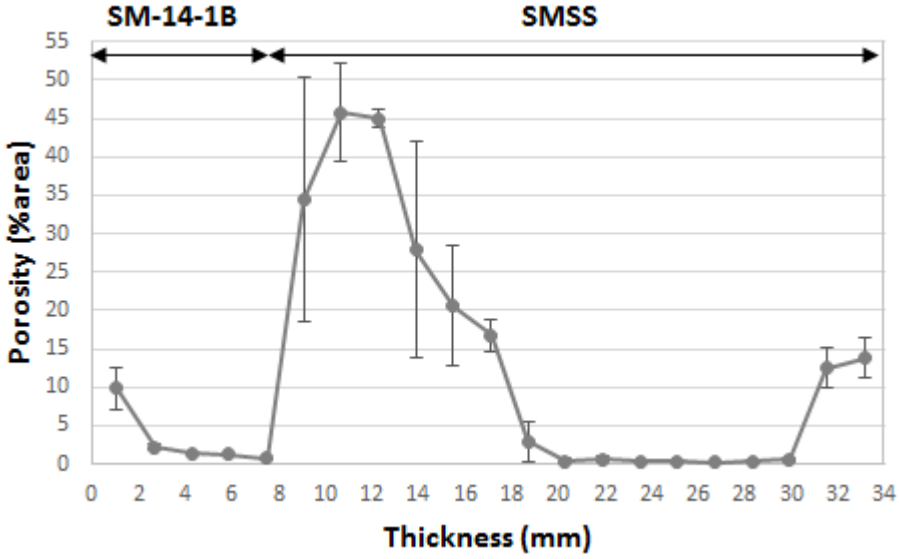

Figure 5.31 - Porosity profile of the bimetallic pipe spray-formed in the SF3 run.

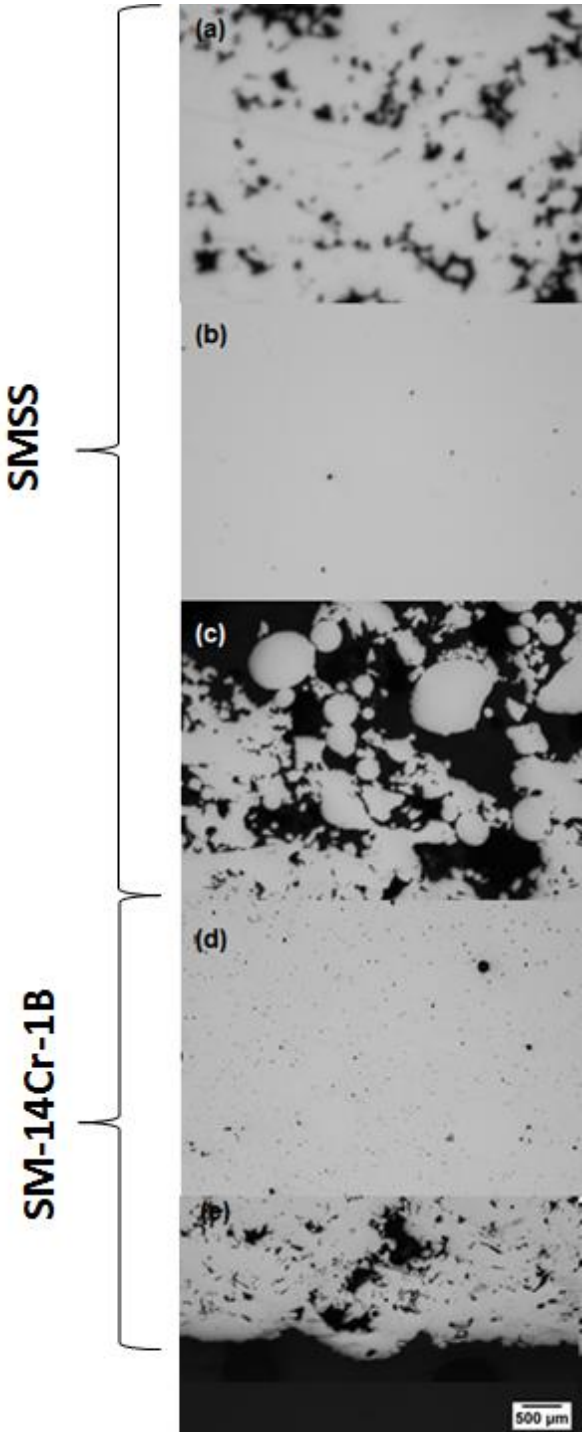

Figure 5. 32 - OM images showing the porosity profile of the SF3 spray-formed pipe. Region **(a)** near the top surface, **(b)** middle, and **(c)** near the interface of the SMSS layer. **(d)** Middle and **(e)** bottom region of the SM-14Cr-1B layer.

Figure 5.33 (a) and (b) present charts of the surface temperature measured by optical pyrometer along the measuring range and the spray time, for the SF2 and SF3 runs, respectively. The black dashed lines in both charts shows the region of the surface exactly under the centerline of the SM-14Cr-1B spray cone (only spray cone of the SF2 and first spray cone of the SF3), where the highest surface temperatures are found. Figure 5.34 (a) presents a graphic showing the evolution of the surface temperature under the center of the spray cones (along line 1 in both charts). One can see that during almost the whole spraying period, in both runs, the temperature surface under the centerline of the spray cone was kept practically constant around 1250 ºC. It can be seen that the surface temperatures measured in SF2 was always slightly higher than in SF3, which resulted from the slightly lower melt flow rate of the last one. However, the difference in the measured temperatures is almost negligible, which means that the process conditions were successfully reproduced in both runs.

One can see that the maximum surface temperature lies between the SM-14Cr-1B *liquidus* and *solidus* temperatures, in accordance with the results presented by Uhlenwinkel and Ellendt [45], who demonstrated that low porosity levels, as observed in the SM-14Cr-1B layers in both SF2 and SF3 runs, are obtained when the surface temperature of the deposit is above the alloy's *solidus* temperature. Moreover, the constant maximum temperature indicates that a steady state was maintained during almost the whole process period, meaning that the thermal history of the spray-formed pipe was the same in the whole pipe length. This is corroborated by the porosity profiles of the SF3 pipe at different lengths – Figure 5.35 – which are practically the same regardless the position.

The graphic shown in Figure 5.34. (b) presents the surface temperature throughout the pyrometer measurement range at two different process times (red dashed lines - lines 2 and 3 - in Figure 5.4 (a) and (b)), for both SF2 and SF3 runs. It can be seen that the surface temperatures at the beginning of the measurement range are around 850 ºC for both runs. Such temperature corresponds to the substrate temperature before entering under the SM-14Cr-1B spray cone. This result shows that the temperature of the substrate drops about 100 ºC since it leaves the induction preheating system until entering the

deposition zone. When the substrate reaches the deposition zone, the surface temperature increases almost linearly up to about 1250 ºC (maximum temperature at the centerline of SM-14Cr-1B spray cone). In the SF2 run, after the maximum temperature is reached, the surface temperature decreases linearly from the cone center to until the end of the measuring range. Such inverted V-shaped temperature profile explains the higher porosity levels at the bottom and top regions of the SF2 pipe, once it makes clear that these are the regions subjected to colder processing conditions. On the other hand, in the SF3 run, the surface temperature decreases until a minimum temperature and increases again when it reaches the second spray region. The minimum temperature found in this case was about 1060 ºC. This explains the high porosity levels found in the SMSS layer near the interface region. As the *solidus* temperature of the SMSS (1414 ºC) is considerably higher than this minimum temperature, the first layers of SMSS are cooled down and rapidly solidified due to heat transfer to the cooler surface of the SM-14Cr-1B layer, generating a high level of cold porosity. Although the profile temperature under the complete SMSS spray cone could not be measured because of the limited measurement range, it can be seen that the surface temperature also tends to increase linearly. Since the porosity profile of the SMSS layer also presents high porosity regions at the bottom (near interface) and top regions with a quite compact region at the middle, it is safe to assume that a similar inverted V-shaped temperature profile occurs in this case as well. Furthermore, the low porosity level at the center also indicates that the maximum temperature under the centerline of the SMSS spray cone must be above its *solidus* temperature. In next section, it will be shown that the thermal profiles along the deposition zone has also great influence on the microstructure of the spray-formed pipes throughout their thickness.

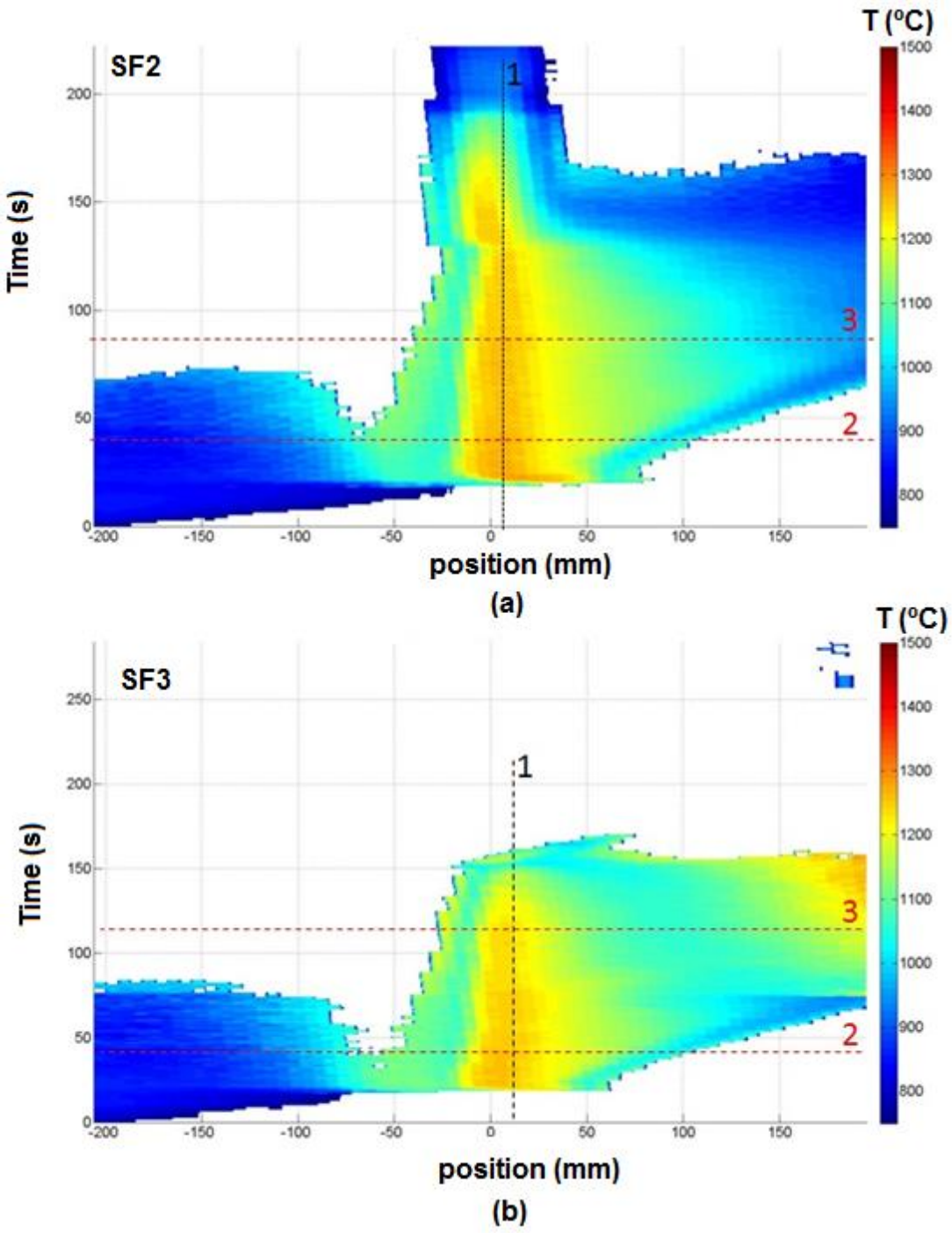

Figure 5.33 - Surface temperature charts from the optical pyrometer measurements. **(a)** SF2 and **(b)** SF3 run.

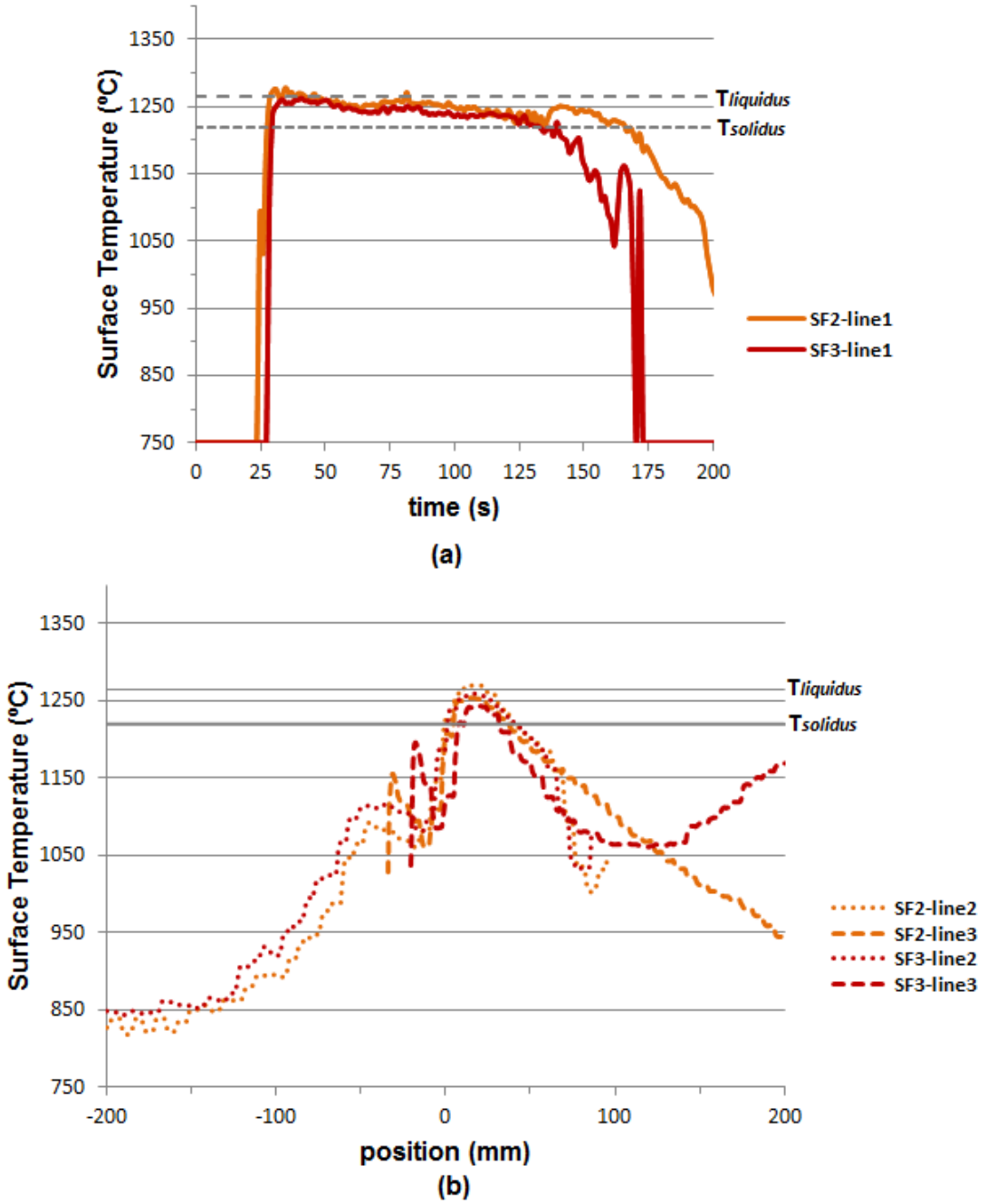

Figure 5.34 - Surface temperature **(a)** at the center of the first spray cone - defined by line 1 in Figure 5.4 (a) and (b) ; **(b)** at two different process time - defined by lines 2 and 3 in Figure 5.4 (a) and (b) – throughout the pyrometer measurement range, for both SF2 and SF3 runs.

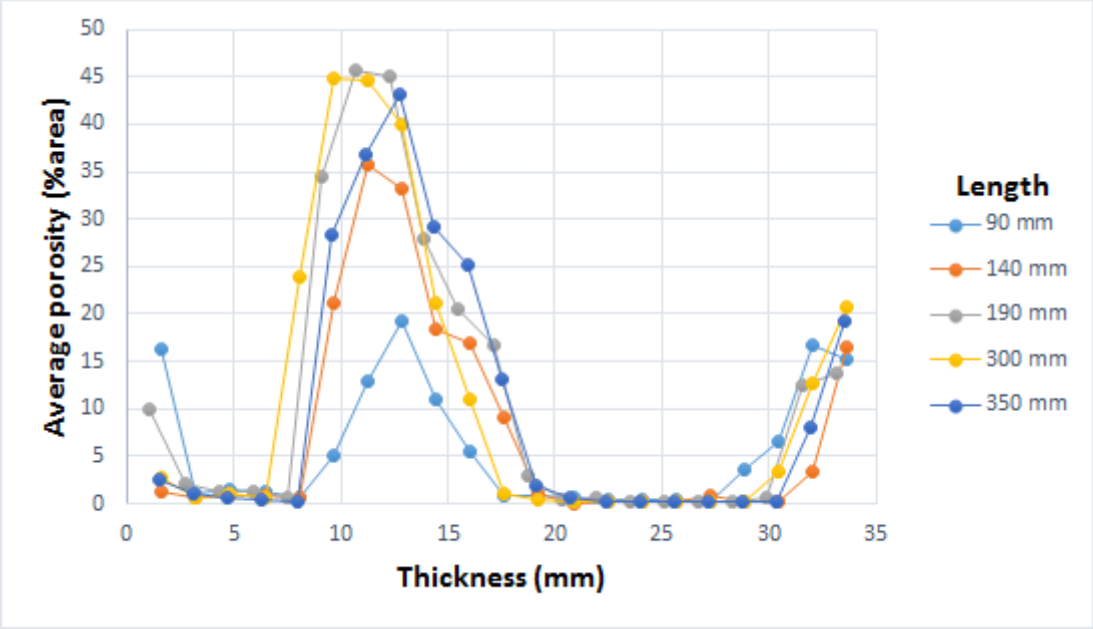

Figure 5.35 - Porosity profile at different lengths of the SF3 bimetallic pipe.

5.2.2 Effect of temperature profile on the pipe microstructure.

Figure 5.36 shows the microstructure of the SM-13Cr-1B layer of the SF1 bimetallic pipe at the bottom and middle part (1 mm and 6 mm from the substrate, respectively). One can see that at the middle part – Figure 5.36 (c) – the microstructure is composed of equiaxed martensitic grain size with the interconnected eutectic M_2B-type borides network. The eutectic boride network can be seen in detail in Figure 5.36 (d). Such microstructure is similar than those observed in the laboratory scale deposits (section 5.1.1). On the other hand, the microstructure at the region next to the substrate – Figure 5.36 (a) –, which was subjected to higher cooling rates, is considerably finer with high amounts of round M_2B boride precipitates. The round precipitates, observed in detail in Figure 5.36 (d), are spread along the microstructure next to some eutectic-like borides. Such borides precipitation at the bottom region and the absence of boride precipitates at the middle region of the SM-13Cr-1B layer is strong evidence that the back-diffusion mechanism takes place during the solidification of the boron-modified SMSS, as described in section 5.2.1. At the middle section of the SM-13Cr-1B the equilibrium temperature of the deposition zone must be above the alloy's

solidus temperature and, consequently, the eutectic borides present in the complete solidified droplets are remelted/dissolved, increasing the boron content of the liquid in the deposition zone. Moreover, the boron in solid solution in the primary dendrite (which must be boron-supersaturated because of the high cooling rate during the atomization process) diffuses back toward the liquid and all borides are then formed in the eutectic reaction. On the other hand, since the bottom region is subjected to higher cooling rates caused by intense heat loss to the cold substrate, the equilibrium temperature of the deposition zone next to the substrate must be lower, and around the alloy's *solidus* temperature (much probably below it). In this case, the solidification in the deposition zone is considerably faster than in the first case, and there is no time for the back-diffusion mechanism to occur. Consequently, the primary phase solidifies boron-supersaturated. After solidified, once boron has practically nil solubility in steel, the borides precipitate in solid-state reaction within the steel matrix, generating the microstructure observed in Figure 5.36 (a) and (b).

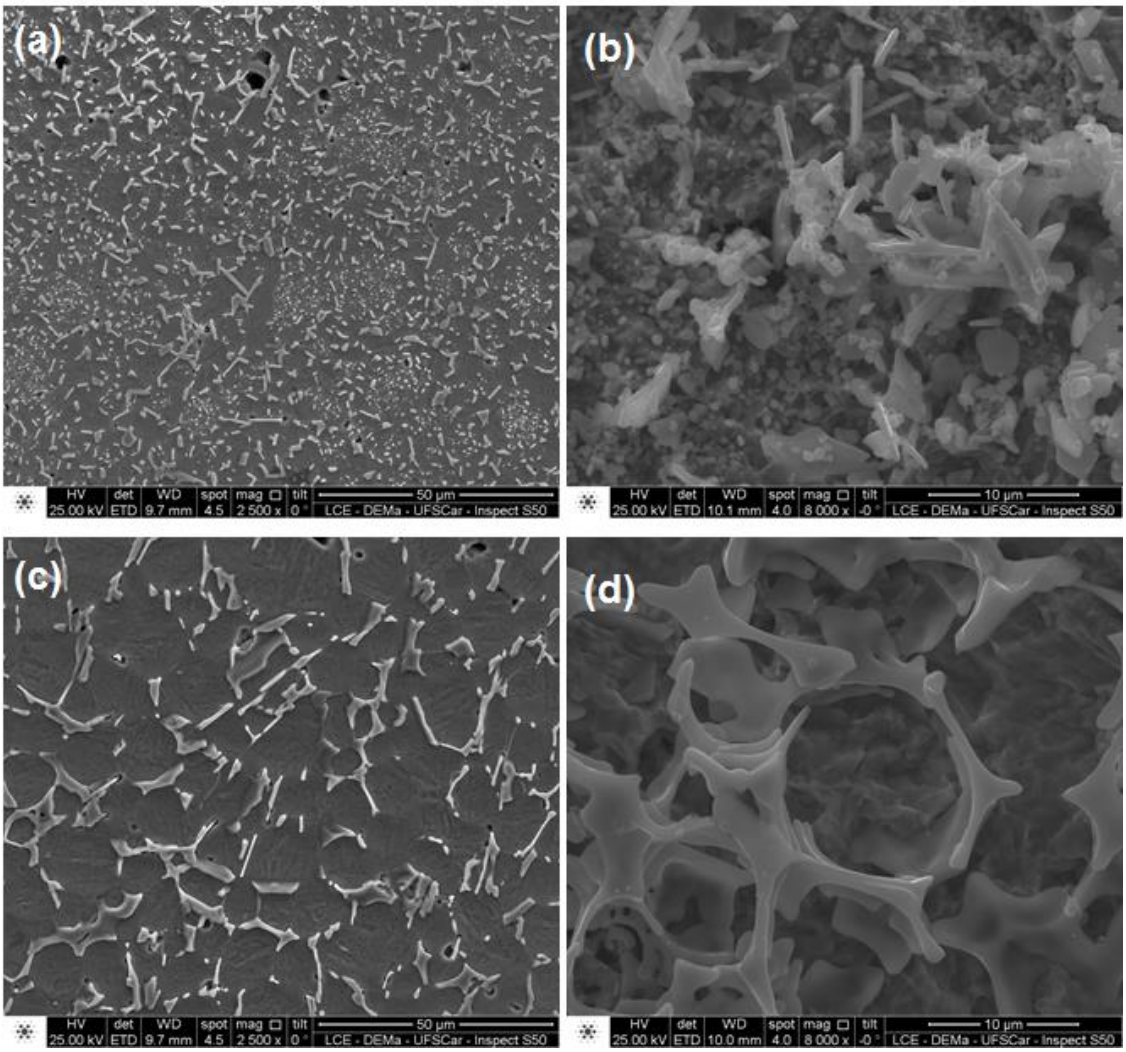

Figure 5.36 - Microstructure and borides morphology (deep etching) of the SM-13Cr-1B layer from the SF1 run at **(a)** and **(b)** bottom part (1 mm from substrate); and **(c)** and **(d)** middle part (6 mm from substrate).

Figure 5.37 presents optical microscopy images of the SM-14Cr-1B layers of both SF2 and SF3 pipes at different positions along their thickness. It can be seen that, in both cases, the microstructure at the bottom regions – Figures 5.37 (a) and (d) – and top regions – Figures 5.37 (c) and (f) – are finer than the microstructures at the middle regions – Figures 5.37 (b) and (d). By observing the borides morphologies shown in Figure 5.38, it can be seen that boride precipitation is limited to the regions next to the substrate – see Figure 5.38 (a). Just above it – Figure 5.38 (b) – it is possible to observe that all borides are interconnected in the eutectic network without visible precipitated borides. The

red circles in Figures 5.38 (b), (c), and (d) show regions previously occupied by martensitic matrix (removed by deep etching), indicating what would be the martensitic equiaxed grain size at the different positions.

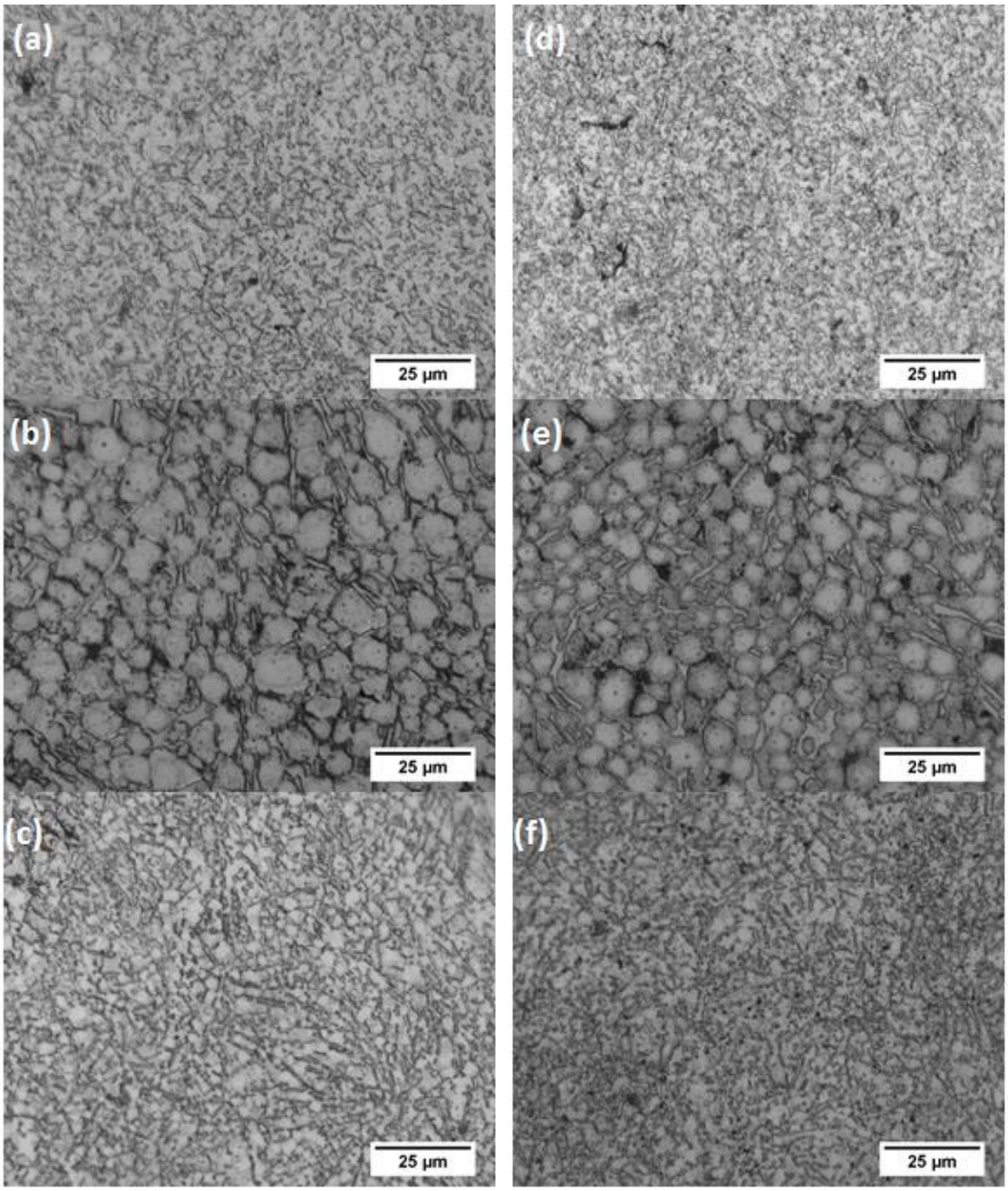

Figure 5.37 - OM images showing the microstructure of the SM-14Cr-1B SF2 pipe at **(a)** 3 mm, **(b)** 6 mm, and **(c)** 10 mm from the substrate; and the SM-14Cr-1B layer of the SF3 pipe at **(d)** 1.5 mm, **(e)** 4 mm, and **(f)** 7 mm from the substrate.

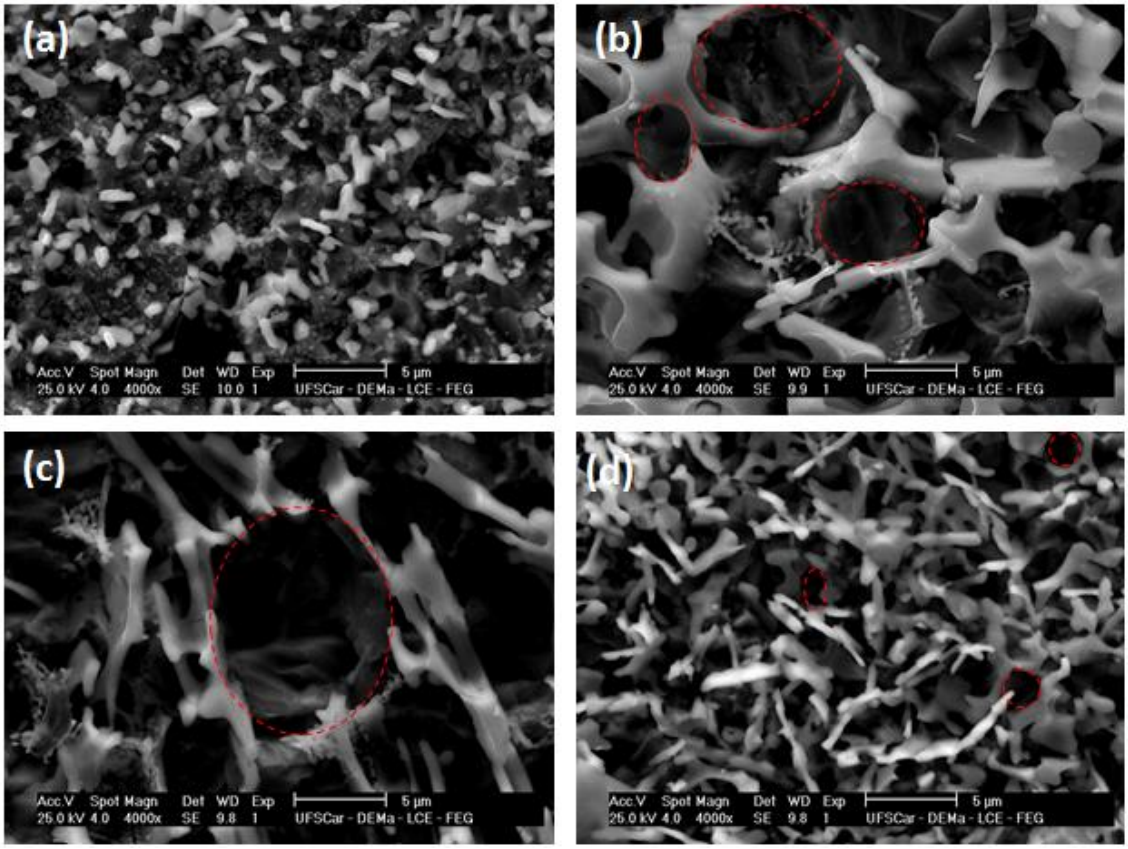

Figure 5.38 - Boride morphologies of the SM-14Cr-1B layer of the SF3 pipe at **(a)** 1 mm, **(b)** 2 mm, **(c)** 4 mm, and **(d)** 7.5 mm. (Deep etching)

It can be seen that, although the borides morphologies are the same, the average grain size at each position along the thickness of the SF3 pipe is quite different. Similar variation of prior austenite grain size in the SMSS layer can be observed in Figure 5.39. Figure 5.40 shows the grain size profiles through the thickness of both SF2 and SF3 pipes. It can be seen that average grain size of the SM-14Cr-1B vary from 4 µm to 12 µm for the SF2 pipe, and from 4 µm to 10 µm for the SF3 pipe. On the other hand, the SMSS layer of the SF3 pipe have grain sizes ranging from 50 µm to 225 µm, considerably coarser than the boron-modified layer. Such coarser grain size results from the fact that the SMSS does not have the presence of borides at the grain boundaries, which would hinder the grain growth. Therefore, since after solidification the cooling rate of the deposit is quite slow, the austenite is subjected to considerable grain growth before to transform into martensite.

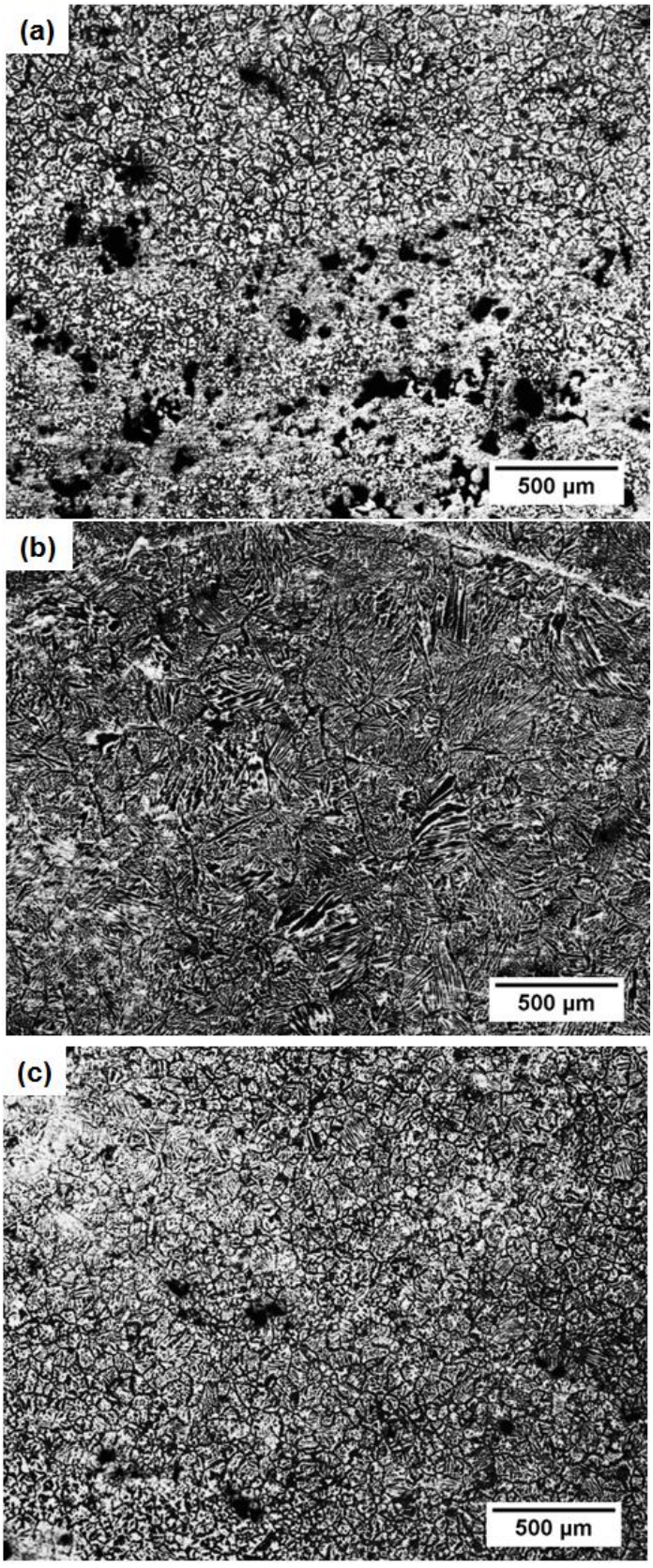

Figure 5.39 - OM images showing the prior austenite grain size of the SMSS layer of the SF3 pipe at **(a)** 16 mm, **(b)** 22 mm, and **(c)** 30 mm from the substrate.

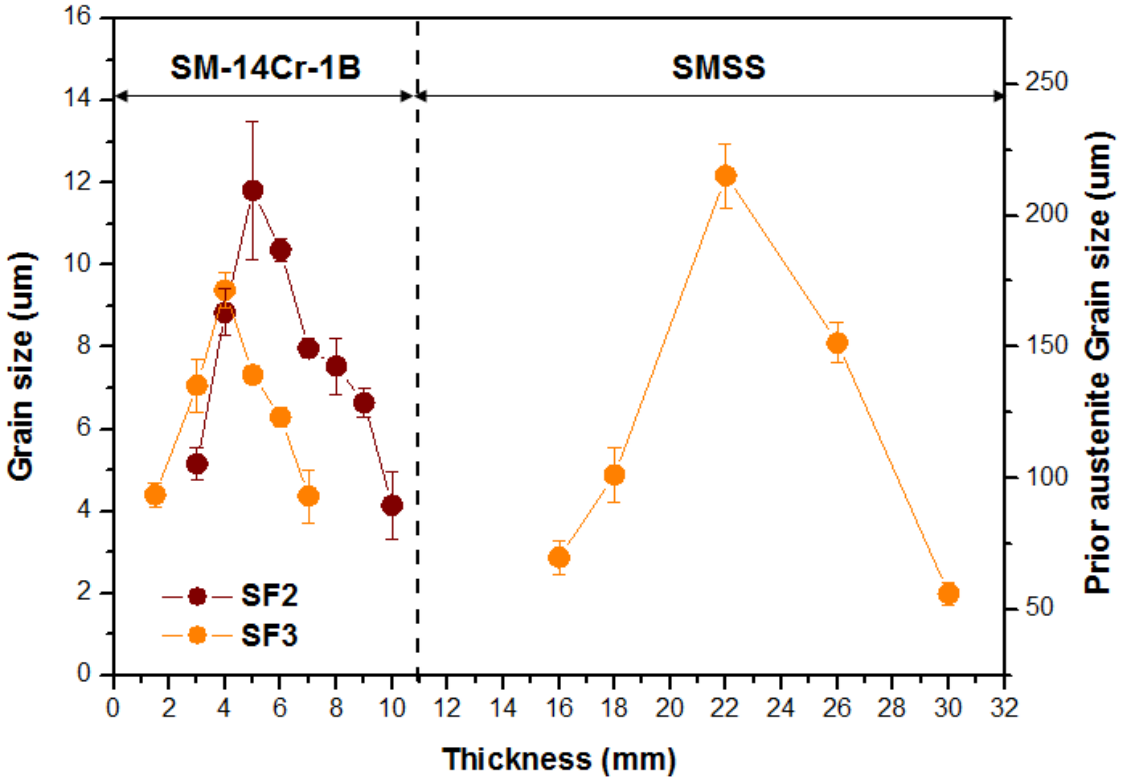

Figure 5.40 - Grain size profiles of the SF2 and SF3 pipes.

The most interesting is that the grain size profiles present an inverted-V shape, similar to the surface temperature profiles shown in Figure 5.34 (b). These results suggest that the grain size evolution throughout the thickness of spray-formed pipes is directly related to their surface temperatures. Based on the previous results and the solidification model proposed in section 5.21, a model to describe the grain size evolution in spray-formed pipes (and spray forming in general) will be addressed.

Let us consider the spray forming of a single layer pipe as schematized in Figure 5.41 (a). As previously demonstrated, the surface temperature profile under the spray cone presents an inverted-V shape with the maximum temperature placed under its centerline. This means that the first and last deposited layers (whose material is delivered from the spray cone edges) are deposited in relatively colder spray conditions when compared to the intermediate layer deposited under the cone centerline. Such gradient of surface temperature

relative to the pipe thickness will generate a gradient of equilibrium temperature, also inverted V-shaped, as represented in Figure 5.41 (b).

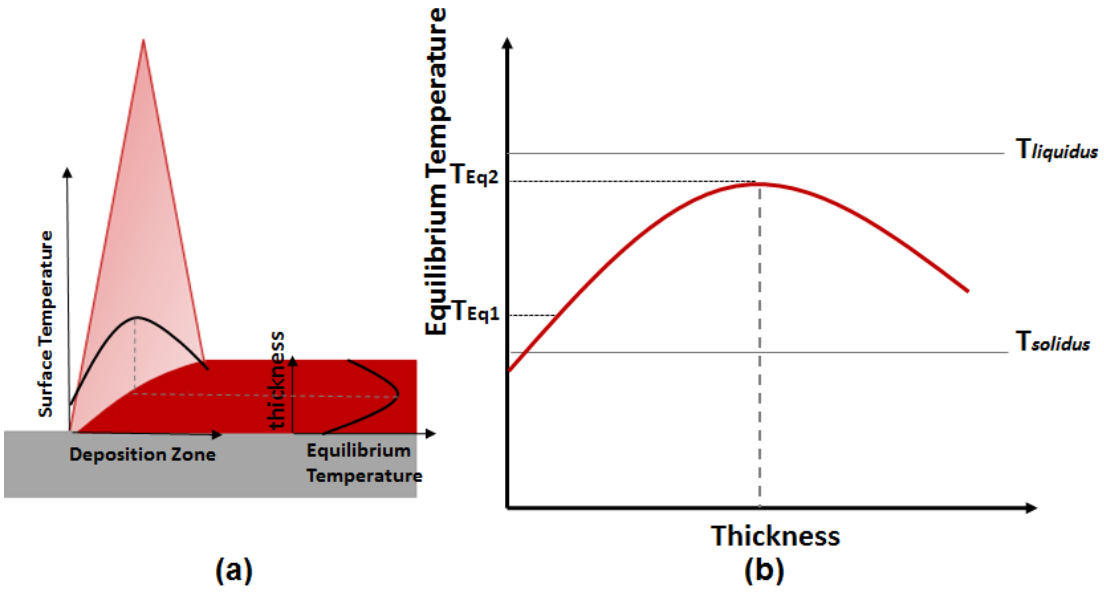

Figure 5.41 - Schematic representation of **(a)** the relationship between the surface temperature profile and **(b)** the equilibrium temperature profile of spray-formed pipes.

As demonstrated in the solidification model presented in section 5.2.1, the equilibrium temperature must be above the alloy's *solidus* temperature in order to attain the equiaxed grains typical of spray-formed alloys. Thus, the equilibrium temperature profile (relative to the pipe thickness) must be placed within the solidification temperature range of the alloy. The surface temperature measurements (Figure 5.34) support this assumption. Let us take as example the same boron-modified SMSS (SM-1B) used to describe the solidification model in section 5.2.1, which has the simplified pseudo-binary phase diagram presented in Figure 5.42.

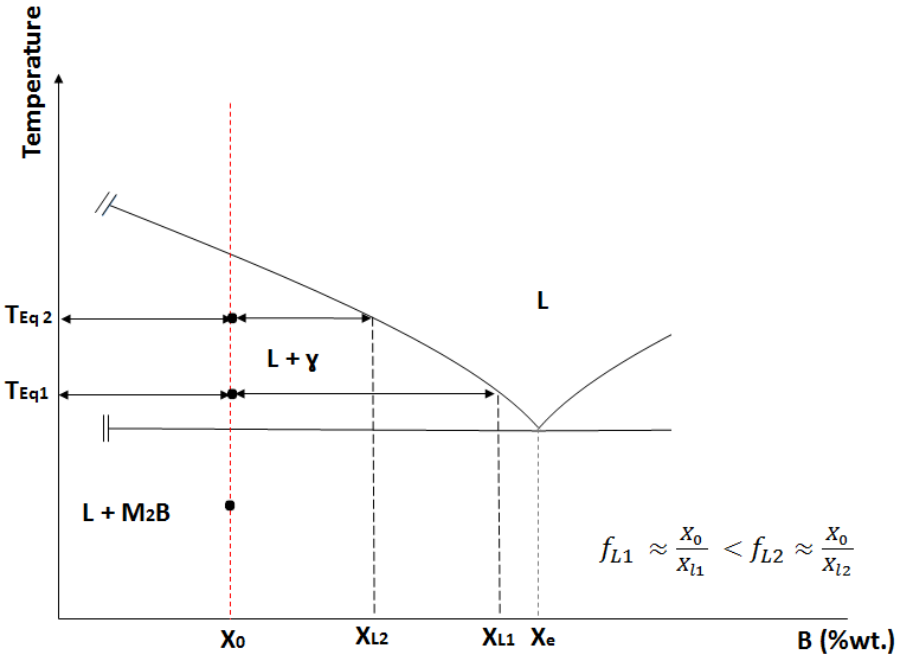

Figure 5.42 - Pseudo-binary phase diagram of the SM-1B showing the equilibrium liquid fraction at two different equilibrium temperatures.

In this case, it can be seen that for different equilibrium temperatures ($T_{Eq1} < T_{Eq2}$), the respective equilibrium liquid fractions are also different ($f_{L1} < f_{L2}$) – see Figure 5.42. This means that for high equilibrium temperatures the amount of particles remelted/redissolved within the deposition zone is also high. Therefore, once the equilibrium is established, the number of remaining “nuclei” which will grow equiaxed within the deposition zone is low. On the other hand, when the equilibrium temperature is low, the amount of remelting/redissolution of particles is lower when compared to the last case, leaving several particles to act as “nuclei” once the equilibrium is established. In both cases, the “nuclei” grow without any preferential direction consuming the liquid that become richer in boron. When high numbers of “nuclei” are able to grow, after small growth, the liquid reaches the eutectic composition, and the solidification is completed through the eutectic reaction. In this case, the as-solidified microstructure is composed of small equiaxed γ-austenite grains with fine eutectic constituent (γ + M_2B) at the grain boundaries. In the former case, where the equilibrium temperature is higher, the few “nuclei” present in the deposition zone must grow considerably more to consume the same amount of liquid until achieving the

eutectic composition. In this case, the as-spray formed microstructure is composed of coarser ɣ-austenite equiaxed grains with the eutectic constituent at the grain boundaries. Such sequence of events is schematically represented in Figure 5.43. Therefore, based on the proposed model for grain size evolution in spray forming, if the equilibrium temperature profile throughout the thickness of the spray-formed pipe has an inverted-V shape, its grain size profile should behave in the same way.

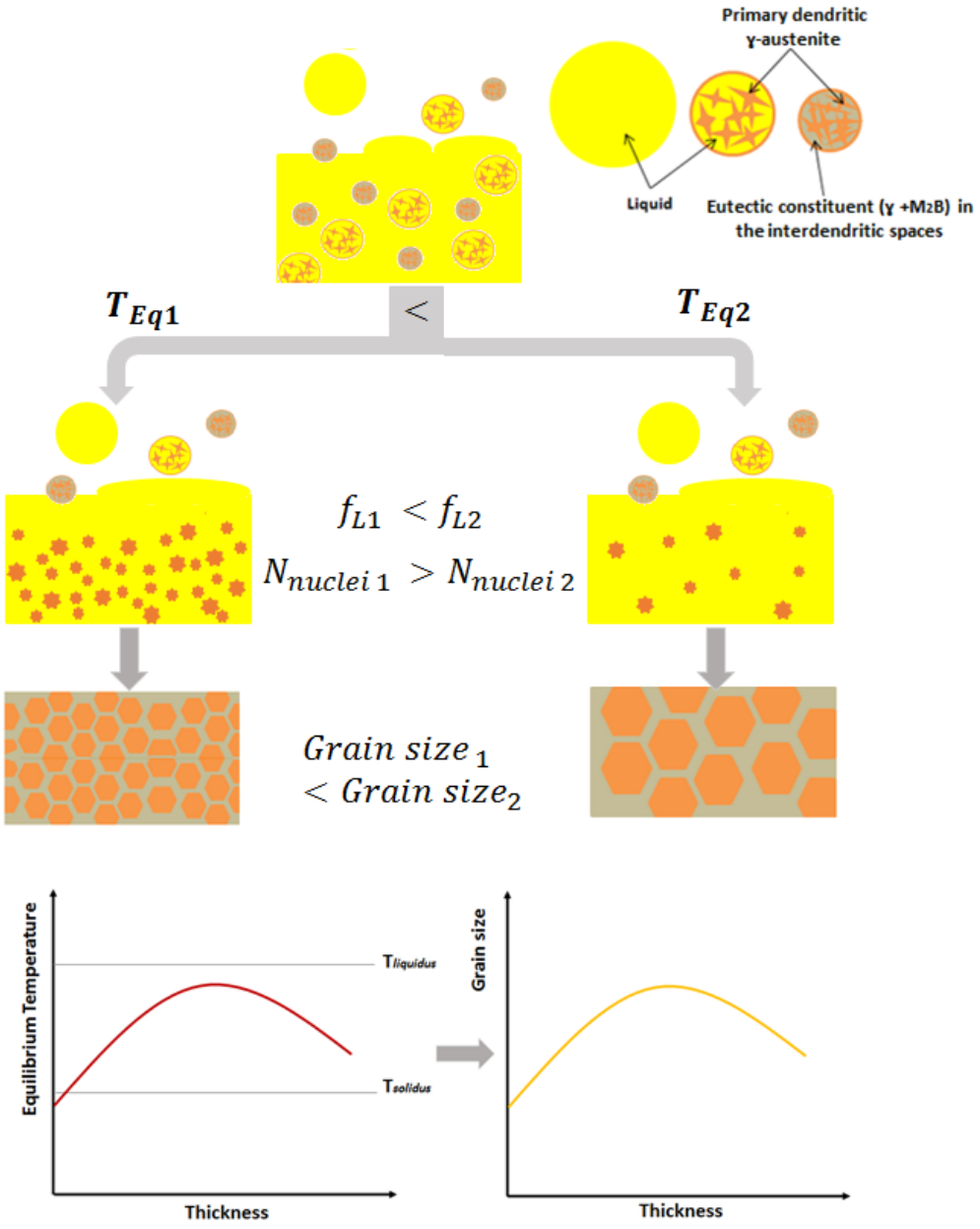

Figure 5.43 - Schematic representation of the proposed model for grain size evolution in spray forming.

This model demonstrates that different grain sizes can be obtained for the same spray-formed alloy if the equilibrium temperature of the deposition zone is placed at different position within its solidification range. This is well supported by the correlation between measured surfaces temperature profiles and the grain size profiles, both having the same inverted-V shape. Moreover, it can be seen that the slightly higher maximum temperature observed in the SF2 run (which should result in slightly higher maximum equilibrium temperature within the deposition zone) – Figure 5.34 (a) – also results in slightly higher maximum grain size in the SM-14Cr-1B layer – Figure 5.40 – when compared to the SF3 run.

5.2.3 Effect of temperature profile on the interface's porosity.

As demonstrate so far, the surface temperature profile during the deposition process has great influence on the porosity and microstructure of spray-formed pipes. Based on this, it is possible to assume that the high porosity levels next to the interface between the SM-14Cr-1B and SMSS layers (in SF3) reflects of the thermal history at this region. It was shown that the Gaussian-like mass flux and heat flux distribution of the spray cone results in and inverted V-shaped surface temperature of the deposit during deposition, which is quite stable during the whole process. Furthermore, it was shown that the surface temperature profile has a direct relationship with the equilibrium temperature profile within the deposition zone, which also has an inverted-V shape.

In the SF3 run, the experiment was set up in such a way that the first spray cone (SM-14Cr-1B) was tilted aiming at reducing the distance to the second spray cone (SMSS), but without overlapping between them. In this case, the melt flow rate, pouring temperature and GMR applied to the SM-14Cr-1B (0.10 kg/s, 1564 ºC, 3.86, respectively) led to considerably colder process conditions when compared to those applied to SMSS (0.47 kg/s, 1633 ºC, 0.79, respectively). Thus, it is expected the surface temperature profiles under both spray cones to be considerably different, with the maximum surface temperature under the SMSS spray cone being much higher than the one under the SM-14Cr-1B. Figure 5.44 (a) presents a schematic representation of the surface temperature profile

in this case, and its relationship with the equilibrium temperature along the pipe thickness. As previously demonstrated, the equilibrium temperature profile along the pipe thickness will behave similar than the surface temperature profile. It was demonstrate by the surface temperature measurements, and microstructural analyses, that the equilibrium temperature along the thickness of the SM-14Cr-1B layer must be within its solidification range. Figure 5.44 (b) represents in detail this situation. However, the surface temperature measurements (Figure 5.34 (b)) showed that the surface temperature of the SM-14Cr-1B layer was reduced down to 1060 ºC before to start increase due to the heat input supplied by the SMSS spray cone. This means that the first deposited layers of the SMSS were thermally balanced with the colder SM-14Cr-1B surface, which resulted in equilibrium temperatures under the SMSS *solidus* temperature. It is worth stressing that the SMSS *solidus* temperature (1414 ºC) is considerably higher than the *liquidus* temperature of the SM-14Cr-1B (1265 ºC). In this case, while the equilibrium temperature is under the SMSS *solidus* temperature, the region next to the interface is likely to have high fraction of cold porosity. However, due to the inverted V-shaped profile, the equilibrium temperature of the SMSS layer increases from the interface and, at certain point, it reaches the alloy's *solidus* temperature. From this point, the porosity level is considerably reduced and maintained practically constant (see Figure 5.34). Once the equilibrium temperature profile is placed within the SMSS solidification range, the porosity is no longer a problem, and its greater influence is on the grain size.

Cui et al. [52] have shown that it is possible to reduce the interfacial porosity of co-spray formed tool steel plates by tilting and overlapping both spray cones. The authors have also shown that by overlapping the spray cones an intermediate layer with gradient chemical composition is generated between both spray-formed alloys. Figure 5.45 shows the schematic representation of the effect of overlapping the SM-14Cr-1B and SMSS layers on the surface and equilibrium temperatures. One can see that the equilibrium temperature profile throughout the pipe thickness is similar than in the case without overlapping. However, in this case, above the SM-14Cr-1B layer, the equilibrium temperature increases while the gradient zone is deposited. This means that the interfacial porosity will no

longer be determined by the *solidus* temperature of the SMSS, but by the solidification range of the gradient zone.

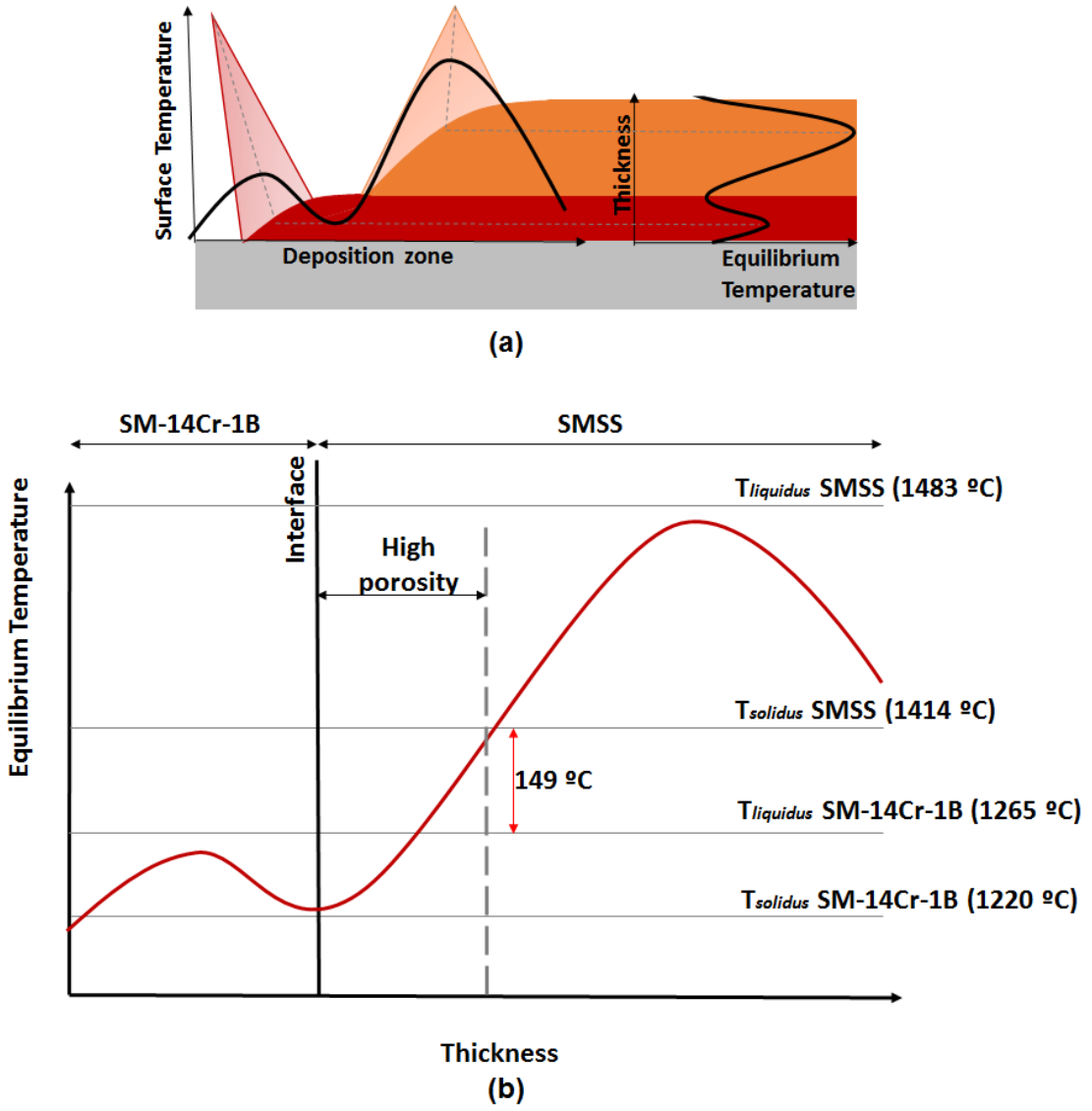

Figure 5.44 - Schematic representation of **(a)** the surface temperature and **(b)** equilibrium temperature profiles without overlapping between the SM-14Cr-1B and SMSS spray cones.

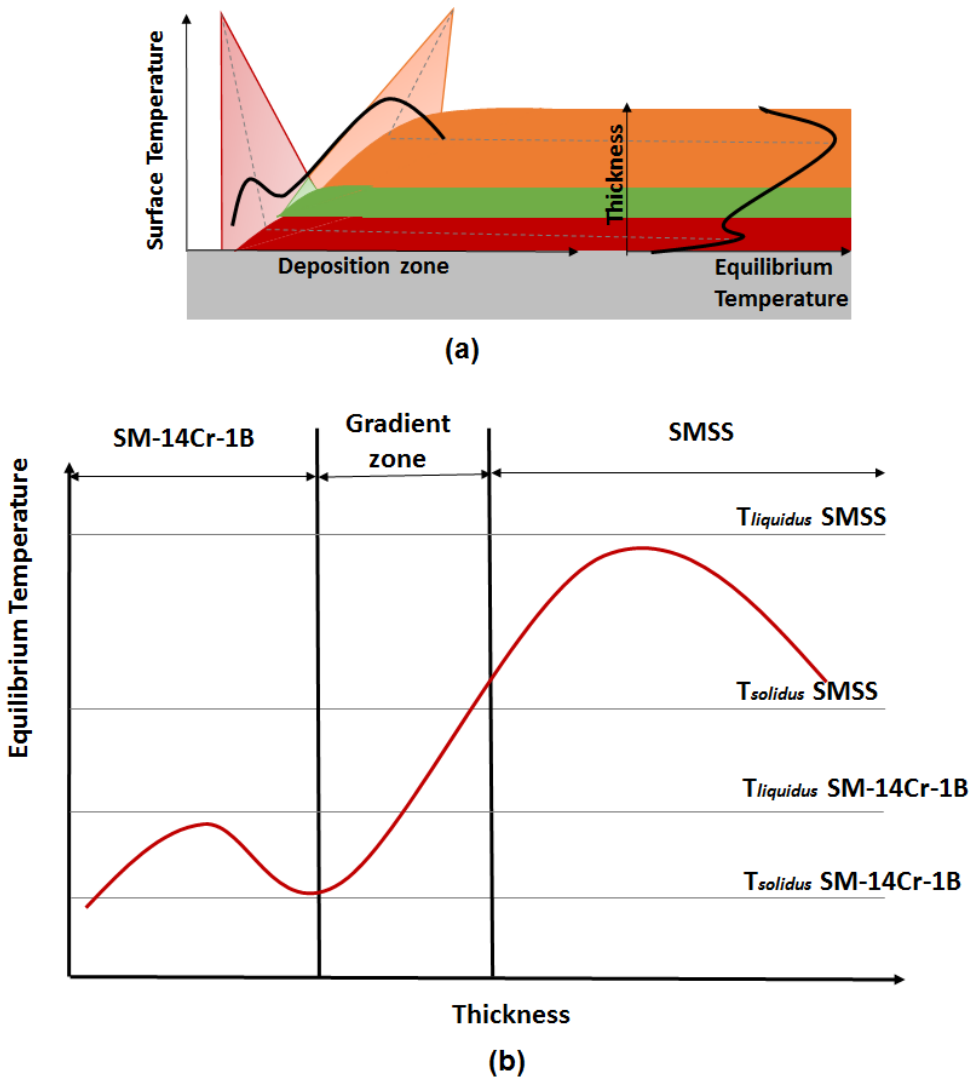

Figure 5.45 - Schematic representation of **(a)** the surface temperature and **(b)** equilibrium temperature profiles with overlapping between the SM-14Cr-1B and SMSS spray cones.

Since both layers are based on the same alloy, it is not difficult to imagine how it will be the chemical composition gradient at the intermediate zone. Figure 5.46 shows the chemical gradient for an arbitrary overlapping range, assuming a linear variation. Regardless the amount of overlapping, which should change the slope of the chemical gradient, it is safe to assume that the Cr and B content will decrease from about 14 %wt. and 1% wt. (at the SM-14Cr-1B interface) to 12 %wt. and 0.0 %wt (at the SMSS interface), respectively, while the Ni and Mo content (which are practically the same in both alloys) will be kept constant.

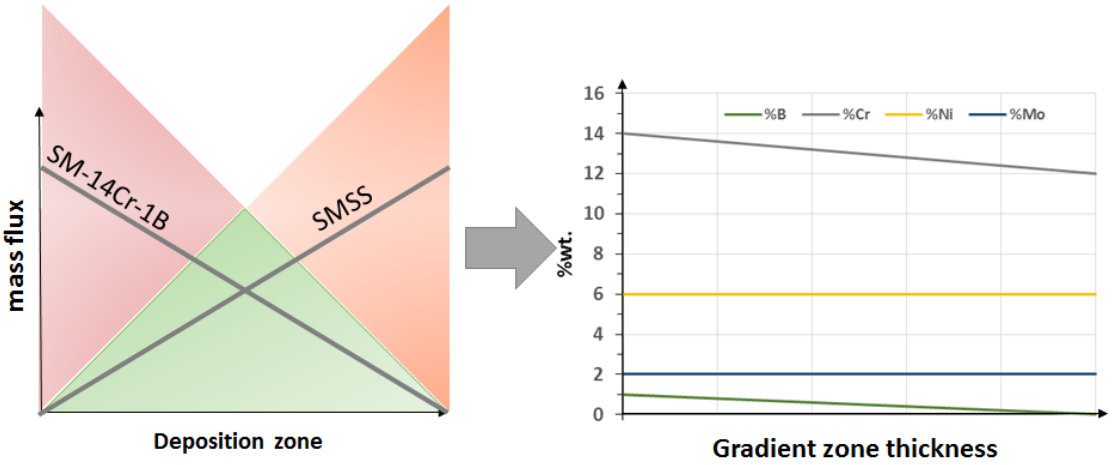

Figure 5.46 - Schematic representation of the gradient chemical composition of the gradient zone for an arbitrary overlapping between the SM-14Cr-1B and SMSS spray cones.

Assuming that the variation of boron content from 1.0 %wt. to 0.0 %wt. will have a greater effect on the alloy's solidification range than the small Cr variation is quite reasonable. Therefore, it can be assumed that the gradient zone behaves as a boron-modified SMSS with the average chemical composition containing 0.03%C, 13 %wt. Cr, 5.8 %wt. Ni, and 2 %wt. Mo., with boron content varying between 1 %wt. to 0.0 %wt. Figure 5.47 (a) shows the calculated pseudo-binary phase diagram of this composition as function of boron content. One can see that it is an eutectic phase diagram (as already mentioned in section 5.2.1) with practically no solubility boron solubility in the solid steel phases. This gives to the gradient zone an important characteristic: The decrease of boron content increases the alloy's *liquidus* temperature while keeping the same *solidus* temperature (it is worth to point out that the calculated *solidus* temperature is overestimated when compared to the measured one, but does not bring any drawback to this analysis). Observing the low boron content corner of the diagram – Figure 5. 47 (b) – It can be seem that the *solidus* temperature increases only when the boron content is as low as 0.003 %wt.

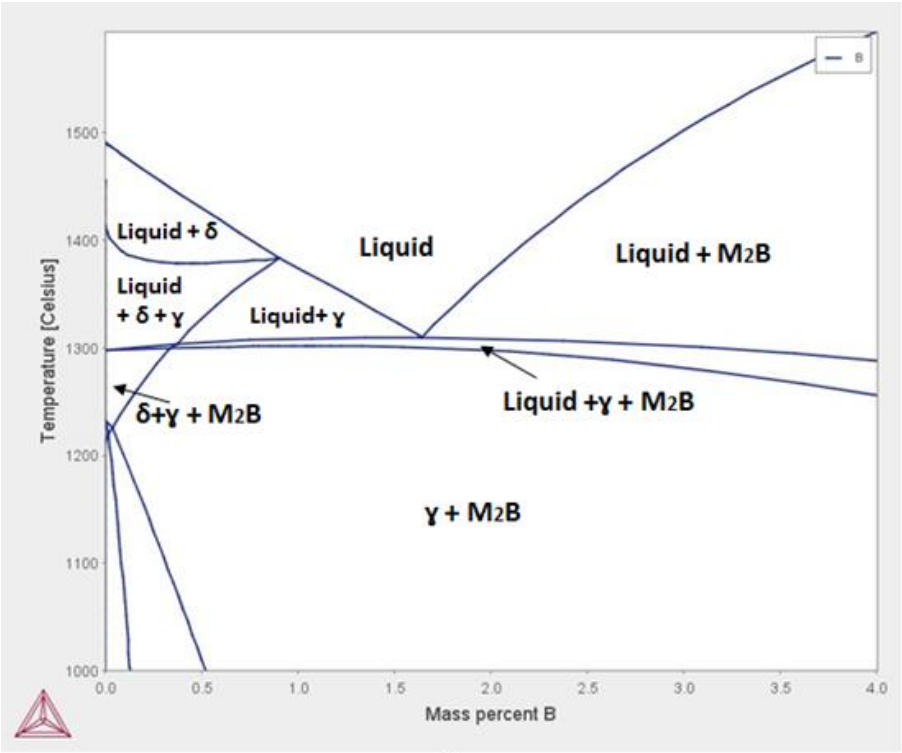

(a)

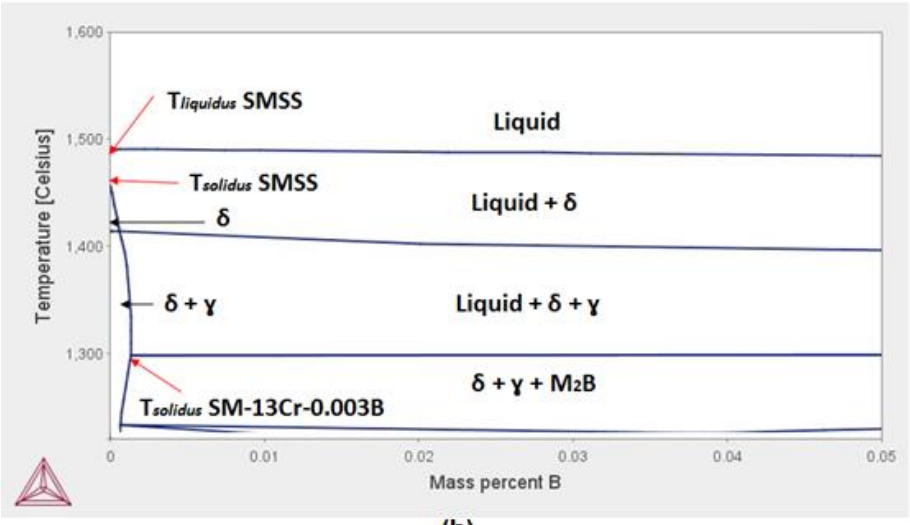

(b)

Figure 5.47 - **(a)** Pseudo-binary phase diagram of the 0.03C13Cr-5.8Ni-2Mo-XB (%wt.), and **(b)** zoom of the low boron region.

This is a quite interesting result, since it shows that:

(i) Overlapping the SM-14Cr-1B and SMSS spray cones will promote the increase of the equilibrium temperature throughout the gradient zone.

(ii) The mixture of both alloys will generate a gradient zone with decreasing boron content throughout it.

(iii) The decreasing of boron content will promote the increase of the *liquidus* temperature up to the SMSS *liquidus* temperature, while maintaining the *solidus* temperature practically constant throughout the gradient zone.

(iv) This allows the equilibrium temperature to lie within the solidification range during the whole deposition period of the gradient zone. This will guarantee a low porosity level of the gradient zone.

(v) Finally, if the overlapping is enough to increase the equilibrium temperature of the gradient zone in such a way that it reaches the SMSS *solidus* temperature before the deposition of the SMSS layer, the equilibrium temperature of the last one will also lie within its *solidification* range resulting in low porosity level as well.

The ideal equilibrium temperature profile of the gradient zone in order to obtain a low porosity interface is sketched in Figure 5.48.

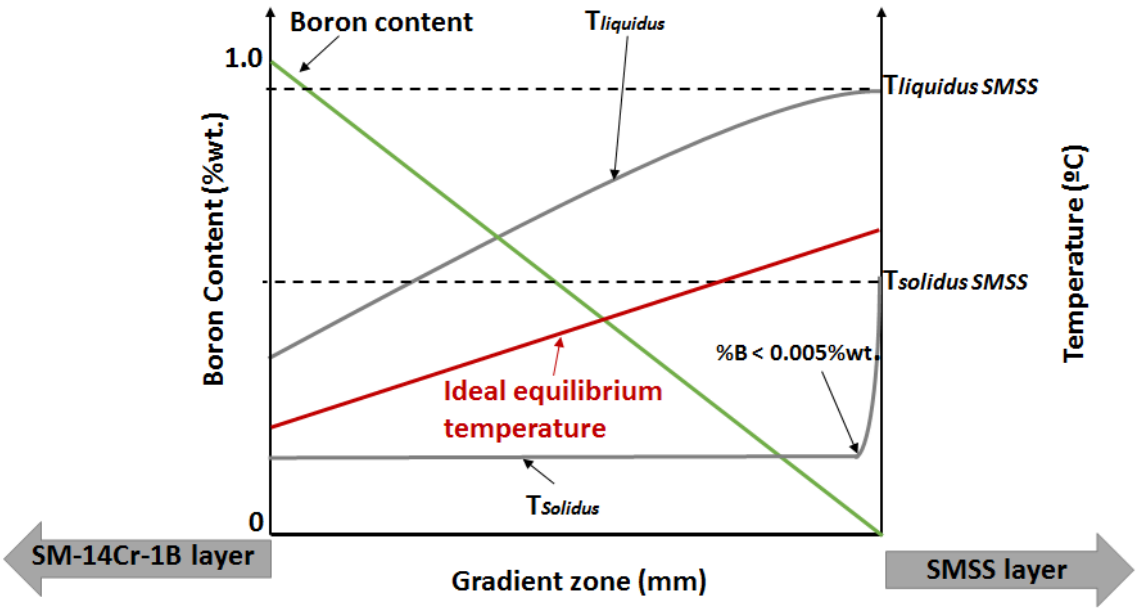

Figure 5.48 - Effect of the decreasing boron content within the gradient zone on the alloy's *solidus* and *liquidus* temperature, and the ideal equilibrium temperature profile to produce a low porosity level interface.

To obtain such equilibrium temperature profile within the gradient zone should not be difficult in practical. In the SF3 run, where no spray overlapping was applied, the high porosity region was about 10 mm-thick, which means that above this distance from the SM-14Cr-1B layer, the equilibrium temperature was already above the SMSS *solidus* temperature. Considering that overlapping both spray cones will make the equilibrium temperature to rise faster, it must be possible to attain the same equilibrium temperature by producing a gradient zone thinner than 10 mm, which, based on the arguments above, should lead to a low porosity interface. Unfortunately, it was not possible to carry out the last spray-forming run with overlapped sprays.

5.3 Mechanical Properties

5.3.1 Hardness and Heat treatments

This section aims at studying the effect of heat treatments on the mechanical properties of the SF3 bimetallic pipe. However, it is worth stressing that the heat treatments aim to improve the mechanical properties of the SMSS layer, which is the structural component of the bimetallic pipe. Nevertheless, as in practice both layers must be subjected to the same heat treatment, the effect of the heat treatments on the SM-14Cr-1B layer will also be analyzed.

Figure 5.49 shows the dilatometry curve of the spray-formed SMSS. It can be seen that the AC_1 and AC_3 transition temperatures are 672 ºC and 712 ºC, respectively. This means that the austenitization temperature for quenching heat treatment must be above 712 ºC. Moreover, it means that the tempering temperature must not be above 672 ºC in order to avoid the presence of reverse austenite. Figure 5.50 presents the diagram showing the amount of phases in equilibrium as function of temperature of the SMSS. One can see that in the temperature range between 720 ºC and 800 ºC, the χ-phase precipitates. The χ-phase is a Mo-rich phase, which is reported in literature as detrimental to both toughness and corrosion resistance of stainless steel [74]. This result shows that the austenitization temperature for quenching heat treatment of the SMSS must also be higher than 800 ºC.

Based on these results, a sample of the SF3 bimetallic pipe was subjected to quenching heat treatment as follow: 30 min at 850 ºC followed by oil quenching. Figure 5.51 and Figure 5.52 show, respectively, the microstructure and the XRD patterns of the SMSS layer in both as-spray formed and quenched condition. Practically no differences can be seen in both microstructures. Furthermore, the XRD patterns show the peak relative to the (111) diffraction plane of the ɣ-austenite in both cases. This shows that both samples contain some amount of retained austenite. Figure 5.53 shows the hardness of both as-spray formed and quenched samples. It can be seen that the quenching heat treatment did not increase the alloy's hardness. In both conditions, the hardness values are around 34 HRC, which is considerably high. Rodrigues, C. et al. [65] have shown that for

the medium-alloyed SMSS grade with some addition of Ti the maximum desired hardness to obtain the requested mechanical properties is 28 HRC. These results show, at first glance, that the quenching heat treatment has no beneficial effect on the spray-formed SMSS microstructure.

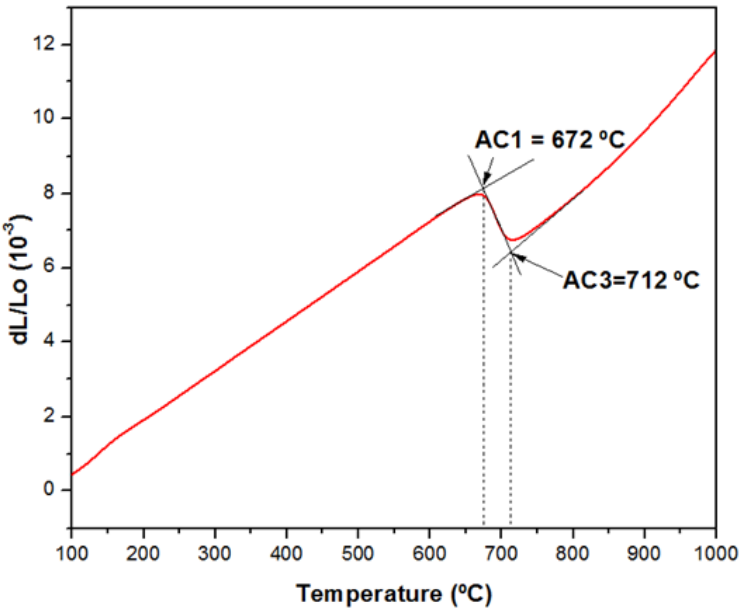

Figure 5.49 - Dilatometry curve of the spray-formed SMSS layer. Heating rate: 5 ºC/min.

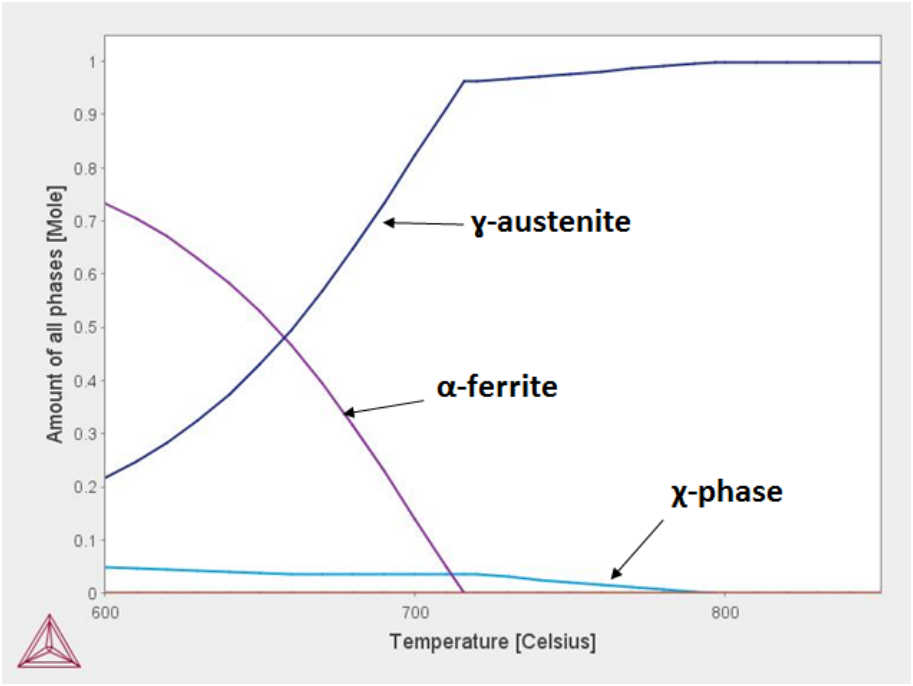

Figure 5.50 - Amount of equilibrium phases as function of temperature showing the presence of χ-phase in temperature range of 720-800 ºC.

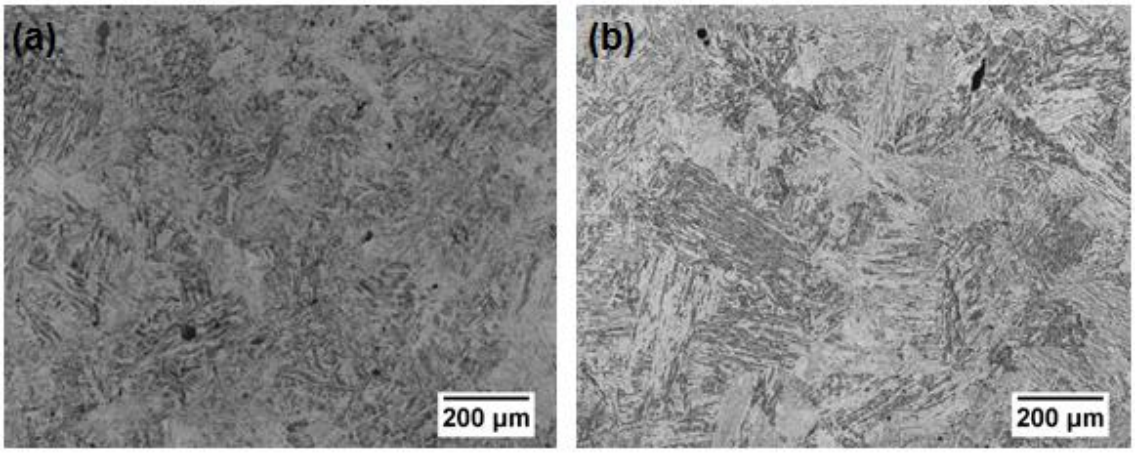

Figure 5.51 - OM images showing the microstructure of the **(a)** as-spray formed and **(b)** quenched SMSS layer.

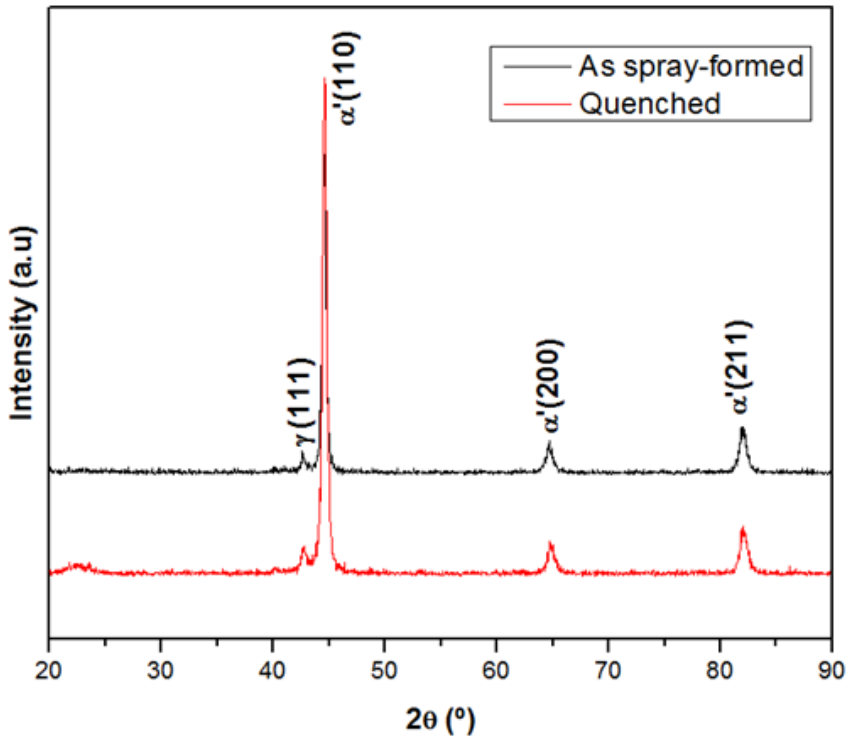

Figure 5.52 - X-ray diffraction patterns of the as-spray formed and quenched SMSS layer.

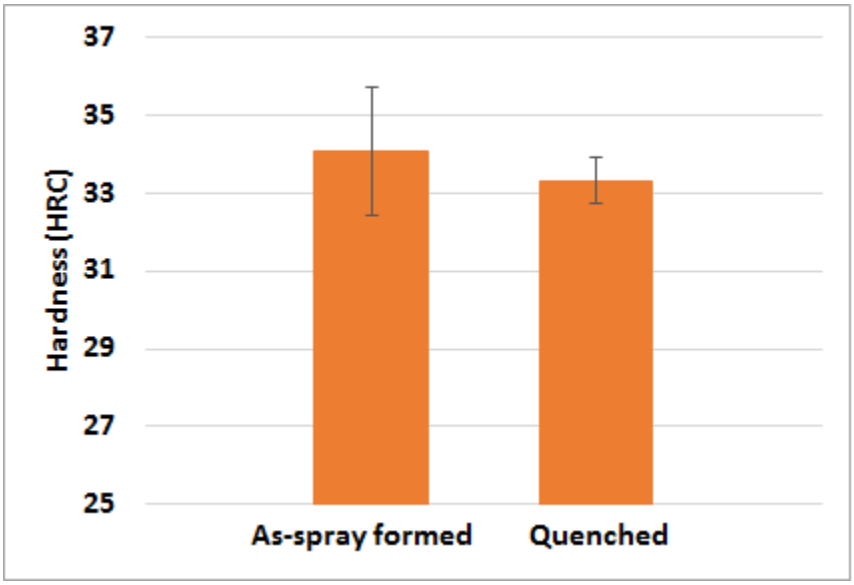

Figure 5.53 - Rockwell C Hardness of the as-spray formed and quenched SMSS layer.

Based on the previous results, it was established that the tempering heat treatments could be carried out directly from the as-spray formed pipe. Three tempering conditions were applied: (i) 630 ºC for 2 h, (ii) 650 ºC for 2 h, and (iii) 650 ºC for 6h. The tempering heat treatment aimed to achieve the minimum possible hardness. Figure 5.54 (a) shows the tempering curve for the SMSS layer. One can see that the hardness decreases from 34 HRC to 31 HRC when tempered at 630 ºC for 2 h, and to 29 HRC when tempered at 650 ºC for 2 h. Tempering at 650 ºC for 6 h it was not effective to reduce the hardness to 28 HRC (the maximum desired hardness). It is worth stressing that increasing the tempering temperature is not possible since the AC_1 temperature is about 670 ºC. This means that above such temperature, some reverse austenite will be present and, when cooled down, it will transform into non-tempered martensite, which would increase the alloy's hardness. The microstructures of the alloys tempered directly from the as-spray formed condition can be seen in Figure 5.55 (a), (c) and (e). Further studies must be carried out in order to understand why the hardness of the spray-formed SMSS is higher when compared to the conventional one (the commercial SMSS used as feedstock material has 25 HRC of hardness). However, such deeper study is out of the scope of this thesis.

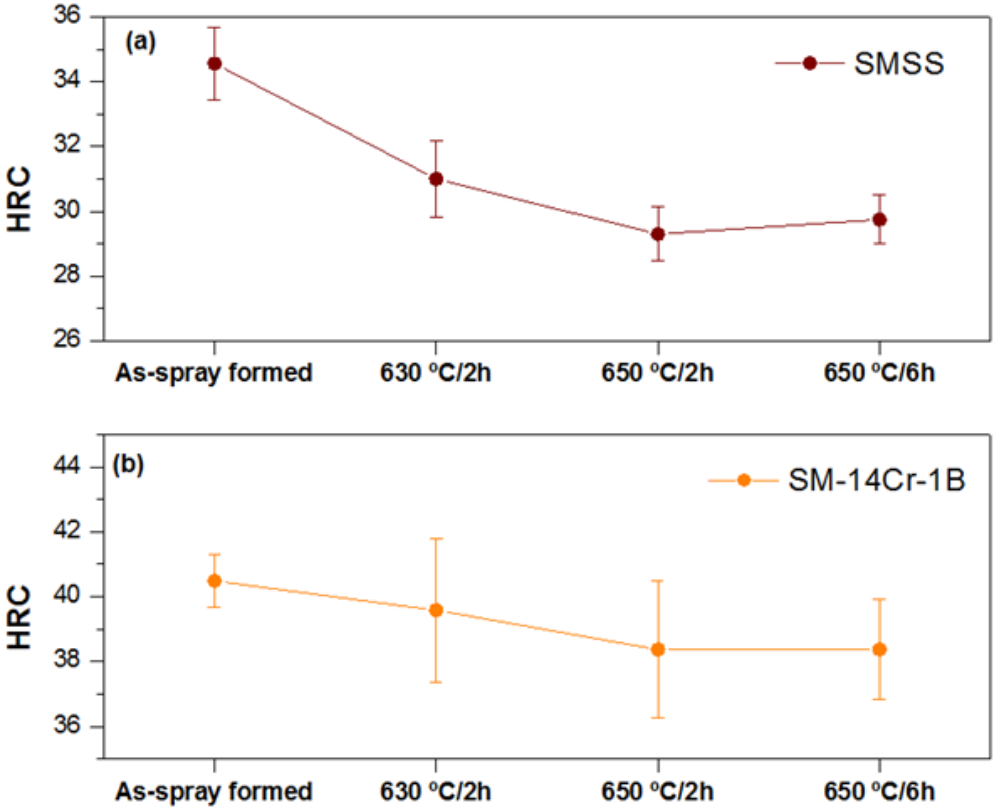

Figure 5.54 - Tempering curves directly from the as-spray formed conditions of **(a)** SMSS, and **(b)** SM-14Cr-1B layer.

Figure 5.54 (b) shows the tempering curve of the SM-14Cr-1B layer. One can see that it has the same behavior than the SMSS layer. The hardness reduces from 40.5 HRC for the as-spray formed condition to 39.6 HRC when tempered at 630 ºC for 2h. Tempering at 650 ºC for 2 h and 6 h results in the same hardness of 38.4 HRC. The microstructure of the SM-14Cr-1B tempered at different conditions is shown in Figures 5.55 (b), (d), and (f). The martensitic matrixes present typical characteristics of tempered martensite. It can be seen that the morphology of the eutectic boride network is not changed. This is an expected result because of the high thermal stability of the M_2B-type borides.

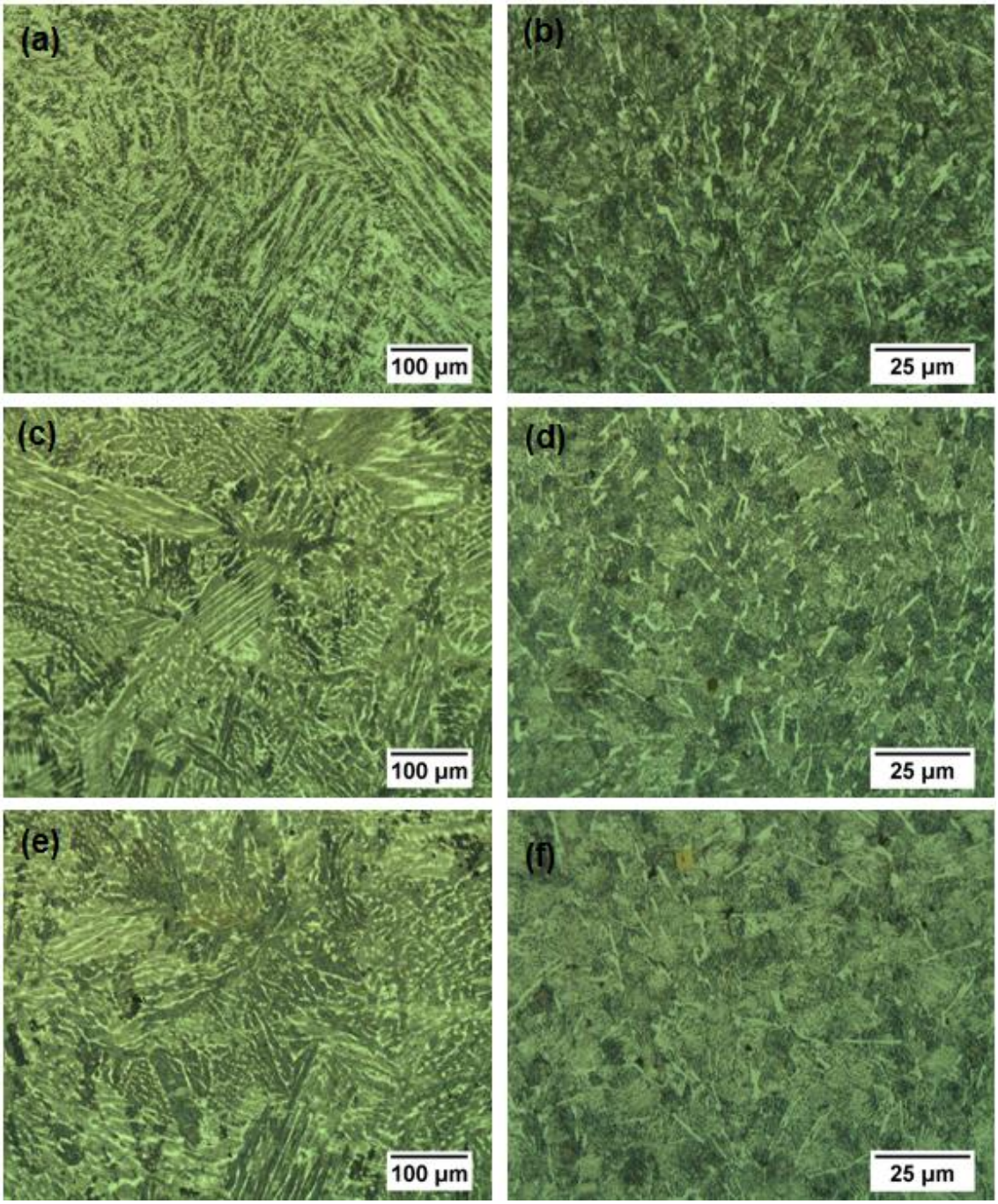

Figure 5.55 - OM images showing the microstructure of the SMSS layer tempered at **(a)** 630 ºC for 2 h, **(c)** 650 ºC for 2h, and **(e)** 650 ºC for 6h; and SM-14Cr-1B layer tempered at **(b)** 630 ºC for 2 h, **(d)** 650 ºC for 2h, and **(f)** 650 ºC for 6h.

5.3.2 Mechanical properties of the SMSS layer

In the last section it was demonstrated that the minimum hardness values are obtained when tempering the SF3 bimetallic pipe at 650 ºC for 2 h. Based on this, the mechanical properties of the SMSS layer was evaluated in both as-spray formed and after tempering at 650 ºC for 2h. Figure 5.56 (a) and Table 5.5 show the results of the tensile test of the as-spray formed SMSS specimens. One can see that the four tested specimens presented high yield stress ranging from 914 MPa to 1000 MPa, and high ultimate tensile strength ranging from 1014 MPa to 1073 MPa. However, two different behaviors regarding the elongation and area reduction were observed. The specimens 3 and 4 presented elongation values of 15.3% and 11.7% and area reduction of 62.4% and 52.7%, respectively. Both specimens presented cup-and-cone fracture type, as can be seen in Figure 5.57 (a) and (b). Observing the fracture surface of the specimen 4, it can be seen a dimpled fracture surface typical of ductile fracture. On the other hand, the specimens 1 and 2 presented extremely low elongation (5.7% and 4.3%) and area reduction values (17.1% and 9.5%), respectively. These specimens fractured at 45 degrees relative to the axial load. Figure 5.58 (a) and (b) show the photography and SEM image of the fracture surface of the specimen 1. Figure 5.58 (c) shows the presence of a flaw (within the region defined by the red square 1 in Figure 5.58 (b)), which is a pore resulted from the spray-forming process. Such pore resulted from solidification shrinkage. As described in section 5.2.1, during the solidification the “nuclei” within the deposition zone grow until touching each other, generating the equiaxed grains. However, when the last remaining liquid within some region of the deposition zone solidifies, the contraction due to the liquid-solid transition leads to an unfulfilled space, resulting in a pore. The presence of pores, which are stress concentrators, reduces both the elongation and area reduction. Figure 5.58 (d) shows that the upper part of the fracture, which is pore free, presents dimpled fracture surface.

Figure 5.56 (b) and Table 5.5 presents the tensile test results of the SMSS layer after tempering at 650 ºC for 2 h. One can see that the heat treatment was effective to reduce the average yield stress and ultimate tensile strength.

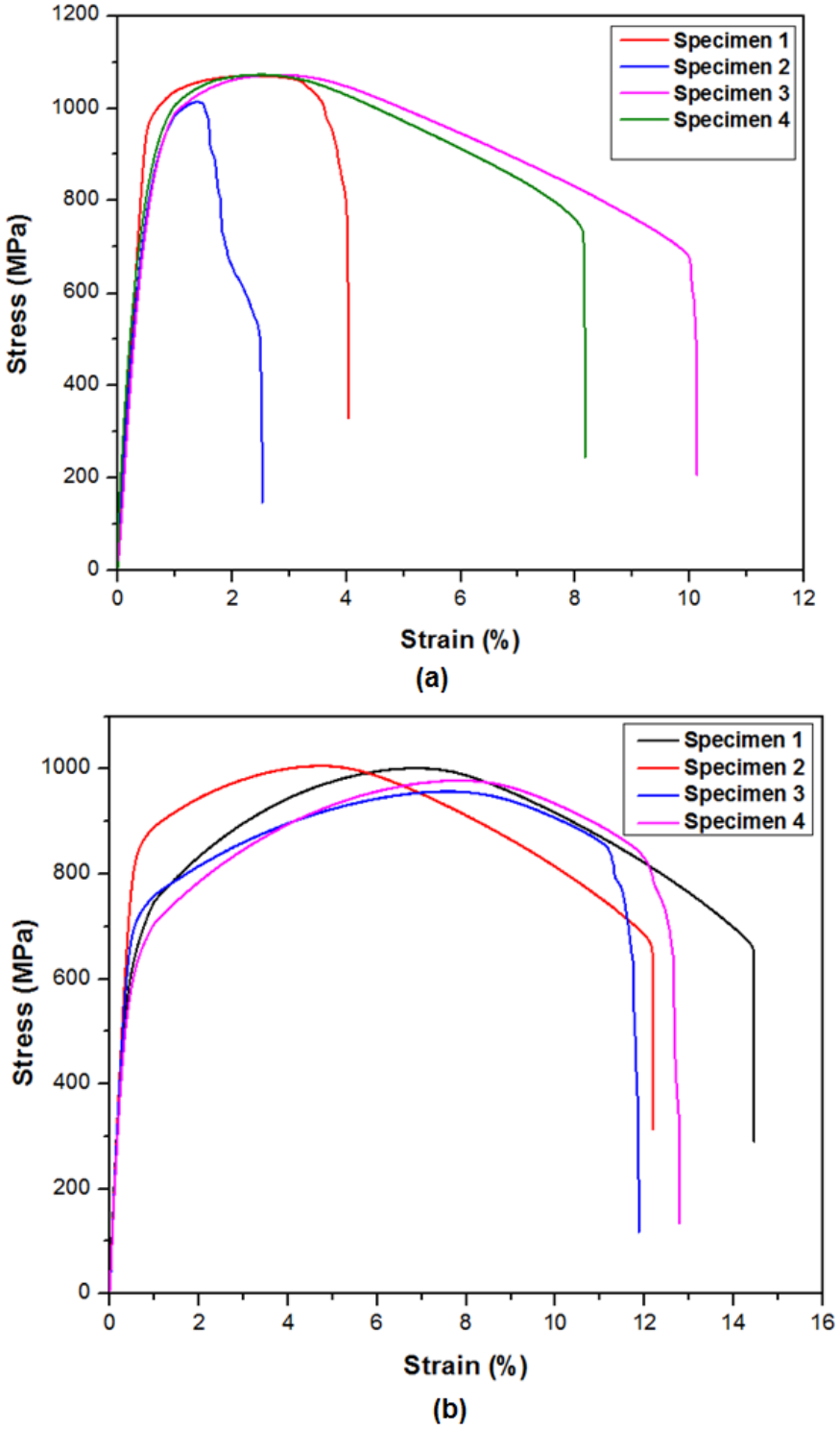

Figure 5.56 - Tensile test results of the SMSS layer **(a)** as-spray formed and **(b)** tempered at 650 ºC for 2h.

Table 5.5 - Tensile properties of the of the SMSS layer as-spray formed and tempered at 650 ºC for 2h.

As-spray Formed					
	YS (MPa)	**UTS (MPa)**	**Elongation 4D (%)**	**Area Reduction (%)**	**Fracture type**
Specimen 1	1000	1070	5.7	17.14	45 degrees
Specimen 2	914	1014	4.3	9.49	45 degrees
Specimen 3	925	1073	15.3	62.38	Cup-and-cone
Specimen 4	923	1073	11.7	52.73	Cup-and-cone
Tempered at 650 ºC for 2 h					
	YS (MPa)	**UTS (MPa)**	**Elongation 4D (%)**	**Area Reduction (%)**	**Fracture type**
Specimen 1	654	1002	17.2	61.60	Cup-and-cone
Specimen 2	853	1006	17.8	60.99	Cup-and-cone
Specimen 3	715	957	15.7	30.97	45 degrees
Specimen 4	635	978	15.5	37.04	45 degrees

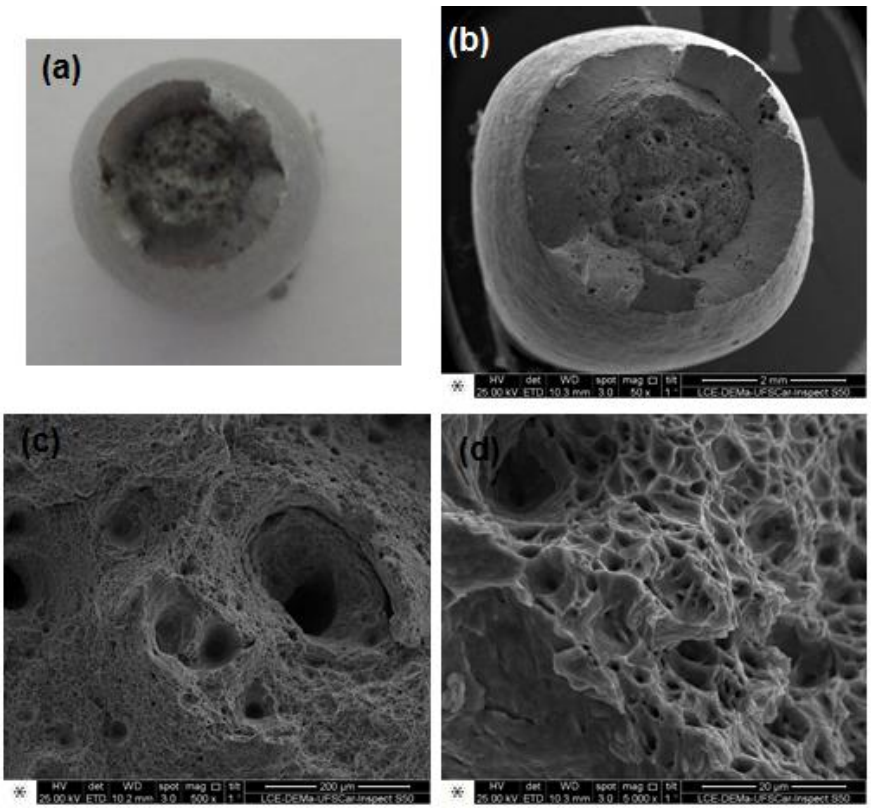

Figure 5.57 - **(a)** Photography and **(b)** SEM image of the cup-and-cone fracture (specimen 4) of the as-spray formed SMSS. **(c)** and **(d)** dimpled fracture surface.

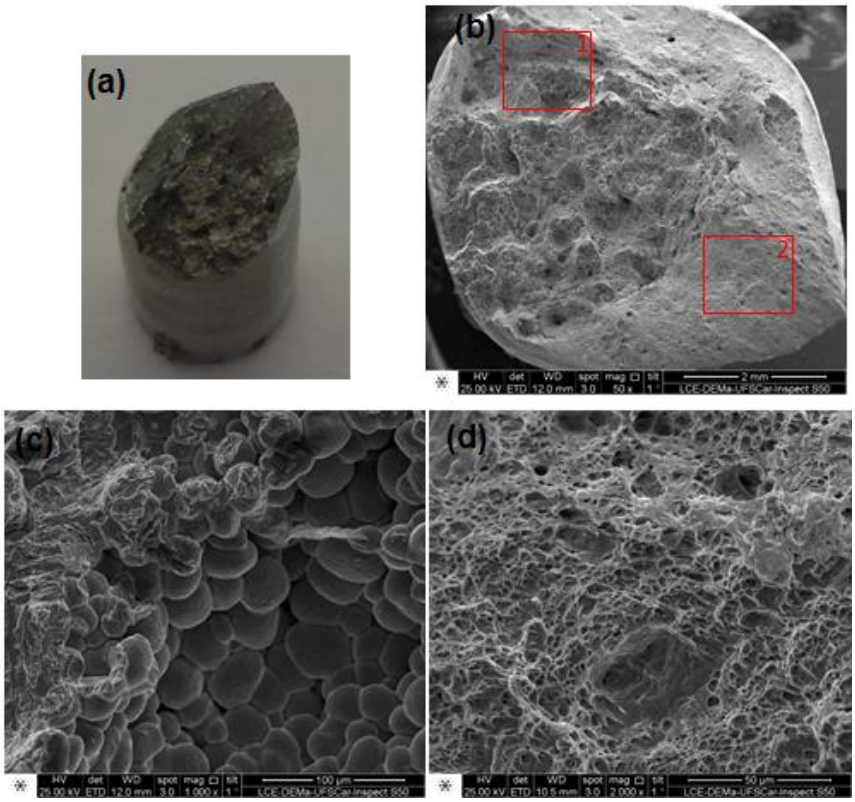

Figure 5.58 - **(a)** Photography and **(b)** SEM image of the 45 degrees fracture (specimen 1) of the as-spray formed SMSS. **(c)** Shrinkage solidification pore and **(d)** dimpled fracture surface.

The specimens 1, 3 and 4 presented considerable reduction of yield stress (654 MPa, 715 MPa and 635 MPa, respectively) and of ultimate tensile strength (1002 MPa, 957 MPa and 958 MPa, respectively) when compared to those values presented by the as-spray formed SMSS. Only the specimen 2 presented higher values of yield stress and ultimate tensile strength, 853 MPa and 1006 MPa, respectively. Similar to the previous case, two of the four tested specimens presented cone-and-cup fracture and the other ones presented 45 degrees fracture type. It is worth pointing out that the specimens that presented 45 degrees fracture type presented only slightly lower elongation values (15.5% and 15.7%) when compared to those with cone-and-cup fracture type (17.2% and 17.8%). However, the area reductions of the 45 degrees fractured specimens (30.9% and 37.0%) were considerably lower than the cone-and-cup fractured ones (61.6% and 61.0%). Figure 5.59 shows the fracture surface of the cone-and-cup fractured specimen (specimen 1). The typical dimpled fracture surface

of ductile alloys can be observed. Figure 5.60 shows the fracture of the 45 degrees fracture specimen (specimen 4). In this case, the same flaw characteristic of shrinkage solidification pore can be seen in Figure 5.60 (c) and (d). These results show that the spray-formed SMSS layer of the SF3 bimetallic pipe presents high tensile properties. However, the presence of porosity derived from the spray forming process impairs the alloys ductility. Reducing the hardness through tempering heat treatment leads to reduction of the tensile properties (YS and UTS) accompanied by a substantial increase of the alloy's elongation. Nevertheless, the area reduction is still impaired by the presence of porosity.

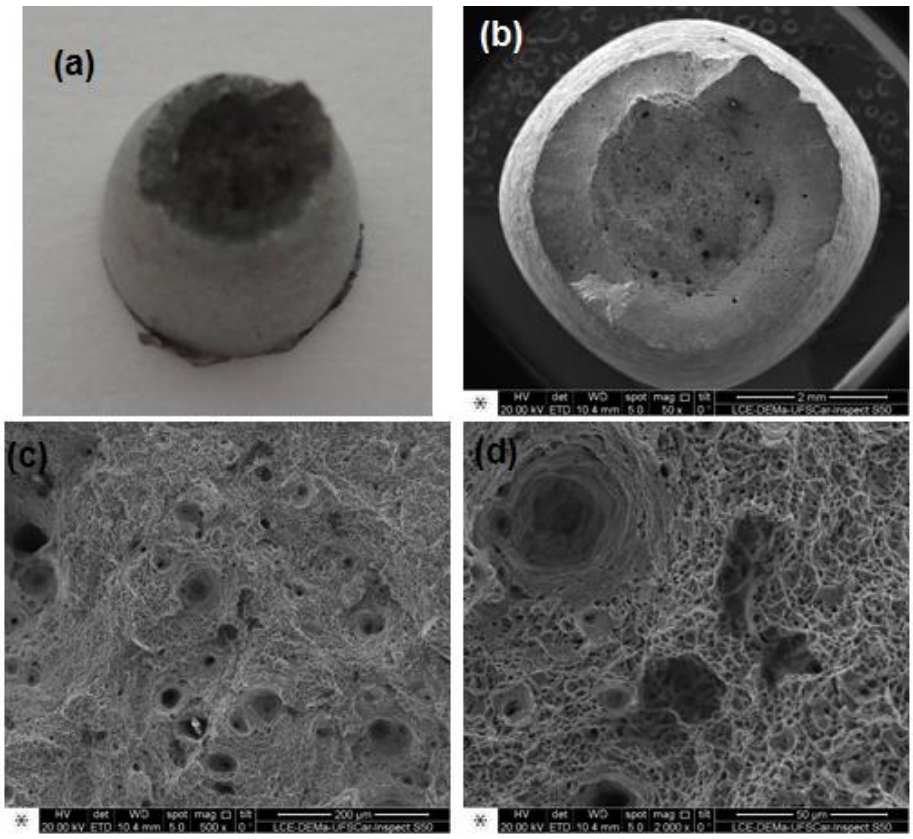

Figure 5.59 - **(a)** Photography and **(b)** SEM image of the cup-and-cone fracture (specimen 1) of the SMSS after tempering at 650 ºC for 2h. **(c)** and **(d)** dimpled fracture surface.

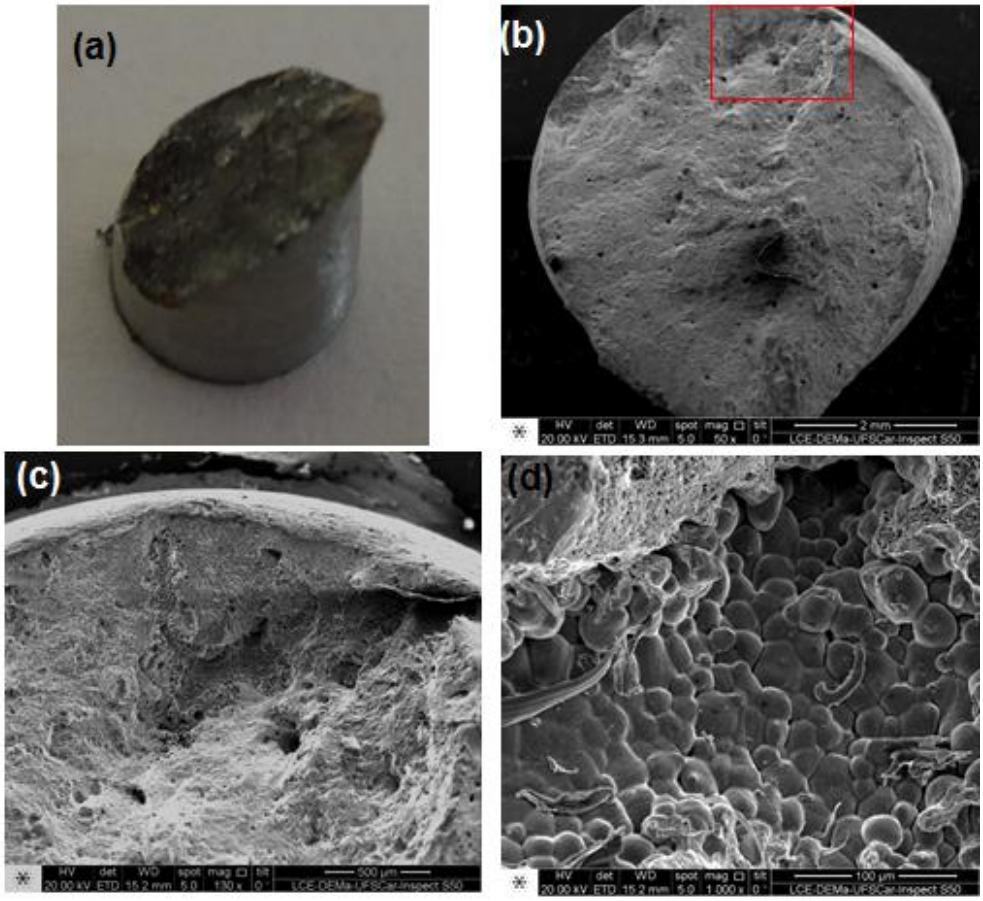

Figure 5.60 - **(a)** Photography and **(b)** SEM image of the 45 degrees fracture (specimen 4) of the as-spray formed SMSS. **(c)** and **(d)** Shrinkage solidification pore.

Figure 5.61 presents the results of the Charpy-V impact test at room temperature for the spray-formed SMSS in both as-spray formed and tempered conditions. The average absorbed energy of the as-spray formed SMSS is about 50 J, which is considerably low for a medium-alloyed SMSS grade. The reported values of impact resistance at room temperature for this steel grade is typically above 200 J [56,65]. Figure 5.62 shows the fractured surface of an as-spray formed SMSS Charpy-V specimen. It can be clearly seen in Figures 5.62 (b), (c), and (d), that the fracture surface consists of mixed cleavage/dimple fracture type. The presence of cleavage regions on the fracture surface, which is brittle fracturing mode, may be explained by the high hardness of the as-spray formed SMSS (about 34 HRC). Tempering the spray-formed SMSS at 650 ºC for 2 h increased the average impact resistance to about 90 J (see Figure 5.61).

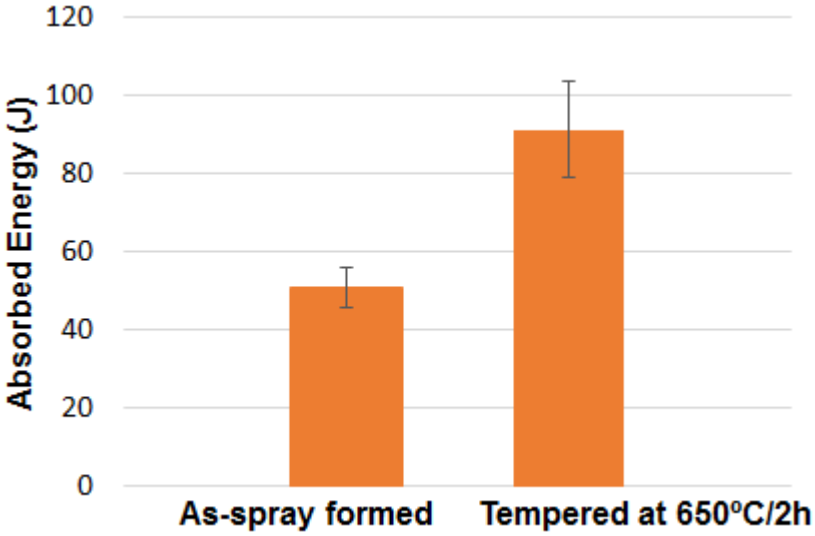

Figure 5.61 - Charpy-V impact resistance at room temperature of the as-spray formed and tempered SMSS layer.

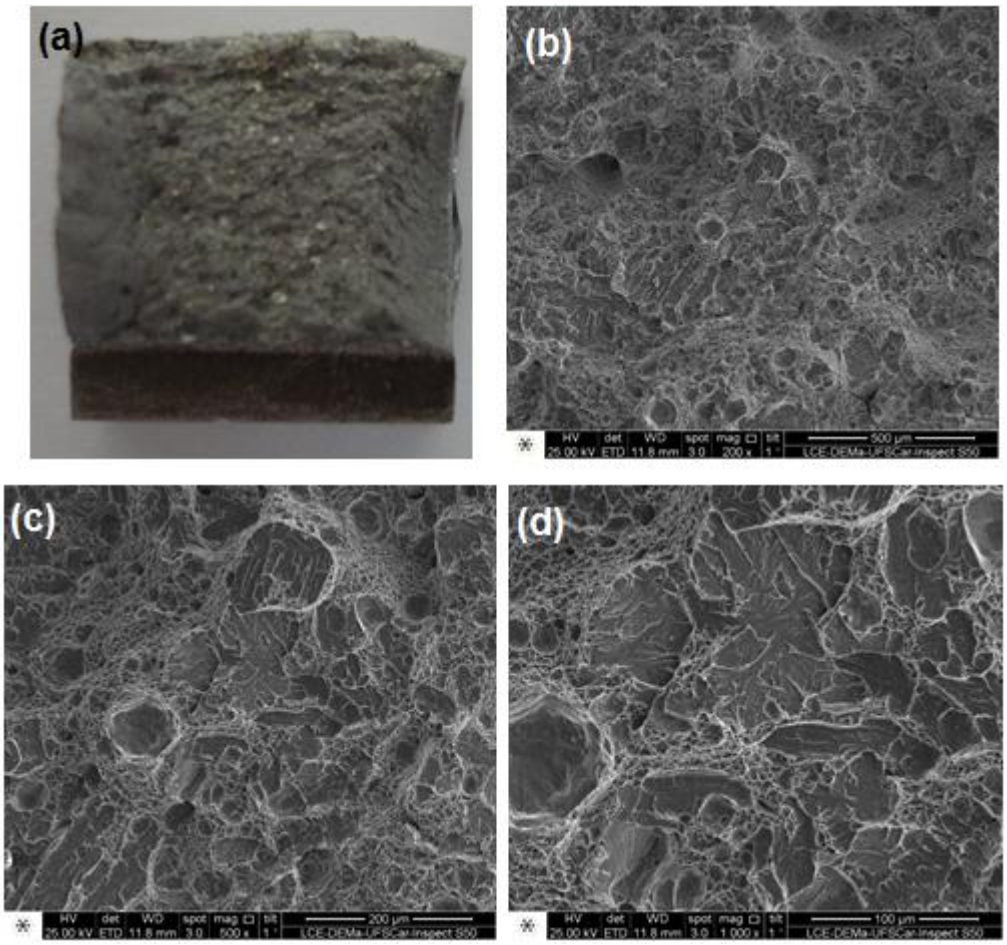

Figure 5.62 - **(a)** Photography of the Charpy-V fracture surface and **(b)**, **(c)** and **(d)** mixed cleavage/dimple fracture surface of the as-spray formed SMSS.

By observing the fracture surface in Figure 5.63 (b), it is possible to note that the fracture surface of the spray-formed SMSS after tempering heat treatment is preferentially composed by dimples. Thus, the hardness reduction derived from tempering was sufficient to change the fracturing mode from partially brittle to completely ductile. However, the impact resistance was still considerably low. This may be explained by the presence of the shrinkage solidification pores presented in the specimens, as can be observed in Figure 5.63 (c) and (d). Therefore, the presence of shrinkage solidification pores impair both the tensile and impact properties of the spray-formed SMSS.

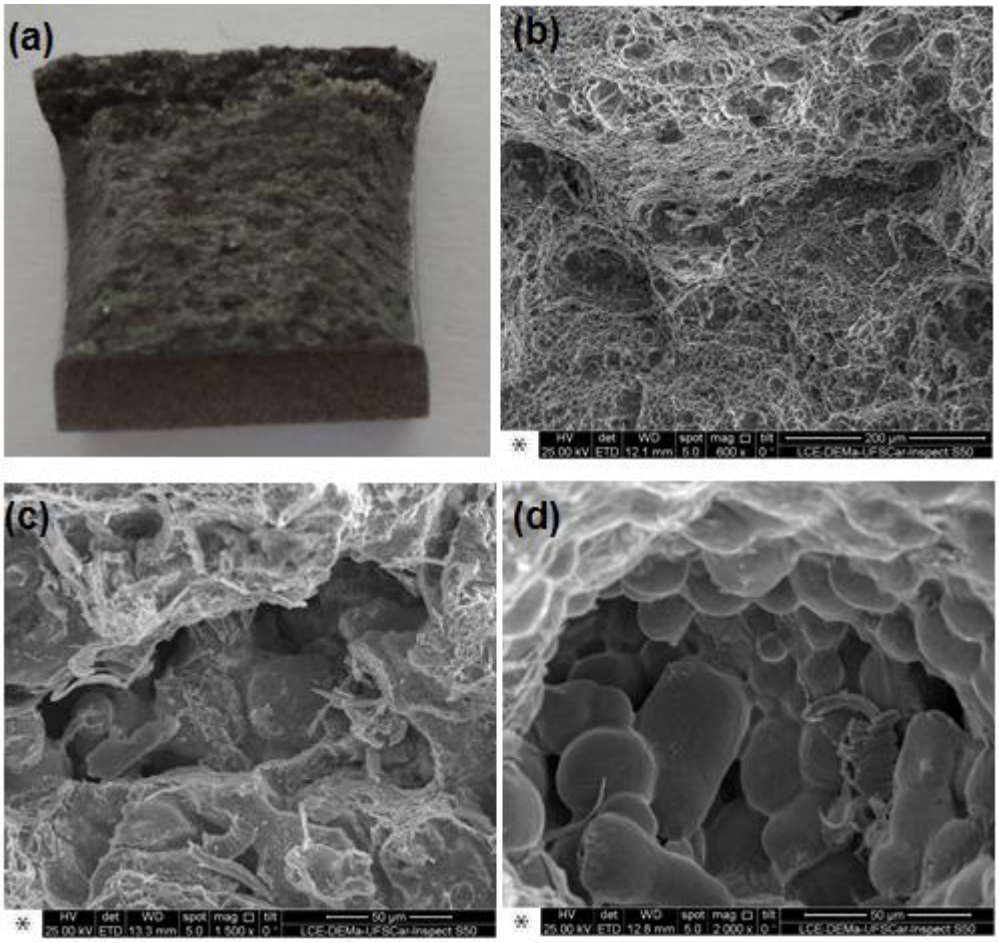

Figure 5.63 - **(a)** Photography of the Charpy-V fracture surface and **(b)** dimpled fracture surface of the spray-formed SMSS after tempering at 650 ºC/2h. **(c)** and **(d)** Shrinkage solidification pores.

5.3.3 Mechanical properties of the SM-14Cr-1B layer

Once both layers of the bimetallic pipe must be subjected to the same heat treatment, the mechanical properties of the SM-14Cr-1B layer were also evaluated in both, as-spray formed and tempered at 650 ºC for 2 h. Figure 5.64 and Table 5.6 shows the results of the as-spray formed SM-14Cr-1B. As the boron-modified SMSS may not present high elongation due to the presence of the M_2B borides in the microstructure, the specimen 1 was loaded without using extensometer. Based on this test, safe strain value to remove the extensometer was determined. By observing the tensile curve of the specimen 1 (Figure 5.64 (a)) it can be seen that the stress increase almost linearly until the ultimate tensile stress, indicating that the as-spray formed SM-14Cr-1B presents practically no plastic deformation. It was established that strain of 0.6-0.7% as safe values to remove the extensometer. The ultimate tensile strength of the as-spray formed specimens varied from 1163 MPa to 1232 MPa, which is considerably high. However, the elongation ranged from 3.0% to 2.9%, and the area reduction from 2.3% to 2.9%. Thus, as expected, the presence of the M_2B-type borides network promoted both effects: (i) increased the tensile resistance, and (ii) reduced the ductility of the alloy. The four specimens presented flat fracture surfaces characteristic of brittle alloys, as shown in Figure 5.65 (a) and (b). Figure 5.65 (d) presents a longitudinal view of the fracture surface. It shows that the fracture mode is intergranular taking place next to the M_2B borides-matrix interface. Figure 5.65 (c) shows a shrinkage solidification pore in the alloy microstructure. However, in the boron-modified SMSS the presence of the borides network has greater detrimental effect on its mechanical properties than the low porosity fraction.

Figure 5.6 (b) and Table 5.6 presents the tensile test results of the SM-14Cr-1B layer after being tempered at 650 ºC for 2 h. The tempered specimens presented well-defined yield stress ranging from 627MPa to 694 MPa. The ultimate tensile stress was considerably reduced when compared to the as-spray formed alloy, varying between 867 MPa and 928 MPa. Such reduction of the tensile properties resulted from the lower hardness of the tempered martensitic matrix.

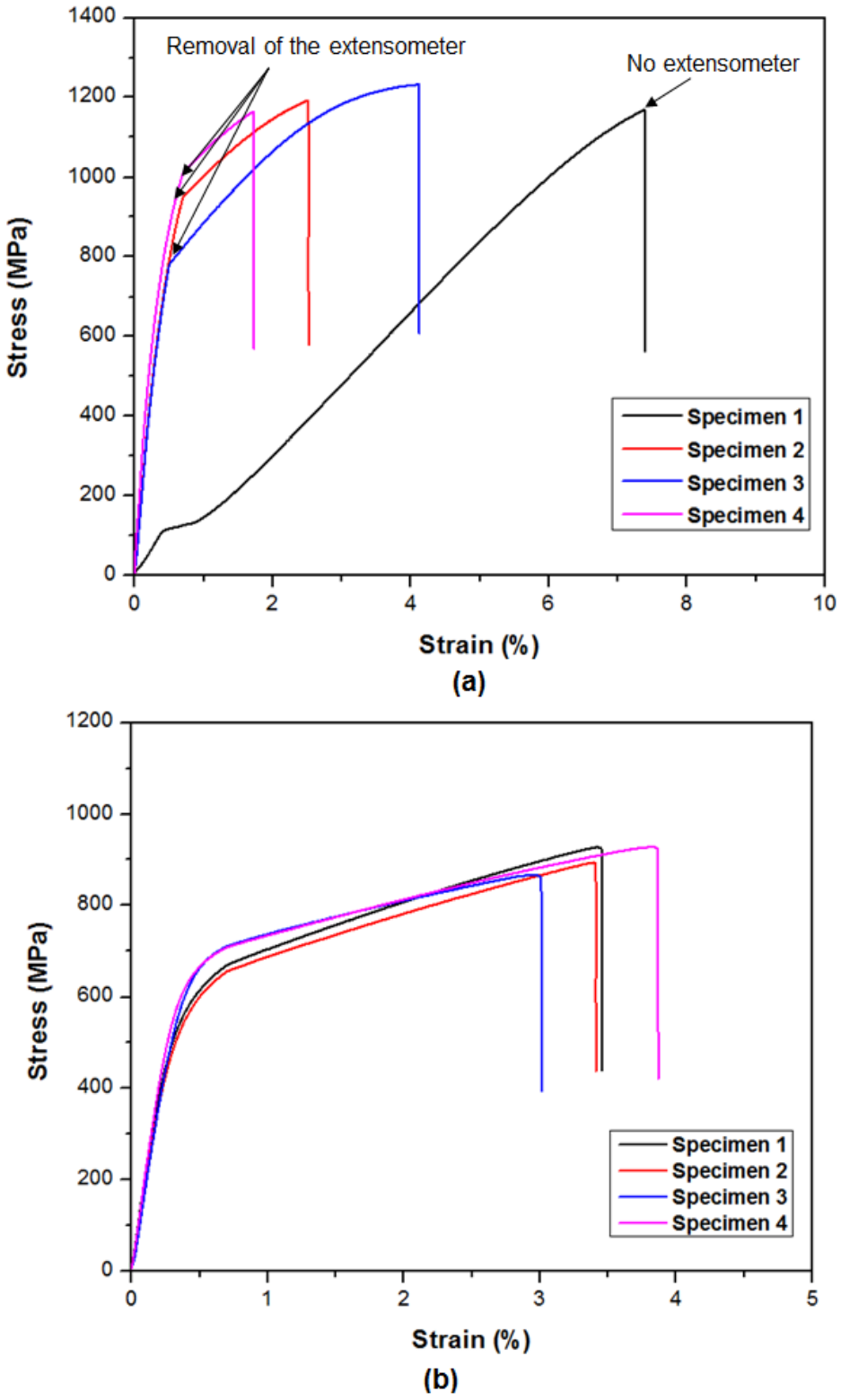

Figure 5.64 - Tensile test results of the SM-14Cr-1B layer **(a)** as-spray formed and **(b)** tempered at 650 ºC for 2h.

Table 5.6 - Tensile properties of the as-spray formed and tempered at 650 ºC for 2h SM-14Cr-1B layer.

As-spray Formed					
	YS (MPa)	**UTS (MPa)**	**Elongation 4D (%)**	**Area Reduction (%)**	**Fracture type**
Specimen 1	-	1168	3.0	2.9	Brittle
Specimen 2	-	1192	Failed out of gauge length		Brittle
Specimen 3	-	1232	3.9	2.29	Brittle
Specimen 4	-	1163	Failed out of gauge length		Brittle
Tempered at 650 ºC for 2 h					
	YS (MPa)	**UTS (MPa)**	**Elongation 4D (%)**	**Area Reduction (%)**	**Fracture type**
Specimen 1	636	928	4.5	1.63	Brittle
Specimen 2	627	894	Failed out of gauge length		Brittle
Specimen 3	694	867	3.0	1.96	Brittle
Specimen 4	683	928	3.6	1.96	Brittle

However, the reduction of the tensile strength did not increase the ductility of the spray-formed boron-modified SMSS. The elongation ranged from 3.0% to 4.5% and the area reduction from 1.6% to 2.0%. As can be seen in Figure 5.66 (a)-(c), the surface fractures of the tempered SM-14Cr-1B was quite similar to the as-spray formed one. The longitudinal view of the fracture – Figure 5.66 (d) – shows that the tempered martensitic matrix presents higher level of plastic deformation when compared to the as-spray formed SMSS – Figure 5.65 (d). Nevertheless, the fracture is still intergranular next to the boride-matrix interface. These results show that the hardness of the martensitic matrix has great influence on the tensile properties such as yield stress and ultimate tensile strength of the spray-formed boron-modified SMSS. However, the elongation and area reduction of the alloy are controlled by the strength of the boride-matrix interface. Figure 5.69 presents the results of the impact tests at room temperature of both as-spray formed and tempered SM-14Cr-1B.

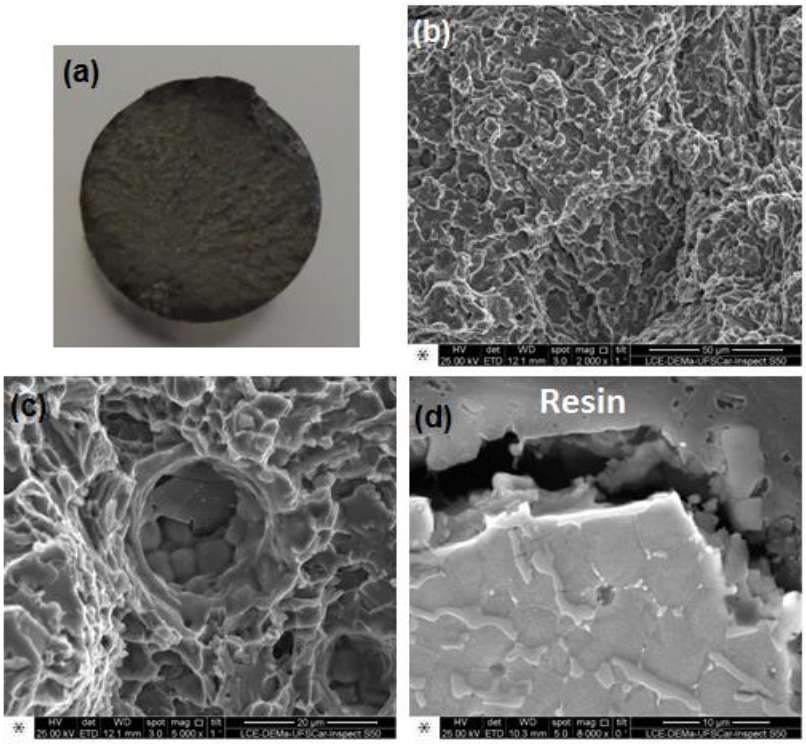

Figure 5.65 - **(a)** Photography and **(b)**-**(c)** SEM image of the brittle fracture (specimen 1) of the as-spray formed SM-14Cr-1B. **(d)** Longitudinal view of the fracture.

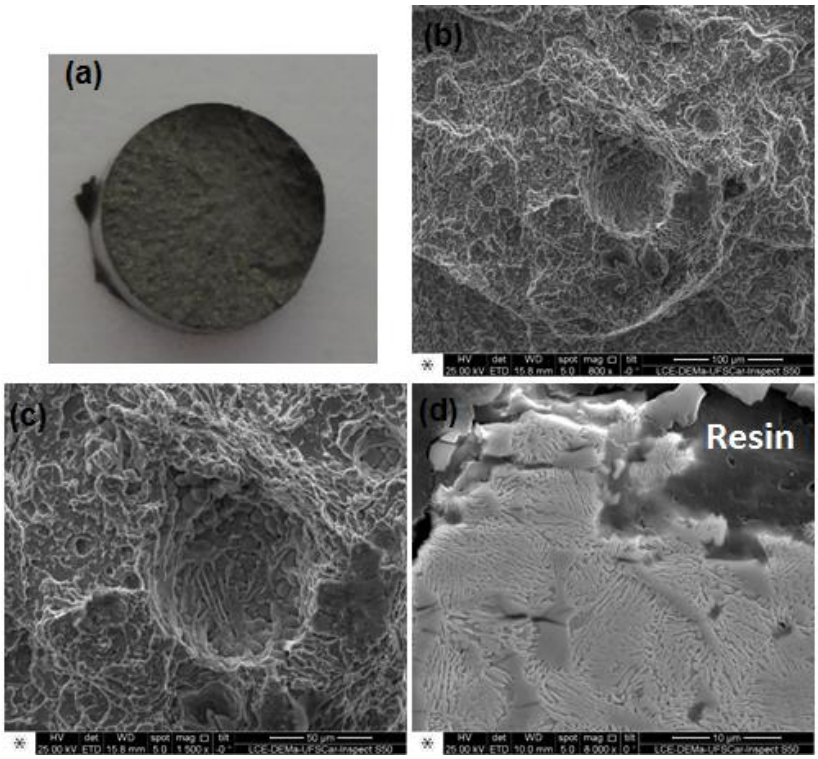

Figure 5.66 - **(a)** Photography and **(b)**-**(c)** SEM image of the brittle fracture (specimen 1) of the SM-14Cr-1B after tempering at 650 ºC for 2 h. **(d)** Longitudinal view of the fracture.

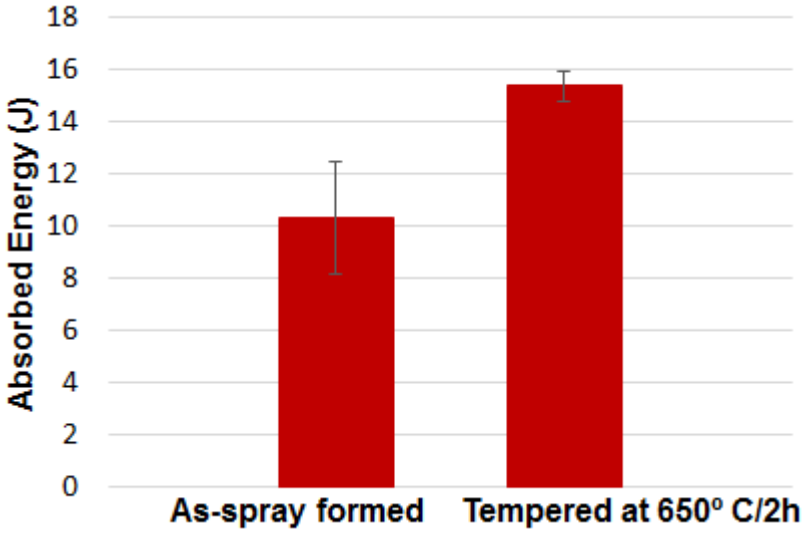

Figure 5.67 - Impact resistance of the as-spray formed and tempered SM-14Cr-1B layer.

One can see that the impact resistance of the tempered SM-14Cr-1B (about 15 J) is slightly higher than that of the as-spray formed (about 11 J). Such small increase in the impact resistance is also resulted from the lower hardness of the martensitic matrix after being tempered. In this, case the low hardness martensite is able to absorb more energy during the impact. The fracture surfaces of both as-spray formed and tempered specimens are displayed in Figure 5.68 and Figure 5.69, respectively. It can be seen that the fracture surfaces are identical to those observed in the tensile specimens, indicating that the fracture mode was intergranular in both cases. Therefore, it can be concluded that the tempering heat treatment reduces the overall hardness of the spray-formed boron-modified SMSS by reducing only the hardness of the martensitic matrix. Such hardness reduction slightly alters the mechanical properties of the alloy. However, the M_2B borides-matrix interface controls the fracture mode.

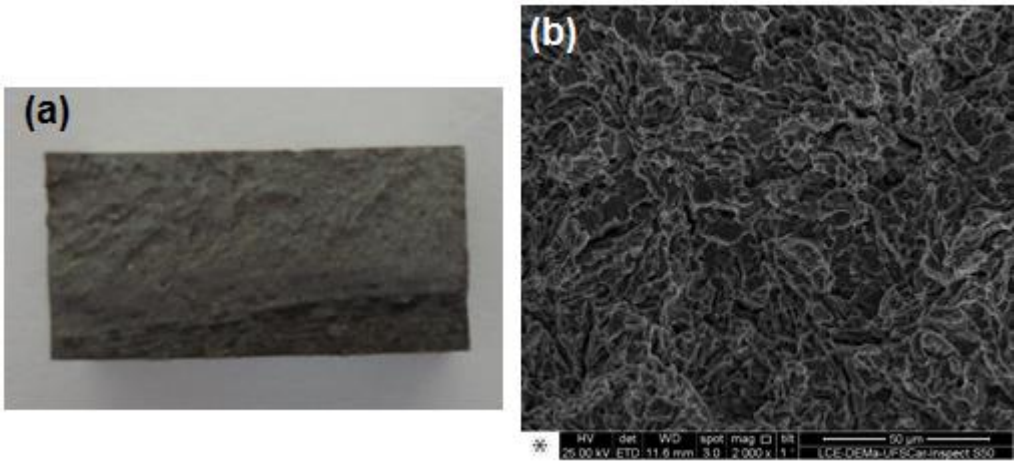

Figure 5.68 - **(a)** Photography and **(b)** SEM image of the fracture surface of the as-spray formed SM-14Cr-B after impact test.

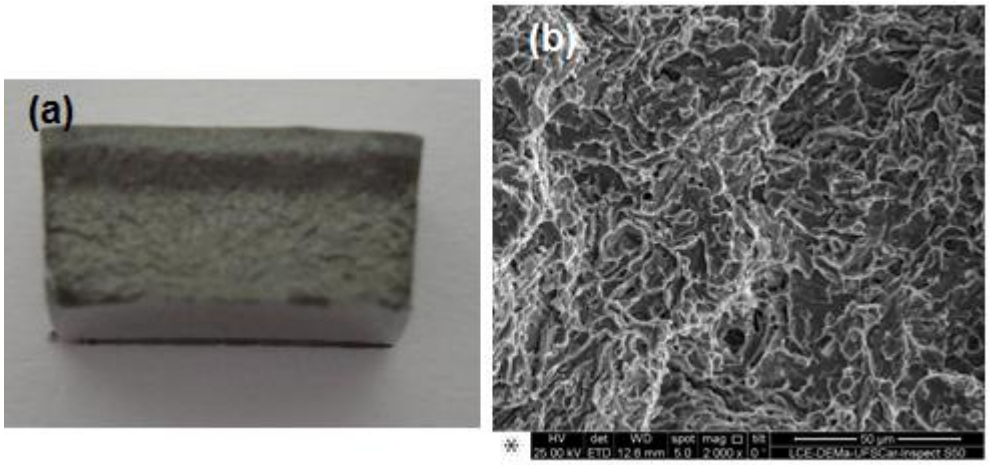

Figure 5.69 - **(a)** Photography and **(b)** SEM image of the fracture surface of the tempered SM-14Cr-1B after impact test.

6 GENERAL DISCUSSION

This thesis aims to demonstrate the technological feasibility of producing a spray-formed bimetallic pipe, which combines the high wear and good corrosion resistance of a boron-modified SMSS to the high mechanical and corrosion properties of the medium-alloyed SMSS grade. From the results presented here, four aspects can be discussed:

(i) The solidification and grain size evolution models in spray forming;
(ii) The effect of using semi-industrial scale in the microstructural evolution of the spray-formed bimetallic pipe;
(iii) The relationship between the microstructure and wear and corrosion properties of the spray-formed boron-modified SMSS;
(iv) The relationship between the mechanical properties and the microstructure of the spray-formed bimetallic pipe.

In this work, it was proposed a solidification model to described formation of the characteristic equiaxed grains of spray-formed products. Differently from what reported for several authors, which consider spray forming as a rapid solidification technique [43,44], the model proposed here states that spray-formed steels (with low porosity levels) solidify under near equilibrium conditions. The main assumption of the solidification model is that during the deposition process the liquid droplets, partially solidified droplets and completely solidified droplets are thermal balanced reaching an equilibrium temperature. This notion of equilibrium temperature within the deposition zone has been previously shown by Grant, P. in [9]. The author has shown that considering the thermal diffusivity of metals (with typical values of about $\alpha = 10^{-5}$ m^2 s^{-1}) and a representative equilibration distance (d) of up to hundreds of microns (considering the largest depositing droplets), the time for thermal equilibration ($t_{eq} = d/\alpha$) is relatively short, about 0.1 s. It was shown that the equilibrium temperature must be above the alloy's *solidus* temperature in order to attain low porosity levels. When the equilibrium temperature lies within the solidification temperature range of the alloy, the completely solidified droplets are partially remelted, generating the "nuclei" that

will grow in the deposition zone. Such “nuclei” will grow without any preferential direction because of the high turbulence in the deposition zone caused by the continuous atomization process, generating the equiaxed grains. The model states that the “nuclei” solidify following the equilibrium solidification path. This last statement was validated by analyzing boron as a tracer element in the boron-modified SMSS. The presence of an interconnected boride network in the microstructure with no precipitates of M_2B borides within the equiaxed grain, demonstrate that: (i) the boron was completely segregated into the liquid present in the deposition zone, and (ii) the last remaining liquid in the deposition zone was continuous and, therefore, no “droplet regions” were preserved after deposition. The assumption of having an equilibrium temperature above the alloy’s *solidus* temperature was validate by measurements of the surface temperature during the deposition of the SF2 and SF3 pipes. Furthermore, it was demonstrate that the “back diffusion” mechanism may take place when elements with high mobility and low solubility in the steel matrix, such as the case of boron, are present. In this case, if the “nuclei” are boron-supersaturated due to the high cooling rate at the atomization process, the boron diffuses through the solid back into the liquid. This hypothesis is corroborated by the appearance of high level of M_2B precipitates in the base of the SF1 pipe, which was subjected to higher cooling rates when compared to the other experiments, and probably presented an equilibrium temperature very close (or below) the alloy’s *solidus* temperature. The high amount of precipitates suggests that faster solidification rates (as in the case of atomization process) may lead to high supersaturation of boron in the steel matrix. Since no precipitates are usually present in the spray-formed boron-modified SMSS, the “back diffusion” mechanism is likely to occur.

A model to describe the grain size evolution of spray-formed alloys was also addressed. This model correlates the amount of “nuclei” within the deposition zone to the final as-spray formed grain size. If the equilibrium temperature at the deposition zone is high, the equilibrium liquid fraction is low and, therefore, the number of “nuclei” is low. Low number of “nuclei” means that these “nuclei” must grow more to consume all the liquid in the deposition zone, resulting in larger grain sizes. On the other hand, low equilibrium temperature (but still above the

alloy's *solidus* temperature) results in low equilibrium liquid fraction and high number of "nuclei". After small growing, the liquid in the deposition zone is completely consumed and the final as-spray formed grain size is small. The effect of temperature on the final grain size have been already reported in literature. Leal, V. [75] has described the microstructure of spray-formed Fe-6%Si deposits with different processing parameters. The author produced deposits recording the temperature with thermocouples inside them during the deposition process. As can be seen in Figure 6.1 (a) the recorded temperatures for two different set of processing parameters where slightly different. In both cases, the measured temperatures lied within the solidification temperature range of the Fe-Si alloy – See Figure 6.1 (b). It can be seen, that the Fe-6%Si alloy has a narrow solidification temperature range, and, therefore, small difference in the equilibrium temperature will generate a large difference in the equilibrium liquid fraction. It can be seen that the deposit temperature for the set of process parameters 1 was 1438 ºC, leading to 0.48 of equilibrium solid fraction – Figure 6.1 (c). On the other hand, the set of parameters 2 led to 1420 ºC of deposit temperature, which results in 0.85 of equilibrium solid fraction. Decreasing 18 ºC increases practically twice the equilibrium solid fraction within the deposition zone, resulting in the final average grain size practically two times smaller – Figure 6.1 (d). The experimental results presented by Leal, V [75] corroborates with the grain size evolution model presented here. It is worth stressing that in the case of the Fe-6%Si alloy, as in the case of the SMSS, grain coarsening takes place after solidification due to the considerably low cooling rate of the deposit. This is not the case of the spray-formed boron-modified SMSSs, which have the grain growth suppressed by the presence of the borides network at the grain boundaries.

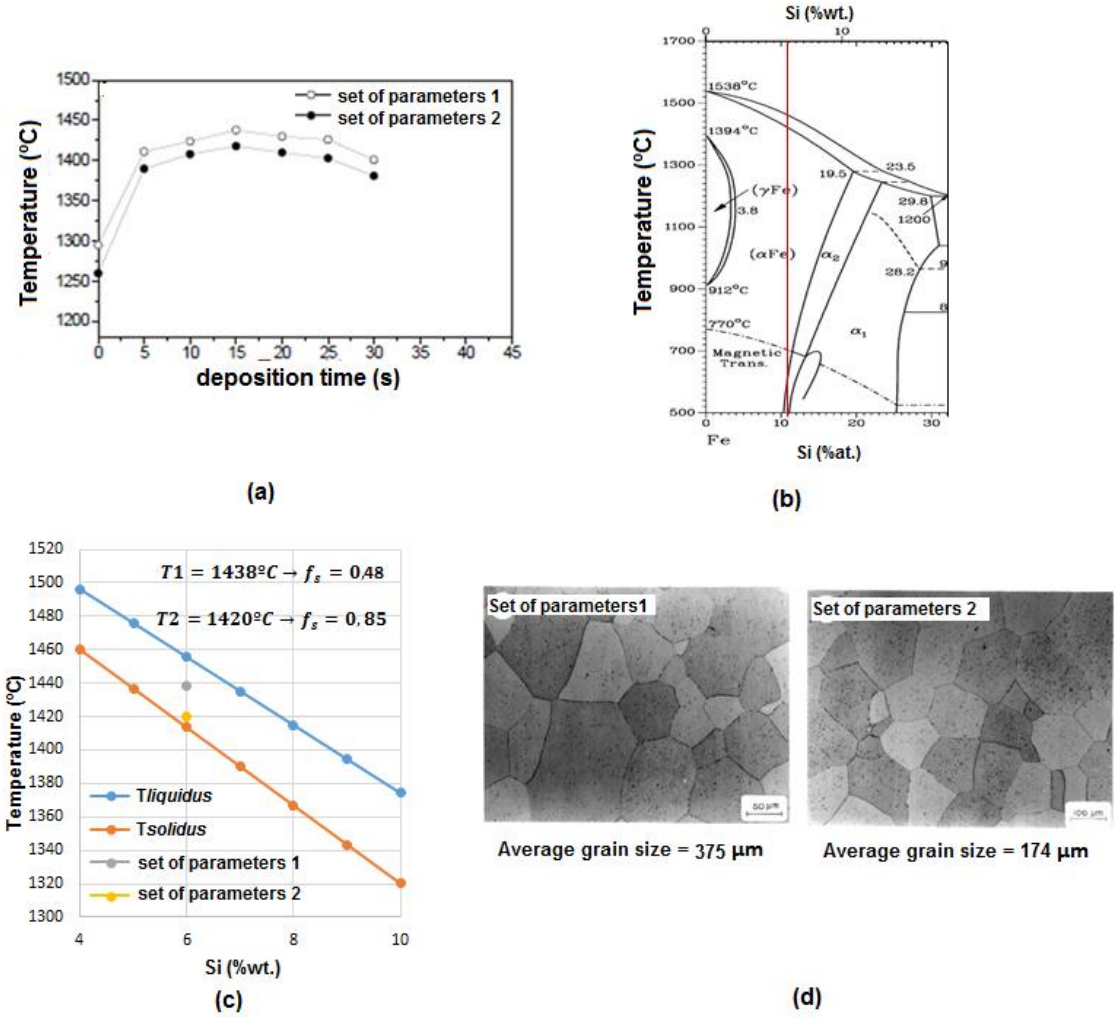

Figure 6.1 - **(a)** Temperature measurements during deposition of Fe-6%Si with two different set of process parameters [75]. **(b)** Fe-Si phase diagram, **(c)** equilibrium solid fraction at both set of process parameters. **(d)** Final microstructure and average grain size of the Fe-6%Si deposited with the two different set of process parameters [75].

The microstructural evolution of the pipes produced in the SF1, SF2 and SF3 runs could be well described by the proposed models. By using semi-industrial spray forming process, it was possible to address important aspects regarding the technological feasibility to produce bimetallic pipes of boron-modified SMSS and conventional SMSS. The first important aspect is the necessity of preheating the substrate before the deposition process. Such procedure is essential to avoid fast contraction of the boron-modified SMSS layer, which leads to its fracture. Another important aspect regards the selection of the processing parameters. It could be seen that the set o process parameters such

as pouring temperature, spray distance, GMR and initial substrate temperature must be chosen in order to achieve equilibrium temperatures in the deposition zones lying within the solidification temperature range of the deposited alloy. Achieving such equilibrium temperatures is essential to develop a low porosity deposit. Uhlenwinkel, V. and Ellendt, N. [45] had already shown that low porosity levels are achieved when the deposit surface temperature is above the alloy's *solidus* temperature. However, the present work has demonstrated that deposit surface temperature, besides the porosity level, also determines the final microstructure of the deposit. It was shown that the surface temperature profile during spray forming of pipes present an inverted-V shape as consequence of the Gaussian distribution of mass and heat flux delivered by the spray cone. Cui, C. et al. [20] have demonstrated by numerical simulations that the temperature profiles of the deposition zone throughout the radius during the deposition of a 100Cr6 steel pipe are also inverted-V shaped – see Figure 6.2. Such temperature profiles corroborates with the idea of an equilibrium temperature profile within the deposition zone with the same inverted-V shape regarding the pipe radius (or thickness). Such equilibrium temperature profile has direct effect on the pipe microstructure, resulting in a grain size profiles throughout the pipe radius with the same inverted-V shape, as suggested by the grain size evolution model proposed.

The third and probably the most important aspect regarding the spray forming of bimetallic pipes is related to the interface between the pipe's layers. It was shown that when the second layer is deposited, it is thermal balanced with the first layer previously deposited. Based on the surface temperature measurements, it could be noted that if the alloy's *solidus* temperature of the second layer is higher than the alloy's *liquidus* temperature of the first layer, high porosity levels are developed next to the interface. Such high porosity levels arise from the fact that next to the interface, the equilibrium temperature of the second layer is likely below its *solidus* temperature. As previously mentioned, equilibrium temperatures below the alloy's *solidus* temperature results in high fraction of cold porosity resulted from the rapid solidification of the remaining liquid within the deposition zone, without particle remelting and liquid homogenization.

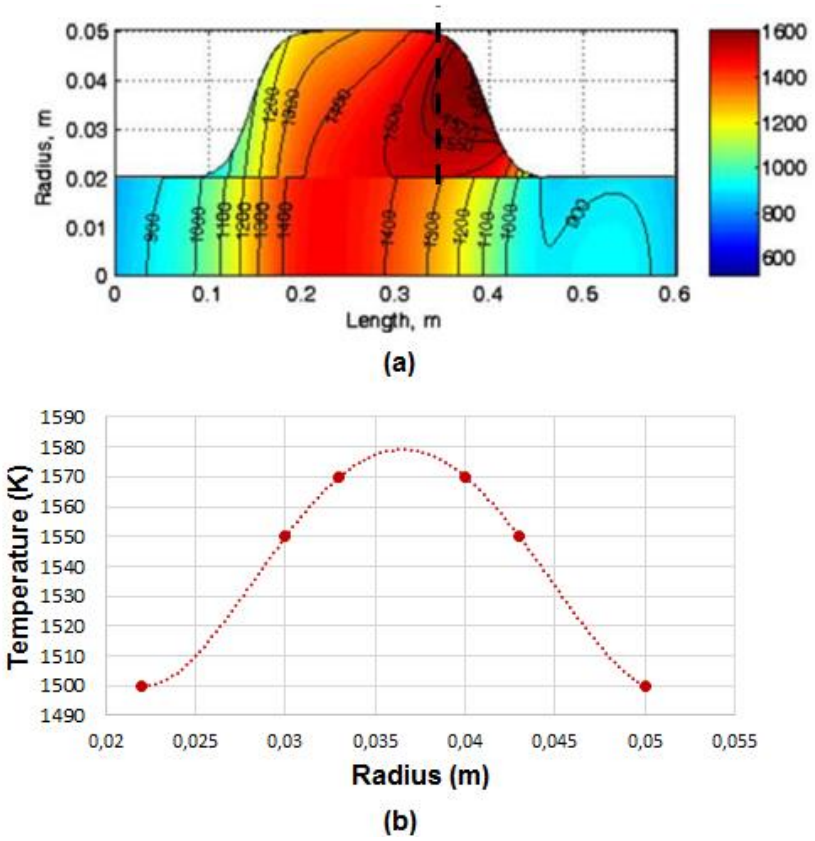

Figure 6.2 - **(a)** Numerical simulation results showing the temperature distribution in a 100Cr6 steel spray-formed pipe during deposition under arbitrary process condition [20]. **(b)** Inverted-V shaped temperature profile (at the dashed line in (a)) regarding the pipe radius (thickness).

Once the *solidus* temperature of the SMSS (second deposited layer) is 1414 ºC and the *liquidus* temperature of the SM-14Cr-1B (first deposited layer) is 1265 ºC, the SMSS layer presented porosity levels up to 50 % in the region next to the interface of the SF3 pipe. However, it was observed that after achieving the highest porosity level, the porosity is reduced to values lower than 1.0 %, which is thereafter kept practically constant. The explanation for this is that increasing the distance from the interface is accompanied by increasing of the equilibrium temperature due to its inverted V-shaped profile. The low porosity level is achieved in the regions where the equilibrium temperature becomes higher than the SMSS *solidus* temperature. It was theoretically demonstrated that bimetallic pipes with low porosity levels at the interface could be obtained by overlapping the spray cones. Cui et al. [52] have reported the production of spray-formed bimetallic pipes of AISI M3:2 and AISI M2 high-alloyed steels. The authors have

shown that an interfacial layer with gradient chemical composition is obtained when the two spray cones are overlapped. In the case of the boron-modified SMSS/ SMSS bimetallic pipe, it was shown that overlapping both spray cones creates a chemical composition gradient zone, which results in a *liquidus* temperature gradient zone due to the reduction of boron content from the boron-modified SMSS layer to the SMSS layer. Such *liquidus* temperature gradient makes possible the equilibrium temperature to lie with the alloys' solidification temperature range during the whole deposition period, which should result in low porosity levels along the whole pipe thickness.

Regarding the bimetallic pipe's properties, the relationship between the wear and corrosion resistance of the boron-modified SMSS grades was addressed in the first part of the work. It was shown that the interconnected M_2B-type boride morphology, resulted from the spray forming process, has great influence on the wear resistance of the spray-formed boron-modified SMSSs. In tribosystems where three-body wear mechanism take place, high fraction of M_2B borides and small grain size are necessary to prevent indentations of rolling abrasive particles and, consequently, to guarantee low wear rate. On the other hand, when wear mechanisms that remove surface material by means of high level of plastic deformation (as in the POC wear test), small fraction of M_2B is sufficient to restrain such deformation. By restraining the plastic deformation, the alloy's wear rate is considerably reduced. It was shown that the boron-modified SMSS presented wear resistance ten times higher than the conventional SMSS, regardless the boron content.

With respect to the corrosion resistance of the boron-modified SMSS, the chemical composition of the martensitic matrix plays the most important role. Once the Cr content of the martensitic matrix remains above 11%wt., the results show that the spray-formed boron-modified SMSS behaves similar to the commercial SMSS in acid chloride media, regardless the boron content. When the chromium content of the martensitic matrix is sufficient to guarantee the passivation, the difference of the spray-formed boron-modified SMSS from the commercial SMSS lies in the repassivation kinetics, which is slower when the M_2B borides are present in the microstructure. It is important to point out that the

microstructural evolution of the spray-formed boron-modified SMSSs also contributes to their good corrosion behavior. Due to the low solubility of boron in the steel matrix, the hard borides (which is the key to increase the wear resistance) are formed exclusively from the eutectic reaction in the last solidification step. Therefore, there is no possibility of borides precipitation in the matrix after solidification, avoiding the formation of strongly Cr-depleted regions in the vicinity of these late precipitates. For instance, once carbon has high solubility in the high temperature austenite, wear resistant tool steels such as AISI D2 and AISI M2:3 (which also have about 12%wt. of Cr), when spray-formed, present high level of Cr-rich carbides (M_7C_3 or MC) precipitation [13,14]. Such precipitation can generate these kind of highly Cr-poor regions reducing their corrosion properties. In summary, it was shown that spray-formed boron-modified SMSSs containing about 0.7-1.0 %wt. of boron and Cr content ranging from 13 %wt. and 14 wt.% present high wear resistance in both wear tests studied here, while maintaining the same level of corrosion resistance in acid chloride media as the conventional medium-alloyed SMSS. The microstructure of the laboratory scale SM-14Cr-1B deposit, composed of equiaxed grains surrounded by M_2B borides eutectic network, were successfully reproduced in the SF2 and SF3 spray-formed pipes, meaning that the same wear and corrosion properties must also be reproduced.

Finally, the evaluation of the mechanical properties of the SMSS layer of the SF3 bimetallic pipe revealed that the presence of shrinkage solidification pores has a detrimental effect on the alloy's ductility. The tensile tests showed that yield stresses ranging from 650 MPa to 850 MPa and ultimate tensile strengths from 950 to 1000 MPa are possible to be achieved with elongations of about 15-17%, after tempering heat treatment. However, the area reduction is considerably reduced when solidification shrinkage pore is present. Nevertheless, the presence of porosity has greater effect on the impact resistance. The higher value of Charpy-V obtained for the spray-formed SMSS, after tempering, was about 90 J, whereas the typical values for medium-alloyed SMSS is above 200 J. By observing the fractured surface was possible to relate the low impact strength to the presence of solidification shrinkage pores. It is

worth stressing that porosity resulted by solidification shrinkage is an intrinsic defect of any casting process. In spray forming, this sort of porosity cannot be eliminated by adjusting process parameters. The fraction of shrinkage solidification porosity is spray-formed products is directly related to the difference between the densities of the liquid and solid phases. For instance, aluminum alloys, which present high contraction during solidification, are likely to present relatively high porosity even being processed under optimized spray-forming conditions. In the case of steels, such as the SMSS, the porosity under optimized conditions is low (lower than 1% as showed in this work), however, will never be null.

Therefore, it can be stated that spray-formed bimetallic pipes of boron-modified SMSS and conventional SMSS can be produced with low porosity levels, and presenting good wear and corrosion properties. However, to achieve the same mechanical properties of the conventional SMSS, some post-thermomechanical process must be applied in order to close the low fraction of solidification shrinkage porosity.

7 CONCLUSIONS

- The spray-formed boron-modified SMSS grades present high wear resistance and corrosion resistance similar to the conventional SMSS. The wear resistance of the alloy is determined by the presence of the interconnected eutectic network of M_2B borides resulted from the spray forming process. Different boron contents leads to different wear resistances depending on the wear mechanism. The corrosion resistance of the boron-modified SMSS is controlled by the chemical composition of the martensitic matrix. In order to have high corrosion resistance, the boron and chromium contents must be balanced in such a way that the remaining Cr content of the martensitic matrix is kept in the composition range of the conventional SMSS.

- The key to produce a spray-formed bimetallic pipe with good metallurgical quality is adjusting the process parameters in such a way that the deposition zone's temperature is kept within the alloy's solidification range during the whole deposition process.

- Preheating the substrate is essential to avoid the fracture of the boron-modified SMSS inner layer.

- Overlapping the spray cones is essential to produce a spray-formed bimetallic pipe of boron-modified SMSS and SMSS with low porosity levels at the interfacial region.

- The as-spray formed microstructure of pipes presents an inverted V-shaped grain size profile regarding the pipe thickness. Such grain size variation arises from the thermal profile (also inverted V-shaped) of the deposition zone, which is caused by the Gaussian-like distribution of mass and heat flux delivered from the spray cone.

- It is technically feasible to produce a spray-formed bimetallic pipe composed of wear and corrosion resistant boron-modified SMSS and conventional SMSS. However, further thermomechanical processing must be applied in order to close the solidification shrinkage porosity, which impairs the

mechanical properties of the SMSS layer. Such sort of porosity is intrinsic to the solidification process, and cannot be avoided by optimizing the process parameters.

8 SUGGESTION FOR FUTURE WORKS

- To produce a spray-formed bimetallic pipe of boron-modified SMSS and conventional SMSS with overlapped spray cones, and evaluating characteristics of the gradient zone.
- Study possible thermomechanical processes able to close the solidification shrinkage pores of spray-formed pipes, without changing their geometries.
- Study the effect of thermomechanical processes on the microstructure and wear resistance of the boron-modified SMSS grades.
- Study the effect of heat treatments on the wear and corrosion resistance of the boron-modified SMSS grades.
- Study the weldability of the boron-modified SMSS grades.

9 REFERENCES

[1] Beraldo LG. Avaliação da resistência ao desgaste de aços inoxidáveis conformados por spray. Universidade Federal de São Carlos, 2011.

[2] Koga GY. Produção por aspersão térmica de revestimentos amorfos resistentes à corrosão e ao desgaste utilizando a liga Fe60Cr8Nb8B24. Universidade Federal de São Carlos, 2014.

[3] Melle AK. Producão e caracterização de recobrimentos de aço, empregando a liga amorfizável Fe-Cr-Nb-B. Universidade Federal de São Carlos, 2012.

[4] Nascimento ARC. Efeito da adição de boro na microestrutura e na resistência ao desgaste do AISI 430 conformado por spray. Universidade Federal de São Carlos, 2014.

[5] Zepon G. Desenvolvimento do aço inoxidável supermartensítico resistente ao desgaste por conformação por spray para aplicação em “risers.” Universidade Federal de São Carlos, 2013.

[6] Silva AMB. Produçao de recobrimentos metálicos a partir de liga de ferros amorfizáveis. Universidade Federal de São Carlos, 2011.

[7] Zepon G, Kiminami CS, Botta WJ, Bolfarini C. Microstructure and Wear Resistance of Spray-Formed Supermartensitic Stainless Steel. Mater Res J Mater 2013;16:642–6. doi:Doi 10.1590/S1516-14392013005000026.

[8] Grant PS. Spray forming. Prog Mater Sci 1995;39:497–545. doi:10.1016/0079-6425(95)00004-6.

[9] Grant PS. Solidification in spray forming. Metall Mater Trans A Phys Metall Mater Sci 2007;38 A:1520–9. doi:10.1007/s11661-006-9015-3.

[10] Cui C, Fritsching U, Schulz A, Tinscher R, Bauckhage K, Mayr P. Spray forming of homogeneous 100Cr6 bearing steel billets. J Mater Process Technol 2005;168:496–504. doi:10.1016/j.jmatprotec.2005.02.250.

[11] Cui C, Fritsching U, Schulz A, Bauckhage K, Mayr P. Control of cooling during spray forming of bearing steel billets. Mater Sci Eng A 2004;383:158–65. doi:10.1016/j.msea.2004.02.058.

[12] Yu H, Wang M, Sheng X, Li Z, Chen L, Lei Q, et al. Microstructure and

tensile properties of large-size 7055 aluminum billets fabricated by spray forming rapid solidification technology. J Alloys Compd 2013;578:208–14. doi:10.1016/j.jallcom.2013.05.117.

[13] Mesquita RA, Barbosa CA. Spray forming high speed steel - Properties and processing. Mater Sci Eng A 2004;383:87–95. doi:10.1016/j.msea.2004.02.035.

[14] Schulz A, Uhlenwinkel V, Escher C, Kohlmann R, Kulmburg A, Montero MC, et al. Opportunities and challenges of spray forming high-alloyed steels. Mater Sci Eng A 2008;477:69–79. doi:10.1016/j.msea.2007.08.082.

[15] Brinksmeier E, Schunemann M. Generation and forming of spray-formed flat products. J Mater Process Technol 2001;115:55–60. doi:Doi 10.1016/S0924-0136(01)00764-6.

[16] Meyer C, Ellendt N, Mädler L, Müller HR, Reimer F, Uhlenwinkel V. Spray forming of high density sheets. Materwiss Werksttech 2014:642–51. doi:10.1002/mawe.201400301.

[17] Mi J, Grant PS. Modelling the shape and thermal dynamics of Ni superalloy rings during spray forming Part 1: Shape modelling - Droplet deposition, splashing and redeposition. Acta Mater 2008;56:1588–96. doi:DOI 10.1016/j.actamat.2007.12.021.

[18] Mi J, Grant PS. Modelling the shape and thermal dynamics of Ni superalloy rings during spray forming. Part 2: Thermal modelling - Heat flow and solidification. Acta Mater 2008;56:1597–608. doi:10.1016/j.actamat.2007.12.022.

[19] Ellendt N, Uhlenwinkel V, Mädler L. High yield spray forming of small diameter tubes using pressure-gas-atomization. Materwiss Werksttech 2014;45:699–707. doi:10.1002/mawe.201400306.

[20] Cui C, Fritsching U, Schulz A, Li Q. Mathematical modeling of spray forming process of tubular preforms. Part 2. Heat transfer. Acta Mater 2005;53:2775–84. doi:10.1016/j.actamat.2005.02.044.

[21] Cui C, Fritsching U, Schulz A, Li Q. Mathematical modeling of spray forming process of tubular preforms: Part 1. Shape evolution. Acta Mater 2005;53:2765–74. doi:10.1016/j.actamat.2005.02.047.

[22] Srivastava VC, Mandal RK, Ojha SN. Microstructure and mechanical properties of Al–Si alloys produced by spray forming process. Mater Sci Eng A 2001;304-306:555–8. doi:10.1016/S0921-5093(00)01514-8.

[23] Bereta L a., Ferrarini CF, Botta F WJ, Kiminami CS, Bolfarini C. Microstructure and mechanical properties of spray co-deposited Al–8.9wt.% Si–3.2wt.% Cu–0.9wt.% Fe+(Al–3wt.% Mn–4wt.% Si)p composite. J Alloys Compd 2007;434-435:371–4. doi:10.1016/j.jallcom.2006.08.156.

[24] Srivastava VC, Rudrakshi GB, Uhlenwinkel V, Ojha SN. Wear characteristics of spray formed Al-alloys and their composites. J Mater Sci 2009;44:2288–99. doi:10.1007/s10853-008-2924-3.

[25] Bereta LA, Ferrarini CF, Botta WJ, Kiminami CS, Bolfarini C. Microstructure and mechanical properties of spray co-deposited Al-8.9 wt.% Si-3.2 wt.% Cu-0.9 wt.% Fe plus (Al-3 wt.% Mn-4 wt.% Si)(p) composite. J Alloys Compd 2007;434:371–4. doi:DOI 10.1016/j.jallcom.2006.08.156.

[26] Godinho H a., Beletati ALR, Giordano EJ, Bolfarini C. Microstructure and mechanical properties of a spray formed and extruded AA7050 recycled alloy. J Alloys Compd 2014;586:S139–42. doi:10.1016/j.jallcom.2012.12.122.

[27] Bereta L a., Ferrarini CF, Kiminami CS, Botta WJF, Bolfarini C. Microstructure and mechanical properties of spray deposited and extruded/heat treated hypoeutectic Al-Si alloy. Mater Sci Eng A 2007;448-451:850–3. doi:10.1016/j.msea.2006.02.241.

[28] Grant PS, Kim WT, Cantor B. Spray Forming of Aluminum-Copper Alloys. Mater Sci Eng a-Structural Mater Prop Microstruct Process 1991;134:1111–4. doi:Doi 10.1016/0921-5093(91)90935-G.

[29] Mazzer EM, Afonso CRM, Bolfarini C, Kiminami CS. Microstructure study of Al 7050 alloy reprocessed by spray forming and hot-extrusion and aged at 121 degrees C. Intermetallics 2013;43:182–7. doi:DOI 10.1016/j.intermet.2013.08.004.

[30] Guerra APDB, Ellendt N, Uhlenwinkel V, da Silva PSCP, Bolfarini C. Microstructure of a recycled AA7050 alloy processed by spray forming followed by hot extrusion and rotary swaging. Materwiss Werksttech

2014;45:568–73. doi:DOI 10.1002/mawe.201400217.

[31] Cui C, Fritsching U, Schulz a., Bauckhage K, Mayr P. Spray formed bearing steel insensitive to distortion: Part I material characterization. J Mater Sci 2004;39:5639–45. doi:10.1023/B:JMSC.0000040070.23441.2d.

[32] Cui C, Schulz A, Fritsching U, Bauckhage K, Mayr P. Spray formed bearing steel insensitive to distortion - Part II - Distortion behavior. J Mater Sci 2005;40:1673–80. doi:DOI 10.1007/s10853-005-0668-x.

[33] Lachenicht V, Scharf G, Zebrowski D, Shalimov a. Spray forming - A promising process for making high-quality steels and alloys. Metallurgist 2011;54:656–68. doi:10.1007/s11015-011-9354-1.

[34] Schulz a., Uhlenwinkel V, Bertrand C, Kohlmann R, Kulmburg a., Oldewurtel a., et al. Nitrogen pick-up during spray forming of high-alloyed steels and its influence on microstructure and properties of the final products. Mater Sci Eng A 2004;383:58–68. doi:10.1016/j.msea.2004.02.036.

[35] Lin Y, McHugh KM, Zhou Y, Lavernia EJ. Modeling the spray forming of H13 steel tooling. Metall Mater Trans A Phys Metall Mater Sci 2007;38 A:1632–7. doi:10.1007/s11661-007-9159-9.

[36] Mi J, Grant PS. Modelling the shape and thermal dynamics of Ni superalloy rings during spray forming. Part 2: Thermal modelling – Heat flow and solidification. Acta Mater 2008;56:1597–608. doi:10.1016/j.actamat.2007.12.022.

[37] Mi J, Grant PS, Fritsching U, Belkessam O, Garmendia I, Landaberea a. Multiphysics modelling of the spray forming process. Mater Sci Eng A 2008;477:2–8. doi:10.1016/j.msea.2007.08.083.

[38] Hanlon DN, Rainforth WM, Sellars CM. The rolling/sliding wear response of conventionally processed and spray formed high chromium content cast iron at ambient and elevated temperature. Wear 1999;225-229:587–99. doi:10.1016/S0043-1648(99)00053-8.

[39] Matsuo TT, Kiminami CS, Fo WJB, Bolfarini C. Sliding wear of spray-formed high-chromium white cast iron alloys. Wear 2005;259:445–52. doi:10.1016/j.wear.2005.01.021.

[40] Hanlon DN, Rainforth WM, Sellars CM. Effect of spray forming on the microstructure and properties of a high chromium white cast iron. J Mater Sci 1999;34:2291–301. doi:10.1023/A:1004573524282.

[41] Kasama AH, Mourisco AJ, Kiminami CS, Botta Fo WJ, Bolfarini C. Microstructure and wear resistance of spray formed high chromium white cast iron. Mater Sci Eng A 2004;375-377:589–94. doi:10.1016/j.msea.2003.10.093.

[42] Lavernia EJ., Wu Y, Ltd JW& S. Spray Atomization and Deposition. Spray At. Depos. 1st ed., John Wiley & Sons Ltd: 1996, p. 331–42.

[43] Henein H. Why is spray forming a rapid solidification process? Materwiss Werksttech 2010;41:555–61. doi:10.1002/mawe.201000642.

[44] Lavernia EJ. The Evolution of Microstructure during Spray Atomization and Deposition. Int J Rapid Solidif 1989;5:47–85.

[45] Uhlenwinkel V, Ellendt N. Porosity in Spray-Formed Materials. Mater Sci Forum 2007;534-536:429–32. doi:10.4028/www.scientific.net/MSF.534-536.429.

[46] Kramer C, Uhlenwinkel V, Bauckhage K. Spray forming: The sticking efficiency and its dependency on affecting parameters. Solidif 1998 1998:401–13.

[47] Kramer C, Bauckhage K, Uhlenwinkel V. The Sticking Efficiency at the Spray Forming of Metals. 3rd Int. Conf. Spray Form. , vol. 1, Cardiff, UK: 1996, p. 273–80.

[48] Buchholz M, Uhlenwinkel V, Ellendt N. The Effect of Deposit Temperature on the Sticking Efficiency during Spray Forming. 4th Int. Conf. Spray Form., vol. 1, Baltimore-Md, USA: 1999.

[49] Bergmann D, Fritsching U. Sequential thermal modelling of the spray-forming process. Int J Therm Sci 2004;43:403–15. doi:10.1016/j.ijthermalsci.2003.10.004.

[50] Meyer O, Fritsching U, Bauckhage K. Numerical investigation of alternative process conditions for influencing the thermal history of spray deposited billets. Int J Therm Sci 2003;42:153–68. doi:10.1016/S1290-0729(02)00015-7.

[51] Cui CS, Schulz A, Uhlenwinkel V. Co-Spray Forming of Gradient Deposits from Two Sprays of Different Tool Steels Using Scanning Gas Atomizers. Steel Res Int 2013;84:1075–84. doi:DOI 10.1002/srin.201200266.

[52] Cui C, Schulz a., Uhlenwinkel V. Materials characterization and mechanical properties of graded tool steels processed by a new co-spray forming technique. Materwiss Werksttech 2014;45:652–65. doi:10.1002/mawe.201400302.

[53] Grohmann O, Meyer C, Schulz A, Uhlenwinkel V, Heinzel C. Hot forming tool generated via co-spray forming of composite material. 5th Int. Conf. Spray Depos. Melt At., vol. 1, Bremen, Germany: 2013.

[54] Smith L, Celant M, Team P. Martensitic stainless steels in context. Supermartensitic Stainl Steels 2002 Brussels, 17 2002:1–10.

[55] Kondo, K., Ueda, M., Ogawa, K., Amaya, H., Hirata, H., Takabe, H., Miyazaki Y. Alloy design of super 13Cr martensitic stainless steel (Development of super 13Cr martensitic stainless steel for line pipe-1). Supermartensitic Stainl. Steels 99, Brussels, Belgium: 1999, p. 11–8.

[56] Dufrane JJ. Metallurgical basis for the development of weldable martensitic stainless steels. Supermartensitic Stainl. Steels 99, Brussels, Belgium: 1999, p. 19–24.

[57] Widen H, Toussaint P, Courdreuse L. Past, present and future of weldable supermartenstic alloys. Supermartensitic Stainl. steel 2002, vol. 1, Brussels, Belgium: 2002, p. 9–13.

[58] Kimura M. Corrosion resistance of high-strength modified 13% Cr steel. Corrosion 1999;55:756–61. doi:10.5006/1.3284030.

[59] Carrouge D, Bhadeshia HKDH, Woollin P. Effect of delta-ferrite on impact properties of supermartensitic stainless steel heat affected zones. Sci Technol Weld Join 2004;9:377–89. doi:Doi 10.1179/136217104225021823.

[60] Thibault D, Bocher P, Thomas M. Residual stress and microstructure in welds of 13%Cr–4%Ni martensitic stainless steel. J Mater Process Technol 2009;209:2195–202. doi:10.1016/j.jmatprotec.2008.05.005.

[61] Thibault D, Bocher P, Thomas M, Lanteigne J, Hovington P, Robichaud P.

Reformed austenite transformation during fatigue crack propagation of 13%Cr–4%Ni stainless steel. Mater Sci Eng A 2011;528:6519–26. doi:10.1016/j.msea.2011.04.089.

[62] Bilmes PD, Solari M, Llorente CL. Characteristics and effects of austenite resulting from tempering of 13Cr-NiMo martensitic steel weld metals. Mater Charact 2001;46:285–96. doi:10.1016/S1044-5803(00)00099-1.

[63] Olden V, Thaulow C, Johnsen R. Modelling of hydrogen diffusion and hydrogen induced cracking in supermartensitic and duplex stainless steels. Mater Des 2008;29:1934–48. doi:10.1016/j.matdes.2008.04.026.

[64] Solheim KG, Solberg JK, Walmsley J, Rosenqvist F, Bjørnå TH. The role of retained austenite in hydrogen embrittlement of supermartensitic stainless steel. Eng Fail Anal 2013;34:140–9. doi:10.1016/j.engfailanal.2013.07.025.

[65] Rodrigues CAD, Lorenzo PLD, Sokolowski A, Barbosa CA, Rollo JMDA. Titanium and molybdenum content in supermartensitic stainless steel. Mater Sci Eng A 2007;460-461:149–52. doi:10.1016/j.msea.2007.01.016.

[66] Ma XP, Wang LJ, Liu CM, Subramanian S V. Role of Nb in low interstitial 13Cr super martensitic stainless steel. Mater Sci Eng A 2011;528:6812–8. doi:10.1016/j.msea.2011.05.065.

[67] Shadrichev E V, Ivanov AE. Relative Wear-Resistance of Single-Phase and 2-Phase Boride Layers. Met Sci Heat Treat 1984;26:235–9. doi:Doi 10.1007/Bf00703870.

[68] Shadrichev E V, Rumyantsev SI. Wear Kinetics of a 2-Phase Boride Layer. Met Sci Heat Treat 1982;24:495–8. doi:Doi 10.1007/Bf00773158.

[69] Hall K.P. RWM. Contact Pressure Threshold: An Important New Aspect of Casing Wear. Soc Pet Eng 2005;SPE 9430:1–7.

[70] Adler TA., Walters RP. Corrosion and wear of 304 stainless steel using a scratch test. Corros Sci 1992;33:1855–76. doi:10.1016/0010-938X(92)90189-A.

[71] Uhlenwinkel V, Ellendt N. Porosity in spray-formed materials. Prog Powder Metall Pts 1 2 2007;534-536:429–32.

[72] Freyberg A V., Buchholz M, Uhlenwinkel V, Henein H. Droplet solidification

and gas-droplet thermal coupling in the atomization of a Cu-6Sn alloy. Metall Mater Trans B 2003;34:243–53. doi:10.1007/s11663-003-0011-3.

[73] Zepon G, Ellendt N, Uhlenwinkel V, Bolfarini C. Solidification Sequence of Spray-formed Steels. Metall Mater Trans a-Physical Metall Mater Sci 2015;Accepted f. doi:10.1007/s11661-015-3253-1.

[74] Lo KH, Shek CH, Lai JKL. Recent developments in stainless steels. Mater Sci Eng R Reports 2009;65:39–104. doi:10.1016/j.mser.2009.03.001.

[75] Leal VS. Conformação por spray da liga Fe-6%Si: estudo do processamento e da microestrutura. Universidade Federal de São Carlos, São Carlos-SP, Brasil, 1999.

[76] Lefrou C, Nogueira RP, Huet F, Takenouti H. Electrochemistry. Shreir's Corros., vol. 1, Elsevier; 2010, p. 13–51. doi:10.1016/B978-044452787-5.00003-2.

[77] Barsoukov E, Macdonald JR. Impedance Spectroscopy. 2005. doi:10.1002/0471716243.

[78] Orazem ME, Tribollet B. Electrochemical impedance spectroscopy. vol. 48. 2008.

[79] Bertocci U, Kruger J. Studies of passive film breakdown by detection and analysis of electrochemical noise. Surf Sci Lett 1980;101:A454. doi:10.1016/0167-2584(80)90164-4.

[80] Iverson WP. Transient Voltage Changes Produced in Corroding Metals and Alloys. J Electrochem Soc 1968;115:617 – &. doi:Doi 10.1149/1.2411362.

[81] Dawson JL, Ferreira MGS. Electrochemical studies of the pitting of austenitic stainless steel. Corros Sci 1986;26:1009–26. doi:10.1016/0010-938X(86)90130-7.

APPENDIX A

A basic electrochemical approach of steel corrosion

The corrosion rate of a metallic piece in an aggressive medium depends on many factors such as the nature of the metal and the environment, temperature, pressure and so on. Regardless the rate of the process, it is important to bear in mind that any corrosion process evolves under a long-term out-of-equilibrium conditions. If a metal is corroding, oxidation reactions inevitably take place at its surface. For instance, when a piece of iron is corroded in an acid media, the oxidation reaction represented by equation A.1 is present. Despite the non-equilibrium condition of the system, when the corrosion process takes place, no net current flux crosses the metal-acid media interface. This means that at every instant the amount of current by the oxidation reactions have to be balanced by cathodic counterparts. This implies that anodic and cathodic reactions must be occurring simultaneously and at the same magnitude in modulus. In the case of the iron-acid media system, the anodic reaction (equation A.1) is mostly balanced by the hydrogen reduction reaction shown in equation A.2.

$$Anodic\ reaction: Fe \rightarrow Fe^{2+} + 2e^{-} \quad (A.1)$$

$$Cathodic\ reation: 2H^{+} + 2e^{-} \rightarrow H_2 \quad (A.2)$$

Corrosion phenomena, therefore involves at least two different redox couples, one or more supplying the anodic current and the other one (or more) supplying the cathodic current ensuring the zero current balance. It is important to notice that, in a corrosion scenario, the above-mentioned redox reactions always take place in a macroscopic interface between the metallic surface (an electronic conductor, hereinafter called electrode) and the media (usually an ionic conductor, hereinafter called electrolyte). In the previous example, if the four species from equation A.1 and A.2 are present at the metal-electrolyte interface, the two individual theoretical equilibrium potentials for both reactions (Eeq,Fe^{2+}/Fe and E_{eq},H^{+}/H_2) can be defined by the Nernst law. This issue is illustrated — taking the metal / cation equilibrium as an example — by equation

A.3, where E_0 is the standard electrochemical potential of the M/M^{z+} redox couple, R is the universal gas constant, T is the absolute temperature and F is the Faraday constant.

$$E_{eq} = E^0 + \frac{RT}{zF}\ln[M^{z+}] \quad (A.3)$$

For any single forward-backward redox reaction, for instance, $M \leftrightarrow M^{z+} + z^{e-}$, if the equilibrium is observed the overall current which characterizes this electrochemical system is null (in other words, if $E = E_{eq}$ then $I = 0$). If an overvoltage $\eta > 0$ (defined as $\eta = E - E_{eq}$) is applied to the metal-electrolyte interface, the equilibrium will be dislocated in the forward direction, producing more M^{z+} until the new equilibrium concentration of the electrolyte is reached. In the transient period, a non-zero current balance ($I > 0$, anodic current corresponding to a net oxidation) is established. On the other hand, if an overvoltage $\eta < 0$ is applied, the equilibrium is dislocated to the backward direction and M metallic will be deposited in the interface yielding in a negative current ($I < 0$, cathodic current corresponding to net reduction). The relationship between the potential (or the overvoltage) applied and the overall current can be graphically expressed through a polarization curve, whose shape is a function of the thermodynamic and kinetics attributes of the couple. Based on this, the corrosion of an iron piece in an acid media may be thought from their individual polarization curves, as shown in Figure A.1. Since iron is oxidized when corroding, it is logical to think that it must be polarized in somewhere along the anodic branch of the Fe/Fe^{2+} polarization curve. Moreover, as the zero overall current must be ensured, it is quite evident that the H^+ must be reduced to consume the electrons supplied by the anodic reaction. In this way the H^+/H_2 couple must be polarized in some point on the cathodic branch of its polarization curve. The corrosion process is then iron dissolution with hydrogen evolution according to equations A.1 and A.2. The exact situation is graphically determined by the potential for which $|I_c| = I_a$, as shown in Figure A.1. From this, two fundamentals parameters of corrosion processes can be defined: (i) the corrosion

potential (E_{corr}), also called rest potential or open-circuit potential (OCP), which is the exact potential for which $|I_c| = I_a$; and (ii) the corrosion current (I_{corr}) which is defined as $I_{corr} = |I_c| = I_a$. Experimentally, the E_{corr} corresponds to the potential assumed spontaneously by the electrode when in contact with the electrolyte and is easily measured by help of an reference electrode (as it will be seen later).

Several electrochemical techniques (such as, potentiometry, amperometry, potentiodynamic polarization, electrochemical impedance spectrometry, electrochemical noise, etc) may be used for studying the cathodic and anodic currents by controlling the potential or current around the E_{corr}, in the cathodic and/or anodic branches of an electrode-electrolyte interface, and measuring the respective responses from the system. Such electrochemical techniques are powerful tools for characterize the corrosion resistance of an electrode in a specific electrolyte. Next, it will be presented a brief description of a conventional electrochemical cell and the electrochemical techniques applied to evaluation of corrosion resistance of steels important for the present work.

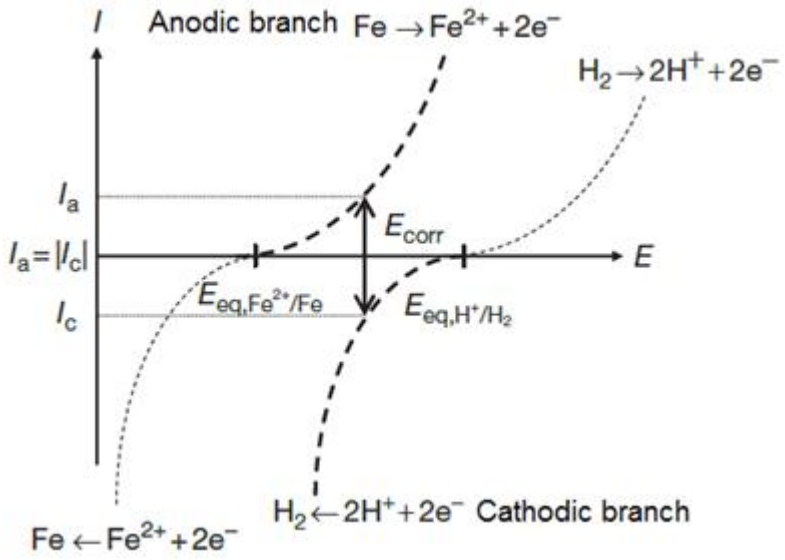

Figure A.1: Schematic representation of the polarization curves of the two redox couples around their respective equilibrium potential allowing the corrosion potential E_{corr}, at which $|I_c| = I_a$, to be determined [76].

Electrochemical Cell

Although in most corrosion processes the electrochemical phenomena occur on a single electrode, the understanding and quantitative analysis of these phenomena are usually performed by using three electrodes in contact with the same electrolyte in the so-called electrochemical cell. These three electrodes are: (i) the working electrode (WE), which is the electrode under study, in other words, is the metallic material whose corrosion resistance is under evaluation; (ii) the counter electrode (CE), the role of which is to ensure the current flow across the cell. For corrosion studies an inert CE, usually a platinum grid or sheet is used; and (iii) the reference electrode (RE) versus which the potential of the WE is measured. In practical, secondary electrodes (REs) which are calibrated against the standard hydrogen electrode (SHE) are commonly used. Typical RE used in corrosion studies is the (SCE) for saturated calomel electrode ($Hg|Hg_2Cl_2$ in saturated KCl solution, with potential versus the SHE of +0.24 V), and the silver electrode (Ag|AgCl in KCl or NaCl solution of fixed concentration, with potential versus the SHE depends on the concentration of the salt solution). The electrochemical analysis are performed by controlling the electrode potential (by mean of a potentiostat) or the current flow across the electrode (by using a galvanostat), and measuring the respective response (the current when a potential is applied and the potential when a current is applied) [76]**.**

Potentiodynamic Polarization

Potentiodynamic polarization method involves the control of the potential, which is swept at a pre-determined rate (typically from 0.1 to 1 $mV.s^{-1}$ for steel corrosion studies), along a desired range: around the corrosion potential E_{corr}, in the anodic and/or cathodic domains. The resulting current (I), is monitored as function of the applied potential (E). If the working electrode surface is known, the current density (j), normally given in $A.cm^{-2}$, can be estimated. The polarization curves give us several useful information about the corrosion behavior of a steel in a determined electrolyte such as: (i) the corrosion potential (E_{corr}); (ii) the corrosion current density (j_{corr}) which are direct related to the

corrosion rate of the steel; (iii) the presence or formation of a passive film; and (iv) the stability of the passive film and its susceptibility to localized corrosion.

Figure A.2 shows polarization curves of the AISI 430 ferritic stainless steel in a 2M NaCl solution with different pHs. In corrosion studies, the potential is usually swept from few mV below the E_{corr} to high potential values. One can see that considerably different curve shapes are obtained only by changing the pH of the solution. The black curve (pH = 7) is a typical curve of stainless steel presenting a passive film. It can be seen that initially the modulus of the current density (cathodic branch) decreases reaching extremely low values at the E_{corr}, for which the theoretical overall net current is zero. Above the E_{corr} the current density increases again (anodic branch) but rapidly a plateau is formed, where the current density stays practically constant in the called passive plateau. At higher values of potential, the current density suddenly increases to very high values. In the case of stainless steels in chlorides electrolytes, such sudden increase in the current density is very frequently due to pitting corrosion (a localized breakdown of the passive film favored by the chloride ions). It is worth mentioning that in different situations the increasing of current density for high over potentials can be caused by different phenomena such as transpassive dissolution (rapid increase in the corrosion rate of the metal also related to passive film breakdown or dissolution), and oxygen evolution (in materials with very protective passive film, which do not suffer any attack, the increase in current density is caused by the evolution of oxygen in a very specific potential). The potential related to the increase of the current caused by pitting is called pitting potential ($E_{pitting}$).

The polarization curve obtained in pH = 2 (pink trace) deserves a specific comment since it presents a quite different behavior. Indeed, after the E_{corr}, the current density increases up to a maximum value before collapsing down to the formation of a passive plateau. This behavior indicates that in this case, when the anodic branch started, the surface of the steel was in an active zone, which means that no protective film was present, and the metal oxidation is the dominant reaction. However, unlikely to non-passivating metallic surfaces, this current increase does not correspond to free corrosion, but to the onset of the

formation of the passive film. When the peak current density, also called critic current density for passivation or j_p, is achieved at the passivation potential (E_p), the passive film is about recovering the ensemble of the surface. From this point the current density decreases continuously. When the passivation is complete the current density stays practically constant up to the $E_{pitting}$. A similar behavior is observed in the curve with pH =1 (green line), however the passive plateau is considerably shorter and, in this case, the monotonic increase of the current may be related to transpassive dissolution phenomenon due to the combination of very acidic and oxidizing conditions. As mentioned before, these polarization profiles are characteristic of self-passivating metal-electrolyte interfaces. Very often, depending on the electrolyte, the current density can increase monotonically from the E_{corr} to high current density values without showing a passivation plateau. In such conditions, the steel surface is under active condition during the whole test.

Figure A.2 also illustrates one way of how to estimate the values of the corrosion current density (j_{corr}) of two different curves (pH 1 and 7). In polarization curves of stainless steel, the classical determination of the corrosion current density through the interception between the linear section of cathodic and anodic branches (in log scale) as proposed by the Tafel's theory is not possible due to the presence of the passivation phenomenon, which masks the anodic branch linearity. Based on this, for stainless steels, the corrosion current density can be estimated by the intersection between the linear domain (in log scale) of the cathodic branch and the line of the E_{corr} value, mainly in cases where the passivation plateau is preceded by a anodic current peak like at low pHs in the Figure A.2, otherwise the current density can be straightforwardly assimilated to the passivation current at the plateau level. Although the accuracy of these methods is not as good as that of the ideal Tafel analysis (very often hardly obtainable), the estimated j_{corr} is still an important parameter of the material corrosion resistance. Thus, the corrosion resistance of a stainless steel, in a determined electrolyte, will be consider to be as better as it presents: (i) higher values of E_{corr}; (ii) lower values of I_{corr} or j_{corr} and j_p, the passivation current density;

(iii) and higher domain of passivity, which can be numerically determined by the difference between the $E_{pitting}$ to the E_{corr} or E_p.

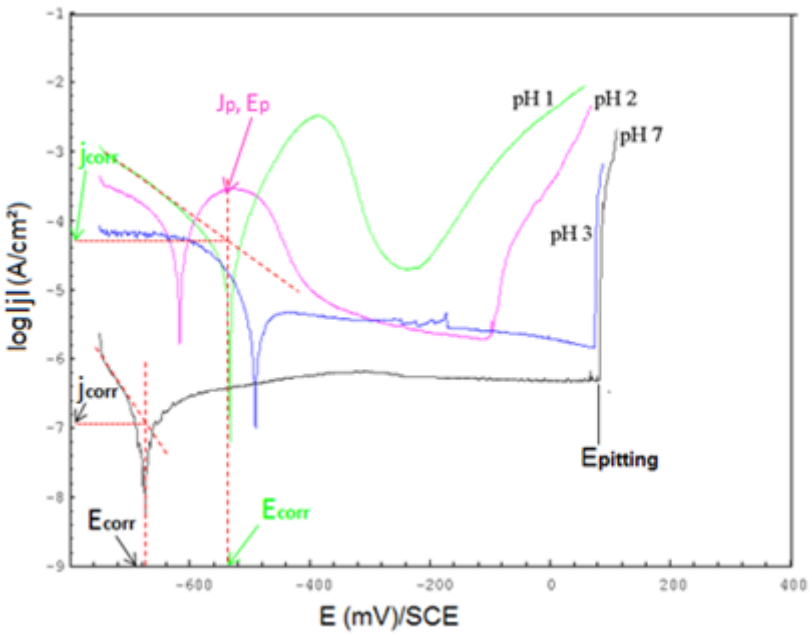

Figure A.2: Polarization curves of AISI 430 ferritic stainless steel in 2M NaCl solution (2M) with different pHs.

Electrochemical impedance spectroscopy (EIS)

EIS technique consists of applying periodic signals of small amplitudes to perturb an electrode-electrolyte interface and measuring the cell response while varying the frequency. For instance, when a sinusoidal potential perturbation with small amplitude and specific frequency (f) is applied to an electrode-electrolyte interface, the interface can be considered as a linear system. In this sense, it is expect to show, as a response to the small amplitude potential (current) excitation, current (potential) signal of the same excitation frequency. In this case, the relationship between the applied potential and measured current response signals is the impedance (Z(ω)), which is expressed in Ohm's law-like form as shown in equation A.4. Where ω is the angular frequency (ω = 2πf, f in Hz), φ is the phase shift between the applied and the response signals, $|Z|$ is the impedance modulus and i is the imaginary number.

$$Z(\omega) = \frac{E(\omega)}{I(\omega)} = \left|Z\right| \exp(i\varphi) = ReZ + iImZ \quad (A.4)$$

Equation A.4 shows that the impedance Z(ω) is a complex quantity presenting a real component (ReZ) and an imaginary (ImZ) component which are expressed by equations A.5 and A.6.

$$ReZ = \left|Z\right| \cos\varphi \quad (A.5)$$

$$ImZ = \left|Z\right| \sin\varphi \quad (A.6)$$

In corrosion experiments, it is common to apply a sinusoidal potential perturbation, with amplitude typically about 10 mV_{rms} (usually around the E_{corr}), to electrode-electrolyte interface. By measuring of the resulting current signal, the impedance of the interface for a specific excitation frequency can be determined. The spectroscopic character of EIS technique results from the fact that Z (ω) is measured over a range of discrete frequencies, usually from 1 mHz to 1 MHz, and presented in impedance diagrams. The two diagrams used to present impedance results are: (i) Nyquist plot where the real and imaginary components of impedance (ReZ and ImZ) are plotted (see Figure A.3 (a)); (ii) Bode plot where impedance is plotted with log frequency on the x-axis and both the modulus value of the impedance (|Z|) and phase-shift (φ) on the y-axis (Figure A.3 (b)). The interpretation of EIS diagrams may bring important information about corrosion process and mechanisms. In stainless steel corrosion, for instance, EIS can give important information about the passive film quality and about the active-passive transition mechanisms [77,78].

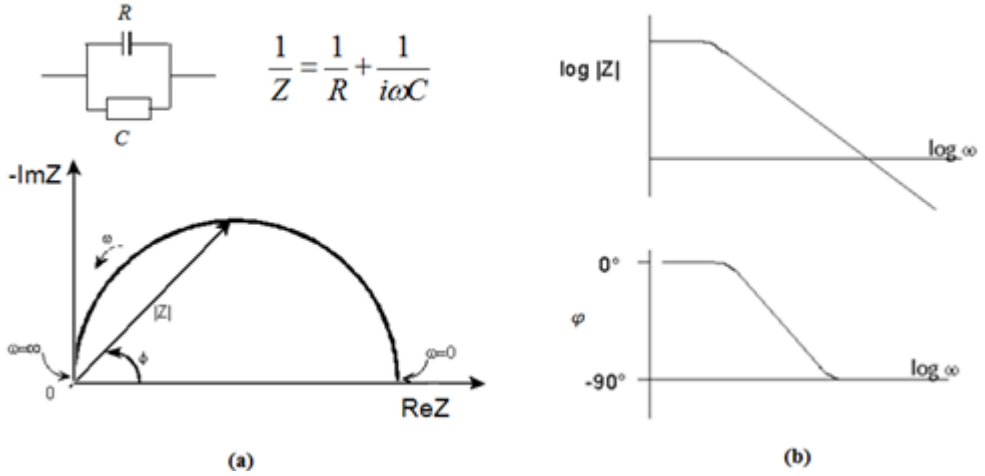

Figure A.3: (a) Nyquist plot and **(b)** Bode plot of a theoretical resistance-capacitor (RC) circuit.

Electrochemical Noise (EN)

Electrochemical noise is referred to the spontaneous current or potential fluctuations in free or polarized electrode-electrolyte interface. In corrosion context, EN phenomena are considered as the result of stochastic processes that can arise from various sources such as time-related uniform or localized corrosion activities taking place on the surface of a corroding metal. Valuable information about the corrosion mechanisms can be obtained from EN data [79–81]. The EN is usually measured using a Zero Resistance Ammeter (ZRA) which combine the potential record with the measurement of the coupling current flowing between two freely corroding electrodes without any external perturbation, thus closely simulating ambient real-world conditions. The ZRA can also be used to measure the galvanic coupling current between two dissimilar electrodes. However, when applied to two identical electrodes like most of the time in corrosion studies, no couple current should a priori be expected to be seen. However, in real situations, even for the same nominal material, two electrodes will always be slightly different, one being more anodic or cathodic than the other and a small coupling current will exist.